PHOTOCHEMICAL PROCESSES FOR DILUTE METHANE OXIDATION AND ATMOSPHERIC METHANE REMOVAL

A DISSERTATION
SUBMITTED TO THE DEPARTMENT OF MECHANICAL ENGINEERING
AND THE COMMITTEE ON GRADUATE STUDIES
OF STANFORD UNIVERSITY
IN PARTIAL FULFILLMENT OF THE REQUIREMENTS
FOR THE DEGREE OF
DOCTOR OF PHILOSOPHY

Richard Randall
November 2025

Abstract

This thesis reports on several years' research on atmospheric methane removal and the mitigation of dilute methane point sources. Methane is a greenhouse gas responsible for a considerable portion of the warming that the earth now experiences, and arresting global methane emissions is a major challenge for global climate change mitigation. The first chapter introduces methane and describes its sources, sinks, and current effects on the climate system. It then reviews the many approaches that have been proposed to chemically destroy methane to prevent its emission or to break down methane in atmospheric air. It concludes with a preview of the following chapters' contents.

The second and third chapters concern methane destruction ("oxidation") using photocatalysts, a class of materials that consume light in order to activate chemical bonds. The second chapter reports experimental work that measured and improved on the performance of methane-oxidizing photocatalysts. The third chapter reports models of the cost-effectiveness of deploying these materials in the real world. Taken together, these chapters suggest that photocatalytic methane oxidation is far from real-world practicality.

The fourth, fifth, and sixth chapters concern methane destruction via "gas-phase advanced oxidation," a promising catalyst-free way to break down gaseous pollutants. The fourth chapter reports experimental work that measured the effectiveness of methane oxidation with chlorine, taking advantage of chlorine radicals' excellent reactivity towards methane. The fifth chapter reports cost modeling of this system's deployment. Taken together, these chapters suggest that chlorine-based methane oxidation is rather costly in most scenarios and its prospects are uncertain. The sixth chapter reports experimental results on gas-phase advanced oxidation with hydrogen

peroxide, which we found to be ineffective for oxidizing methane.

The thesis finishes by discussing the prospects and future of dilute methane oxidation and atmospheric methane removal. This conclusion highlights the ways in which this thesis's research has improved on known methane oxidation processes and has advanced the understanding of which processes are likely or unlikely to be viable. Based on that understanding, it then suggests several possible paths forward for research in the field. Chlorine-based advanced oxidation, thermal oxidation, and thermal catalytic oxidation on methane point sources and chlorine-based advanced oxidation on methane in atmospheric air are called out as particularly promising areas for future work.

A final appendix chapter describes a suite of open-source lab automation software that was developed to streamline benchtop experimental work.

Acknowledgements

I am immensely grateful to the academic community and to the friends and family that have supported me throughout my doctoral research. Though my appreciation is best delivered individually and face-to-face, I will also briefly note it here.

My first thanks go to Arun Majumdar, my doctoral advisor and creator of the Magic Lab at Stanford. Thank you first for creating an environment in which I was free to choose interesting problems and to tackle them in the ways that I thought were best. Knowing that our goals were aligned—to mitigate real methane and to do interesting science along the way—made my research feel like an exciting mission in which I was incredibly well-supported and resourced. Thank you as well for the countless incisive technical comments as well as for the high-level nudges to send my projects in more useful directions. Thank you finally for creating such a rich and diverse environment of students and postdocs from whom I could constantly learn.

I am also grateful for the rest of my research community at Stanford. To Rob Jackson, thank you for letting me informally join your research group for connecting me to the broader methane-mitigation community. To the other members of the Majumdar Lab, thank you for your fellowship in the research trenches and for countless small discussions, lessons, and favors. To Max in particular, I couldn't have asked for a better colleague with whom to explore this field, whether we were thinking big thoughts about methane or wrestling with troublesome pipe fittings. To the members of the Jackson Lab and to the staff of the Product Realization Lab, thank you for giving me my second and third homes at Stanford in the last few years.

Finally, I owe a great debt to my friends and family for their love and encouragement. To my parents, thank you for guiding me to this path and for supporting me along it in every possible way. Without our family values of pursuing education

and working on important problems, I doubt I'd be here. To Chloe, thank you so inexpressibly much for being my closest companion throughout this program. I hope I will soon have the chance to repay you with an equal measure of love and support towards your own dreams. To William, thank you as always for being my oldest friend and for offering good conversations when the times get hard. To all my other friends both near and far, I'm grateful for every minute together over the last few years in activities both exciting and mundane. Those times have been a vital counterbalance to my days working in the lab and have made this period of my life more fun and rich than I could ever have expected.

Contents

Abstract **iv**

Acknowledgements **vi**

1 Introduction **1**

1.1 Climate Forcing and Methane 2

1.1.1 The Effects of Climate Change 2

1.1.2 Methane's Role in the Warming Climate 4

1.1.3 Dilute Methane Sources as "Hard-to-Abate" Emissions 7

1.1.4 Oxidizing Methane to Reduce its Warming Effect 8

1.1.5 Methane Neutrality and Global Sustainability 11

1.2 A Review of Methane Oxidation Approaches 13

1.2.1 The Existing Methane Budget 13

1.2.2 Possible Sites for Methane Oxidation 14

1.2.3 Cross-Cutting Challenges for Methane Oxidation 16

1.2.4 Chemical Processes for Methane Oxidation 19

1.2.5 Outlook 31

1.3 This Thesis's Contribution to the Field 33

1.3.1 The Prior State of the Art 33

1.3.2 Our Lab's Approach: Experiments and Cost Models 34

1.3.3 A Preview of the Thesis's Structure 35

2 Experiments on Photocatalytic Methane Oxidation **37**

2.1 Introduction 38

2.2 Experimental Setup and Reactor Qualification 41

2.2.1 Lessons Learned in Apparatus Design 43
2.2.2 Assessing the Role of Mass Transfer Effects 44
2.2.3 A Typical Experiment with 2-ppm Methane 45
2.3 Figures of Merit: Rates and Quantum Yields 46
2.4 Photocatalyst Synthesis and Characterization 48
2.4.1 Photocatalyst Synthesis 48
2.4.2 ICP-MS Characterization 49
2.4.3 UV-Vis Characterization 50
2.4.4 Transmission Electron Microscopy 51
2.4.5 X-Ray Diffraction 51
2.5 Photocatalytic Rate Measurements in Dry Air 51
2.6 Effects of Light Intensity 55
2.7 Effects of Residual Water and Humidity 56
2.8 Inhibition of Photocatalysts by Humidity 63
2.9 A Humidity-Tolerant Photocatalyst 64
2.10 Conclusion 67

3 Cost Modeling of Photocatalytic Methane Oxidation 69
3.1 Introduction 70
3.2 A Shared Cost Modeling Approach 71
3.2.1 Model of Rate-Limiting Steps for CH_4 Oxidation 71
3.2.2 Further Cost Modeling Assumptions 75
3.3 Photocatalyst-Painted Rooftops 77
3.3.1 Cost Modeling Approach 78
3.3.2 Results 81
3.4 Fan-Driven Photoreactors 82
3.4.1 Cost Modeling Approach 84
3.4.2 Results 88
3.5 Aerosol-Based Solar Photocatalysis 89
3.5.1 Cost Modeling Approach 89
3.5.2 Results 93
3.6 Conclusion 95

4 Experiments on Advanced Oxidation with Chlorine 97
4.1 Gas-Phase Advanced Oxidation 98
4.2 Introduction to Cl_2-GPAO 100
4.3 Experimental Setup and Reactor Qualification 102
4.3.1 Lessons Learned in Apparatus Design 107
4.3.2 A Typical Experiment with 30-ppm CH_4 108
4.3.3 Chlorine Radical Counting Methodology 109
4.3.4 Figures of Merit: Cl_2 and Cl• Efficiencies 112
4.4 Cl_2-GPAO Reaction Products 113
4.4.1 Screening for Chlorinated Hydrocarbons 113
4.5 Effects of Varying the Residence Time 114
4.6 Effects of Varying Inlet Cl_2, CH_4, and H_2O 115
4.7 Effects of Co-Fed Gases 118
4.8 Application-Based Experiments 121
4.9 Conclusion 123

5 Cost Modeling of Advanced Oxidation with Chlorine 124
5.1 Introduction 125
5.2 Modeling Reactor Sizes and Efficiencies 126
5.2.1 UV-Cl_2 Absorption Model with Internal Reflection 126
5.2.2 Model Outputs for Reactor Size 128
5.3 Structure of the Cl_2-GPAO Cost Model 130
5.3.1 Assumed Reagent, Electricity, and LED Prices 130
5.3.2 Relating Efficiencies to Cl_2 and Lighting Costs 133
5.3.3 Modeling Cl_2 and HCl Scrubbing Costs 135
5.4 Total Cl_2-GPAO Costs in Different Scenarios 136
5.5 Conclusion 139

6 Experiments on Advanced Oxidation with Hydrogen Peroxide 141
6.1 Introduction 142
6.2 Experimental Setup and Reactor Qualification 143
6.2.1 Lessons Learned in Apparatus Design 145
6.3 Initial Attempts at H_2O_2-GPAO 147

6.4 No CH_4 Oxidation in Our Final Reactor Setup 150
6.5 A Kinetic Basis for H_2O_2's Poor Performance 152
6.6 Conclusion and Future Possibilities 153

7 Concluding Remarks **155**
7.1 Research Directions for CH_4 Point Sources 156
7.1.1 Thermal Oxidizers 157
7.1.2 Thermal Catalytic Oxidizers 158
7.1.3 Gas-Phase Advanced Oxidation 159
7.1.4 Product-Market Fit and Whole-System Design 160
7.2 Research Directions for AMR 161
7.2.1 Open-System Chlorine Release 161
7.3 Final Words 162

A An Open-Source Lab Automation Software Package **165**
A.1 Introduction 166
A.2 The Need for Laboratory Control Software 166
A.3 Software Capabilities and Functionality 169
A.4 Software Architecture 175
A.5 Safety and Pitfalls 177
A.6 Demonstrations 178
A.7 Conclusion 181

References **183**

List of Tables

2.2 ICP-MS Quantification of Photocatalyst Silver Loading 50

3.2 Inputs and assumptions shared by multiple photocatalyst deployment cost models. 76
3.4 Inputs and assumptions for photocatalyst-painted rooftops 80
3.6 Inputs and assumptions for fan-driven photoreactors 86
3.8 Inputs and assumptions for fan-driven photoreactors (Continued) . . 87
3.10 Inputs and assumptions for aerosolized photocatalysts 92

4.2 Gas tanks used in chlorine experiments 105
4.4 Steps in a standard CH_4-oxidation experiment with chlorine 107
4.6 Gas mixtures in application-based Cl_2-GPAO experiments 121

A.2 List of PyOpticon Widget Types 173

List of Figures

1.1 Global warming effects of various greenhouse gases 5
1.2 Historical atmospheric methane concentrations from 1010 to 2025 . . 6
1.3 Global methane emissions by source concentration 14

2.1 Mechanisms of photocatalytic CH_4 oxidation 39
2.2 Reactor setup for photocatalytic CH_4 oxidation 42
2.3 2 ppm photocatalytic CH_4 oxidation 46
2.4 Photocatalyst UV-Vis Characterization 50
2.5 Mass balance of photocatalytic CH_4 oxidation 52
2.6 Rate data from selected photocatalysts 53
2.7 Additional photocatalyst rate data 54
2.8 Effects of UV flux on CH_4 oxidation rates 55
2.9 Photocatalyst in-situ DRIFTS results 57
2.10 Gases Released in TPD Experiments 58
2.11 Residual surface species on photocatalysts 60
2.12 TEM characterization of ZnO-Ag (1wt%) 61
2.13 TEM characterization of TiO_2-based materials 61
2.14 Post-TPD Oxidation of 2-ppm CH_4 62
2.15 Effects of humidity on photocatalytic CH_4 oxidation 63
2.16 Characterization of TiO_2-FS 64
2.17 TEM characterization of TiO_2-FS 65
2.18 Photocatalytic CH_4 oxidation with TiO_2-FS 67

3.1 Graphical summary of photocatalyst deployment strategies 72
3.2 Mass transfer model for a photocatalyst-painted rooftop 78

3.3 Modeled costs of rooftop photocatalytic CH_4 oxidation 81
3.4 Mass transfer model and cost model for fan-driven photoreactors . . . 83
3.5 Modeled costs of CH_4 oxidation in fan-driven photoreactors 88
3.6 Schematic and mass transfer model of photocatalytic aerosols 90
3.7 Modeled costs of CH_4 oxidation on photocatalyst aerosols 93

4.1 Summary of gas-phase advanced oxidation processes 99
4.2 Graphical summary of Cl_2-GPAO 101
4.3 Experimental setup for CH_4 oxidation with chlorine 103
4.4 Image of the chlorine photoreactor 104
4.5 Demonstration of CH_4 oxidation with chlorine radicals 108
4.6 Measurements of chlorine radical production 111
4.7 Demonstration of CH_4 oxidation with chlorine radicals 112
4.8 Effects of residence time on CH_4 oxidation with chlorine 115
4.9 Effects of basic parameters in CH_4 oxidation with chlorine 117
4.10 Chlorine radical production in various conditions 118
4.11 Effect of contaminants on CH_4 oxidation with chlorine 119
4.12 Chlorine-based CH_4 oxidation with realistic gas mixtures 122

5.1 Relationships between chlorine photoreactor size and efficiencies . . . 129
5.2 Costs of reagents and electricity in different scenarios 131
5.3 Chlorine-based CH_4 oxidation costs in different scenarios 137

6.1 Schematic of setup for CH_4 oxidation with hydrogen peroxide 144
6.2 Images of setup for CH_4 oxidation with hydrogen peroxide 146
6.3 Early results for CH_4 oxidation with hydrogen peroxide 149
6.4 Experimental results for CH_4 oxidation with hydrogen peroxide . . . 151

A.1 A PyOpticon dashboard in use 170
A.2 Detail image of a PyOpticon widget 171
A.3 Schematic of the processes inside a PyOpticon dashboard 176
A.4 Image of the PyOpticon dashboard used in the demonstration 179
A.5 Results from a PyOpticon demonstration experiment 181

Chapter 1

Introduction

1.1 Climate Forcing and Methane

1.1.1 The Effects of Climate Change

In the past ten years, during which the entirety of my engineering education took place, global climate change has evolved from a selfdom-discussed environmentalists' and academics' concern to an unignorable fact of life. The multi-year drought in California ending in 2017 was the longest on record. In Spring of 2019, a heat wave overwhelmed Stanford's campus cool-water system, causing everyone in my dorm to spend finals week working in our basement to escape the hundred-degree heat on the other floors. In 2020, the Northern Californian sky turned orange with smoke from wildfires stoked by unseasonable dryness and heat. In January of 2025, large areas of Los Angeles itself burned.

The changes are also clear in less acute ways. The season for warm-weather recreation in the Sierra Nevada now extends through the winter, with shirtsleeve weather in Yosemite commonplace in January. In the summer, even high-altitude areas like Tahoe and Tuolumne Meadows now give little respite from the heat. Glaciers and snowfields referenced in Sierra hiking guidebooks written in the 1970s have now vanished or shrunk to tiny remnants. The "atmospheric river" rainstorms that punctuate the Californian winter have become more intense while oceanfront communities are experience increasing rates of coastal erosion.[1–3]

These are only local manifestations of a global transformation. June of 2024 marked the twelfth consecutive month with global average temperatures more than 1.5°C above the pre-industrial average, marking the passage of a milestone that was once an optimistic target for climate action.[4] 2024's annual minimum and maximum extents of arctic sea ice were each the second-lowest on record.[5] A global set of reference glaciers has lost, on average, more than 25 tons of ice per square meter (corresponding to ∼27m of thickness) since 1970, with the rate of ice loss continuing to increase during the 2020s.[5] In 2024, the World Meteorological Organization reported 152 weather events of "unprecedented" intensity, of which 57 were heat waves, 30 were rain events, and 23 were floods.[6] Climate modeling has allowed the attribution of an increasing number of such events to climate change: for example, models have estimated that the summer 2021 heat wave in the Pacific Northwest would have been

1-2 orders of magnitude less likely without anthropogenic climate effects.[7, 8] The world's average ocean surface temperature in 2024 was ~ 0.6°C above a 1981-2010 baseline, with much greater temperature anomalies occurring at particular places and times.[9] As of April 2025, a multi-year global coral bleaching event that began in 2023 was ongoing, with more than 83% of global coral reef area have experienced enough heat stress to cause coral bleaching.[10] During the last such event, which lasted at a global scale from 2014 to 2017, the Great Barrier Reef lost 30% of its coral cover within a single eight-month period.[11, 12]

The human impracts of climate change are already felt in a number of ways. Changing climactic conditions, particularly aridity and drought, already substantially influence global migration patterns, particularly in agriculture-dependent regions.[13] Low-lying and island nations already experience the effects of rising sea levels.[14, 15] It has been projected that by 2050 more than 140 million people in the Global South will have been displaced by climate change-related events, including drought, food scarcity, and sea level rise.[16] A variety of particularly severe past weather events, each with substantial human impacts, have been directly attributed to climate change through climate modeling.[17] For example, the 2021-22 drought in the Horn of Africa region, which left over 4 million people in need of humanitarian aid due to crop failures and livestock deaths, was intensified by climate change.[18] Although it affected two developed countries with widespread access to air conditioning, the previously mentioned 2021 Pacific Northwest heat wave led to over 800 deaths in the United States and Canada.[19] Such events will only grow more common, and the causal links with climate change easier to draw, in the coming decades.

The main mechanism behind climate change is the greenhouse effect.[20] Governed by the laws of black-body radiation, the sun mostly transmits energy to the earth as visible light, while the earth releases energy back into space as infrared light. Like the glass in a greenhouse, molecules that let visible light pass but absorb infrared light allow energy to enter the earth-atmosphere system but prevent it from leaving, tending to increase the earth's temperature. Carbon dioxide released by fossil fuel combustion causes the most warming of any individual greenhouse gas, although methane, which this thesis mainly concerns, also plays a significant role.

Following more than a century of research on various climate-forcing and meteorological phenomena, modern climate science paints a clear and detailed picture of a planet that is being warmed (and otherwise affected) by emissions from a wide variety of human activities.[20] The current state of the field, aggregated from hundreds of individual peer-reviewed publications, is regularly summarized by the Intergovernmental Panel on Climate Change (IPCC). In its Sixth Assessment Report in 2021 [21], the IPCC wrote that *"it is unequivocal that human influence has warmed the atmosphere, ocean and land"* and that *"climate change is already affecting many weather and climate extremes in every region across the globe."* It warned that *"warming of 1.5°C and 2°C will be exceeded during the 21st century unless deep reductions in CO_2 and other greenhouse gas emissions occur."* The engineering, science, organizing, and policy work required to do so constitutes one of the great challenges of our time.

1.1.2 Methane's Role in the Warming Climate

Methane (CH_4) causes the second most global warming of any human-emitted gas and as such is a major contributor to climate change. As shown in figure 1.1, in 2019 the warming due to emissions of methane was 0.6°C while that due to carbon dioxide was 1.0°C. These values add up to more than the actual ∼1°C of warming experienced in 2019 because other human emissions like sulfur dioxide have substantial cooling effects. Carbon dioxide has received the most attention to date, both because of its large warming effect and because the main remedy is fairly simple: stop burning fossil fuels. Methane has historically received somewhat less attention, but it has become increasingly clear that carbon dioxide mitigation alone will be insufficient to stop climate change.[22] Methane has consequently enjoyed a wave of interest in the research community in the last several years, a trend that helped to launch and sustain the work in this thesis.

Methane is emitted from a variety of natural and anthropogenic sources.[24] Fossil methane is released from underground geologic reservoirs by human activity. Some fossil methane is extracted as natural gas and leaks as "fugitive" emissions throughout the natural gas value chain. Other fossil methane is released as an unwanted byproduct of oil and coal extraction. Biogenic methane is produced by methanogenic microorganisms that fuel themselves by decomposing complex hydrocarbons into

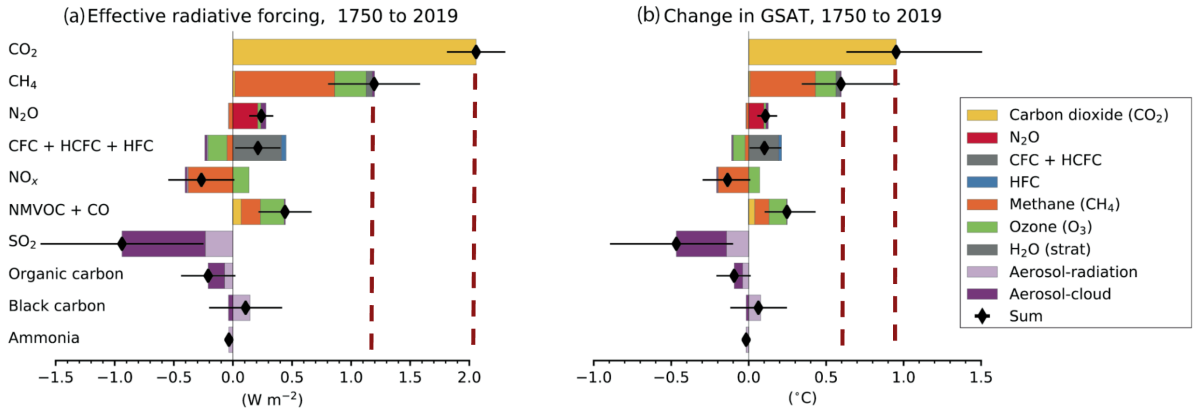

Figure 1.1: Climate effects of different greenhouse gases, reproduced from the IPCC 6th Assessment Report.[23] Horizontal bars show the changes in a) radiative forcing from 1750 and b) global surface average temperature (GSAT) from 1750 attributable to different gases and aerosols. Each row corresponds to the effects of *emissions* of a single gas, while each horizontally-stacked bar within a row corresponds to the gas that *actually interacts with light* For example, emitting methane (2nd row) causes warming due both to methane's own greenhouse effect (orange bar) and due to released methane's indirect effect of boosting tropospheric levels of the greenhouse gas ozone (green bar).

methane in anaerobic environments, which occurs wherever organic matter decomposes underwater or with poor ventilation. This takes place in landfills, wastewater systems, rice paddies, and natural wetlands, as well as in in ruminant animals' (e.g., cows') digestive tracts. Collectively, human activities have raised atmospheric methane concentrations from ∼0.6 parts per million (ppm) in pre-industrial times to ∼1.9 ppm in 2024 [24], as shown in 1.2 I will return later to the contributions of different source types to global methane emissions.

Methane differs from carbon dioxide in that its per-molecule warming potential is far higher and its atmospheric lifespan is much shorter.[28] Each molecule of methane traps about 41 times as much heat as each molecule of carbon dioxide. Converted into more commonly used mass-based global warming potentials (GWPs), a kilogram of methane just after its emission causes 114 times as much warming as a kilogram of carbon dioxide. However, since free radicals in the atmosphere slowly oxidize methane to carbon dioxide, methane's average atmospheric lifespan is only 7-12 years.[25] In

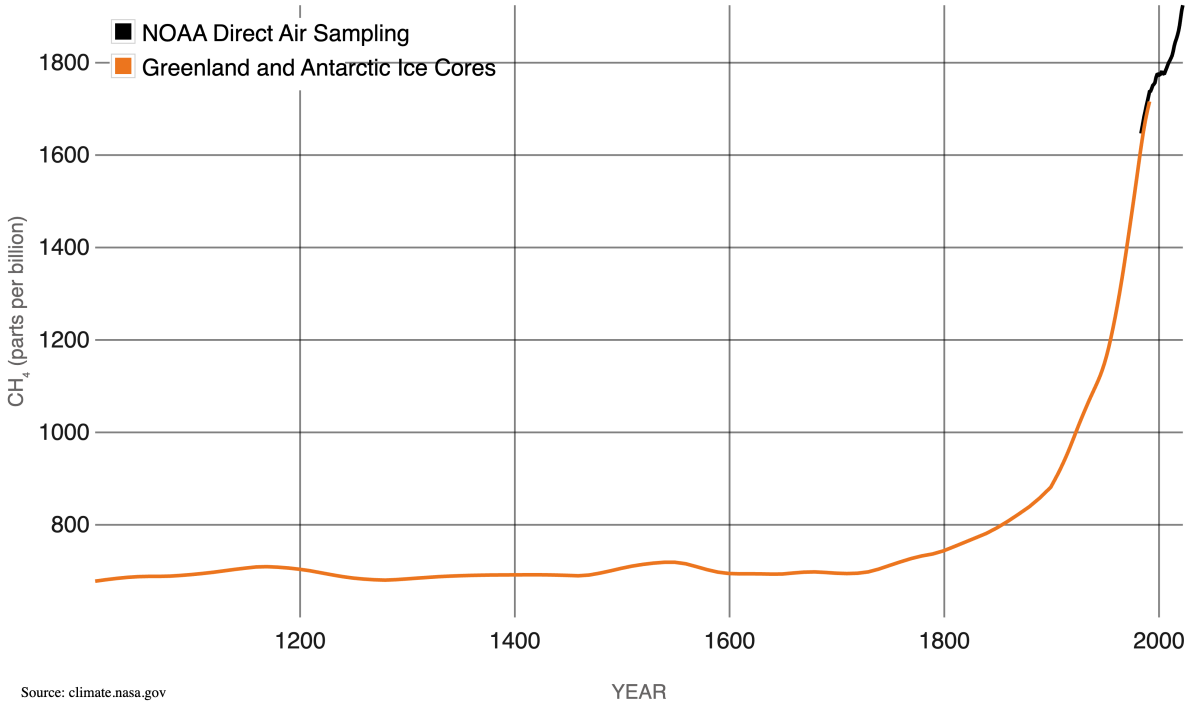

Figure 1.2: Historical atmospheric methane concentrations from 1010 to 2025, reproduced from NASA.[25] The underlying data are from the NOAA Global Monitoring Laboratory and from Etheridge at al. 1998.[26, 27]

comparison, carbon dioxide's lifespan is over 100 years.[28] Thus, while a pulse of carbon dioxide causes steady warming over many decades, a pulse of methane causes a several-year spike of warming that quickly dissipates as the methane breaks down.

These fundamentally different warming behaviors complicate the valuation of methane abatement relative to carbon dioxide abatement. Implicit in a methane-to-carbon dioxide conversion factor is the choice of a time horizon over which warming is integrated, which is essentially a judgement on the relative values of avoiding near-term and long-term warming effects. The twenty-year global warming potential (GWP20) of methane is 81.2, while the more commonly-used hundred-year global warming potential (GWP100) is 27.9.[23] I will return later to how these considerations can inform concrete cost targets for methane abatement strategies.

1.1.3 Dilute Methane Sources as "Hard-to-Abate" Emissions

The recent history of fossil fuel displacement has mainy been the history of a few highly successful technologies. Electrical utilities worldwide have rapidly adopted solar energy, wind energy, and lithium-ion batteries as manufacturing advances have driven down their costs.[29] Electric car adoption has also accelerated substantially, in part due to declining production costs.[29, 30] A number of other energy end uses, including building heating, water heating and various light industrial loads, can be electrified relatively easily with current technology.[31, 32] The net result is that there now exist plausible pathways to zero-emission power grids, vehicles, and buildings, althougg much more work is needed to ensure their continued growth and deployment.

With the "decarbonization" of these sectors well under way, the world in the 2020s is grappling with other more challenging emissions sources. Much academic and translational research currently focuses on so-called "hard-to-abate" sectors of the economy, sometimes also termed "hard-to-decarbonize" where mainly carbon dioxide is emitted.[33, 34] Hard-to-abate sources of carbon dioxide include shipping, aviation, dispatchable power generation, and heavy industries like steel, cement, and fertilizer.[33] In each case, fossil fuels are hard to displace due to some combination of their cheapness and energy density. In some cases such as cement production, the underlying chemical reaction also releases carbon dioxide, meaning that switching energy sources is not enough to eliminate the process's emissions.

Methane abatement has similarly received attention in the last several years as a next frontier of engineering research for climate change mitigation.[35, 36] This attention in part reflects an understanding that methane abatement is essential to meeting warming targerts and in part reflects the technical challenge of abating most methane sources outside of the fossil fuel industry. As in the hard-to-decarbonize sectors, with many such sources there is no obvious way to produce the same product or service without methane emissions. Also like the hard-to-decarbonize processes, the methane-emitting processes tend to provide very cheap products or services (whether making beef, growing rice, or decomposing food waste) to buyers who are resistant to price increases.

Hard-to-abate sectors can be dealt with in several ways: reducing demand, developing alternative zero-emission processes, capturing/destroying emissions at their

source, or offsetting emissions via atmospheric greenhouse gas removal. In the hard-to-decarbonize sector of steelmaking, these options might correspond to building with wood rather than steel, developing zero-emissions electrochemical steelmaking, applying post-combustion carbon capture to an existing steel mill, and offsetting a steel mill's emissions using carbon dioxide removal.[37] In the hard-to-abate sector of beef ranching, they might correspond to convincing people to eat less red meat, developing cattle vaccines or feed additives that reduce enteric methane production, installing methane-destroying devices in barn ventilation systems, and performing "atmospheric methane removal" to offset a herd's emissions.[38] Reducing the demand for methane-intensive products and developing low-methane ways to make the same products are essential areas of research and are likely to yield substantial opportunities for emissions reductions.[39] However, it is possible that in some sectors these efforts will not be enough, making the study of other options worthwhile.

1.1.4 Oxidizing Methane to Reduce its Warming Effect

Methane's global warming effects can be largely mitigated if it is chemically oxidized. This mainly takes place according to the following thermodynamically favorable net reaction:

$$CH_4 + 2O_2 \rightarrow CO_2 + 2H_2O \tag{1.1}$$

In this reaction, the products have only 4-10% of the global warming potential of the reactants depending on the time horizon chosen, meaning that the reaction reduces methane's warming effect by 90-96%.[28] In some instances, methane may alternatively be oxidized to carbon monoxide according to this net reaction, which is also thermodynamically favorable:

$$2CH_4 + 3O_2 \rightarrow 2CO + 4H_2O \tag{1.2}$$

In that reaction, the products have a global warming potential of 6-21% of the global warming potential of the reactance, since carbon monoxide has a small indirect global warming potential.[40] While carbon dioxide is the preferred reaction product,

oxidizing methane to carbon monoxide is still climate-beneficial and may be acceptable where the final carbon monoxide concentration is below the safe exposure level of ∼50 ppm.[41]

A qualitative appeal of methane oxidation is that it can in principle take place anywhere and generate no byproducts besides benign gases released into the air. In this respect it is different from carbon dioxide capture, whether from point sources or from atmospheric air, in which some kind of carbon-containing product must be isolated and permanently sequestered. Indeed, at fossil fuel and waste management sites where gas with high ($> 4\%$) methane concentrations must be disposed of, it is common practice to "flare" (combust) it rather than "vent" (release) it.[42] Flaring is a technically straightforward and highly climate-beneficial process that prevents most of the methane from reaching the atmosphere.[43] Capturing a similar 4% carbon dioxide from a power plant's exhaust is, in contrast, a highly complex and rarely undertaken emissions-reduction option.[44, 45]

Despite that appeal, methane oxidation is highly challenging because of methane's typical low concentrations and its molecular properties.[46] Whereas exhaust fossil fuel combustion usually contains 1-20% carbon dioxide, most methane sources outside of the oil and gas sector have methane concentrations of less than 0.1% (1000 ppm).[42] Similarly, atmospheric air contains ∼440 ppm of carbon dioxide but only ∼2 ppm of methane. Methane is also highly stable, with an activation energy of 414kJ/mole (4.6 eV per bond) for its C-H bonds, meaning that despite the favorable thermodynamics of methane oxidation, it is relatively difficult to instigate an oxidation reaction without high temperatures.[47] These challenges mean that, although methane oxidation is thermodynamically downhill, oxidizing dilute methane generally requires a net energy input. Finally, methane is nonpolar, making it insoluble in water and impractical to separate via its dipole or quadrupole moments as can be done with carbon dioxide.[46] I will discuss these challenges and their possible solutions in more detail later.

The Appeal of Methane Oxidation at Dilute Point Sources

While methane oxidation at high-concentration point sources (i.e., flaring) is a mature technology, there is good reason to develop ways to do so at low-concentration point sources. I use the terms "dilute" and "low-concentration" interchangeably to refer

to methane sources whose exhaust contains fewer than 1000 ppm of methane. This describes most methane sources outside of the oil and gas sector, including sources in ranching, farming, and waste management.[42] Abating the methane emissions from some such sources could be a valuable way to mitigate their global warming effect without dramatically changing the underlying processes or curtailing demand for their products.

The Appeal of Atmospheric Methane Removal

Where abatement of hard-to-decarbonize sectors fails, carbon dioxide removal (CDR) may provide a way to offset ongoing emissions. CDR has recently been a topic of considerable research and development interest, with various approaches (mechanical, geochemical, biological, and otherwise) aiming to inexpensively capture and permanently sequester atmospheric carbon dioxide.[48] A number of IPCC scenarios include large amounts of CDR to offset ongoing emissions.[39] CDR also serves in these scenarios to "undo" historic emissions and return atmospheric carbon dioxide to its pre-industrial concentration.

"Atmospheric methane removal" (AMR) could plausibly offset hard-to-abate methane emissions in the same way that CDR can offset hard-to-abate carbon dioxide emissions.[49] A viable AMR process would be highly appealing because, as noted above and explained in greater detail below, a majority of methane emissions are hard to abate at their source. Given the difficulty of, for instance, eliminating beef from the global food system, a cost-effective and scalable AMR process to offset emissions from cattle would be quite valuable for reaching methane neutrality. Additionally, natural methane emissions are subject to a number of global temperature feedbacks. AMR could provide a way of mitigating accelerated natural methane emissions due to, for instance, millions of square miles of warming wetlands around the world.[49] Although AMR is extremely challenging, a cost-effective and practical AMR process would be a great boon for climate change mitigation, a thought that motivated me to choose this field for my doctoral research.

1.1.5 Methane Neutrality and Global Sustainability

Although this thesis is necessarily narrow in focus, I wish to note that climate neutrality is about more than simply abating or offsetting the greenhouse gas emissions from our current patterns of consumption, and also that sustainability is about more than greenhouse gas neutrality.

First, the greenhouse effect is only one of many ways that our environmental impacts are harming humanity's welfare and the earth's biosphere. Particulate air pollution, which causes millions of deaths per year, is a disastrous effect of fossil fuel use entirely aside from the release of carbon dioxide and methane.[50, 51] The widespread destruction of natural ecosystems, e.g. razing tropical forests to create farmland and ranchland, is as catastrophic to global biodiversity as it is to the climate.[52, 53] Many of the extractive industries and chemical conversion processes that underpin modern life release hazardous pollutants into neighboring ecosystems and communities.[54–57] Challenges of land use, energy availability, and pollution will only grow as more of the planet's eight billion inhabitants attain the material- and energy-intensive lifestyle that we in the United States take for granted.[58]

Second, environmental justice is a key aspect of the climate transition that can be lost in purely technical and economic framings of the problem. The impacts of climate change will most severely affect the countries and invididuals with the fewest resources to adapt.[59] Conversely, wealthy countries and individuals emit the most and have the most resources to reduce their emissions, but may be less incentivized to do so because they can adapt more easily. The existing energy, transportation, industrial, and agricultural sectors disproportionally pollute and otherwise affect historically disadvantaged populations, such as communities of color.[60, 61] In rebuilding each of these systems to eliminate their emissions, we must be sure not to repeat the same pattern. Finally, despite offering a steadily rising quality of life, the modern world economy allows striking levels of inequality and precarity to persist even in "wealthy" countries.[62, 63] This is a challenge worth facing for its own sake, but is also closely linked to climate action. On the one hand, seemingly unfulfilled promises of economic prosperity tend to strengthen reactionary populist movements that oppose climate action. On the other hand, political agendas that package climate action with other social and economic programs may generate broader support than could be found for

narrowly targeted environmental agendas.

A sustainable and just world must find solutions the full range of these challenges; however, the narrower goal of reducing net greenhouse gas emissions remains a dire necessity with a strict deadline. To that end, this thesis focuses on strategies to abate methane's climate-warming effect by destroying it at its sources or by removing it from the atmosphere. However, especially in a thesis that often references "dollars per ton of methane abated" as a useful figure of merit, it is essential to remember that global sustainability cannot and must not be equated with simply finding the least-cost greenhouse gas-neutral replacement for the exact economy and energy system that we have today.

1.2 A Review of Methane Oxidation Approaches

1.2.1 The Existing Methane Budget

Despite the urgency of addressing climate change, anthropogenic methane emissions and global methane concentrations continue to rise. Between 2018 and 2020, total global methane emissions averaged about 610 megatons (teragrams) per year, contributing 0.6°C of warming.[64, 65] Of those, 370 megatons were from direct anthropogenic sources such as fossil fuel production, waste, and agriculture. This value has risen 15%-20% since the period from 2000-2002. The remaining 240 megatons are a combination of indirect anthropogenic sources like reservoirs and natural sources like wetlands. More than two thirds of total methane emissions were from direct or indirect anthropogenic sources. Roughly trebling the pre-industrial flux of methane into the atmosphere has led to global methane concentrations about 2.6 times the pre-industrial average.[64]

The atmosphere's natural oxidizing capacity accounts for nearly all of the existing methane sink.[64] This oxidation is mediated by radicals, which are unstable but highly reactive gas species generated by atmospheric photochemistry. The hydroxyl radical (OH•), generated by a series of reactions initiated by the photolysis of ozone, accounts for about 93% of natural methane oxidation.[64] Soil microbes account for about 6%. The chlorine radical (Cl•), generated by sea salt-related photochemistry near the ocean surface, accounts for about 0.5%. In total, in 2018-2020 these sinks oxidized about 540 megatons of methane per year, causing the atmospheric methane stock to increase by about 70 megatons per year over that period.[64]

It is also worth noting that substantial fluxes of methane are oxidized before they ever reach the atmosphere. On the order of 3300 megatons of natural gas, which consists of >90% methane, is burned each year.[66, 67] The few percent of natural gas that leaks without burning contributes a large fraction (∼120 megatons per year) of anthropogenic methane emissions. Methane-consuming bacteria in a variety of human-impacted and natural landscapes also oxidize methane produced by biomass decomposition that would otherwise enter the atmosphere[68, 69]

1.2.2 Possible Sites for Methane Oxidation

Figure 1.3 gives some intuition for where methane oxidation might be deployed. For reasons that I will discuss below, different methane oxidation approaches work best in different ranges of methane concentrations. For instance, at more than $5{\cdot}10^4$-ppm (5%) levels, methane can simply be flared/burned in a flame, but at lower levels, some type of oxidizing device is required. It is therefore useful to categorize methane emissions sources by the methane concentration in the emitted gas stream and to consider which concentration ranges offer the greatest potential for methane abatement.

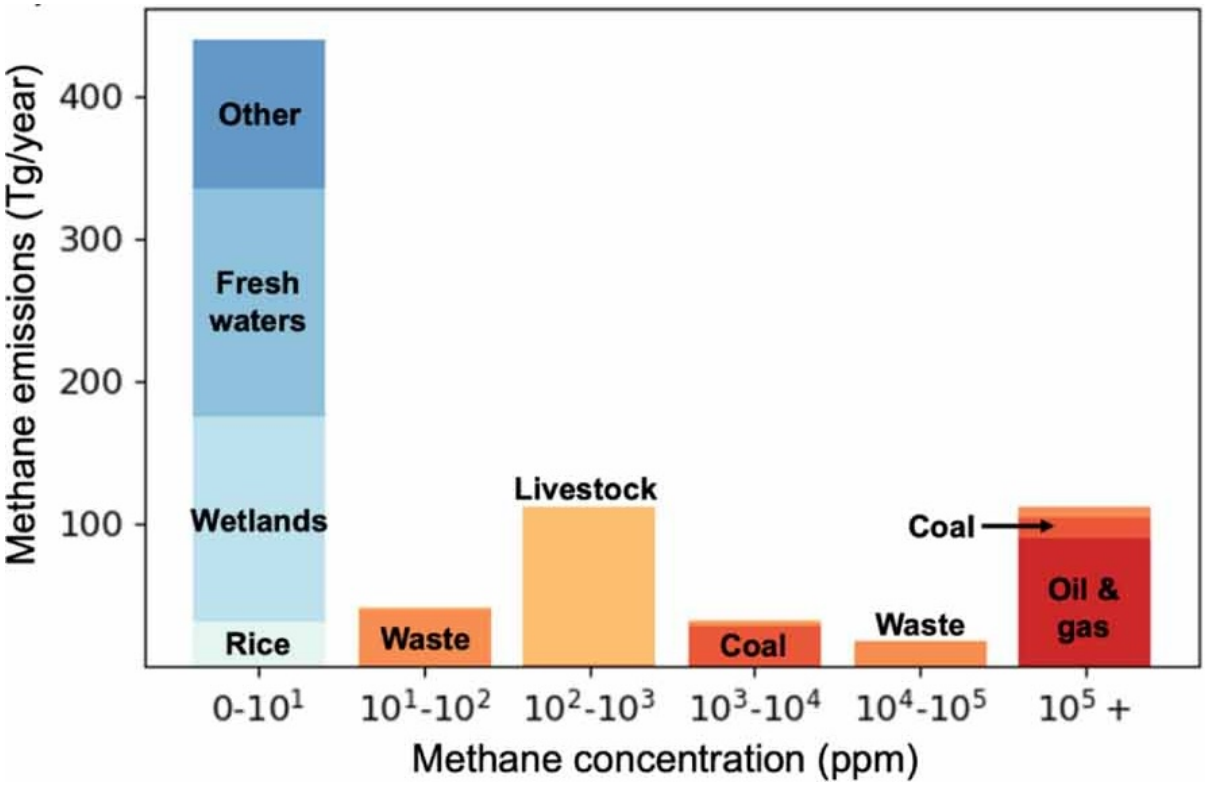

Figure 1.3: Global methane emissions grouped by their estimated average concentrations at the points of emission, reproduced from Abernethy et al. 2023.[42]

Methane emitted at above 1000 ppm, shown in the rightmost three columns in Figure 1.3, contributes a large portion of methane emissions but can be abated with

current commercial technologies. Highly concentrated sources with $>10^5$ ppm of methane can be abated with flaring, which could contribute up to about 110 megatons of methane emissions reductions. Thermal oxidizers and perhaps biofilters, both discussed below, can oxidize methane at concentrations of 10^3-10^5 ppm. These devices could enable a further about 50 megatons of additional methane emissions reductions. Well-known oxidizing technologies like these (as well as emissions avoidance measures) should be deployed with all possible haste. Together, they could address 20-25% of global methane emissions and about 0.23℃ of global warming.[42]

Methane emitted at between 10 and 1000 ppm cannot be oxidized with current commercial devices, though doing so would be helpful for mitigating climate change. I term such devices 'dilute point-source methane oxidation' or 'methane scrubbers.' Oxidizing or avoiding all methane emitted in this range would address about 150 megatons of emissions and would avoid a further 0.15℃ of global warming.[42] However, I note that 110 megatons of this is from livestock, where the authors of Figure 1.3 used a value of 600 ppm sampled directly from a cow's breath. Whereas most of the other concentrated methane streams are in a duct or flow where a large fixed device could be deployed, implementing point-source oxidation on 600-ppm cow breath is likely to be difficult in practice. One approach is to target the lower but still elevated methane concentrations in enclosed barns [70], though this does not help address emissions from cattle that spend their time outdoors.

Finally, a huge amount of methane is emitted from highly diffuse (2-10 ppm) sources that are not amenable to "flow reactor" oxidation schemes. Figure 1.3 shows that such sources account for more than half of global methane emissions. Some fraction of these emissions may be avoided by intervening at anthropogenic sources (e.g., rice paddies and reservoirs) or in natural systems. However, doing so may not drive these sources' emissions all the way to zero, and climate feedbacks may tend to boost them in spite of avoidance efforts. In this context, cost-effective atmospheric methane removal (AMR) – which would offset these highly dilute methane sources – could be very useful, whether to negate ongoing anthropogenic emissions or to counter rising natural methane emissions. In principle, AMR could mitigate all of methane's current warming effect or even force methane levels below pre-industrial levels to create a cooling effect.[42]

1.2.3 Cross-Cutting Challenges for Methane Oxidation

Methane's Stability and Apolarity

Methane (CH_4) is a difficult molecule to chemically manipulate for two main reasons. First, it consists of four identical and very stable carbon-hydrogen (C-H) bonds. Each has a relatively high activation energy of 414kJ/mole (4.6 eV per bond).[47] This bond is thermally activated at temperatures around 900℃ [71], a number that catalysts or enzymes can lower.[46] Charge carriers and/or radicals can also overcome the activation barrier at temperatures where thermal activation cannot occur. Second, methane has a symmetrical tetrahedral structure with neither a dipole moment or quadrupole moment.[46] This means that it absorbs very weakly on most materials, which makes methane concentration via selective sorption impractical and also makes it difficult for methane-oxidizing catalysts to acheive high rates. Finally, methane has a very low aqueous solubility and a low Henry's law coefficient in water, hindering any processes like microbial methane oxidation that take place in aqueous solution.

Process Engineering Challenges at Low Methane Concentrations

Methane's chemical traits and available concentrations create both opportunities and challenges for developing climate-beneficial methane oxidation processes. On one hand, the combination of low available concentrations and slow rates makes methane a difficult oxidation target, especially with current materials. On the other hand, the prospect of destroying methane and simply releasing the products to the atmosphere is quite appealing. Unlike carbon capture, such a process would generate no product to be sequestered, and in principle could proceed only with the energy contained in methane's bonds. Several authors have pointed out the challenges of dilute methane oxidation and especially of AMR for the above reasons.[72, 73] However, in my opinion, only detailed study of individual approaches can reveal whether and where dilute methane's oxidation's upsides can overcome its difficulties to enable useful and scalable processes.

Low target gas concentrations are a challenge for greenhouse gas and pollutant abatement processes, though they are not insurmountable on their own. Industrial pressure- and temperature-swing gas separations such as the amine-based processes

used in point-source carbon capture have historically mainly been used with gas streams containing more than about 1% of the target gas.[74] However, there has been some commercial success using temperature-swing sorbents to capture 440-ppm atmospheric carbon dioxide.[48] A variety of other reaction-based (rather than sorption-based) processes have also been developed to capture 440-ppm carbon dioxide. Additionally, mature industrial emissions-control devices can reactively capture single or tens of ppm of gaseous pollutants from exhaust gas streams.[75, 76] These "gas scrubbers" are often deployed to mitigate 1-1000 ppm levels nitrogen oxides (NOx), sulfur oxides (SOx), hydrogen chloride, and hydrogen fluoride. Some of these dilute gas scrubbing processes attain costs in the hundreds or thousands of dollars per ton mitigated.[77], comparable to the cost targets for methane mitigation that are discussed below.

However, the combination of methane's chemical traits and low concentrations make it a challenging target for emissions controls or air capture. For the reasons mentioned above, no commercial sorbents are available to selectively bind methane and most heterogeneous (surface-based) methane oxidation processes are very slow.[46] With slow rates, air must remain in contact with the active material (i.e., the catalyst or biofilm) for a long time in order for a large fraction of its methane to react: while a power plant NOx/SOx scrubber has a residence time of a few seconds [78], a methane-consuming biofilter needs one of around 10-15 minutes [79] In enclosed systems, this means that for a fixed air throughput the air must be forced through a deeper bed of catalyst to achieve a given conversion. A deeper bed increased the costs of both the reactor and the electricity used in fans and/or blowers. Minimizing the "pressure drop" that the fans/blowers must overcome becomes critically important when low (<1000 ppm) gas concentrations are targeted.[80] Doing so is possible with fast rates, like those of hydrogen chloride or carbon dioxide with strong aqueous bases, but is very challenging with sluggish reactions. Optimizing catalysts' and microbes' reaction rates with dilute methane is therefore an important area of research.

These difficulties beg the question of whether we can somehow bypass the difficulties of surface-based methane oxidation in flow reactors. One possibility is to use heterogeneous reactions with some sort of natural air circulation rather than

fans. Strategies to do so include painting photocatalysts on rooftops, enhancing natural soils' uptake of atmospheric methane, and deploying methanotrophic biocovers over methane area sources. Another strategy is to use processes that do not require methane transport onto a surface or into solution. Gas-phase advanced oxidation and atmospheric oxidation enhancement are two such approaches. Purely thermal oxidation is in a sense another such approach, since surfaces heat the bulk air stream and do not rely on any surface interactions with methane molecules in particular. All of these options are discussed in detail below.

Cost Targets for Scalability

Last, for a methane oxidation approach to be viable, someone must be willing to pay the cost to deploy and operate it. While different actors' actual willingness to pay will not be known until the methane abatement market matures, at this stage of research it is still useful to have rough cost targets to benchmark cost models' outputs. We can generate specific cost targets in several ways.

A simple approach is to interconvert carbon dioxide and methane mitigation cost targets using methane's global warming potential (GWP). Because of methane's short lifespan its GWP varies by a factor of more than 3 between 20 and 100-year time horizons, making any resulting cost target fairly crude, though perhaps still useful. Converting a dioxide removal cost target range of $25-100 per ton [81] using 20 and 100-year methane GWPs of 27.9 and 81.2 [28] gives a target methane mitigation cost range of $700-$8100 per ton of methane.

An alternative approach would be to use a "social cost of methane" (SCM). These numbers attempt to calculate the social and economic damage caused by emitting a marginal ton of methane in a given year. Estimates span a wide range of values. One study estimated that the SCM in 2020 was $4000.[82] A different study estimated an SCM of $930.[83] The U.S. Environmental Protection Agency estimated SCMs of $1600 in 2020, $2400 in 2030, $3300 in 2040, and $4200 in 2050.[84]

One can also look to existing and proposed government policies that value methane abatement. The United States' Inflation Reduction Act of 2022 planned to impose a fee of $1500 per ton on methane emissions from oil and gas infrastructure, the first fee of its kind in the world.[85] The fee has since been cancelled. Anaerobic

digesters in California have also historically been incentivized with compliance credits worth on the order of $2000 per ton of methane, although the exact value fluctuates considerably based on the credit prices.[86]

A final approach would be to assess the "green premium" that comsumers are willing to pay for a methane-free product over a conventional one. For instance, a recent study in Denmark found that buyers would pay 7.4 Danish Kroner (∼$1.1) per liter for low-methane milk.[87] Since only about 20 grams of methane are emitted per liter of milk produced [88], this implies that those consumers are willing to pay a whopping $50000 per ton of methane mitigated. On the other hand, a recent study in the U.S. found consumers willing to pay only $0.36 per pound ($0.79/kg) of low-methane beef.[89] With an emissions intensity of ∼600g methane per kilogram of beef [90], this implies a much lower willingness to pay of $1320 per ton of methane. As these two results hint at, appetites for green premiums are likely vary widely across different countries, demographics, and products. For our purposes, it is simply worth nothing that some niche markets (especially consumer-facing ones) may be able to sustain methane mitigation approaches that appear too expensive at first glance.

I will leave the reader to consider these various possible cost targets rather than setting a single "magic number" to use throughout this thesis. However, I note that a process with cost of less than ∼$1500 per ton of methane abated would be highly desirable and one costing more than ∼$8000 per ton of methane abated would likely be useful only in niche markets, if anywhere. The outlook for processes with costs between those values is harder to predict. Overall, greenhouse gas mitigation processes are fairly cost-constrained compared to other separation and pollutant-control processes with higher values per unit of target species isolated or destroyed.[72]

1.2.4 Chemical Processes for Methane Oxidation

Thermal Oxidation

The simplest way to oxidize methane is to heat it to a high temperature in the presence of oxygen, as occurs in the flame of a gas burner or flare. However, below methane's lower flammability limit of 5% by volume, heating some amount of gas to its ignition temperature takes more energy than is released by burning its methane content.[91]

Therefore, with less than 5% methane in the incoming gas stream, a steady-state open flame cannot exist. To overcome this challenge and thermally oxidize lower-concentration methane streams, one can preheat the incoming gases with energy from an external source or with heat recovered from the exhaust gases.[71] In practice, using heat recovered from exhaust gases tends to be more practical. Devices that do so are called "regenerative thermal oxidizers" (RTOs).

RTOS are a commercially mature technology for oxidizing sub-5% methane concentrations.[71] They have been used since the 1970s to address the hazard of methane explosions in ventilation air from coal mines.[92] Using a variety of recuperative heat exchanger architectures, they pre-heat incoming gases using heat from exiting exhaust gases, maintaining an internal combustion temperature of around 900-1000℃.[71] Internal ceramic surfaces serve as heat transfer media but do not play a catalytic role and thus do not get fouled or deactivated. Methane conversions are generally between 85% and 95%. A number of large-scale methane RTOs are deployed throughout the world, mainly at coal mines, although far wider deployment is needed in order to mitigate coal mining's contribution to global methane emissions.[71]

The minimum methane concentrations on which RTOs can be deployed are limited by the capital cost of heat recovery systems. In order to sustain the required internal temperature with energy from methane oxidation alone, more and more effective heat recovery is required as the concentration (and thus energy content) of incoming methane descreases. Below a certain methane concentration, the amount of heat recovery equipment required to make the reaction self-sustaining is no longer worth it to the buyer. Commercial RTOs recover 90-97% of the heat from the exhaust gas and can operate stably without supplemental heating on methane concentrations as low as 0.1% (1000 ppm).[92] While operation at 1000 ppm is possible, operation on sources with at least 2500 ppm methane is more common.[92] Researchers aim to develop more cost-effective heat exchangers to allow RTOs to mitigate even lower methane concentrations.[93]

Thermal Catalysis

Thermocatalytic methane oxidizers have architectures similar to purely thermal oxidizers but use catalysts to reduce the temperature at which methane oxidation occurs.

Lowering such devices' internal temperatures reduces the amount of energy that must be transferred between the incoming and outgoing gas streams, which can reduce the sizes and costs of their heat recovery systems.[94] Additionally, lower-temperature devices are simpler to engineer and can use cheaper materials (e.g., metals instead of ceramics). However, unlike inert ceramic heat transfer surfaces in thermal oxidizers, catalysts must overcome challenges of durability, poisining, and methane affinity in order to realize their potential. As of the end of 2024, no thermocatalytic methane oxidizers at a pilot or larger scale were operational.[71]

State-of-the-art thermal catalysts work with a range of methane concentrations, requiring temperatures around 300℃ to oxidize >50% of methane. A copper zeolite was shown to achieve high rates and conversions at a range of methane concentrations between 2 ppm and 2% using a reaction temperature of 310℃. Its performance degraded minimally over 300 hours of reaction.[94] Further work is under way to study this catalyst's durability and resilience to contaminants [95] as well as to scale it into a full-sized reactor.[96] Other copper zeolites have achieved similar performance at a similar temperature.[97] Palladium-based catalysts can convert methane at even lower temperatures in the 150℃-250℃ range.[98] However, palladium is expensive and performs poorly in the presence of water vapor, and thus has not yet been targeted for commercialization.

It is currently unclear as to the lowest methane concentration that thermocatalytic oxidizers could cost-effectively mitigate.[42, 99] As with thermal oxidizers, it is cheapest if the reaction temperature is sustained entirely by the energy released by methane oxidation. Adding supplemental energy to maintain the reaction temperature is possible, although doing so rapidly becomes expensive given the large volumes of air that must be heated.[42] Either way, there is a tradeoff between energy efficiency and capital cost, since capturing a greater fraction of exhaust heat requires building larger heat transfer surfaces. Optimizing the system cost for a given methane concentration, catalyst, and (if applicable) price of supplemental energy is not trivial.

Even so, we can make some rough estimates on the concentrations at which self-sustaining thermocatalytic methane oxidation could be practical. If an RTO designed for a 900℃ internal temperature could achieve the same heat recovery fraction with an internal temperature of 300℃, the energy input required to maintain 300℃ would be

about one third of that required to maintain 900℃. Thus, the minimum inlet methane concentration required to sustain a 300℃ internal temperature with reaction enthalpy alone (assuming a fixed percent methane conversion) would be one third of that required for 900℃. Since current RTOs work with mimimum methane levels of 1000-2500 ppm, we can estimate that zeolite-based thermocatalytic oxidizers might operate at a minimum of 300-800 ppm methane without external energy input. Developing cheaper and higher-performing heat recovery systems could reduce that minumum further.

Photocatalysis

Photocatalysis is appealing for dilute methane oxidation because it uses light to activate stable molecules like methane at room temperature. Thus, no gas preheating or heat recovery is required. Photocatalysts' base materials are semiconductors, most often metal oxides like zinc oxide and titanium dioxide. When hit by an energetic photon (e.g., for plain titanium dioxide, an energy >3.0eV or a wavelength <410nm.[100]), photocatalysts generate an electron and a hole that can migrate to the surface and participate in redox reactions there. Photocatalysts are generally fabricated in nanofilms or nanoparticles to allow these charge carriers to reach the surface before they recombine and are wasted.[101] Photocatalysts can facilitate a wide variety of reactions under sunlight or artificial light, with photocatalytic air purification a well-established subfield of research and with methane oxidation an area of relatively recent interest.[101, 102]

Known photocatalysts can oxidize methane at concentrations as low 2 ppm, but their rates are low and any moisture inhibits the reaction. The first major study on photocatalytic methane oxidation, published in 2016, found that zinc oxide outperformed titanium dioxide and showed that adding a small amount of silver to zinc oxide improved its performance further.[102] That study showed high conversions at methane concentrations as low as 100 ppm. A follow-on study replaced the silver cocatalyst with cheaper copper oxide and found it to be similarly effective.[103] A number of catalysts have also been shown to oxidize higher-concentration (>500 ppm) methane.[99] My doctoral research demonstrated that zinc oxide and titanium dioxide can oxidize 2 ppm methane. It quantified several photocatalysts' methane

oxidation rates at methane concentrations between 2 ppm and 5000 ppm (0.5%). It also found that any realistic level of humidity completely inhibits the reaction for all previously known photocatalysts, which had previously only been tested in extremely dry gas. We found that adding a hydrophobic coating can allow titanium dioxide to remain active when humidity is present, although the reaction remains relatively slow. These results are discussed in Chapter 2

My doctoral work also showed that orders-of-magnitude improvements in photocatalyst performance are required for them to be a cost-effective methane abatement strategy. This work is described in Chapter 3. Previously, some articles had suggested deploying photocatalysts in flow reactors (for methane point sources) or on rooftops (for atmospheric methane removal) but had not assessed the practicality of doing so.[46, 73] I built cost models for deploying methane-oxidizing photocatalysts in fan-driven artificially-lit flow reactors, on rooftops with natural airflow and sunlight, and as sunlit aerosols scattered in the lower troposphere. The models output methane oxidation costs as functions of the photocatalyst's rates, whether actual or hypothetical. Even with >500x improvements in photocatalysts' rates at 2 ppm, the modeled costs for rooftop atmospheric methane removal (the lowest-cost of the three systems) were >$10000 per ton of methane. We concluded that photocatalytic methane oxidation is unlikely to be a practical methane mitigation tool in the near future.

Electrocatalysis

Much like photocatalysis, electrocatalysis offers a way to facilitate a variety of reactions at room temperature. In principle, electrocatalysis can achieve high rates compared to thermal catalysts and photocatalysts.[99] A number of sources have used electrocatalysts to oxidize >10% methane, typically with the goal of producing methanol or other high-value products.[104] Some of those studies use high-temperature electrochemical cells that are unlikely to be practical for dilute methane oxidation, although others use room-temperature cells. However, research on electrochemical oxidation of dilute methane is in its very early stages and to my knowledge no studies report electrochemical oxidation of <1000 ppm methane, leaving a clear whitespace for future experiments.[42] Additionally, to my knowledge, no efforts have been made to model

the scale-up and economics of electrochemical reactors for dilute methane oxidation.

Microbial Oxidation

Microbes known as "methanotrophs" can also oxidize methane under ambient conditions. In so doing, they extract the energy contained in the methane and use it to grow. Like thermal catalysis and unlike electrocatalysis and photocatalysis, no external energy input is required, except sometimes in the form of supplemental nutrients for the microbes to conume.[79] The enzyme that most of these microbes use, methane monooxygenase (MMO), can in some sense be considered a "room-temperature thermal catalyst" that has been optimized by nature over millions of years.

Biofilters and biocovers are mature technologies for mitigating many different gaseous odorants and pollutants, and such devices targeting percent-level methane are already in widespread use. Biofilters (flow reactors operating on a gas stream) and biocovers (a layer over a landfill or other area sources through which gas diffuses) contain cultures of diverse microbes that consume methane and other organic compounds.[79] In some cases, the colonies sustain themselves on gaseous reducing agents alone. In other cases, they require supplementary energy from consumable materials (e.g., wood chips) forming the medium in which they live. These devices can operate well below methane's lower flammability limit and are also highly effective at mitigating odors, a desireable co-benefit in many situations. Biofilters and biocovers are widely used to oxidize 2-100% methane in landfill gases.[105, 106] Biofilters have also been used on gases from livestock manure tanks and wasterwater treatment plants with percent-level methane.[79, 107] In a field trial at a coal mine, a biofilter successfully oxidized 0.25% (2500 ppm) methane.[108]

Research on methanotrophy at lower (<2500 ppm) methane concentrations mainly focuses on developing strains of microbes that can oxidize (and ideally subsist on) such low methane contentrations. As early as 2009, a lab-scale bacterial biofilter successfully oxidized ∼40% of a 1300 ppm methane stream.[109] More recently, a bacterial strain that could grow using only 200 ppm methane was reported.[110] A fungal biofilter subsisting on both methane and a wood chip substrate have oxidized ∼25% of a 20 ppm methane stream.[111]

While these results are promising, methanotrophs' rates of methane oxidation

present another obstacle. Since MMO operates in an aqueous environment, methane's dissolution in water and tranport to the enzyme is often a rate-limiting step.[79] Biofilters therefore tend to require relatively long residence times (∼15 minutes), making it difficult for them to efficiently process large volumes of gas. It has been projected that using current biofilter designs to process 500 ppm methane would result in impractically high mitigation costs on the order of $20000 per ton of methane oxidized, with costs roughly inversely proportional to methane concentration.[112] In response to this challenge, some researchers aim to develop novel biofilter designs with better mass transfer and lower pressure drops.[113–115] There have also been efforts to stabilize the MMO enzyme in a cell-free environment to essentially work as a methane-oxidizing catalyst, but this work is in its very early stages.[116, 117]

Enhancing the earth's natural soil methane sink has also been discussed as a strategy for atmospheric methane removal.[115] Natural methanotrophic microbes in soil are already responsible for about 34 million tons per year of atmosphetic methane removal, contributing about 6% of the natural methane sink.[64] Soil amendments (e.g., with biochar or sulfates) that boost soil methanotrophy in methane-emitting areas like rice paddies have already been shown to be effective.[46] Alternatively, it has been suggested that amendments to supply the elements needed for the MMO enzyme – copper, phosphorous, and iron – could boost soil methanotrophy.[118] Much work is needed to explore such strategies' effects on ecosystems and on carbon dioxide and nitrous oxide cycling.

Gas-Phase Advanced Oxidation

Gas-phase advanced oxidation (GPAO) uses short-wavelength light to split specific "precursor" molecules into highly reactive gaseous radicals that oxidize methane and other reducing agents at room temperature. The name GPAO refers to well-known "advanced oxidation" strategies in wastewater treatment that perform a similar radical-mediated oxidizing chemistry in the liquid phase.[119] The process is also inspired by the natural radical-mediated atmospheric processes that oxidize methane. Unlike all of the previously mentioned chemistries, GPAO involves no gas-solid or gas-liquid interfaces, avoiding the methane mass transfer constraints that bedevil microbial and catalytic approaches. These processes' pressure drops can extremely

low, since the reactors are hollow optical cavities rather than packed beds or honeycombs through which air must be forced.[120] This makes them very appealing for use on very low (2-100 ppm) methane concentrations. Existing literature contains GPAO chemistries involving ozone (O_3), chlorine (Cl_2), and oxygen (O_2) as radical precursors. I will refer to them as O_3-GPAO, Cl_2-GPAO, and O_2-GPAO.

Ozone GPAO O_3-GPAO was the first reported GPAO process.[121] In the prototype system, an off-the-shelf ozone generator produced ozone that was mixed into a gas stream containing hydrocarbon contaminants. The gas mixture was then exposed to 254 nm UV-C light from mercury vapor lamps, splitting each ozone to produce an oxygen radical ($O(^1D)$) and eventually a hydroxyl radical (OH•) according to the following reactions:

$$O_3 + hv_{(310nm)} \rightarrow O(^1D) + O_2 \tag{1.3}$$

$$O(^1D) + H_2O \rightarrow 2OH\bullet \tag{1.4}$$

$$OH\bullet + CH_4 \rightarrow H_2O + CH_3\bullet \tag{1.5}$$

The hydroxyl radicals oxidize any hydrocarbons present by extracting hydrogens from their C-H bonds. O_3-GPAO was commercialized as an odor control technology and was field-tested at several industrial sites.[119] However, its designers expressed the opinion that a hydroxyl radical-based system was ill-suited for dilute methane oxidation due to hydroxal radicals' low rates towards methane and high rates of self-recombination.[120] To my knowledge, published sources have not reported or projected costs for O_3-GPAO systems.

Chlorine GPAO Cl_2-GPAO was the next reported GPAO process.[120] The process's developers refer to it as the "Methane Eradication Photochemical System," or "MEPS". Chlorine gas is mixed into the methane-containing gas stream and the mixture is exposed to 365-nm UV-A light. The light splits the chlorine into chlorine radicals (Cl•, sometimes also referred to as chlorine atoms) which then oxidize methane according to the following reactions:

$$Cl_2 + hv_{(365\ nm)} \rightarrow 2Cl\bullet \tag{1.6}$$

$$\mathrm{Cl}\bullet + \mathrm{CH_4} \rightarrow \mathrm{HCl} + \mathrm{CH_3}\bullet \tag{1.7}$$

The chlorine radical also oxidizes any other hydrocarbons that may be present, including downstream products of reaction 1.7, by extracting hydrogen atoms from their C-H bonds. The process results in a mixture of carbon monoxide and carbon dioxide. This photochemical process must be paired with a downstream scrubbing process to remove chlorine gas and hydrochloric acid (HCl) before the gas is exhausted into the atmosphere. The process has been successfully field-tested at agricultural facilities (a pig barn, a dairy barn, and a biogas plant) where it oxidized ∼80% of 40 ppm methane.[70]

Research in this thesis confirms that Cl_2-GPAO can rapidly oxidize dilute methane but cautions that it is likely to be cost-effective only under very favorable circumstances. We found that the process could achieve high conversions across a range of methane concentrations from 2-90 ppm, with a conversion of about 65% striking a good balance of conversions and energy-efficiency. We found it to be fairly resilient to humidity and to the contaminants toluene, ammonia, and hydrogen sulfide. However, we found that in various scenarios the costs of chlorine gas and ultraviolet light alone amount to more than $3000 per ton of methane oxidized, already close to the maximum cost at which such a technology is likely to be useful. This neglects capital costs for the photoreactor, delivery costs for the inputs, and all costs associated with the hydrogen chloride scrubber. Given that most other strategies are likely to be even more expensive, we argue that Cl_2-GPAO should continue to be studied, but optimism for its scalability should likely be tempered.

Oxygen GPAO A recent paper has reported a precursor-free O_2-GPAO process involving a mixture of 185-nm vacuum-UV and 254-nm UV-C light.[122] The authors referred to the process as "Vacuum-UV Methane Oxidation," or "VUMOX". This process is noteworthy in that it requires no additional radical precursor. Rather, by using a shorter wavelength of light than the previous two processes, it directly splits both oxygen and water to generate hydroxyl radicals via the following reactions:

$$\mathrm{O_2} + \mathrm{h\nu_{(185\ nm)}} \rightarrow \mathrm{O(^1D)} + \mathrm{O(^3P)} \tag{1.8}$$

$$O(^1D) + H_2O \rightarrow 2OH\bullet \tag{1.9}$$

$$H_2O + hv_{(185\ nm)} \rightarrow OH\bullet + H\bullet \tag{1.10}$$

$$OH\bullet + CH_4 \rightarrow H_2O + CH_3\bullet \tag{1.11}$$

An ozone-mediated cycle that converts $O(^3P)$ to $O(^1D)$ and various other reactions are not shown for brevity. The hydroxyl radical • OH also oxidizes any other hydrocarbons that may be present, including downstream products of reaction 1.11, by extracting hydrogen atoms from their C-H bonds. O_2-GPAO was shown to achieve >80% methane conversions at inlet methane concentrations ranging 2 ppm methane to 2%. The quantum yield (methane molecules oxidized per photon supplied) increased as the inlet methane concentration rose, varying from 0.03% at 2 ppm to 4.1% at 2 %. However, these values are a combination of reactor geometry and photochemistry effects, and further work is required to assess the process's cost-effectiveness at various methane concentrations. No cost analyses for the process have yet been published.

Hydrogen Peroxide GPAO To our knowledge, H_2O_2-GPAO has not been reported in existing literature. If possible, it would proceed in a manner similar to O_3-GPAO, with methane oxidation mediated by hydroxyl radicals:[123]

$$H_2O_2 + hv_{(555\ nm)} \rightarrow 2OH\bullet \tag{1.12}$$

$$OH\bullet + CH_4 \rightarrow H_2O + CH_3\bullet \tag{1.13}$$

This thesis contains a discussion of and preliminary results on H_2O_2-GPAO. Its qualitative appeal is that hydrogen peroxide is a cheaper precursor than ozone and, unlike chlorine, would not require a downstream scrubbing step for toxic reagents. We did not observe the process to oxidize any methane in a series of benchtop experiments using approximately 30 ppm of methane and 30 ppm of hydrogen peroxide. However, more work could be done to confirm this result and test whether H_2O_2-GPAO is effective against odorants or other reducing gases.

Open-System Atmospheric Oxidation Enhancement

Finally, several strategies have been suggested to enhance the atmosphere's natural sink of methane, effectively shortening methane's atmospheric lifespan. These approaches's effectiveness is difficult to predict and, even if they were deployed, their methane drawdown would be difficult to verify. Additionally, as "open-system" interventions that cannot be confined to a particular device or even to a particular region, issues of social license and governance would be very challenging. Nonetheless, they might offer atmospheric methane removal at lower costs than any of the "closed systems," and therefore may be worth considering as a last resort for limiting atmospheric methane concentrations. Atmospheric oxidation enhancement is a large and active field of research whose contours I will only briefly outline here.

Hydrogen Peroxide or Chlorine Release The simplest concepts for atmospheric oxidation enhancement are essentially gas-phase advanced oxidation in the open atmosphere. Chlorine gas or vaporized hydrogen peroxide would be released from towers on the earth's surface and would eventually photolyze under sunlight into oxidizing radicals. The dissociation reactions, identical to those in Cl_2-GPAO and H_2O_2-GPAO, are as follows:

$$Cl_2 + h\nu_{(365\ nm)} \rightarrow 2Cl\bullet \tag{1.14}$$

$$H_2O_2 + h\nu_{(555\ nm)} \rightarrow 2OH\bullet \tag{1.15}$$

Modeling has suggested that hydrogen peroxide release could indeed substantially reduce global methane levels.[124] However, a very large amount of hydrogen peroxide must be released per unit of methane oxidized. For example, 1250 megatons of hydogen peroxide released per year would reduce the steady-state atmospheric methane concentration by about 5%, an effect equivalent to avoiding on the order of 30 megatons of methane emissions. This is a very inefficient use of hydrogen peroxide, so hydrogen peroxide costs would likely make this approach impractical. Additionally, releasing so much hydrogen peroxide could substantially affect local air quality.[124]

The same modeling study found that chlorine release could be far more efficient at oxidizing atmospheric methane, although the environmental risks are greater.[124] In the model, releasing 1250 megatons of chlorine per year resulted in a 67% reduction

in the steady-state atmospheric methane concentration. This effect is comparable to avoiding on the order of 400 megatons of methane emissions. Assuming a chlorine price of $250 per ton.[125], the process's chlorine demand would cost about $780 per ton of methane mitigated. This is a relatively low value that, if realized in practice, would portend a cost-effective and perhaps scalable methane removal process. However, one hazard is the unintended co-release of bromine, which can negate the process's climate benefit.[124] Another concern is that the release of so much chlorine gas and hydrochloric acid could have severe environmental effects. It has been suggested that basic sodium hydroxide, a co-product of chlorine production, be released into the air or ocean so that the acid/base fluxes into the environment would neutralize each other.[126] However, whether and how this would work in practice has not been studied.

Iron Salt Aerosols Iron salt aerosols (ISA), first proposed in 2017, might offer a way to greatly enhance that atmosphere's chlorine radical sink by emitting a relatively small amount of aerosolized iron oxide (rust) particles. The initial study drew attention to the effect of natural windblown dust from the Sahara desert on the chlorine radical methane sink over the south Atlantic ocean.[127] They suggested a cyclic process in the iron salt solution on each particle's surface whereby aerosolized aqueous sea salt (NaCl) undergoes an acid displacement reaction with trace ambient sulfuric acid, ultimately releasing chlorine gas that photolyzes into a chlorine radical. They further suggested that this process could be boosted by the artificial release of iron oxides, e.g., by putting them in marine fuel to be lofted with ships' warm exhaust plumes. Since iron oxide is cheap and each particle facilitates many, many chlorine release events, the initial study's authors argued that ISA could be an extremely inexpensive methane removal strategy.

In the intervening years, many researchers have contributed to recent efforts to evaluate ISA's effectiveness and feasibility.[128] Insofar as a brief summary is possible, this work has shown that ISA is a highly complex process whose effectiveness is strongly location-dependent.[129] There are certain types of locations (for instance, those with certain nitrogen oxide concentrations) where ISA is likely to have a net climate-warming effect rather than a climate-cooling one.[130] The actual chemistry

taking place in the aqueous layer on each iron particle remains poorly understood and is difficult to probe experimentally.[129] The direct warming or cooling effect of the aerosols must also be taken into consideration. All of these effects must be understood better before any trustworthy cost model of ISA can be built. Despite early enthusuasm for ISA in the field of atmospheric methane removal, the process's overall usefulness, safety, and practicality remain undertain.[129]

1.2.5 Outlook

To conclude this section, I will offer some opinions on what technologies are, and may soon be, best suited to abate different methane sources. However, this field is rapidly evolving and many questions remain about each of the processes described. There is therefore considerable room for reasonable people to disagree on the relative merits and promises of different methane oxidation strategies.

Thermal, thermocatalytic, and microbial methane oxidation appear to be best suited to medium and high-concentration methane streams. Today, commercial thermal (noncatalytic) oxidizers and biofilters are already effective for methane concentrations above 0.1% (1000 ppm), although most actual deployments are at concentrations above 0.5%. Engineering work is under way to extend both technologies' concentration ranges downwards through more efficient heat/mass transfer, which in my judgment might reduce the lowest inlet methane concentration they can cost-effectively abate by a factor of ∼2-3 (i.e., to 300-500 ppm). Moving from purely thermal oxidation to thermal catalytic oxidation could reduce thermal devices' operating temperatures by a similar factor, further enhancing their economics on low-concentration methane streams. Efforts to commercialize such devices are under way. In my opinion it is plausible, though not guaranteed, that regenerative catalytic oxidizers could cost-effectively mitigate gas streams with 100-1000 ppm methane in the near future.

Although oxidizing gas streams with 10-100 ppm methane is quite challenging, gas-phase advanced oxidation (GPAO) may provide a practical way to do so. Critically, these processes avoid surface-based reactions, allowing them to rapidly process huge volumes of air in hollow reactors with low pressure drops. Chlorine-based GPAO is currently the farthest along the path to commercialization. Our own experiments

and modeling show that, although the process is effective, it is likely to be somewhat expensive (though perhaps not prohibitively so). Alternative GPAO chemistries, photocatalysts, and thermal catalysts appear unlikely to be useful for reactors targeting this range of methane concentrations. Electrocatalytic methane oxidation has not been tested enough to make any judgment. While flow reactor-like biofilters at these concentrations are unlikely to be practical, biocovers on area sources of low-concentration methane (e.g., landfills and rice paddies) may prove a useful methane oxidation strategy.

Finally, atmospheric methane removal (AMR) remains a tantalizing but very difficult prospect. None of the photocatalytic AMR strategies that I modeled in my thesis research appear likely to be cost-effective or practical. Despite great enthusiasm and study in the last several years, it remains unclear whether the "Iron Salt Aerosol" strategy to boost the natural chlorine methane sink would actually result in a net methane drawdown, let alone whether it would be practical to execute. Recent modeling efforts have shown that releasing hydrogen peroxide (which eventually forms hydroxyl radicals) into the atmosphere would likely be a costly and inefficient way to achieve AMR. In contrast, releasing chlorine gas (which eventually forms chlorine radicals) into the atmosphere could be highly effective for AMR. However, far more research would be needed on this approach's environmental side effects and ways to mitigate them.

1.3 This Thesis's Contribution to the Field

1.3.1 The Prior State of the Art

When I began my doctoral research in early 2022, prior literature had identified various possible strategies for 2-500 ppm methane oxidation and in some cases had provided experimental proofs of concept. Methanotrophic bacteria were suggested for atmospheric methane removal (AMR) as early as 2009.[112] The "iron salt aerosol" strategy for AMR, in which iron particles released over the ocean drive a catalytic cycle in which chlorine radicals oxidize methane, was proposed in 2017 and a 2021 study reported oxidation of 2 ppm methane using chlorine radicals.[127, 131] AMR using thermal catalysis was suggested in 2019 and a 2022 study observed oxidation of 2-500 ppm methane on a zeolite catalyst at 200°C.[49, 94] AMR using photocatalyst-painted rooftops was proposed in 2021, building on a 2016 study that reported the oxididation of 100 ppm methane using zinc oxide-based photocatalysts.[73, 102] Higher-level articles on the merits and drawbacks of AMR and point-source dilute methane oxidation each listed a handful of these options.[46, 73]

Surveying this landscape of hypothetical approaches and basic proofs-of-concept, my collaborators and I saw a need for research to clarify how far these strategies were from real-world practicality, both with atmospheric methane and at point sources. Given the importance of rapidly reducing net methane emissions, such work would allow the direction of resources towards scaling approaches that were already practical or that required only engineering but not fundamental breakthroughs. Conversely, where fundamental breakthroughs were required, this work could help direct research by identifying key figures of merit and setting targets for them.

The case of photocatalysts is illustrative. By 2022, photocatalysts had been shown to oxidize 100 ppm methane in very dry air.[102, 103] However, no attempts had been made to model the cost or feasibility of mitigating ∼100-ppm methane point sources using these materials. It was also unclear whether the rates measured without water present were applicable to real-world humid conditions. Additionally, despite discussion of AMR with photocatalysts, no rates at <100 ppm had been reported. With 2-ppm data on methane unavailable, one feasibility analysis on AMR with photocatalyst-painted rooftops used rate data from other small hydrocarbons like

formaldehyde.[73] Similarly, a study of AMR in solar updraft towers extrapolate photocatalytic oxidation rates of 2 ppm methane from data taken at >100 ppm.[132] These analyses also stopped short of projecting costs per ton of methane oxidized. A lack of both measured rates and rigorous cost models made it difficult to judge either strategy's overall viability, a challenge shared by each of the other strategies for dilute methane oxidation.

1.3.2 Our Lab's Approach: Experiments and Cost Models

My colleagues and I aimed to contribute to this field by conducting complementary campaigns of cost modeling and benchtop experiments. For a given methane-oxidizing chemical process, building a cost model allowed us to identify the key figures of merit that are measurable at a bench scale but determine the performance of a full-size system. We were then able to design experiments to probe these figures of merit and, in some cases, to improve them. By feeding those measurements into the cost model, we were able to estimate the costs of methane abatement if the process were deployed at large scale. These costs could then be compared to fixed cost benchmarks and to the costs of other greenhouse gas abatement strategies. The goal was not to identify "good" or "bad" approaches to dilute methane abatement, but rather, as stated earlier, to get a realistic sense of what fundamental breakthroughs and/or engineering efforts would be required for a given strategy to be practical at large scale.

This approach was in part inspired by the series of papers that laid the groundwork for the now-flourishing field of carbon dioxide direct air capture (DAC). In 2011, several studies concluded that forcing atmospheric air through an "air contactor" to strip out a substantial fraction of its ∼440 ppm carbon dioxide would be very energy-intensive and cost more than \$600 per ton of carbon dioxide (tCO_2).[133, 134] However, a seminal 2012 cost modeling paper using data from a 2008 experimental campaign showed that air-liquid contactors with aqueous hydroxide solutions might bind carbon dioxide for at little as \$60/tCO_2.[135, 136] This result suggested that DAC was within the realm of possibility and deserved further study. Of course, this preliminary cost model was only the first step. Dozens of person-hours of engineering were required before another paper, based on several years of pilot plant data and

detailed construction quotes, projected that DAC could be achieved for a total cost of less than \$100/tCO_2.[80] Another seven years later, the first full-sized DAC plant based on this technology is under construction; once it is finished a ton of carbon dioxide may actually be captured for less than \$100.[137]

At the outset of our work, we hoped that our work might be to AMR what the 2008 and 2012 studies were to DAC. AMR is highly counterintuitive given methane's stability, nonpolarity, and very low concentration in air.[72] A study showing a likely pathway to low methane mitigation costs would provide motivation and direction for future researchers in the field. However, we also recognized that cost-effectively oxidizing 2-ppm atmospheric methane was likely to be more difficult than cost-effectively oxidizing concentrated methane from point sources. Our experiments and cost models therefore represented both AMR and dilute point-source methane oxidation.

1.3.3 A Preview of the Thesis's Structure

My colleagues and I are fortunate to have been free to pursue the methane-oxidation strategies that we thought most promising without being confined to a particular class of materials or processes. The overall arc of this thesis reflects a few years' evolution of our beliefs about which methane-oxidizing approaches are most promising. We began by studying heterogeneous catalysis (photocatalysts) but, based on those results, eventually shifted our focus to entirely gas-phase reactions (gas-phase advanced oxidation), first with chlorine and then with hydrogen peroxide.

This thesis's first two chapters examine photocatalytic methane oxidation. At the outset, photocatalysts seemed highly promising, offering ambient-temperature sunlight-driven methane conversion and making use of existing expertise and equipment within our lab. Chapter 2 describes experimental work that characterized and improved photocatalysts' methane-oxidizing performance. Chapter 3 contains cost models of scaled-up photocatalytic methane oxidation systems. It concludes that, barring 2-3 order of magnitude improvements in their rates, photocatalysts are unlikely to enable cost-effective methane abatement solutions.

The next two chapters examine gas-phase advanced oxidation using chlorine radicals. This process also takes place at room temperature but avoids two pitfalls that

we observed with solid photocatalysts: slow mass transfer and inhibition by moisture. Chapter 4 describes experiments that thoroughly characterized chlorine radical-mediated methane oxidation under various environmental conditions and operating parameters. Chapter 5 contains cost models of scaled-up chlorine-based gas-phase advanced oxidation systems. It finds that such systems' economics at field sites are challenging, though perhaps not wholly prohibitive, due to high energy and reagent costs. A final experimental chapter, Chapter 6, attempts to perform a similar gas-phase advanced oxidation process using hydrogen peroxide instead of chlorine, but finds it to be ineffective at oxidizing methane.

In my conclusion, I discuss my work's implications for the field of dilute methane oxidation. I comment on the real-world prospects of photocatalytic methane oxidation and gas-phase advanced oxidation. I also comment on the areas of research that I feel are most critical for the field going forward. For point-source methane oxidation, I highlight paths forward in thermal oxidation, thermocatalytic oxidation, and gas-phase advanced oxidation. For AMR, I highlight the possibility of applying chlorine radical-based oxidation in the open atmosphere to achieve lower costs and greater scalability than may be possible at methane point sources.

Finally, expanding my focus from dilute methane oxidation, Appendix A describes a suite of lab automation software that I wrote to streamline my and my colleagues' experiments. This open-source Python package, which I have named *PyOpticon*, allows one to create on-screen control panels for a computer to command the many devices that constitute a benchtop experimental setup. The package allows researchers (such as graduate students) with minimal coding experience to reap the benefits of modern controls, automation, and data acquisition. PyOpticon proved highly valuable in executing the experiments described in this thesis and I hope that others will find it similarly useful.

Chapter 2

Experiments on Photocatalytic Methane Oxidation

2.1 Introduction

Photocatalysts are materials that use absorbed light to overcome the activation barriers of chemical reactions. As discussed above, they are qualitatively appealing for dilute methane oxidation because they can activate highly stable molecules at room temperature. Room-temperature operation is a necessity for processes targeting highly dilute or atmospheric CH_4 streams. Some authors draw parallels between photocatalysts' mechanisms of action and the atmosphere's natural hydroxyl radical-mediated self-cleaning behavior.[101] While this analogy is intuitive, photocatalytic oxidation is a mixture of radical-mediated oxidation (in which the catalyst creates radicals that later encounter the target molecule) and of catalytic oxidation (in which the target molecule adsorb at active sites and react).[138] Identifying which mechanism is at work is often not trivial.

Photocatalysts consist of semiconductor "base materials" (or "base photocatalysts") and, in some cases, additional "cocatalysts".[139] Photons that hit the base materials produce electron-hole pairs that then migrate to the surface and facilitate various reactions. The base material's band structure must allow at least one electron-scavenging reaction (electron reaction) and at least one hole-scavenging reaction (hole reaction). These reactions may involve the target molecule itself (e.g., CH_4) or they may produce radicals from ambient O_2 or H_2O. The former is known as a "direct mechanism" and the latter is known as an "indirect mechanism". Various cocatalysts, such as noble metals, can be added to base photocatalysts in order to make them more efficient and performant.

For several reasons, metal oxides such as titanium dioxide (TiO_2), zinc oxide (ZnO), and tungsten trioxide (WO_3) are the most common base photocatalysts.[139] First, these oxide materials are highly stable and are not degraded by the charge carriers and radicals that they generate. Second, they have band structures that can facilitate a variety of useful electron and hole reactions. As shown in Figure 2.1, electrons on ZnO and TiO_2 can produce superoxide radicals (O_2^-) from O_2, while holes can produce hydroxyl radicals (OH•) or directly attack methane's C-H bond. ZnO and TiO_2 have wide band gaps, meaning that they are only photocatalytically active under ultraviolet light. Since charge carriers must be able to reach the surface before they recombine, these materials are typically deployed in nanoparticles with

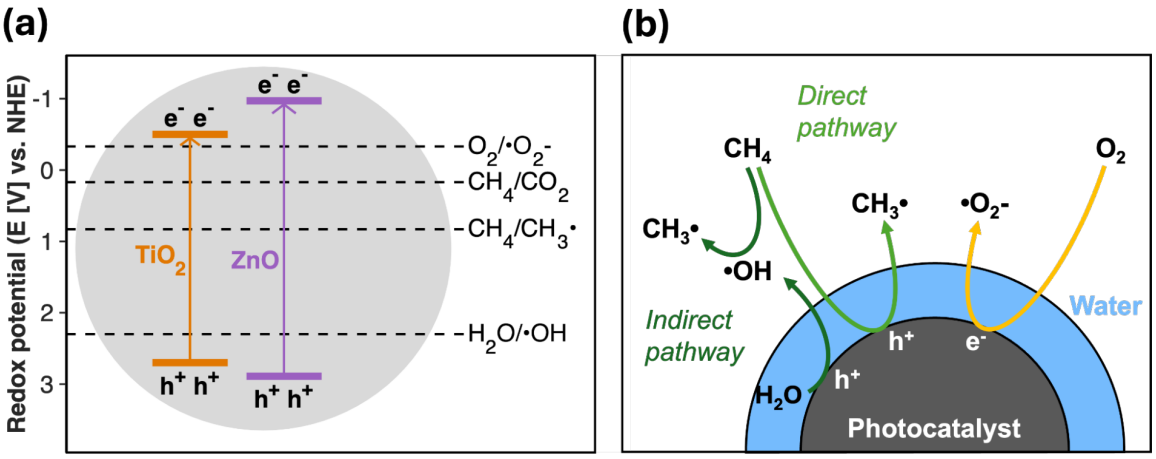

Figure 2.1: Principles of photocatalytic CH_4 oxidation. **(a)** Reduction-oxidation (redox) potentials illustrating that the conduction bands, valence bands, and band gaps of TiO_2 and ZnO are suitable for CH_4 oxidation. Redox data from Li *et al.*[140] and Donat *et al.*[141] **(b)** General mechanisms of CH_4 oxidation on solid photocatalysts.

diameters of tens of nanometers. The nanoparticles can be kept in powder form or immobilized on surfaces.

Photocatalysts have long been of interest for oxidation processes, both for pollutant control and for bulk chemical conversions.[142] They are commercially used for aqueous pollutant destruction in wastewater treatment plants (with suspended TiO_2 particles)[139] There have also been many efforts to use photocatalysts to oxidize gasous pollutants such as volatile organic compounds (VOCs).[101, 143] However, these works focused on destroying larger hydrocarbons that compromise local and/or indoor air quality rather than on destroying greenhouse gases. At a lab scale, many efforts have been made to photocatalytically convert concentrated CH_4 to valuable products like methanol.[144]

Interest in photocatalytic total oxidation of dilute CH_4 to CO_2 is relatively recent. In 2016, Chen *et al.*[102] decorated ZnO with silver (Ag) nanoparticles (0.1% by weight; wt%) to convert nearly all of 100 ppm CH_4 to CO_2. The Ag-modified photocatalyst showed faster CH_4 oxidation reaction kinetics than pristine ZnO or

TiO_2 and is still regarded as the state-of-the-art material for photocatalytic oxidation of dilute CH_4. Similar effects have been reported for both TiO_2 and ZnO with other cocatalysts such as copper oxide.[103, 145, 146] These cocatalysts may facilitate CH_4 oxidation by accelerating surface reactions or by lessening the speed of charge carrier recombination.[140, 147, 148] . Based on these works, and because of TiO_2 and ZnO's availability at commercial scale, ZnO and TiO_2 remain by far the most often-discussed base photocatalysts for dilute CH_4 oxidation.

When my colleagues and I began the research described in this chapter, many critical aspects of photocatalytic dilute CH_4 oxidation had not been experimentally probed. The most useful existing study had observed the oxidation of >100 ppm CH_4 on ZnO and ZnO variants under very conditions.[102] Even so, a number of publications had identified photocatalysis as a promising strategy for atmospheric CH_4 removal.[73, 132] Deployment configurations including photocatalyst-painted rooftops and photocatalytic solar updraft towers had been suggested in the literature. These suggestions, in our view, glossed over the fact that no experimental studies had observed or measured the photocatalytic oxidation of CH_4 at concentrations below 100 ppm, let alone 2 ppm. Even in the intervening years, measurements have been published at 20 ppm but not at 2 ppm.[149] Deployment proposals at the time also ignored the fact that photocatalytic CH_4 oxidation had only been observed under extremely dry conditions, despite the fact that one might naively expect water absorption on hydrophilic oxides to inhibit their reaction with hydrophobic CH_4 molecules.[150, 151]

Given this state of affairs, we felt that the field could benefit greatly from measurements of CH_4 oxidation on common photocatalysts 1) with CH_4 concentrations of 2-100 ppm and 2) at humidity levels reflective of real-world deployment scenarios. Obtaining these measurements was our original research goal. As our work progressed, we learned a considerable amount about the role of inhibitory water layers on oxide photocatalysts, a phenomenon that explains various prior results in literature, including the superiority of ZnO over TiO_2 for dilute CH_4 oxidation. Finally, though it was not initially our goal to do so, we found a way to modify TiO_2 to make it more resilient to inhibition by humidy. This discovery constitutes the final section of this chapter.

2.2 Experimental Setup and Reactor Qualification

Our experimental setup for photocatalyst testing comprised an array of gas tanks and mass flow controllers, a tubular glass photoreactor, and a pair of infrared spectrometers for gas analysis (Figure 2.2). Although previous studies had used both batch and flow photoreactors [102], we chose to exclusively use a flow photoreactor, a choice that we made in order to boost our experimental throughput. The final setup was the result of several months' iteration, particularly around the challenges of messy catalyst loading/unloading and of unwanted CO_2 offgassing from surfaces under UV irradiation. As our research interests evolved, it proved easy to repurpose this setup for other CH_4 oxidation strategies by swapping out the reactor itself while leaving the gas supply and analysis systems largely intact.

The photoreactor itself consisted of a horizontal borosilicate glass tube (length 60 cm and inner diameter 1.5 cm) into which a sample of powder photocatalyst was placed between two quartz wool plugs. The powder was tamped flat to about 0.3 cm deep, 1 cm wide, and 7 cm long before the second plug of quartz wool was inserted. All experiments used 1.50 g of photocatalyst sample, with the exception of experiments with pristine TiO_2, which used 0.50 g of sample because the as-received, lower density TiO_2 powder needed less mass to create the same fill level and surface area. The reactor was illuminated radially from above by a 500W 365 nm LED array (Shenzhen Leader UV Technology Co.). The light generated a UV flux of 4.5 $mW \cdot cm^{-2}$ at the sample's surface, providing an irradiance equivalent to the integrated UV component (280-400 nm) of terrestrial solar irradiance (AM1.5g spectrum). The light intensity was measured during each experiment with a Thorlabs 140C photodiode power sensor adjacent to the photoreactor.

Experiments were conducted by flowing 30 $mL \cdot min^{-1}$ of synthetic air (21% O_2 in N_2) through the photoreactor with varying amounts of CH_4 and H_2O. Primary standard grade Linde Gas cylinders of N_2, O_2, 10 ppm CH_4 in N_2, 1,000 ppm CH_4 in N_2, and 5% CH_4 in N_2 were used to create the desired gas mixtures. For "dry" rate measurements, following the loading of the photocatalyst, the photoreactor was purged for 1 hr by dry, synthetic air to achieve a H_2O concentration of <500 ppm (RH <2%). For "humid" rate measurements, some or all of the gasses were redirected through a H_2O bubbler upstream of the photoreactor to create a H_2O concentration

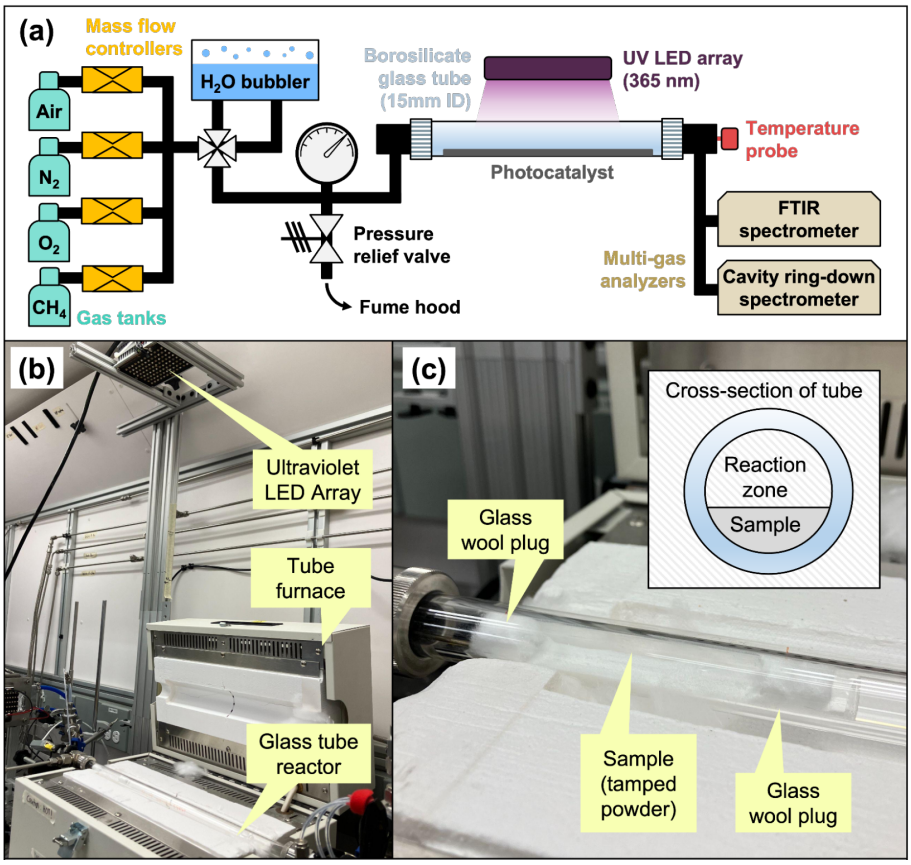

Figure 2.2: Illustrations of the horizontal tube flow reactor. **(a)** Schematic of the reactor system. **(b)** Image of the horizontal tube reactor, light source, and tube furnace. **(c)** detail image of the reaction zone containing the powder sample. Pipe fittings on the reactor system are all stainless steel Swagelok fittings. The ends of the glass tube are sealed with Swagelok Ultra-Torr fittings.

up to 23,000 ppm (80% RH). The gasses exiting the photoreactor were analyzed with a pair of infrared spectrometers. For $\leq$30 ppm CH_4 concentrations, a Picarro G2210-i cavity ringdown spectrometer was used. For >30 ppm CH_4 and for all other gasses, an MKS Multigas 2030 FTIR spectrometer was used, with a background N_2 spectrum collected every 24 hr.

For each reaction condition, the light was cycled on and off several times to obtain multiple CH_4 conversion measurements. By default, the light-on periods lasted 20 min, and the light-off periods lasted 10 min. In each cycle, the 'light-off' CH_4 concentration was averaged over the 5 minutes just before the light was turned on, and

the 'light-on' CH_4 concentration was averaged over the 5 minutes just before the light was turned off again. When investigating the carbon balance, ∼12 hr periods with the light on or off were used to ensure steady state measurement of the ppm-level CO_2 signal. Uncertainty in reaction rates was measured as 95% confidence intervals, accounting for analyzer accuracy, analyzer noise, flow controller accuracy, and the repeatability of the photocatalyst loading process.

2.2.1 Lessons Learned in Apparatus Design

Designing a photoreactor to test powder photocatalysts proved not to be entirely trivial. Our first photoreactor design was a machined block of stainless steel with a shallow square cavity on its top face. A laser-cut gasket was placed into this cavity and capped with a square quartz window, creating a sealed serpentine channel through which gas flowed, the bottom half of which was filled with a powder photocatalyst. However, loading and unloading the photocatalyst was difficult and messy, and the gasket was prone to degradation under UV light (evidenced by considerable release of CO_2). Even without the gasket, the stainless steel offgassed considerable CO_2 under UV light, making the reactor poorly suited for attempting to close the mass balance for CH_4 oxidiation. The horizontal tube design is far easier to load and unload, and also has no gaskets, O-rings, or metal within the UV-illuminated zone, offgassing negligible CO_2 when UV-illuminated in the absence of CH_4.

Outside of the reactor vessel itself, we also learned various lessons about generating gas mixtures and quantifying reaction products. Mixing CH_4-containing synthetic air with a variety of gas tanks and mass flow controllers was mostly straightforward. However, we noted that mass flow controllers suffer from slight drift and stability issues when they are used in series with a bubbler (which we used to humidify the gas stream). For quantification of <30 ppm CH_4 and <1000 ppm concentrations of CO_2, a Picarro g2210-i cavity ringdown spectrometer offered excellent stability, resolution, and response time. For higher CH_4 concentrations and for other gases, we initially used a Stanford Research Instruments 8610c Gas Chromatograph. However, we soon switched to an MKS Instruments MultiGas 2000 FTIR spectrometer, which was able to measure a much wider variety of ppm-level gases at far higher time resolution. The gas chromatograph was occasionally still useful when we wished to cross-check

FTIR measurements to ensure that they were free from effects of overlapping infrared absorption peaks.

2.2.2 Assessing the Role of Mass Transfer Effects

One concern about the horizontal tube reactor is that CH_4 might "bypass" the photocatalyst, since there is about 0.8cm of headspace between the photocatalyst suface and the top of the tube. To obtain accurate measurements of a photocatalyst's reaction rates, it is essential to operate the reactor in a regime where the overall conversion is limited by the reaction on the catalyst surface, not by reagent mass transfer through the gas boundary layer. Mass transfer limitations in benchtop photocatalytic reactors with dilute gas-phase reagents have been studied mainly in relation to the ISO 22197 reactor for photocatalytic NO destruction.[152, 153] That reactor has a rectangular cross-section with the bottom surface covered in photocatalyst and with gas flowing above. In such reactors, the maximum conversion (which occurs in the case where convective mass transfer is the rate-limiting step; i.e., where every reagent molecule that touches the catalyst reacts instantly) can be estimated as follows:[152]

$$\frac{C_{out}}{C_{in}} = \frac{(100 - \%conversion)}{100} = exp\left(\frac{-Sh \cdot D \cdot V}{2h^2 f}\right) \tag{2.1}$$

Where C_{in} and C_{out} are respectively the inlet and outlet concentrations of the reagent, $\%conversion$ is the percent conversion of the reagent, Sh is the Sherwood number (the ratio of convective to diffusive mass transfer), D is the diffusivity of CH_4 in air, V is the reactor volume, h is the reactor height, and f is the flow rate. We approximate the headspace as a rectangle of width 1.2cm and a height $h = 1.5$ cm. For a 7 cm-long photocatalyst sample, the volume of the reaction zone is then $V = 12.6$ cm.^{3} Our experiments used a flow rate of $f = 30$ cm^3·min^{-1} $= 0.5$ cm^3·s^{-1}. CH_4's diffusivity in air is $D = 0.22$ cm^2·s^{-1}. The Reynolds number under these conditions is $Re = 0.88$, calculated from $Re = \frac{v \cdot h}{\nu}$ where $v = 0.28$ cm·s^{-1} is the average flow velocity and $\nu = 0.48$ cm^2·s^{-1} is the kinematic viscosity of air. The flow is therefore very laminar, which is unsurprising for such slow flow in such a small channel. Using the Chilton-Colburn analogy between heat and mass transfer, and using the tabulated Nusselt number for heat transfer to one side of a rectangular channel, we set the

Sherwood number to Sh=4.86.[154]

Evaluating these formulae gives a maximum conversion of 99.75% for a situation in which every CH_4 molecule that touches the photocatalyst reacts. For rate measurements, a best practice is to operate at less than one-tenth of the maximum possible conversion.[152] All rate measurements of as-synthesized catalysts resulted in CH_4 conversions of 10% or less, satisfying that criterion. Additionally, as shown later in Fig. 2.10**(c)**, experiments on catalysts after temperature-programmed desorption (TPD) showed conversions as high as 45%. These results make it quite plausible that our reactor could achieve very high conversions, corroborating the mass-transfer calculations. The TPD experiments, discussed more below, were the only cases where conversions exceeded 10% and mass transfer effects were therefore likely to have been present.

2.2.3 A Typical Experiment with 2-ppm Methane

Figure 2.3 shows a representative time series of CH_4 concentrations measured at the reactor outlet, in this case with the cavity ringdown spectrometer. Though we wish to describe our photocatalyst synthesis and characterization processes before presenting the bulk of this chapter's experimental results, we include this plot here in order to clarify our experimental and data-processing workflow. We also note that these data are, to our knowledge, the first demonstrations of photocatalytic oxidation of CH_4 with a 2 ppm (i.e., atmospheric) inlet CH_4 concentration.

After each sample was loaded in the tube, we flowed dry nitrogen for no less than an hour in order to dry out the photocatalyst surface. We then set the flow controllers according to the desired CH_4 concentration and waited for the measured CH_4 concentration to stabilize. Finally, we cycled the UV light on and off several times. Two such cycles are shown in the figure. With successful photocatalysts, when the light turned on, we observed the measured outlet CH_4 concentration to drop, indicating that some fraction of the CH_4 was being oxidized. When we cycled the UV light with no photocatalyst as a control, no change in the outlet CH_4 concentration was observed. A single experiment typically consisted of setting several different inlet CH_4 concentrations and conducting at least three light cycles at each CH_4 concentration. The percent CH_4 conversions were extracted and converted into rates and quantum

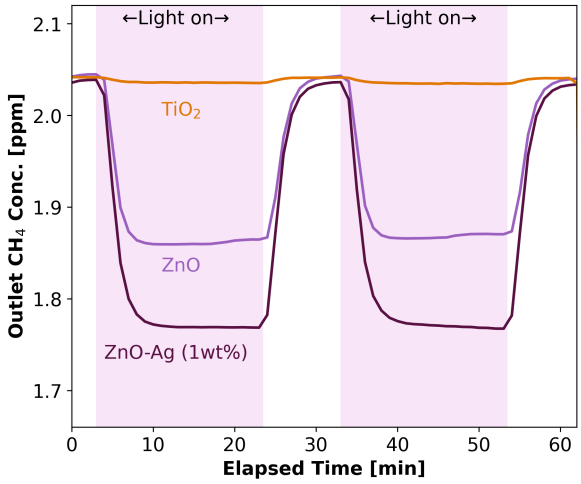

Figure 2.3: Photocatalytic oxidation of 2-ppm CH_4 under dry conditions and 1 sun of UV light. 'Dry' refers to <500 ppm H_2O (<2% relative humidity) and '1 sun of UV light' means 4.5 mW·cm^{-2} flux of 365 nm light, approximately the UV component of an AM1.5g solar spectrum. The catalysts indicated in this plot will be discussed in detail shortly; in brief, they are as-received commercial ZnO, as-received commercial TiO_2, and commercial ZnO decorated with 1% weight of silver as described in Chen *et al.*[102]

yields as described below.

2.3 Figures of Merit: Rates and Quantum Yields

The rate and the apparent quantum yield are the two principle figures of merit for photocatalyst performance. The rate is simply the number of moles of CH_4 oxidized per unit area of catalyst per second. In base units, it is measured in $moles/m^2$s. To make the numbers a more convenient order of magnitude, we mainly report rates in $\mu moles/m^2 s$. The quantum yield is the rate divided by the incident UV photon flux on the photocatalyst surface, giving a measurement of "methane molecules oxidized per incident photon". It is discussed below.

We calculate rates based on the frontal catalyst area presented to the UV light. This is reasonable for photocatalysts that are only active when illuminated and for a reactor in which the gas passes over the catalyst rather than through it. It is different

from the setup typically used in thermal catalysis measurements, in which the gas flows through a packed bed and the relevant surface area is the total surface area of all the catalyst particles in the bed. The catalysts particles deep down in our packed photocatalyst bed see neither light nor gas flow, so including their surface area in the rate calculation would be unhelpful.

We define the "apparent quantum yield" (AQY), which we will occasionally shorten to the "quantum yield", as follows:

$$AQY \;=\; 100\% \cdot \frac{\#\ of\ Target\ GHG\ Molecules\ Decomposed}{\#\ of\ Photons\ (<365nm)\ Incident\ on\ the\ Photocatalyst} = 100\% \cdot \frac{R_{reaction}}{\Phi_{UV}} \quad (2.2)$$

Where $R_{reaction}$ *(moles/m^{2}s)* is the intrinsic reaction rate that is observed in the absence of gas-phase mass transfer limitations and Φ_{UV} *(moles/m^{2}s)* is the incident flux of ultraviolet photons within a certain spectrum, in this case <370nm.

For a given UV flux, the AQY is directly proportional to the reaction rate. For example, since an AM1.5g solar spectrum contains $6.3 \cdot 10^{-5}$ moles/m^{2}s of photons with wavelengths <365nm, an AQY of 3% under our definition corresponds to a reaction rate of $1.9 \cdot 10^{-6}$ moles/m^{2}s under 1 sun of UV radiation. In prior literature, the best reported CH_4-oxidizing photocatalyst had an AQY of ∼1% at 5,000 ppm CH_4..[102] Before our work, AQYs at lower CH_4 concentrations had not been reported. However, in general, it would be expected that a photocatalyst's AQY (as we define it) would decrease along with its rate as the inlet concentration of CH_4 became lower.[155]

We note that the term "quantum yield" can also refer to other quantities.[156] The issue is important for CH_4 oxidation because Chen *et al.* chose to report the quantum yield of charge carriers that participated in a CH_4-oxidizing reaction, giving a value eight times higher than our definition would have.[102] Quantum yields may also be defined under other spectra of light, such as a full solar spectrum, an approach that is appropriate for visible-light photocatalysis but that we did not feel was useful for our own work.

2.4 Photocatalyst Synthesis and Characterization

Our initial experimental goals were to test "known" photocatalysts for their CH_4-oxidizing performance. These included ZnO, TiO_2, and gold-and-silver-cocatalyzed variants of each. Plain ZnO, plain TiO_2, and the state-of-the-art silver-ZnO photocatalyst were of particular interest. We felt that it would be more useful to our field to better test these known materials than to move straight to developing new materials. As will be seen, to mitigate humidity's effect on the above photocatalyst, we later produced a fluorosilane-coated TiO_2 material (TiO_2-FS). TiO_2-FS is also included in this section in order to colocate all information on photocatalyst synthesis and characterization.

2.4.1 Photocatalyst Synthesis

To test the pristine (plain) ZnO and TiO_2 as they would be produced at large scale, commercial 21 nm TiO_2 nanoparticles (>99.5%, Sigma-Aldrich, Product No. 718467, CAS No. 13463-67-7) and 30 nm ZnO nanoparticles (>99.9%, MSE Supplies, Product No. PO0504, CAS No. 1314-13-2) were used as-received. Our exploration did not account for possible variability amongst batches of industrially-produced nanoparticles; if photocatalytic CH_4 oxidation were scaled up, this variability and its potential effects on rates would be important to explore further. Electron microscopy revealed our received nanoparticles' sizes to be close to their nominal values (Figures 2.13, 2.12).

To modify TiO_2 and ZnO with silver (Ag), we used a process similar to that in Chen *et al.*[102] For the Ag-modified photocatalysts, TiO_2 was decorated with 1% Ag by weight (denoted TiO_2-Ag (1wt%)), and ZnO was decorated with 0.1% and 1% Ag by weight (denoted ZnO-Ag (0.1wt%) and ZnO-Ag (1wt%), respectively). In each case, 2 g of commercial TiO_2 or ZnO nanoparticles was mixed in 400 mL deionized H_2O with silver nitrate (>99.0%, Sigma-Aldrich, Product No. 209139, CAS No. 7761-88-8), according to desired weight loading of Ag. The solution was fully evaporated at 80°C while stirring at 500 revolutions per minute (rpm). The precipitates were ground by mortar and pestle and then heated in air through a 2 hr ramp to 350°C and a 2 hr hold at 350°C. The final photocatalyst was ground by mortar and pestle.

For gold (Au)-containing catalysts, an Au colloid was synthesized by dissolving 25.2 mg $HAuCl_3 \bullet 3H_2O$ ($\geq$99.9%, Sigma-Aldrich, USA, Product No. 520918, CAS No. 16961-25-4) and 11.6 mg polyvinylpyrrolidone (Mw 1,300,000, Sigma-Aldrich, USA, Product No. 437190, CAS No. 9003-39-8), a surfactant used to prevent Au nanoparticle aggregation, in 400 mL deionized H_2O. After stirring for 30 minutes (min), the solution was injected with 3.2 mL of freshly prepared $NaBH_4$ (0.1 M, 12 mg) aqueous solution ($\geq$99%, Sigma-Aldrich, USA, Product No. 213462, CAS No. 16940-66-2). After stirring for another 2 hr, the Au colloid was concentrated by heating at 70°C until the solution was reduced to 100 mL. The concentration of Au was quantified with ICP-MS. To synthesize ZnO-Au (0.1wt%) and TiO_2-Au (1wt%), 2 g of commercial TiO_2 or ZnO nanoparticles was mixed in 400 mL deionized H_2O with the prepared Au colloid, according to desired mass loading of Au. The solution was stirred for 6 hr, followed by a 10 min centrifuge at 10,000 rpm to separate the solids from the H_2O. The H_2O was disposed of, and excess H_2O evaporated at 80°C for 6 hr. The precipitates were ground by mortar and pestle and then heated in air (2 hr ramp to 350°C, 2 hr hold at 350°C) to remove ligands and load the Au nanoparticles on the base catalyst. The final catalyst was ground by mortar and pestle.

TiO_2-FS was synthesized through a modified procedure from Pazokifard *et al.*[157], in which 0.465 g 1H,1H,2H,2H-Perfluorooctyltriethoxysilane (>97.5%, Sigma-Aldrich, Product No. 667420, CAS No. 51851-37-7) was dispersed in 40 mL absolute ethanol and then added to 2 g TiO_2 nanoparticles and 20 mL absolute ethanol. The solution was mixed for 18 hr in the dark. The dispersions were then centrifuged for 10 min at 10,000 rpm and washed twice in denatured ethanol. The residues were dried in an oven at 50°C for 48 hr to remove excess ethanol.

2.4.2 ICP-MS Characterization

For cocatalyzed samples, inductively coupled plasma mass spectrometry (ICP-MS) with a Thermo Scientific ICAP RQ ICP-MS was used to confirm the weight loading of Ag and Au. The results are shown in 2.2. The actual loadings were in each case close to the nominal loadings and we conclude that the cocatalyst modification procedure worked as intended.

Catalyst (nominal loading)	ICP-MS-quantified loading
ZnO-Ag (0.1wt%)	0.103 wt% Ag
ZnO-Ag (1wt%)	1.039 wt% Ag
ZnO-Au (0.1wt%)	0.127 wt% Au
TiO_2-Ag (1wt%)	1.095 wt% Ag
TiO_2-Au (1wt%)	0.929 wt% Ag

Table 2.2: Quantification of Ag weight loading on photocatalysts by inductively coupled plasma mass spectrometry (ICP-MS).

2.4.3 UV-Vis Characterization

UV absorption of all samples was collected via ultraviolet-visible light spectrometry (UV-Vis) using an Agilent Cary 6000i UV/Vis/NIR spectrometer with a diffuse reflectance accessory, with powder samples immobilized on slides using grease. The subtraction of a background spectrum was performed in the Agilent software at the time of measurement. The results are shown in Figure 2.4. The spectra are consistent with those from literature (where available) for the same catalysts. The photocatalysts also all exhibit good UV absorption.

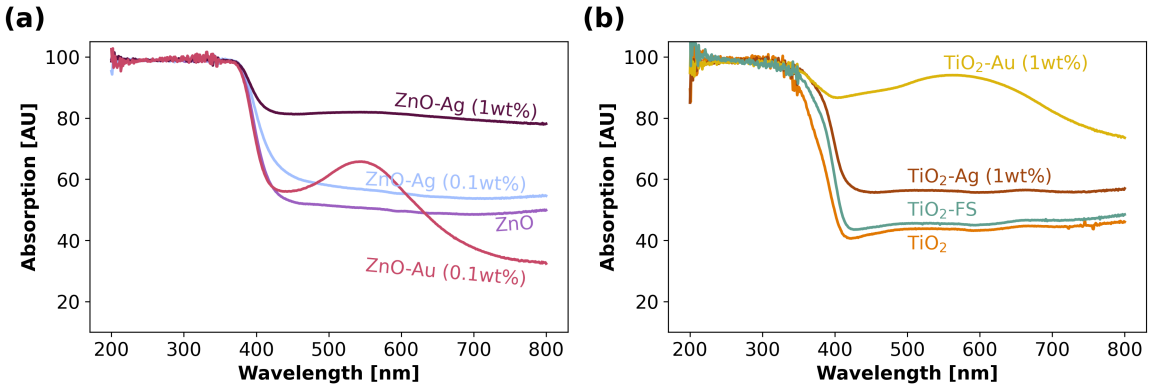

Figure 2.4: Photocatalyst light absorption based on UV-Vis. **(a)** ZnO-based photocatalysts. **(b)** TiO_2-based photocatalysts.

2.4.4 Transmission Electron Microscopy

To confirm the size of the photocatalysts and distribution of Ag and Au particles, atomic number (Z) contrast imaging was conducted via transmission electron microscopy (TEM) with a probe aberration-corrected FEI Titan Cubed Spectra, with a 300 kV voltage, 30 mrad convergence semi-angle, and 91 mm camera length. High-angle annular dark-field (HAADF) imaging was combined with energy dispersive spectroscopy (EDS) to perform elemental mapping. The same procedure was used to verify the presence of fluorisilane's elemental components (F, C, and Si) on the TiO_2-FS sample. TEM images of the various samples are presented further below along with the results of the temperature-programmed desorption (TPD) experiments.

2.4.5 X-Ray Diffraction

For a subset of the photocatalysts, the bulk crystal structure was examined with X-ray diffraction (XRD), using a PANalytical X'Pert PRO diffractometer. XRD only probes the base photocatalysts (not the cocatalysts) [102] and the XRD spectra of ZnO and TiO_2 are well-known, so the results are not plotted here.

2.5 Photocatalytic Rate Measurements in Dry Air

We began by evaluating the TiO_2 and ZnO photocatalysts, pristine and Au/Ag decorated, for the complete oxidation of CH_4 under dry conditions. Figure 2.3 in a previous section illustrates the changes in CH_4 concentration at the photoreactor outlet after passing a near-atmospheric concentration of CH_4 ($\sim$2 ppm) over three photocatalysts. Under UV illumination, the concentration of CH_4 decreased in all cases; without illumination, no change in CH_4 concentration was observed. We collected similar experimental results for a variety of photocatalysts at a variety of CH_4 concentrations. In call cases, CO_2 was the majority reaction project. Representative data from a trial with 100 ppm inlet CH_4 are shown in Figure 2.5. In all cases, the measured CO production was very small (¡1 ppm) and difficult to distinguish from noise in the gas analyzer.

ZnO-Ag (1wt%) exhibited the highest reaction rate of the photocatalysts tested

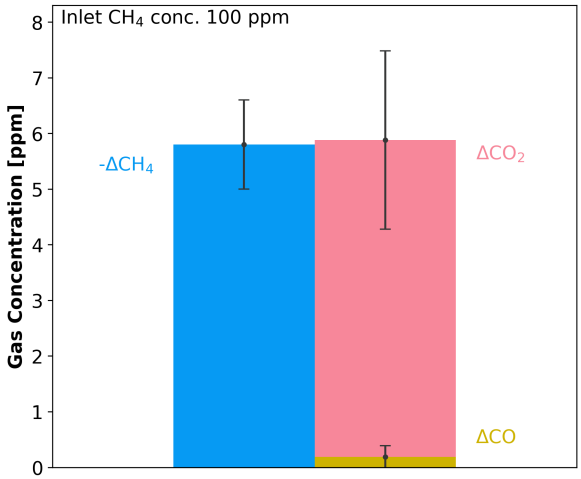

Figure 2.5: Carbon mass balance on the reactant and products of conversion of 100-ppm CH_4 on pristine ZnO. The concentrations were allowed to stabilize for 12 hours due to the very slow stabilization of the carbon dioxide signal.

for 2 ppm CH_4 oxidation. To apply the same cocatalyst to TiO_2, we also tested TiO_2-Ag(1wt%), though it performed poorly. Carbon mass balance measurements of the reactants and products showed that the photocatalysts converted CH_4 nearly entirely to CO_2 (Fig. 2.5).

Although we tested a number of photocatalysts, we identified ZnO, TiO_2, and ZnO-Ag (1wt%) as those of the greatest interest. Chen *et al* found ZnO to be fairly high-performing and, as a pristine material, it is already available in large quantitites as nanoparticles.[102] Although Chen *et al* found plain TiO_2 to work poorly for CH_4 oxidiation, TiO_2 is the most widely-used commercial photocatalyst and is therfore of interest. Finally, ZnO-Ag (1wt%) exhibited the highest reaction rate of all photocatalysts tested for low-concentration CH_4 oxidation and was the highest-performing of the cocatalyzed materials. While previous literature identified ZnO-Ag (0.1wt%) as a promising CH_4-oxidizing photocatalyst at >1,000 ppm CH_4,[102] we failed to see any performance boost in the 2-100 ppm CH_4 range at 0.1% weight loading, and so we used a higher Ag loading of 1% in order to clearly distinguish the cocatalyst's benefit at low CH_4 concentrations. Rate data for ZnO, TiO_2, and ZnO-Ag (1wt%) from 2-5000 ppm are presented in Figure 2.6, while those for all photocatalysts from 2-100 ppm are presented in Figure 2.7. To our knowledge, these were the first reported CH_4

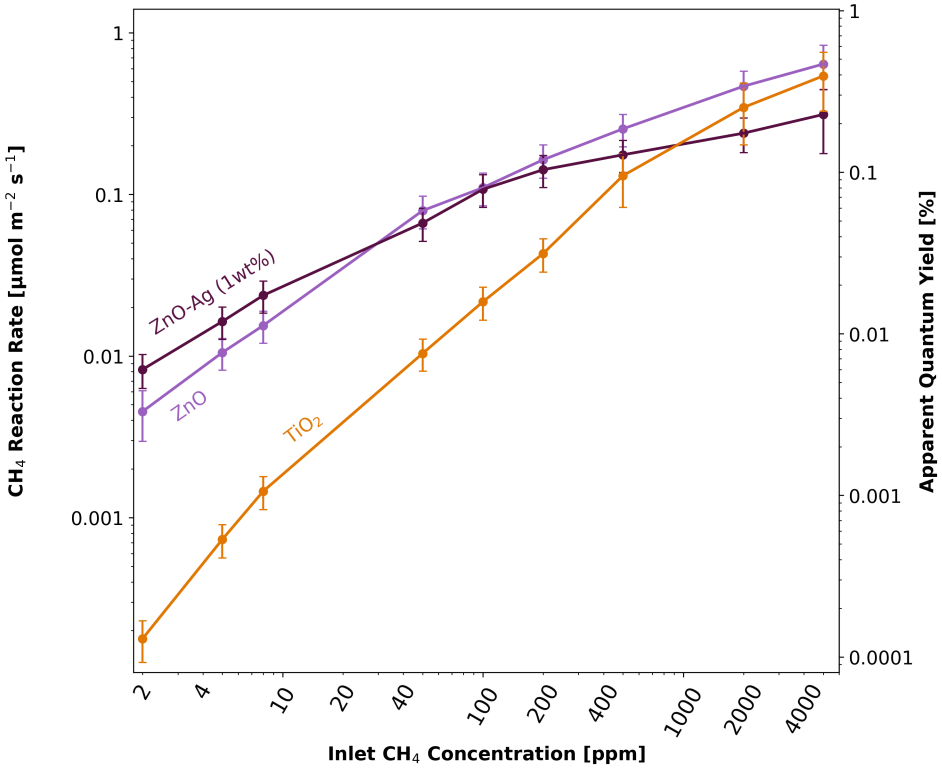

Figure 2.6: Photocatalytic CH_4 oxidation rates and AQYs for selected photocatalysts under dry conditions and 1 sun of UV light.

oxidation rates for any of these materials at <100 ppm.

We found the reaction rates and AQYs of the photocatalysts to depend positively on the inlet CH_4 concentration. Each rate plot in Figure 2.6 is concave-down, with rates decreasing rapidly with lower CH_4 concentrations. Such rate laws are common to photocatalysts and can arise from Langmuir-Hinshelwood kinetics in which the overall reaction rate is first-order with respect to CH_4 concentration on account of adsorption limits and approaches zero order with increasing concentration as CH_4 surface coverage saturates.[155, 158, 159] We normalized the reaction rate by the area of the packed photocatalyst bed exposed to UV illumination and defined AQY [unitless] as the ratio between the normalized reaction rate [µmol $CH_4 \cdot m^{-2} \cdot s^{-1}$] and the incident UV flux [µmol photon$\cdot m^{-2} \cdot s^{-1}$].[160, 161] These conventional definitions hold, and are thus useful, for planar reaction geometries. While planar reactions are common in photocatalytic systems (e.g., painted surfaces and monolith reactors),

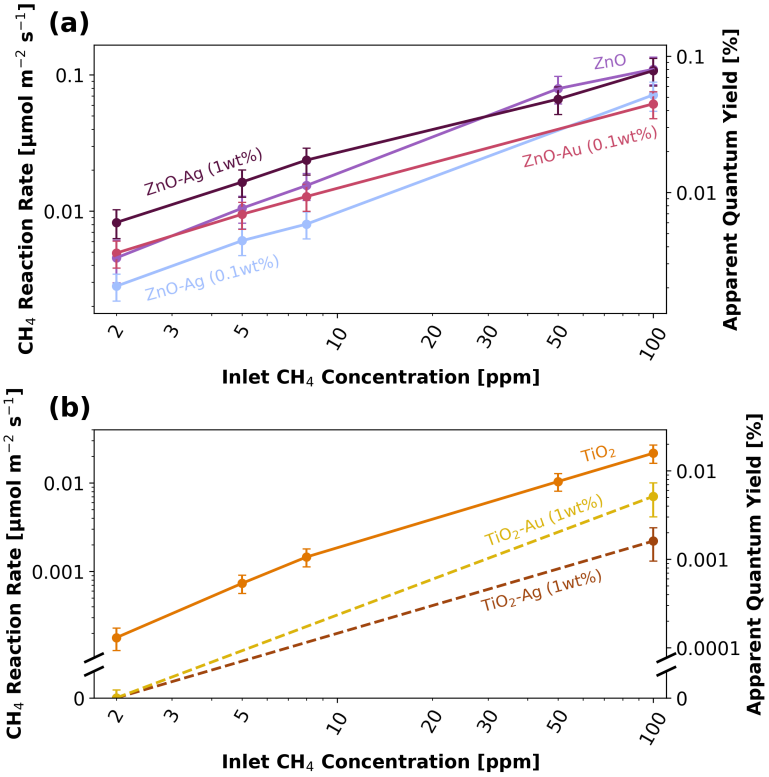

Figure 2.7: Photocatalytic CH_4 oxidation rates and AQYs for all photocatalysts under dry conditions and 1 sun of UV light. **(a)** ZnO-based photocatalysts. **(b)** TiO_2-based photocatalysts. TiO_2-Au and TiO_2-Ag showed no statistically significant CH_4 conversion at 2 ppm; their lines are dashed because they cross the broken part of the Y-axis.

there may be other deployment types (e.g., packed or fluidized bed reactors and aerosols) for which these results are less useful.

Fig. 2.6 also shows that for all three photocatalysts, the normalized reaction rates significantly decreased with lowering CH_4 concentration. ZnO outperformed TiO_2, especially for CH_4 concentrations below 1,000 ppm. While Ag modification on ZnO is known to enhance charge separation and can boost rates at CH_4 low concentrations where adsorption is a rate-limiting step, at high CH_4 concentrations where surface saturation becomes dominant, the intrinsic accessibility of active sites may become a more dominant factor.[102, 158]

2.6 Effects of Light Intensity

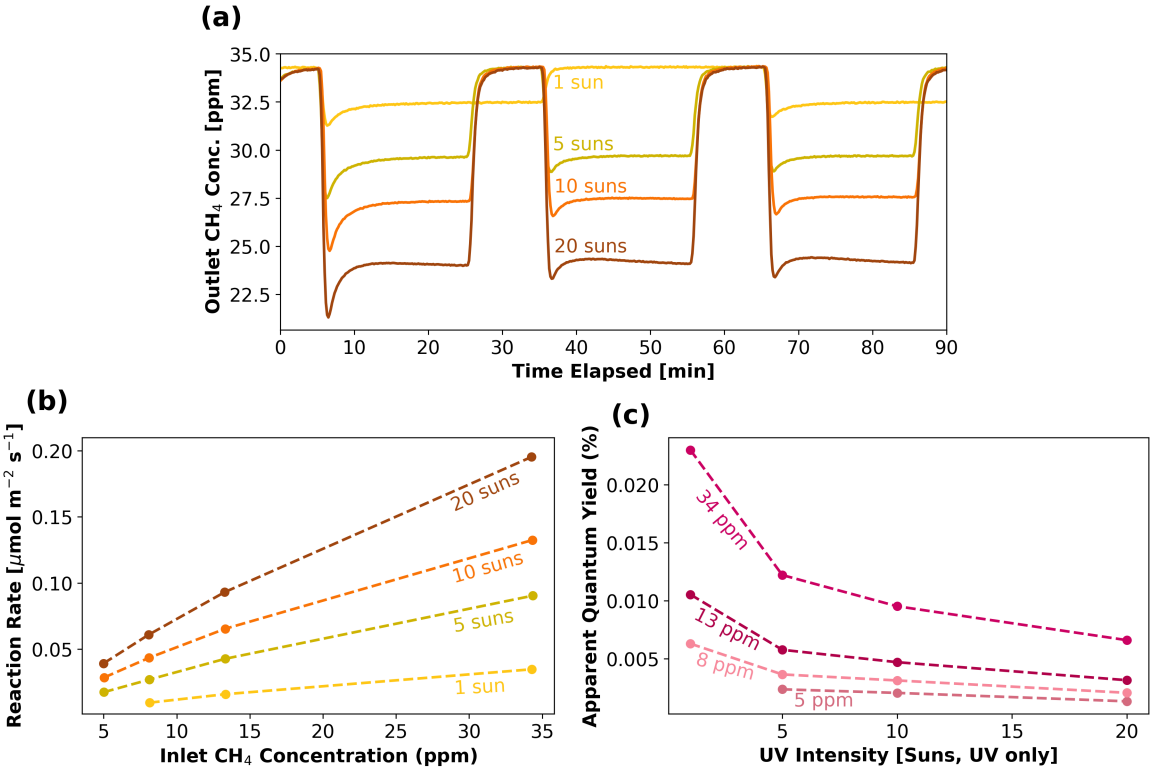

Figure 2.8: The effects of UV light flux on CH_4 oxidation. '1 sun' refers to a UV flux of 4.5mW·cm^{-2}, equal in intensity to the <365nm component of an AM1.5g reference solar spectrum. **(a)** Time series of CH_4 concentrations at the photoreactor outlet for pristine ZnO and 34-ppm inlet CH_4 under different light concentrations. Higher light fluxes cause higher CH_4 conversions, albeit with diminishing returns. **(b)** Reaction rate as a function of inlet CH_4 concentration for different light intensities. In all cases, rates increase with both concentration and light flux. **(c)** Apparent quantum yield as a function of light intensity for different inlet CH_4 concentrations. For a given inlet CH_4 concentration, raising the light flux causes the AQY to decrease.

We briefly explored the effects of light intensity on ZnO's dilute CH_4 oxidation rates. Our results are consistent with the general principle that increasing the light intensity boosts photocatalysts' rates, but with diminishing returns for higher irradiances..[155] These findings are illustrated in Figure 2.8 This behavior occurs because as higher irradiances make charge carriers abundant at the photocatalyst surface,

other processes (such as reagent sorption) become rate-limiting, causing charge carriers to be wasted. The net effect is that as the light intensity increases, the rate increases but the quantum yield decreases. The practical implication is that one cannot boost a photocatalyst's rate arbitrarily high by using extremely strong artificial lights; for instance, using 20 suns of UV LED light gives a rate only 8 times higher than the rate at 1 sun. Additionally, deployment schemes using intense artificial lights rather than sunlight are likely find it harder to achieve high photocatalytic quantum yields.

2.7 Effects of Residual Water and Humidity

It was clear from our very first experiments that moisture plays a critical role in determining photocatalysts' CH_4-oxidizing performance. In standard procedure, an hour-long dry nitrogen purge preceded every dry CH_4-oxidation experiment. If we omitted this purge and began cycling the light just after the photocatalyst was loaded in the reactor, its initial performance would be very poor, but it would gradually increase to reach its steady-state value. We hypothesized that this behavior was caused by a thin "residual" layer of water from the room's humidity that stuck to the photocatalyst surface and was gradually removed by the dry gas stream. We also suspected that this water layer was not completely removed even under dry conditions, but rather that some water remained on the surface and inhibited CH_4 oxidation. There had already been reports of similar phenomena of H_2O and carbonates accumulating on oxide photocatalyst surfaces exposed to air and blocking reagents' access to active sites and charge carriers.[162]

To verify the presence of a residual water layer, we heated TiO_2 and ZnO (forcing surface species to desorb) while observing their surfaces with *in-situ* diffuse reflectance infrared spectroscopy (DRIFTS). DRIFTS measurements were performed using a ThermoFisher IS-50 FTIR spectrometer fitted with a Praying Mantis DRIFTS accessory (Harrick Scientific Products). Spectra were collected with a Mercury cadmium telluride detector. The optical path was purged with dry air. Photocatalyst powders were loaded into a high-temperature environmental chamber with zinc selenide

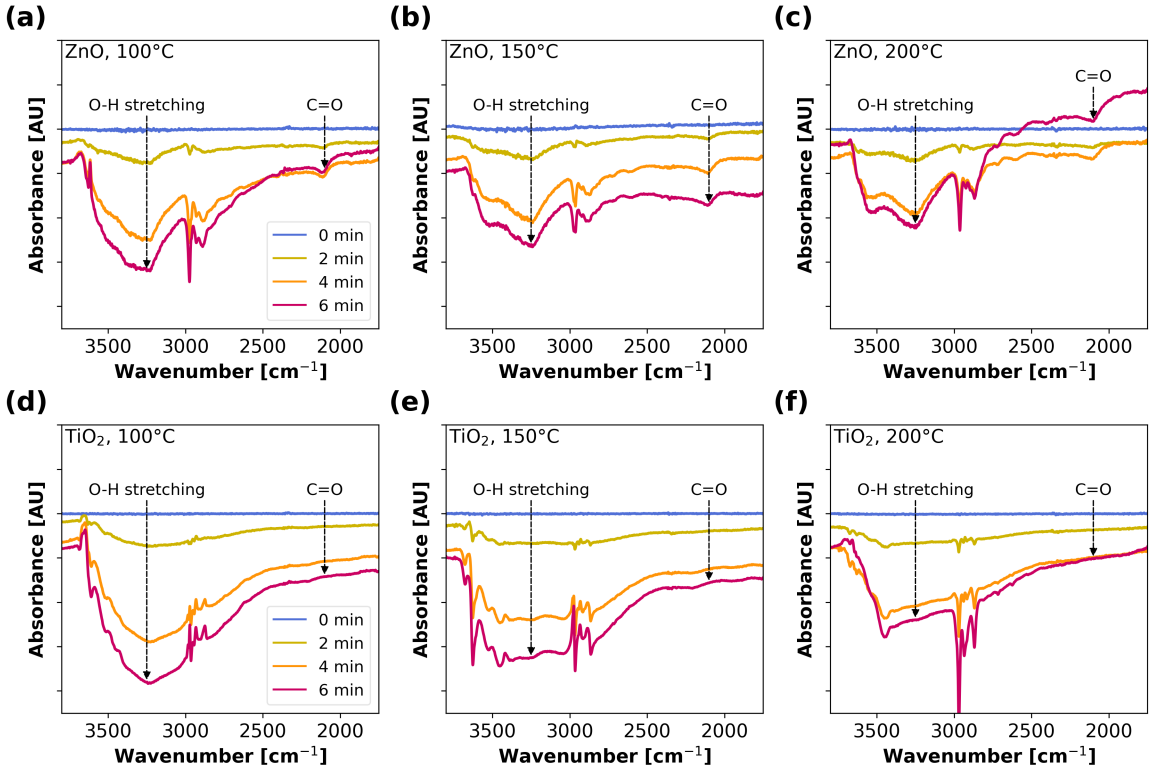

Figure 2.9: DRIFTS spectra of ZnO and TiO_2. The top row of subplots shows ZnO, and the bottom row shows TiO_2. The subplot columns represent isothermal trials at 100°C, 150°C, and 200°C. Each plot shows data during the first six minutes, by the end of which the spectra had stabilized. The vertical scale is the same across all subplots and represents absorbance according to $-log(I/I_0)$, where I_0 and I are the spectra of background (flat blue line) and during the holding period, respectively. The approximate locations of changes associated with OH and CO_2 are indicated.

windows for *in situ* measurements. The photocatalysts were heated from room temperature to 50°C, 100°C, 150°C, 200°C, 250°C, and 300°C under 30 mL·min^{-1} of 21% O_2 in argon, held at each temperature for 10 min. After the sample reached the specified temperature, a background spectrum was collected by averaging 16 scans. The DRIFTS spectrum was repeatedly measured throughout the 10 min holding period, with 16 scans collected in each spectrum.

We found H_2O to be the dominant species released from the surface, indicated by

changes in O-H stretching (Figure 2.9). The release of H_2O started at low temperatures, with only minor release of CO_2 as indicated by changes in C=O stretching occurring at high temperatures. This can be explained by the physical desorption of H_2O requiring lower temperature than the chemical decomposition of carbonates that form CO_2.[163]

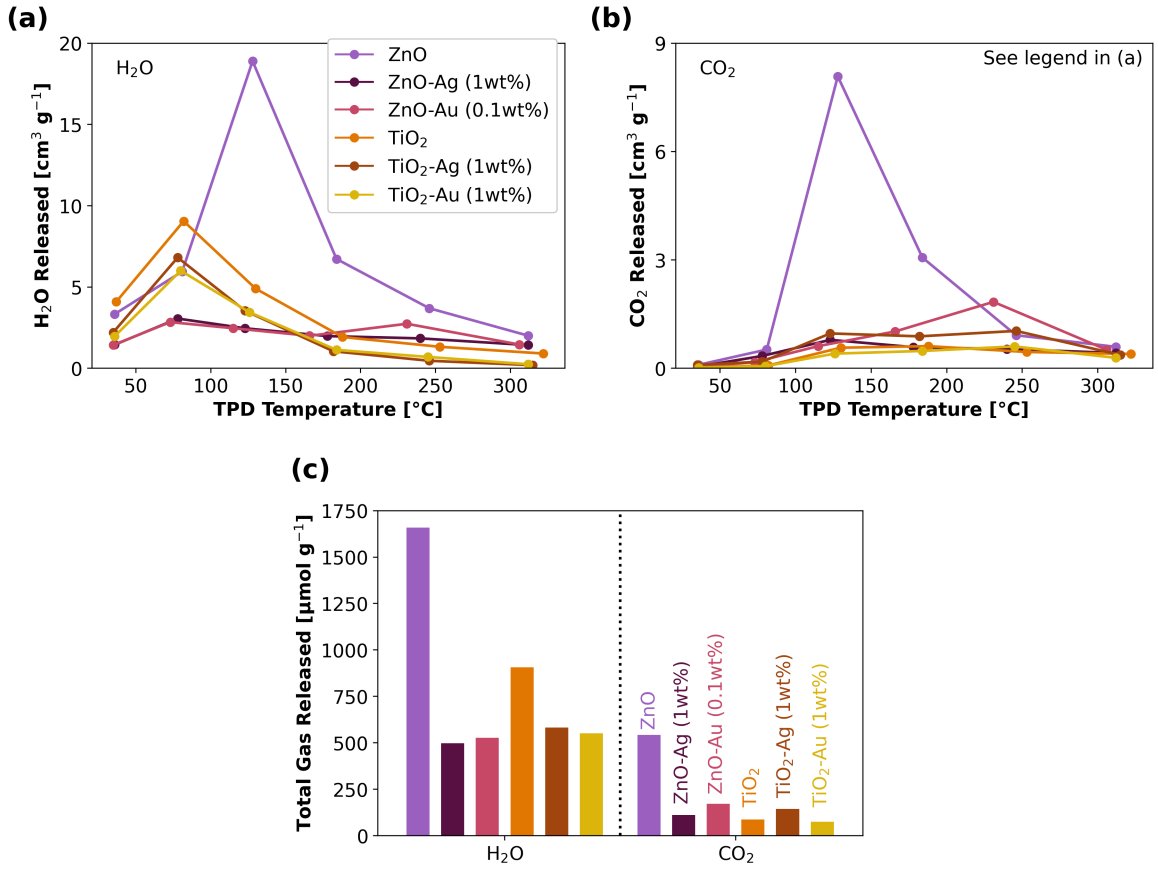

Figure 2.10: Gases desorbed from photocatalysts during TPD experiments. Released quantities of **(a)** H_2O and **(b)** CO_2 as functions of temperature, normalized by photocatalyst mass. **(c)** Total amounts of H_2O and CO_2 released over the course of the entire TPD experiment, normalized by photocatalyst mass.

We then pursued a campaign of temperature-programmed desorption (TPD) experiments on a variety of photocatalysts. These tests revealed 1) which gases desorbed from the photocatalyst during a temperature ramp up to 325°C and 2) how

the photocatalyst's performance changed after these species had desorbed. For these experiments, the reactor tube rested in a horizontal tube furnace (Thermcraft) such that UV light was not blocked when the furnace lid was open (Figure 2.2). After a photocatalyst was loaded, a baseline photocatalytic rate measurement at 100 ppm CH_4 was conducted. The furnace lid was then closed and the temperature setpoint was increased in steps, each 1 hr long, during which time the released gasses were measured with the FTIR spectrometer. The temperature inside the reactor tube was measured with an internal thermocouple. After stepping to 75°C and 125°C, the furnace lid was opened and the reactor was allowed to cool to room temperature under synthetic air, at which time a 'post-125°C TPD' photocatalytic rate measurement at 100 ppm CH_4 was collected. The furnace was then closed and the temperature returned to 125°C to drive off any CH_4 oxidation reaction products (CO_2 and H_2O). Finally, the temperature was stepped to 175°C, 225°C, 275°C, and 325°C, after which the furnace was opened and a final, 'post-325°C TPD' photocatalytic rate measurement at 100 ppm CH_4 was collected.

As shown in Figure 2.10 TPD experiments on TiO_2 and ZnO, both pristine and with cocatalysts, revealed that both H_2O and CO_2 desorbed from the surface at elevated temperatures. For all photocatalysts, ∼3 times more H_2O was released than CO_2, and ZnO released several times more H_2O and CO_2 than any other catalyst. In agreement with the DRIFTS results, H_2O was released at lower temperatures than CO_2. These results confirm that there is indeed a residual layer of water and, to a lesser extent, carbonates that remains on the photocatalyst's surface even under nominally "dry" conditions.

Substantial changes to CH_4 reaction rates were observed for the photocatalysts after heat treatment (Fig. 2.11). Reaction rates of pristine ZnO increased when H_2O was driven post-125°C TPD and then declined post-325°C TPD. Post-TPD ZnO took on a slight yellow color, a sign of surface phase change through loss of oxygen at high temperatures.[164] For ZnO samples before and after heat treatment, we conducted X-ray diffraction (XRD) to examine their bulk crystal structures, which were found to be identical. Thus, we conclude that the degraded performance of ZnO post-325°C TDP was due to changes on the ZnO surface. ZnO-Ag (1wt%) followed a similar trend to pristine ZnO of peaking in performance post-125°C TPD, though maintaining a higher

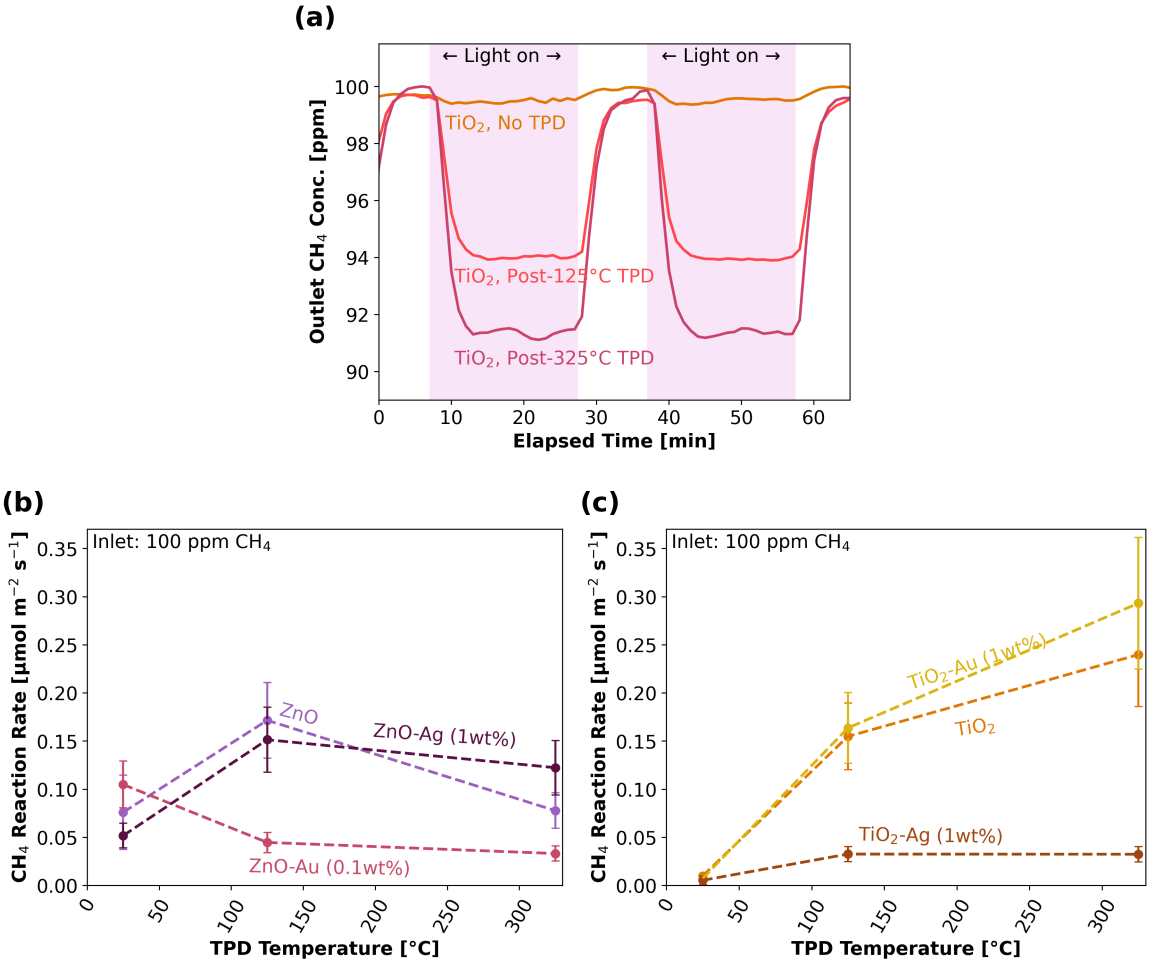

Figure 2.11: Residual surface species and their effects on reaction rates.

reaction rate post-325°C TPD than pristine ZnO. TEM imaging (Figure 2.12) revealed that the Ag particles aggregated upon heat treatment, a known effect.[165, 166] In addition to Ag aggregation, oxidation of the Ag nanoparticles may have degraded the active metal sites and reduced the performance at high temperatures.[167, 168]

The CH_4 reaction rates on pristine TiO_2 increased with TPD temperatures. Indeed, TiO_2-Au post-325°C TPD showed the highest rate of any heat-treated photocatalyst tested at 100 ppm CH_4. Unlike ZnO, TiO_2's high thermal stability likely allowed it to remain active after heat treatment.[169] TEM imaging showed that the Au cocatalyst *did* aggregate into larger particles, as seen in Figure 2.13, suggesting

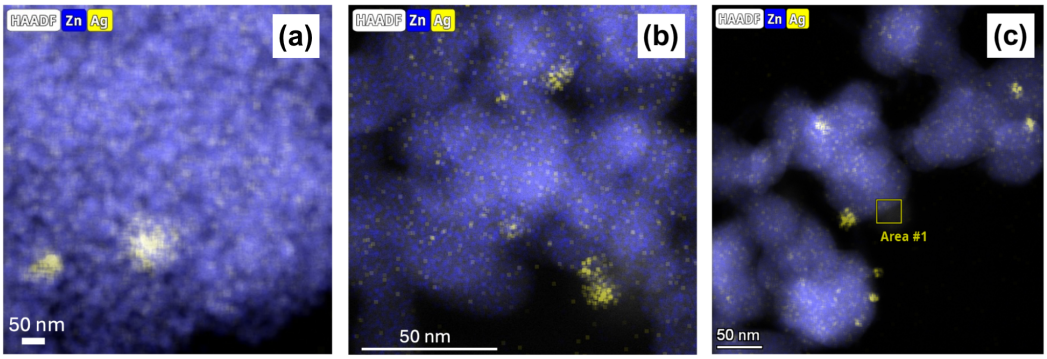

Figure 2.12: TEM images of ZnO-Ag (1wt%) with elemental mapping. **(a)** as-synthesized, **(b)** after time on-stream in the reactor, and **(c)** after a TPD experiment at up to 325°C.

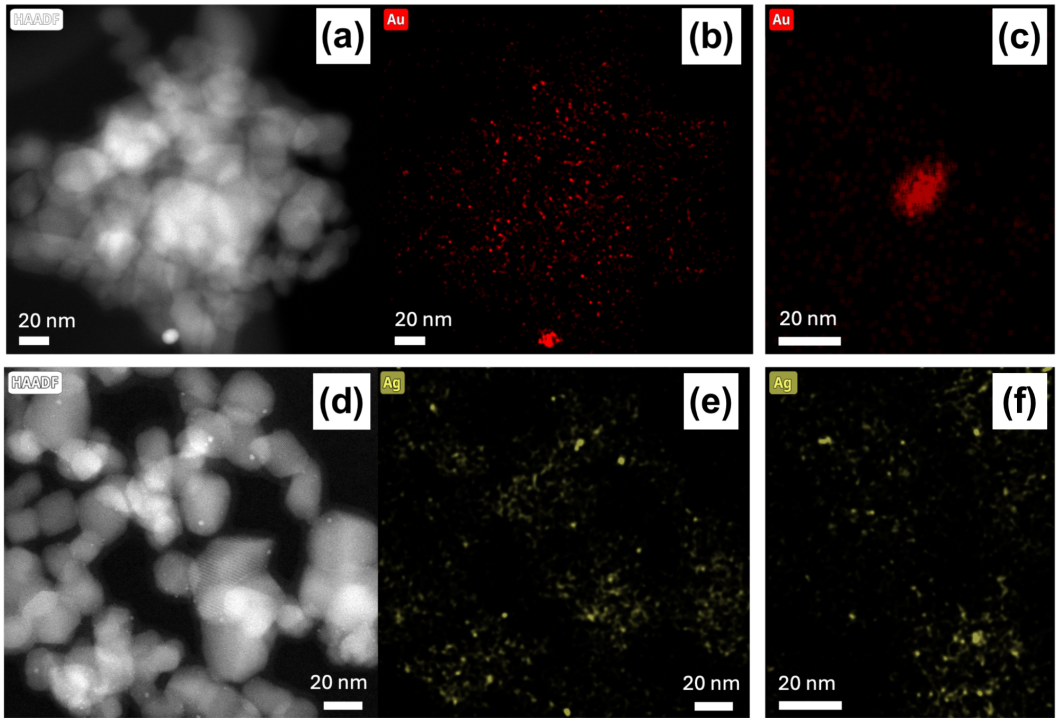

Figure 2.13: TEM imaging of TiO_2-based materials. TiO_2-Au (1wt%) **(a)** pre-TPD under HAADF, **(b)** pre-TPD under EDS elemental mapping of Au, and **(c)** post-325°C TPD under elemental mapping of Au. TiO_2-Ag (1wt%) **(d)** pre-TPD under HAADF, **(e)** pre-TPD under EDS elemental mapping of Ag, and **(f)** post-325°C TPD under elemental mapping of Ag.

that the cocatalyst remained effective after aggregation. The reaction rates of TiO_2-Ag (1wt%) slightly increased post-125°C TPD and then plateaued post-325°C TPD. TEM imaging did not reveal growth of Ag nanoparticles on TiO_2 post-325°C TPD (Figure 2.13), suggesting that the poor performance may be due to surface oxidation of the Ag nanoparticles rather than to particle aggregation. That the rates of heat-treated TiO_2-Ag (1wt%) were substantially lower than those for pristine TiO_2 is an interesting result that could be explored in future studies.

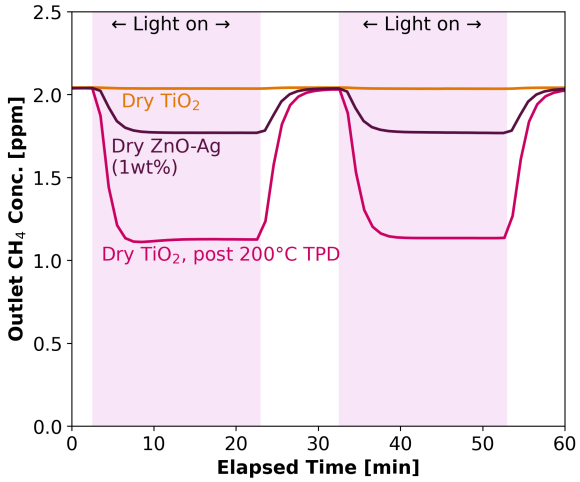

Figure 2.14: Time series of 2 ppm CH_4 concentrations at the photoreactor outlet for TiO_2 after a 200°C TPD trial. Non-heat-treated TiO_2 and non-heat-treated ZnO-Ag (1wt%) under the same conditions are shown for reference.

Finally, we conducted a one-off experiment with heat-treated TiO_2 and 2 ppm (rather than 100 ppm) CH_4. We chose TiO_2 because of its excellent post-TDPD performance. In this case, we conducted a TPD at 200°C and then conducted a CH_4 oxidation experiment with 2 ppm CH_4. The result, shown in Figure 2.14, was a >40% CH_4 conversion, by far the highest seen in any experiment. The conversion steadily declined from this value over the course of several hours of continuous light cycles. This result gives an interesting demonstration of what rates could be possible if a photocatalyst were to completely solve the issue of residual surface water.

2.8 Inhibition of Photocatalysts by Humidity

Based on the TPD experiments and on the initial experience of photocatalysts working poorly just after loading, we hypothesized that photocatalysts would struggle to oxidize CH_4 in a humid environment. As noted, this question had not been experimentally investigated in prior literature. Realistic applications of CH_4 oxidation often have relative humidities (RH) of 30% or higher, making the issue fairly important. Water was also already known to inhibit palladium-based CH_4 oxidization thermocatalysts.[170, 171]

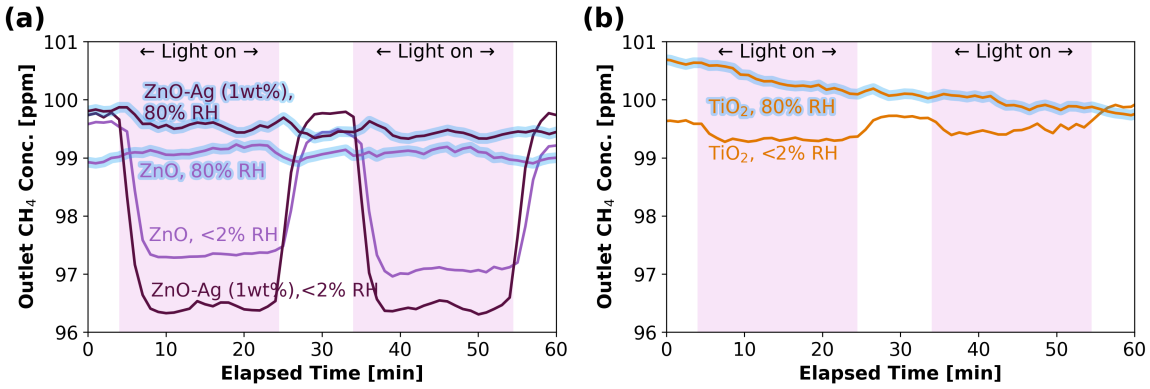

Figure 2.15: The impact of humidity on photocatalytic CH_4 oxidation. Time series of CH_4 concentrations at the photoreactor outlet under dry (<2% RH) and humid (80% RH) conditions for **(a)** ZnO and ZnO-Ag (1wt%) and **(b)** TiO_2. The humid TiO_2 signal drifts somewhat due to inherent stability issues when MFCs are placed upstream of bubblers; however, any CH_4 oxidation would still have been visible if present.

After testing each photocatalyst under ~80% humid conditions, we did not observe statistically significant CH_4 conversion for any of them (Fig. 2.15). Though we did not test intermediate humidities due to the limitations of our setup at the time, the initial post-loading results suggest that intermediate humidities would also completely inhibit CH_4 oxidation. By way of explanation, although the availability of H_2O could plausibly boost the formation of OH•, we suggest that instead H_2O formed a thick layer on the hydrophilic oxide surfaces that CH_4 and/or OH• could not penetrate. The water layer would be impermeable to these species because of the low solubility

of CH_4 and the extremely short lifetime of OH• in H_2O The .

These results confirmed our hypothesis about the severe inhibitory role of humidity in photocatalytic CH_4 oxidation. The inability of known photocatalysts to work in humid environments is a serious challenge to the viability of photocatalytic CH_4 oxidation in real-world deployment scenarios.

2.9 A Humidity-Tolerant Photocatalyst

The detrimental effect of humidity on the previously tested photocatalysts led us to explore using a hydrophobic coating to repel H_2O from the catalyst surface. Hydrophobic coatings such as silane groups can be chemically grafted to semiconductor surfaces as self-assembled layers, an approach that has been successfully used on TiO_2.[172] In particular, the C-F bonds in 1H,1H,2H,2H-Perfluorooctyltriethoxysilane (henceforth referred to as fluorosilane or FS) is chemically inert and cannot be cleaved by OH• at room temperature.[157]

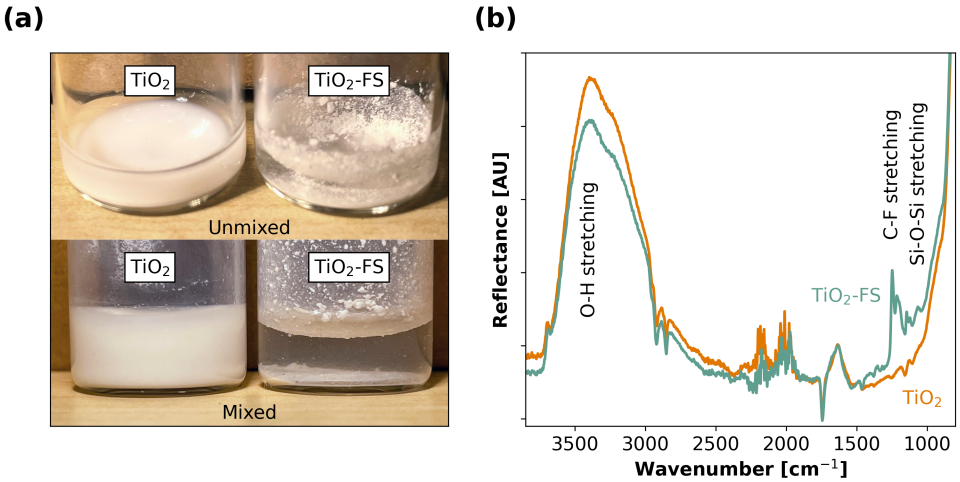

Figure 2.16: Characterization of TiO_2-FS. **(a)** Dispersion of the nanoparticles in distilled water, before and after mixing. **(b)** Results from attenuated total reflectance Fourier transform infrared spectroscopy (ATR-FTIR).

Following the procedure in Pazokifard *et al.*,[157] we modified the surface of TiO_2 nanoparticles with ∼20 wt% fluorosilane (TiO_2-FS). We confirmed the modified material's hydrophobicity by dispersing the nanoparticles in distilled water (Fig. 2.16**(a)**)

and confirmed the presence of FS on TiO_2 with attenuated total reflectance Fourier transform infrared spectroscopy (ATR-FTIR) (Fig. 2.16**(b)**). In Fig. 2.16**(b)**, the peak centered around 3,400 cm^{-1} is characteristic of O-H stretching from H_2O, and the peaks in the regions 1,250-1,130 cm^{-1} and 1,080-1,060 cm^{-1} may be attributable to the stretching of C-F and Si-O-Si, respectively, indicating the presence of fluorosilane.[173, 174] TEM imaging of TiO_2-FS also revealed a uniform distribution of fluorine and silicon with titanium, providing another indication of the grafting of the fluorosilane onto the $TiO_2$2.17.

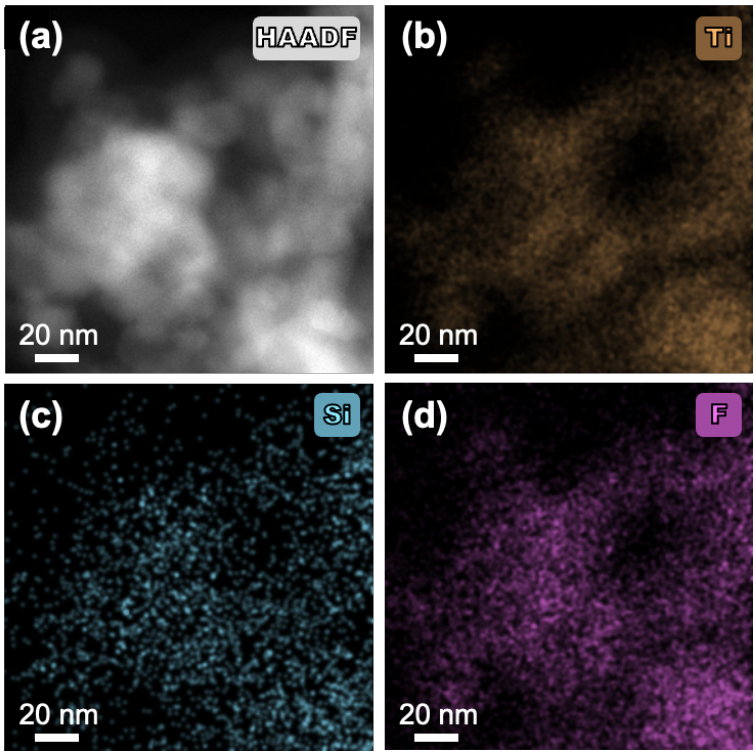

Figure 2.17: TEM imaging of fluorosilane-coated TiO_2 (TiO_2-FS). **(a)** Under HAADF. (b-d) Under EDS mapping of titanium (Ti), silicon (Si), and fluorine **(f)**.

Unlike the other photocatalysts, TiO_2-FS was able to oxidize CH_4 under both dry (<2% RH) and humid (40% RH and 80% RH) conditions (Fig. 2.18**(a)**). Under dry conditions, the CH_4 reaction rate of TiO_2-FS was similar to that of pristine TiO_2 at 100 ppm CH_4 and higher than that of pristine TiO_2 at 2 ppm CH_4. More importantly, Fig. 2.18**(b)** shows that the CH_4 reaction rates of TiO_2-FS are higher under humid

conditions (80% RH) than under dry conditions (<2% RH). This is observed in CH_4 concentrations ranging from 2 to 100 ppm. While it is challenging to precisely control and quantify the thickness of the water layer, our results suggest that under humid conditions the hydrophobic coating not only prevents the accumulation of H_2O on the surface but also enables a better utilization of H_2O as the source of OH•, thus accelerating reaction kinetics. We also note that, for 100 ppm CH_4, the oxidation rates with TiO_2-FS under 80% RH still have substantial room for improvement when compared to the maximum reaction rate for the heat-treated TiO_2 under dry conditions (Fig. 2.18**(b)**). We expect that the combination of the fluorosilane loading, the underlying photocatalyst, and the system humidity level could be optimized in the future to yield higher performance.

To ensure stability of the hydrophobic coating under UV exposure, we performed an extended experiment on TiO_2-FS at 80% RH with ∼5.5 hours of cumulative UV exposure and observed minimal degradation of the sample (Fig. 2.18**(c)**). While TiO_2-FS has been previously tested as a component in hydrophobic paints, we are not aware of a previous demonstration of photocatalytic CH_4 oxidation in humid conditions.

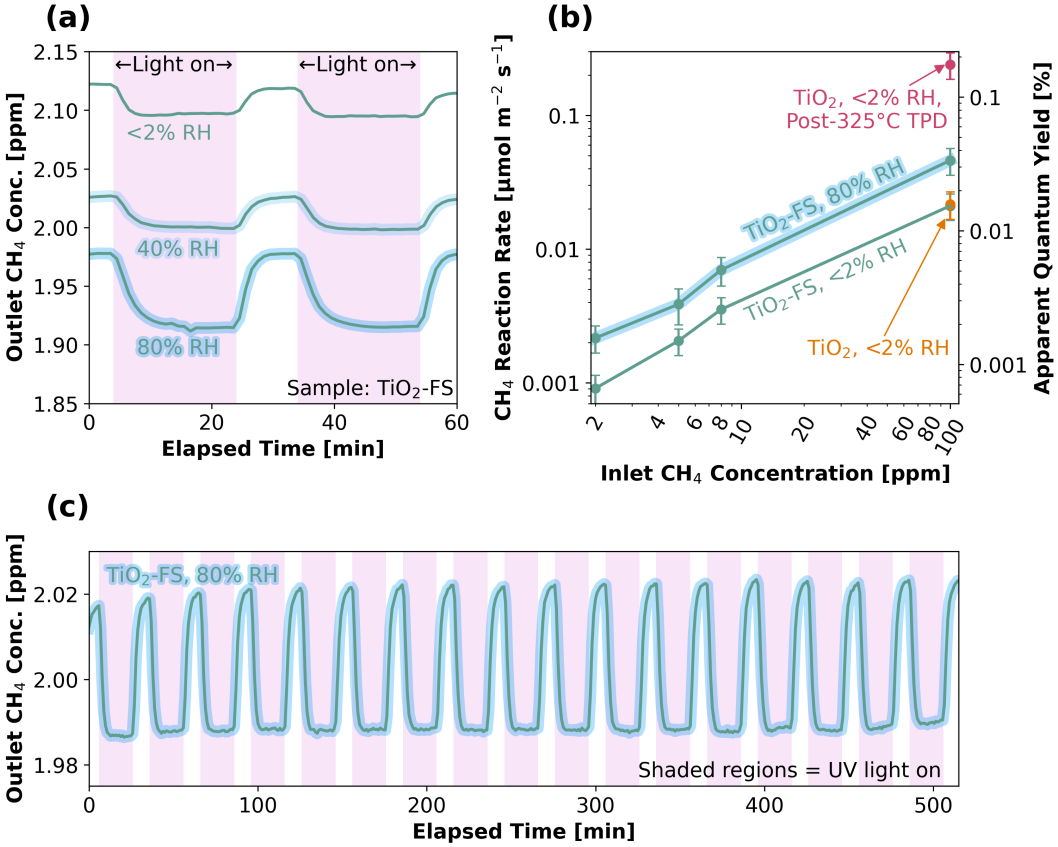

Figure 2.18: CH_4 oxidation performance of TiO_2-FS and comparison to pristine TiO_2. **(a)** Time series of CH_4 concentrations at the photoreactor outlet for TiO_2-FS at <2% and 80% relative humidities (RH). **(b)** Reaction rates and apparent quantum yields as functions of inlet CH_4 concentrations for TiO_2-FS under different humidity levels, shown with 95% confidence intervals. **(c)** Extended experiment of TiO_2-FS at 80% RH with over 8.5 hours of cycling (∼5.5 hours under UV light), showing minimal degradation.

2.10 Conclusion

The research described in this chapter provided the first detailed measurements of any CH_4-oxidizing photocatalysts' rates at <100 ppm of CH_4. To do so, we measured the rate laws (rate-vs.-concentration curves) for several photocatalysts over CH_4 concentrations ranging from 2 to 5000 ppm. The rates observed at these low CH_4 concentrations, and especially at 2 ppm, are quite low. However, we will withhold

discussion of these values' implications for practical photocatalytic CH_4 mitigation until the next chapter.

This work also probed the role of residual surface water in photocatalysts' CH_4-oxidation rates under dry conditions, explaining several previous results. Most important, Chen *et al.* had observed that ZnO considerably outperformed TiO_2 for dilute CH_4 oxidation. We showed that this order is reversed when the water layers are thermally removed from both materials, suggesting that TiO_2 has a better intrinsic performance that is masked by an inhibitory water layer. TiO_2 with the water removed outperformed ZnO-Ag (1wt%) and TiO_2-Au with the water removed only marginally outperformed TiO_2 with the water removed. Despite prior literature's focus on modifying photocatalysts to reduce charge carrier recombination or lower activation battiers, these results suggest that dealing with the inhibitory water layer may provide a better path towards higher peformance.

Finally, having observed that none of the plain or metal-cocatalyzed ZnO or TiO_2 photocatalysts could oxidize CH_4 in humid environments, we developed the humidity-tolerant TiO_2-FS photocatalyst. This material had previously been reported as an ingredient for water-resistant white paint, but it had never before been tested as a photocatalyst. To our knowledge, these experiments on TiO_2-FS are the first instance of photocatalytic dilute CH_4 oxidation under humid conditions. The rates observed on TiO_2-FS under humid conditions are nonetheless somewhat lower than those observed on ZnO and ZnO-Ag (1wt%) under dry conditions.

Chapter 3

Cost Modeling of Photocatalytic Methane Oxidation

3.1 Introduction

When my collaborators and I began the research in this chapter, various deployment strategies for CH_4-oxidizing photocatalysts had been identified, but none had been subjected to rigorous cost modeling. For the most part, photocatalysts were discussed for atmospheric methane removal, although they were also sometimes suggested for deployment on dilute methane point sources. We felt that cost projections *even rough ones* would be very useful for assessing which (if any) of these deployment strategies could be practically viable. Additionally, a tension had arisen between publications that were optimistic [46, 49] and pessimistic [72, 73] about the real-world viability of CH_4 removal. We felt that only cost modeling of specific technologies could help to resolve this debate.

Cost modeling was difficult at the time due to a lack of data about photocatalysts' rates at low CH_4 concentrations. Existing studies on photocatalyst deployment had used photocatalysts' rates with larger organic molecules or had attempted to fit rate laws to empirical data collected at higher CH_4 concentrations.[73, 132] We undertook the previous chapter's research and this chapter's research in parallel, intending for the measured rates to eventually serve as assumptions for the cost models. In the meantime, we presented the model outputs in terms of "CH_4 mitigation costs as functions of rates/AQYs". These outputs could be translated into rate/AQY targets that could be assessed for plausiblility or compared to real measurements when they became available.

At the time, several existing works had discussed the advantages and estimated the costs of different potential dilute CH_4 oxidation systems. One study gave rough cost figures for zeolite thermocatalysis, photocatalysis, and radical generation based mainly on researchers' unpublished models.[175] Air flows, CH_4 removal rates, and costs had been modeled in detail for solar updraft towers with photocatalytic active phases.[176, 177] The lifecycle CH_4 removal of a passive solar photocatalytic device had also been modeled.[178] The overall economic feasibility of 2-ppm CH_4 removal via fan-driven machines had been questioned based on the empirical trend that separation costs often rise linearly with target substance dilution.[72] However, in essentially all sub-fields of dilute CH_4 mitigation, there was (and there continues to be) considerable room for more rigorous and transparent cost analyses.

In this chapter, we present models of three candidate dilute CH_4 oxidation systems (Figure 3.1) that we felt were promising at the outset of our research. We chose systems where we were able to project the costs of widespread deployment by analogy to existing industries (e.g., commercial painting and agricultural aviation) or by adapting existing technoeconomic frameworks (such as those for CO_2-DAC machines). Despite their presence in the literature, we chose not to model solar updraft towers because no full-scale solar updraft tower has ever been built, making it difficult to model their cost. We present modeled deployment costs in dollars per ton of CH_4 ($/t$CH_4$) for all three included strategies using both the photocatalytic rates measured in the last chapter and for a range of hypothetical photocatalytic CH_4 oxidation rates.

3.2 A Shared Cost Modeling Approach

Each model computes the levelized costs of CH_4 removal in similar ways . We assume a certain unit size for each system, an assumption that in our model does not affect the levelized cost of CH_4 removal: 1 m^2 for the rooftop system, a size giving a drawdown of 1 mole of CH_4 per second for the fan-driven system, and 1000 kg of particles for the aerosol system. Each model computes the cost of the system over some period of time (1 year for the ground-based systems, with capital costs inflation-adjusted to 2023 dollars and annualized as discussed below, or the particles' atmospheric residence time for the aerosol-based system). Each estimate then finds the system's total CH_4 drawdown during the same period, evaluating whether surface reaction or convective mass transfer is the rate-limiting step. The total costs are divided by the total CH_4 drawdown to give the levelized cost per ton of CH_4 removed over that time period. The models and their most important assumptions are discussed in detail in their respective sections below.

3.2.1 Model of Rate-Limiting Steps for CH_4 Oxidation

Throughout, we use a simplified model of whether reactions or convective mass transfer are the "rate-limiting step" of photocatalytic CH_4 oxidation. Doing so is important because otherwise, one could get falsely optimistic results by assuming a reaction rate

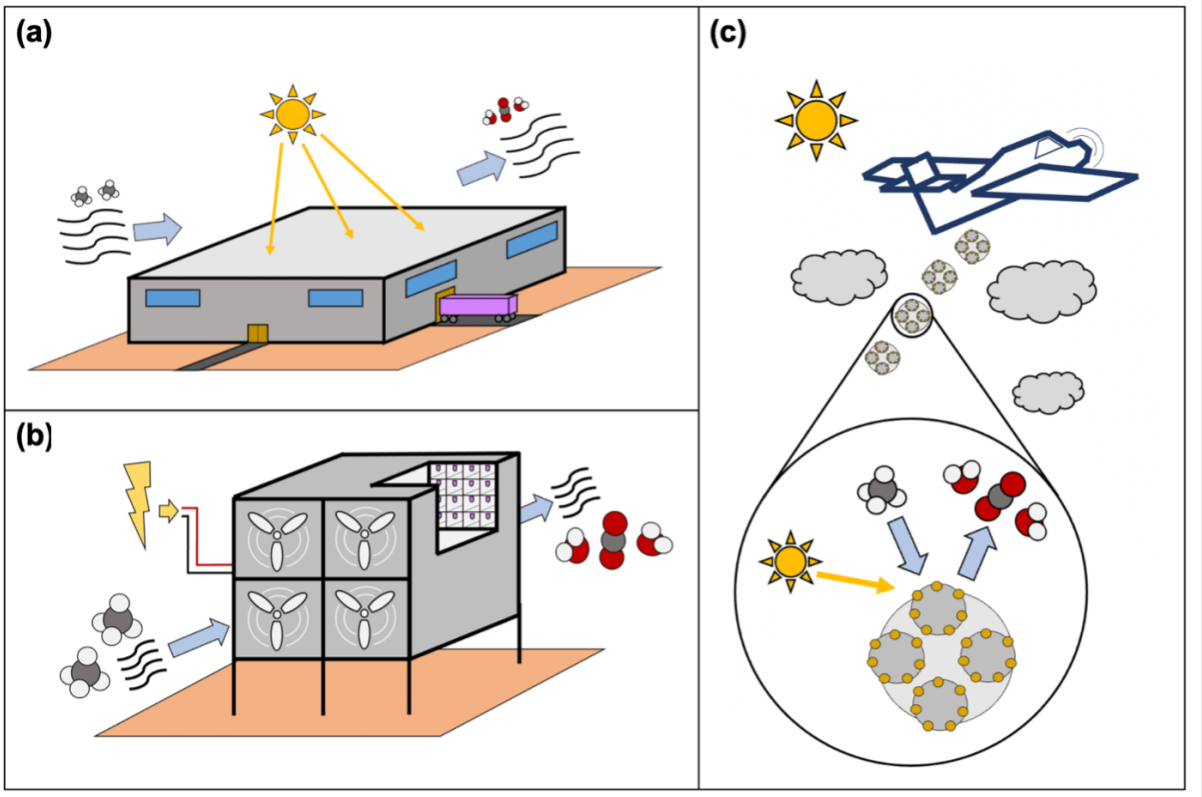

Figure 3.1: Graphical summaries of the three CH_4 oxidation systems considered. The systems are **(a)** a photocatalyst-painted rooftop under sunlight and natural, passive airflow; **(b)** a ground-based electrically driven device using forced airflow and internal LED illumination (drawn with a cutaway to show the internal photocatalyst channels and LEDs); and **(c)** an aerosol-based system using sunlight and photocatalytic particles dispersed in the troposphere.

(or, equivalently, an AQY) far higher than is actually possible given convective mass transfer limitations. At least one existing study has committed that error.[178] Our rate-limiting step approach was previously used in a model of photocatalytic CH_4 oxidation in a solar updraft tower.[176] Our modeled overall rate of CH_4 oxidation is therefore expressed as follows:

$$R_{overall} = min(R_{reaction}, R_{\dot{m}}) \tag{3.1}$$

Where $R_{overall}$ (moles/m^{2}s) is the overall rate of CH_4 drawdown per unit area of deployed photocatalyst, $R_{reaction}$ (moles/m^{2}s) is the intrinsic reaction rate that would be observed in the absence of mass transfer limitations in a benchtop rate study of the photocatalyst under a given light flux, and $R_{\dot{m}}$ (moles/m^{2}s) is the maximum rate of convective CH_4 transfer through the gas boundary layer towards the photocatalyst surface. In reality, as the reaction rate approaches the mass transfer limit, the concentration of CH_4 molecules near the surface drops, reducing the fraction of catalyst surface covered in CH_4 and consequently slowing the reaction rate to equilibrate with the mass transfer rate.[179] Whether there is a sharp or gradual transition, and how closely the catalyst can approach the mass transfer limit, depends strongly on the catalyst's affinity for the CH_4. For simplicity and generality, and consistent with previous work, we model an abrupt transition between the two rate-limiting steps.

Implicit in this approach is an assumption that CH_4-decomposing reactions take place on or very near the photocatalyst surface. Though photocatalysts often generate radicals (e.g., hydroxyl or superoxide) that can in principle exist in gaseous form, a study of TiO_2 found that few of those radicals traveled far from the catalyst surface.[101],[180] Based on these studies and on our experimental work, we thought it unlikely that enough gaseous radicals would travel far from the surface to bypass the need for CH_4 mass transfer towards the surface. Therefore, in our models, the rates and AQYs account for both direct (charge carriers reacting absorbed CH_4) and indirect (gaseous radical-mediated) reaction mechanisms.

The mass transfer rate towards the surface is calculated using the Sherwood number, a dimensionless value that encodes the mass transfer flux of a gas for a given system geometry. It is defined as follows, where h is the convective mass transfer coefficient (m/s), $D_{GHG,air}$ is CH_4's mass diffusivity in air, L_{char} (m) is a characteristic length defined differently for each system.

$$Sh \stackrel{\text{def}}{=} \frac{h \cdot L_{char}}{D_{GHG,air}} \tag{3.2}$$

The mass transfer coefficient is defined as follows, where $M_{GHG,Surface}$ (moles/m^3) is the CH_4 concentration very near the surface of the catalyst. $M_{GHG,Bulk}$ (moles/m^3) is the CH_4 concentration either outside the diffusion boundary layer or, in the case of the fan-driven system, averaged across the cross-section of the channel through which

the air flows. $M_{GHG,Surface}$ and $M_{GHG,Bulk}$ can be expressed more naturally as the product of the CH_4 concentrations $C_{GHG,surface}$ and $C_{GHG,bulk}$ (mole fractions, equal to the corresponding concentrations in ppm times 10^{-6}) and the molar volume of air ($\mathcal{V}_m$, m^3/mole):

$$h \stackrel{\text{def}}{=} \frac{R_{\dot{m}}}{M_{GHG,Bulk} - M_{GHG,Surface}} = \frac{R_{\dot{m}}}{(\mathcal{V}_m)^{-1} \cdot (C_{GHG,Bulk} - C_{GHG,Surface})} \tag{3.3}$$

Thus, given knowledge of Sh, by rearranging the equations above and setting the surface CH_4 concentration to zero, one can easily calculate $R_{\dot{m}}$ and hence $R_{overall}$:

$$R_{\dot{m}} = \frac{Sh \cdot D_{GHG,air} \cdot (\mathcal{V}_m)^{-1} \cdot C_{GHG,Bulk}}{L_{char}} \tag{3.4}$$

$$R_{overall} = min\left(R_{reaction}, \frac{Sh \cdot D_{GHG,air} \cdot (\mathcal{V}_m)^{-1} \cdot C_{GHG,Bulk}}{L_{char}}\right) \tag{3.5}$$

The Sherwood number is calculated in different ways for each system. For the aerosol-based system, it is calculated from an analytical solution for species diffusion to a circular particle. For the two ground-based systems, it is calculated using tabulated empirical relations that give Sh as a function of the Reynolds number (Re), Schmidt number (Sc), surface roughness, and other parameters for a given flow geometry. These relations were originally tabulated for heat transfer modeling, but we repurpose them for mass transfer modeling using the well-known Chilton-Colburn analogy [154], wherein the Schmidt number replaces the Prandtl number and the Sherwood number replaces the Nusselt Number. In general, for some correlation or analytical formula $\mathcal{F}$:

$$Sh = \mathcal{F}(Re, Sh) \tag{3.6}$$

Where:

$$Re = \frac{v_{air} \cdot L_{char}}{v_{air}} \tag{3.7}$$

$$Sc = \frac{\upsilon_{air}}{D_{GHG,air}} \tag{3.8}$$

And where υ_{air} (m^2/s) is air's kinematic viscosity at 1 bar and 300K. We describe the specific Sherwood number expressions that we used in the deployment systems' respective sections below.

3.2.2 Further Cost Modeling Assumptions

In each of our models, we assume that the photocatalysts are highly resistant to deactivation and fouling. We make this optimistic assumption because we aim to evaluate photocatalysts' potential under a future best-case scenario. The rooftop system is modeled to replace its catalysts every ∼20 years and the fan-driven system every ∼6 years, whereas the aerosolized catalysts need only last ∼21 days. More research would be required to realize such durable photocatalysts because many photocatalysts undergo full or partial deactivation after only months in outdoor air.[181] Moreover, current photocatalytic roof treatments (intended to reduce moss growth) require reapplication every year.[182]

For similar reasons, we do not consider full lifecycle emissions (e.g. from construction) from these processes, despite their importance in evaluating negative-emissions technologies.[73] Doing so properly would be complex: painting rooftops affects buildings' heating and cooling energy use in location-dependent ways, aerosols and rooftops have direct effects on planetary albedo, and many processes' and inputs' carbon intensities will decrease as fossil fuel use declines.[183–185] Any processes that look promising here should be subjected to detailed lifecycle analyses in the future; conversely, processes that seem implausible here are unlikely to perform better once full lifecycle emissions are considered.

Where a photocatalyst cost is required, we use \$4,500/ton, based on recent prices of ∼\$3,000/ton for a TiO_2 or ZnO base material and an assumed cost of \$1,500 per ton of photocatalyst from cocatalysts and synthesis.[189, 190] For general validation of the latter assumption, the 0.1% by weight of silver in the state-of-the-art CH_4-oxidizing catalyst reported by *Chen et al.* would cost roughly \$700 per ton of catalyst at 2022's average silver price, though non-material bulk synthesis costs are difficult

Description	**Symbol**	**Value**	**Units**	**Comments**
Max. Wavelength of Incident Light	λ_{light}	365	nm	Many photocatalysts, including the state-of-the-art ones for CH_4, work best under near-UV illumination.
Kinematic Viscosity of Air	υ_{air}	$1.52 \cdot 10^{-5}$	m^2/s	Source[186]
Ambient Temperature	T	300	K	Affects molar volume, average molecular speed, and mean free path. The latter two affect only the aerosol model.
Molar Volume of Air	$\mathcal{V}_m$	$2.46 \cdot 10^{-2}$	m^3/mole	Calculated for an ideal gas at 300K and 1 bar.
Density of Air	ρ_{air}	1.225	kg/m^3	Source[186]
Molar Mass of CH_4	m_{GHG}	16.04	g/mole	Source[187]
Mass Diffusivity of CH_4 in Air	$D_{GHG,air}$	$2.21 \cdot 10^{-5}$	m^2/s	Source[188]
Capital Recovery Factor	CRF	7.5	%/year	Same as the optimistic-case CRF in Keith et al.'s cost analysis of a CO_2-DAC system.[80]
Photocatalyst Cost	$P_{Catalyst}$	4500	\$/ton	Based on \$3,000/ton for base material (from 2023 prices) and \$1,500/ton for cocatalysts and synthesis.[189, 190]
Photocatalyst Density	$\rho_{catalyst}$	5610	kg/m^3	Same density as ZnO.[187]

Table 3.2: Inputs and assumptions shared by multiple photocatalyst deployment cost models.

to estimate.[102],[191]

For ground-based systems, capital costs are annualized using a capital recovery factor (CRF; Eq. 3.9):

$$CRF \stackrel{\text{def}}{=} \frac{Average\ Yearly\ Loan\ Payment}{Total\ Overnight\ Capital\ Cost} \tag{3.9}$$

The CRF converts the overnight capital cost of a project into estimated annual loan payments, abstracting away repayment periods, interest rates, and project finance structures.[192] We use a CRF of 7.5%/yr. throughout, an optimistic value corresponding to a commercially de-risked technology.[80] Unlike the ground-based systems, the aerosol process incurs only operating costs, so a CRF is not relevant.

A number of other assumed values and physical constants are shared by some or all of the cost models. These are summarized in Table 3.2. Values that are only relevant to a single cost model are included in their respective sections. While we present the final equations for the cost models of each system and describe all components of the modeled costs, we do not present the full derivations of the equations, which are somewhat tedious. They are included in Supporting Information of the published version of this chapter.[193]

Throughout, we show \$8000/tCH_4 benchmarks on our cost plots. It is difficult to set a single cost target for dilute CH_4 mitigation and atmospheric CH_4 removal, as is discussed in this thesis's introduction. \$8000/tCH_4 is a price *above which* we feel fairly confident that a CH_4 mitigation strategy would not be viable at scale. It also approximately equals the result of converting a \$100/ton CO_2 price into a CH_4 price using a GWP-20. We feel that this target is necessary but almost certainly not sufficient, and that truly transformative CH_4 mitigations strategies would likely be in the \$2000/tCH_4 or even <\$1000/tCH_4 ranges. These considerations should be borne in mind when interpreting this chapter's results.

3.3 Photocatalyst-Painted Rooftops

The simplest possible photoreactor consists of a photocatalyst surface exposed to sunlight and natural airflow. A few such systems have already been proposed or studied for CH_4 mitigation, including purpose-built solar photoreactors and buildings covered

in photocatalytic paint.[72, 73, 178] We analyze a system in which photocatalytic paint covers the rooftop of a warehouse or commercial building (Figure 3.1**(a)**). As wind blows over the rooftop, CH_4 molecules convect to the photocatalyst, where they react under sunlight. Although we assume that the photocatalyst does not chemically deteriorate, we include the cost of annual pressure-washing to remove accumulated dirt.

3.3.1 Cost Modeling Approach

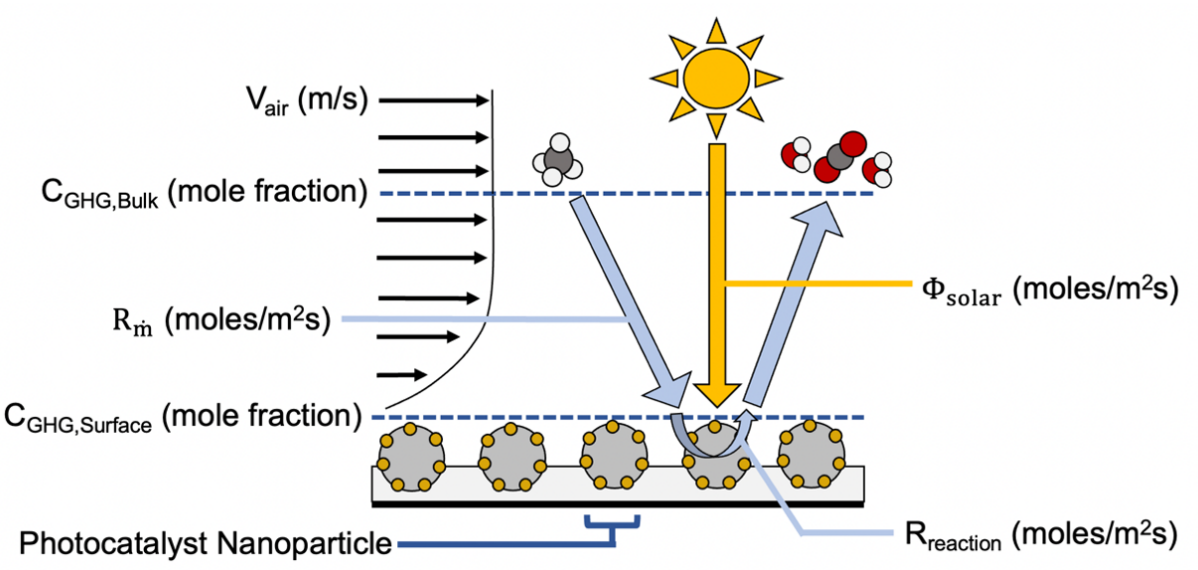

Figure 3.2: We envision a flat commercial rooftop painted with a uniform layer of photocatalytic paint, sketched in full in Figure 3.1. We model the overall CH_4 decomposition flux to be limited either by the reaction flux on the surface ($R_{reaction}$) or by the flux of CH_4 mass transfer to the surface ($R_{\dot{m}}$). The maximum reaction rate is calculated based on an assumed or observed quantum yield at a given CH_4 concentration ($C_{GHG,bulk}$) and photon flux in a certain spectrum (Φ_{solar}). The maximum mass transfer rate is calculated using a mass transfer correlation for fluid flow over a flat rooftop with a given velocity (V_{air}) and CH_4 concentration ($C_{GHG,bulk}$) in the free stream.

This system's levelized cost of CH_4 removal (LCOR; \$/mole) is calculated using Equation 3.10. The numerator of Equation 3.10 represents the system's annualized

costs per unit area of photocatalyst, whereas the denominator represents its annual rate of CH_4 drawdown per unit area of photocatalyst. CRF (%/yr.) is the capital recovery factor. $CAPEX_{painting,m^2}$ ($/m^2) is the cost to apply 1 m^2 of paint to a commercial rooftop, while $CAPEX_{catalyst,m^2}$ ($/m^2) is the cost of the paint itself. $OPEX_{m^2yr.}$ ($/m^2-yr.) is the cost of pressure-washing 1 m^2 of rooftop. UF (%) is the device's utilization factor, which accounts for variations in solar intensity, cloud cover, and day/night cycles.[194] $R_{reaction}$ and $R_{\dot{m}}$ (moles/m^{2}s) are the reaction and mass transfer fluxes illustrated in Figure 3.2, one of which is the rate-limiting step as described above.

$$LCOR = \frac{CRF\cdot(CAPEX_{painting,m^2}+CAPEX_{catalyst,m^2})+OPEX_{m^2yr.}}{UF\cdot\left(3.154\cdot10^7\ \frac{s}{yr.}\right)\cdot min(\ R_{reaction},R_{\dot{m}})} \quad (3.10)$$

The Sherwood number (and hence $R_{\dot{m}}$) is calculated using an empirical heat and mass transfer correlation for flat and low-angle rooftops like those found on warehouses and commercial buildings.[195] The correlation describes the Sherwood number in terms of the Reynolds number (Re) and Schmidt number (Sc). The correlation was tabulated for wind speeds between 0 and 9 m/s for roofs of approximately the same size that we model (a 50-by-50-meter square). Additionally, since this correlation was tabulated using heat transfer data from air with a Prandtl number of 0.7, we expect it to be reasonably accurate for the Schmidt number of CH_4 (0.67). Additionally, v_{air} (m/s) is the free-stream velocity of the air (i.e., the wind speed) and υ_{air} (m^2/s) is air's kinematic viscosity at 1 bar and 300K. R_f is a surface roughness factor.[195]

$$Sh = R_f \cdot 0.037 \cdot Re^{4/5} \cdot Sc^{1/3} \quad (3.11)$$

The values of all inputs and assumptions for the rooftop photocatalyst model are listed in Table 3.4.

Description	Symbol	Value	Units	Comments
Incident Photon Flux	Φ_{solar}	$6.33 \cdot 10^{-5}$	moles/m^2s	Incident photons at <365nm for an AM1.5g solar spectrum.
Paint Application Cost per Exposed m^2	$CAPEX_{painting,m^2}$	15.0	\$/m^2	We use a painting cost of \$0.80/ft^2 based on a 2002 LBL study, which is \$1.39/ft^2 in 2023 dollars.[196, 197] This value covers cleaning, primer, and a liquid coating. It is consistent with more recent commercial estimates.[198, 199] A unit conversion gives \$15.0/m^2.
Cost of Photocatalytic Paint per Exposed m^2	$CAPEX_{catalyst,m^2}$	1.07	\$/m^2	The marginal cost of covering roofs with zinc oxide paint rather than regular paint is about \$0.05-\$0.15/ft^2.[182] Adjusting for inflation gives \$0.06-0.18/ft^2.[196] We use a value of \$0.10/ft^2, or \$1.07/m^2.
Maintenance Cost per Exposed m^2	$OPEX_{m^2yr.}$	1.8	\$/m^2-year	We model the roof to be pressure-washed once per year to remove dirt and dust.[197] This can cost as little as \$0.15/ft^2.[182, 200] Adjusting for inflation gives \$0.17/ft^2-year, or \$1.8/m^2-year.
Characteristic Length	L_{char}	42.5	m	For the Sherwood Number correlation used, L_{char} is defined as the 'effective length' of the roof in question, for which a formula is provided.[195] For a 50m by 50m roof, it evaluates to 42.5 meters.
Roughness Factor	R_f	1.67	1	The roughness factor is an input for Clear et al.'s heat and mass transfer correlation for flat roofs.[195] A value of 1.67 is typical for commercial roofs, with a texture like 'rough plaster'.
Utilization Factor	UF	25	%	Typical utilization factor based on day-night cycle, cloud cover, and sunlight angles for fixed-tilt solar PV.[194]

Table 3.4: Inputs and assumptions for the cost model of photocatalytic rooftops.

3.3.2 Results

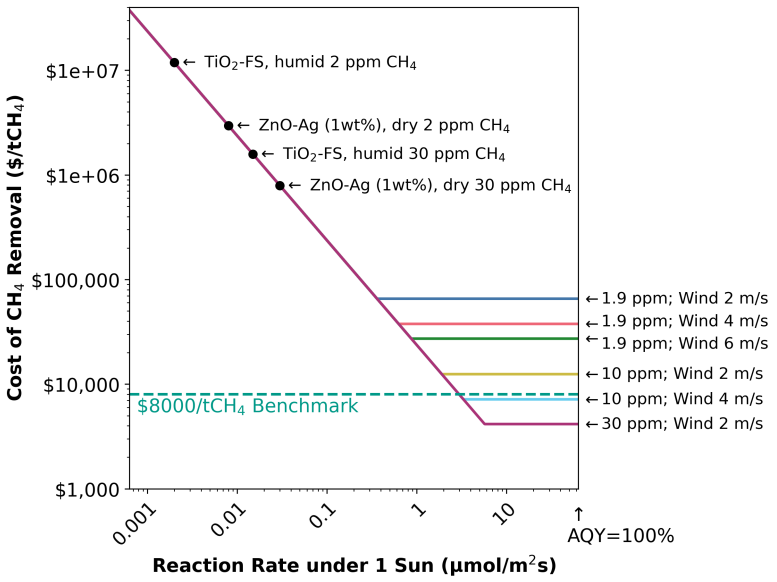

Figure 3.3: Costs of ground-based solar CH_4 removal systems at varying wind speeds and ambient CH_4 concentrations. In the reaction-limited regime at lower intrinsic rates, CH_4 removal costs decrease as the intrinsic rate increases. In the mass transfer-limited regime above a certain rate, higher intrinsic do not increase the CH_4 drawdown rate or decrease the system cost. We do not model the transition regime in detail. Higher ambient CH_4 concentrations or wind speeds boost the maximum mass transfer rate, lowering the system costs achievable at higher intrinsic rates.

Figure 3.3 shows the modeled cost of ground-based solar greenhouse gas-removal systems under varying ambient conditions and catalyst attributes. Average wind speeds of 2-6 m/s are found at a height of 10m above ground level, about the height of a commercial roof, in many locations.[201] These systems are modeled to approach ~\$4000/tCH_4e at very high rates and elevated CH_4 concentrations. However, deploying known photocatalysts with their measured rates would lead to impractically high system costs (>\$1 *million* per tCH_4), and even with ideal photocatalysts with much higher rates, mass transfer limitations with 1.9 ppm CH_4 appear to preclude a cost-effective system (>\$20,000/tCH_4).

We note that the modeled costs are roughly 37% initial painting, 3% catalyst, and 60% annual washing. They also scale in proportion to the cost recovery factor.

We also considered mounting panels of solar photocatalysts on standalone structures that resemble utility-scale fixed-tilt photovoltaic arrays. However, we estimated that the construction cost per square meter of exposed photocatalyst would be ∼7 times that of painting rooftops, making the system unlikely to be cost-effective..[194]

3.4 Fan-Driven Photoreactors

Fan-driven machines with artificial illumination are another option for photocatalytic systems, offering the potential for compact footprints and, unlike solar systems, 24-hour operation. We envision a machine generally resembling the "slab-style" CO_2-DAC contactor described by *Holmes et al.* in 2012 and since commercialized by Carbon Engineering Ltd. (Figure 3.4**(a)**).[135] More recent pilot and engineering studies based on that work have generally validated its cost projections.[80] We model the cost in two decoupled components: 1) that of the air contactor, which blows air over the photocatalyst and whose cost (capital and energy) depends strongly on the inlet CH_4 concentration and the photocatalyst's reaction rates, and 2) that of the LED system, whose size and cost depend mainly on the photocatalyst's AQY.

Holmes et al.[135] modeled the reaction of gaseous CO_2 with an aqueous hydroxide solution using off-the-shelf crossflow tower packing that provides excellent contact between flowing gases and trickling liquids. The packing is made of stacked sheets of inexpensive heat-formed plastic. Since our reactions are gas-solid instead of gas-liquid, we instead imagine "monolith-style" packing consisting of many straight, square, photocatalyst-coated channels. These types of channels offer fast mass transfer at low pressure drops.[202] We envision channels made of stacked heat-formed plastic sheets with volumetric costs similar to *Holmes et al.'s* crossflow packing.

The photocatalyst-coated channels could be illuminated in various ways.[101] UV-transparent packing could be used, or LEDs or optical fibers could be embedded in the plastic layers. We treat LED costs separately from the volumetric cost of packing, assuming that the LEDs can be integrated inexpensively. We assume that the packing is coated in a 1µm layer of photocatalyst and is replaced whenever the LEDs are replaced (every 6 years). The packing contributes <5% of contacting costs

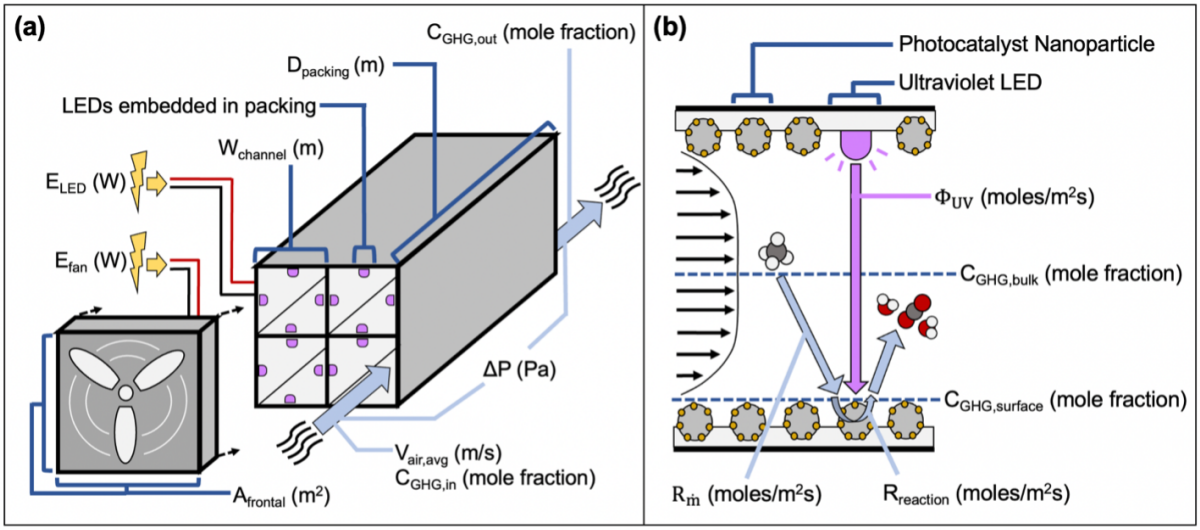

Figure 3.4: We envision a system resembling some devices for the direct air capture of carbon dioxide, using a slab-style contactor where fans blow air through straight, square, photocatalyst-coated channels studded with LEDs. **a)** Our model for this device's cost takes air velocity, channel width, and outlet CH_4 concentration (V_{air}, $W_{channel}$, and $C_{GHG,out}$) as arguments while assuming a fixed inlet CH_4 concentration ($C_{GHG,in}$) and total CH_4 removal capacity. Based on these inputs, the required pressure drop, packing depth, frontal area, and fan power (ΔP, $D_{packing}$, $A_{frontal}$, and E_{fan}) and other intermediate values are calculated, leading to an estimate of the levelized system cost. V_{air}, $W_{channel}$, and $C_{GHG,out}$ are finally optimized to find the minimum system cost at a given $C_{GHG,in}$. **b)** We model the overall CH_4 decomposition flux to be limited either by the reaction flux on the surface ($R_{reaction}$) or by the flux of CH_4 mass transfer to the surface ($R_{\dot{m}}$). The reaction flux is calculated using a first-order rate law from an assumed or observed reaction rate at the ambient CH_4 concentration (1.8 ppm). The maximum mass transfer rate is calculated for a fully developed fluid flow in a square pipe with a given average velocity (V_{air}) and average CH_4 concentration ($C_{GHG,bulk}$).

in all scenarios modeled, so replacing the catalyst more frequently might not be cost-prohibitive. We assume that the light intensity is always set so that the photochemical reaction rate matches the convective mass transfer rate of CH_4 to the catalyst surface.

3.4.1 Cost Modeling Approach

We model the fan-driven air contactor using *Holmes et al.'s* approach.[135] Key variables are labeled in Figure 3.4. We first define an expression (Equation 3.12) for the levelized cost of CH_4 removal ($LCOR$; \$/tCO_2e). We later minimize that expression at a fixed inlet CH_4 concentration ($C_{GHG,In}$; ppm) and electricity price ($LCOE$; \$/kWh) by adjusting the air velocity (V_{air}; m/s), channel width ($W_{channel}$; m), and outlet CH_4 concentration ($C_{GHG,Out}$; ppm).

$$LCOR(V_{air},\ W_{channel},\ C_{GHG,Out}) \ = \ \frac{CAPEX_{Construction}\cdot(1+F_{Contingency})\cdot CRF+OPEX_{Annual}}{UF\cdot RC\cdot(3.154\cdot 10^7\ \frac{s}{yr.})} \quad (3.12)$$

The numerator on the right side of Equation 3.12 is the plant's total annualized cost, which includes its construction cost ($CAPEX_{Construction}$; \$) adjusted by a construction contingency ratio ($F_{Contingency}$; %) and annualized using a capital recovery factor (CRF; %/yr.), as well as the annual operating and energy cost ($OPEX_{Annual}$; %/yr.). The denominator is its annual CH_4 drawdown in moles, which includes its designed removal capacity (RC; moles/s) and utilization factor (UF; %).

Evaluating Equation 3.12 requires calculating various intermediates (Figure 3.4). Holding the machine's overall CH_4 removal capacity fixed, we compute the contactor's frontal area, depth, internal surface area, and electricity demand as functions of V_{air}, $W_{channel}$, and $C_{GHG,Out}$ using pressure drop, mass transfer, reaction rate, and mass balance relations. The mass transfer and pressure drop relations are well-known formulae for fluid flow in square pipes.[154] The contactor's frontal area, internal volume, and internal surface area each determine components of its construction cost ($CAPEX_{Construction}$), while the fan electricity cost, LED electricity cost, and ongoing LED and packing replacement costs are components of operating cost ($OPEX_{Annual}$).

Unlike in the solar systems, multiple suns of UV light may be used to boost rates and decrease the system footprint. However, increasing the light flux gives diminishing returns in terms of the reaction rate (i.e., an arbitrarily high light flux does not lead to an arbitrarily high rate), since other aspects of reaction kinetics limit the rate even when charge carriers are abundant on the surface.[155] To capture this behavior, each model is given the photocatalyst's reaction rate at ambient CH_4 concentrations (1.8

ppm) under a high UV flux. Ideally, this rate and the AQY would be experimentally measured for a specific photocatalyst under a fixed light intensity, e.g., 10 suns of UV. However, one can also choose an 'upper bound' rate, such as the expected reaction rate of 2 ppm CO_2 with a film of aqueous NaOH solution, a rapid reaction whose rate photocatalysts are unlikely to exceed.[135] Figure 3.5**(a)** shows this parameter's effect.

The LCOR is minimized over of V_{air}, $W_{channel}$, and $C_{GHG,Out}$ at a given $C_{GHG,In}$ and electricity price (Equation 3.13) to find the lowest-cost CH_4 oxidation system under those conditions, whose cost we report.

$$LCOR_{\min} = \min_{\substack{V_{air} \in (0.05m/s,\ 10m/s) \\ W_{channel} \in (5mm,\ \ 500mm) \\ C_{GHG,Out} \in (0.01 \cdot C_{GHG,in},\, 1 \cdot C_{GHG,in})}} LCOR(V_{air},\ W_{channel},\ C_{GHG,Out}) \quad (3.13)$$

Our model tends to choose similar device traits across a range of conditions. As an example, the lowest-cost device for an elevated inlet CH_4 concentration of 20 ppm, an LCOE of 4c/kWh, and a catalyst with a reaction rate of 0.1µmol/m^{2}s at 1.8ppm has monolith channels 2.0 cm wide and 12.6 m deep. It blows air at 3.1m/s through a 151 Pa pressure drop, achieving an outlet CH_4 concentration of 6.6 ppm. The flow is turbulent (Re $\approx$ 4200) inside the channels. Fan electricity and the contactor frame respectively contribute 23% and 34% of the total contacting cost.

All inputs and assumptions for this system's cost model are listed in Tables 3.6 and 3.8.

Description	Symbol	Value	Units	Comments
CH_4 Removal Capacity	RC_{GHG}	1	moles/s	While actual CH_4removal plants would be very large, we consider a subsection of such a plant with a 1 mole/s CH_4 removal capacity. This choice does not affect the end result, since RC_{GHG} is normalized out later.
Utilization Factor	UF	85	%	Same value used by Holmes et al. for a CO_2 direct air capture contactor.[135]
Contactor Framing Cost	$CAPEX_{Frame}$	5000	$\$/m^2$	Holmes et al. found that a contactor's frame is sized for peak wind loads, which scale with frontal area, leading the framing cost to also be proportional to frontal area.[196] They used a value of $\$3700/m^2$ based on contractor quotes. Adjusting for inflation from 2012 to 2023 gives $\$5000/m^2$.
Contactor Packing Cost	$CAPEX_{Packing}$	340	$\$/m^3$	Holmes et al. use a value of \$250/m3 for structured packing consisting of heat-formed layers of PVC plastic.[135] Adjusting for inflation from 2012 to 2023 gives $\$340/m^3$.[196] We elsewhere add some additional cost to account for the catalyst coating.
Photocatalyst Layer Thickness	T_{layer}	1	µm	For TiO_2, a 1µm layer provides plenty of optical depth to utilize a large fraction of incident photons.[203]
Contactor Maintenance Cost	$OPEX_{Non\text{-}Energy}$	5	%	We follow Holmes et al. in assuming that annual non-energy operating and maintenance costs are roughly 5% of the equipment's upfront capital cost.[135]
Construction Contingency Cost	$F_{Contingency}$	20	%	Contingency is used to account for technical and regulatory risk during construction. Our value is consistent with that used by Holmes et al.[135]
Fan Efficiency	η_{fan}	56	%	Same value as in Holmes et al.[135]

Table 3.6: Inputs and assumptions for the cost model of fan-driven photoreactors.

Description	Symbol	Value	Units	Comments
Levelized Cost of LEDs	LC_{LED}	0.074	\$/kWh	We use values from a 2021 UV LED benchmarking study by the US Department of Energy's Lighting R&D Program.[204] The product referred to as "UV-11" in the study costs ∼\$5 and consumes ∼1.6W of electricity while producing 365nm light at 60% efficiency. Manufacturers claim UV LED lifespans above 50,000 hours.[205] So, the modeled LED's lifetime power consumption is: $50,000\ h \cdot 1.6W \cdot \frac{1kWh}{1000Wh} = 80kWh$ And its amortized operation cost is: $\$5 \div 80kWh = \$0.063/kWh$ Adjusting for inflation from 2021 to 2023 gives \$0.074/kWh.[196]
Packing Replacement Interval	$L_{Packing}$	50,000	hours	We assume that the packing is replaced whenever the LEDs are replaced. An LED lifespan of 50,000 hours is assumed as discussed in the cell directly above.[205]
LED Efficiency	η_{LED}	60	%	Same source as above; efficiency of product referred to as "UV-11" at 500mA current.[206]
Ambient CH_4 Concentration for Rate Measurement	$C_{GHG,Ambient}$	1.8	ppm	The photocatalyst's reaction rate at this concentration (measured or assumed) is an input to the model.
Energy per Mole of Incident Photons	$E_{photons}$	$3.377 \cdot 10^5$	J/mole	Calculated from 365nm UV photons with an energy of 3.5eV each.

Table 3.8: Inputs and assumptions for the cost model of fan-driven photoreactors (Continued).

3.4.2 Results

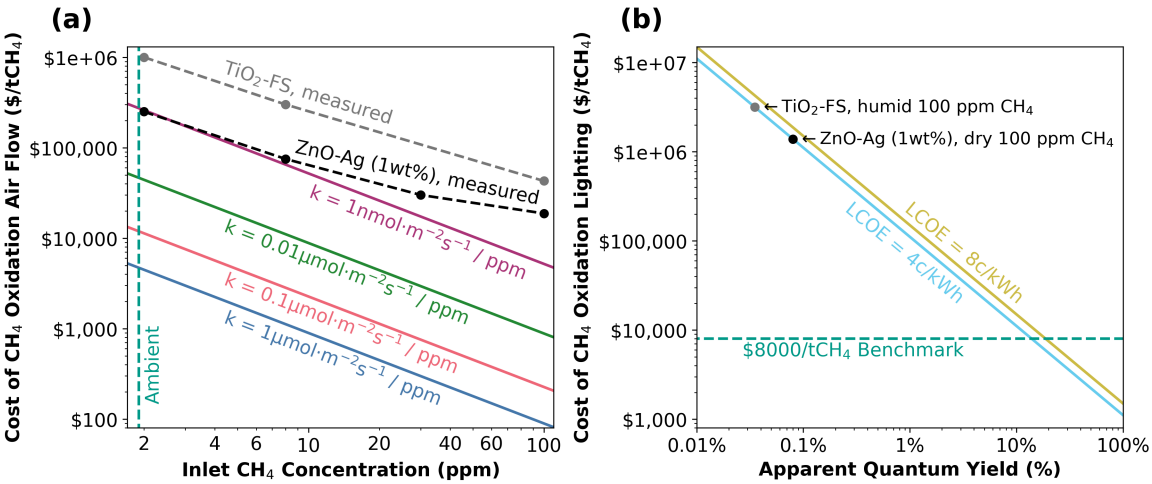

Figure 3.5: Costs of ground-based, fan-driven CH_4 oxidation systems with LED illumination. **(a)** Costs of the "air contacting subsystem," consisting of reactor hardware and fan electricity. Results are shown for several different assumed first-order photocatalytic rate constants, as well as actual rates for selected photocatalysts. The lowest line represents a rate close to the mass-transfer limit in which every CH_4 molecule that touches the catalyst in decomposed, while the second-lowest line represents a rate close to that of the reaction between CO_2 and the surface of an aqueous 1-2M NaOH solution (∼0.2µmol/m^{2}s at 1.8 ppm).[135] **(b)** Costs of the "lighting subsystem," consisting of LED hardware and LED electricity. Two different levelized costs of electricity (LCOE's) are shown. The actual quantum yields of selected photocatalysts are marked.

Figure 3.5 shows the costs of the air contacting and lighting subsystems, which can be summed to estimate the total cost of a CH_4-oxidizing system. Extremely high reaction rates are required to achieve contacting costs below \$8000/tCH_4 at ambient CH_4 concentrations. Lower rates necessitate larger and more expensive contactors. Even a rate constant as high as that of the reaction between CO_2 and aqueous ∼1M NaOH, which *Keith et al.* exploit for their CO_2-DAC system and which would be very difficult to replicate with a photocatalyst, leads to system costs well over \$10000/tCH_4 for 2 ppm CH_4, consistent with others' concerns about the expense of fan-driven contactors for ambient CH_4.[72, 135]

Additionally, to realize lighting costs below \$8000/tCH_4, extremely high AQYs (>10%) are needed for CH_4. Such AQYs are likely to be unrealistic even at elevated CH_4 concentrations. The LEDs themselves cost ∼7 cents per kWh (c/kWh) on a levelized basis, while the electricity that powers them costs 2-6c/kWh[206], so a 50% reduction in LED price would reduce lighting costs by 26-38%.

Applying these cost models to the experimental results from the previous chapter gives cause for skepticism about these devices. Even ignoring ZnO-Ag (1wt%)'s poor humidity tolerance, deploying that material in a fan-driven reactor on 100-ppm CH_4 would incur contactor costs of $> \$20,000/tCH_4$ and lighting costs of $> \$1,000,000/tCH_4$. These costs are far too high to be practical.

One might also combine CH_4 removal with CO_2-DAC.[46] In the best case, the LEDs and photocatalyst would be added to unused surfaces within the CO_2-DAC system, incurring no additional pressure drop. The lighting subsystem cost in figures 3.5**(b)** can be considered a lower bound on such a modification's cost, to which catalysts and construction expenses would be added. Thus, co-deploying photocatalysts with direct air capture does not solve the key issue of low AQYs on known photocatalysts.

3.5 Aerosol-Based Solar Photocatalysis

Rather than moving air across a photocatalyst surface, one could in principle "bring the catalyst to the atmosphere" by dispersing aerosolized photocatalysts. Fine powders have extremely high specific surface areas, allowing fast mass transfer and rapid reactions. Figure 3.6**(a)** illustrates the general process we envision. We model the physical processes only, without considering social factors in whether deployment of such a technology would or should be allowed.

3.5.1 Cost Modeling Approach

We model particles as either pure photocatalyst (≤2µm particles) or a 1µm layer of photocatalyst around a silica core (>2µm particles), with the photocatalyst assumed to cost \$4,500/ton. We model aircraft dispersing catalyst particles either in the lower troposphere (altitudes 0.5-1.5 km) or upper troposphere (>1.5 km). We

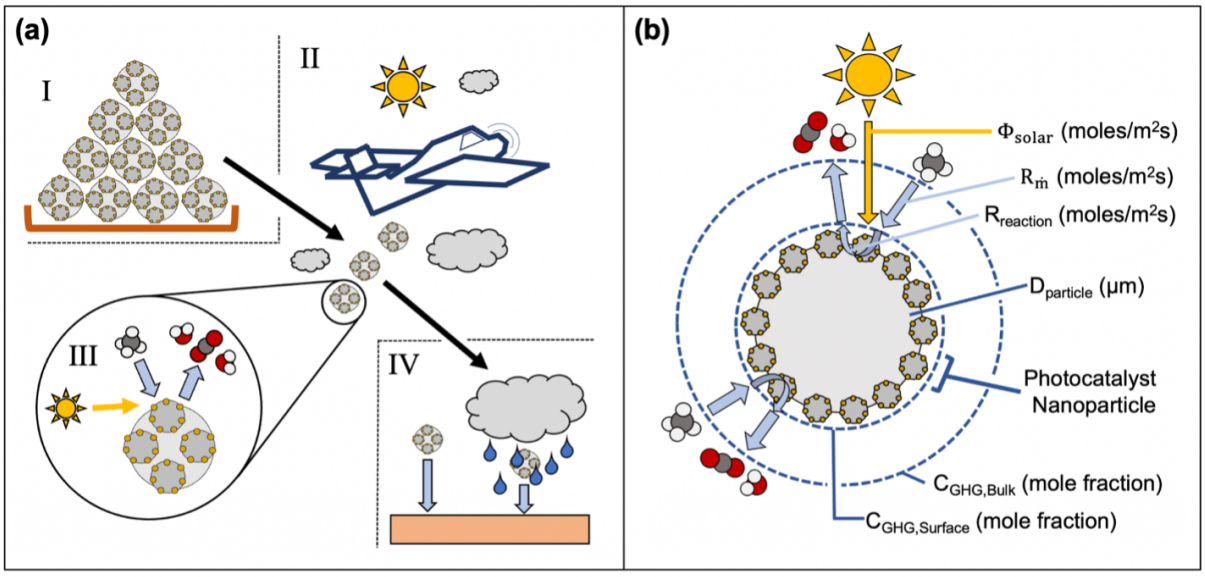

Figure 3.6: The modeled aerosol-based system using sunlight and photocatalytic powders dispersed by aircraft. **(a)** The process modeled involves several steps. I) The aerosol powder is synthesized, with each particle consisting either of agglomerated photocatalyst nanoparticles or of a layer of photocatalyst nanoparticles around an inert core. II) The particles are dispersed in the troposphere by small aircraft III) While the particles remain suspended, CH_4 diffuses to the surface and reacts in sunlight. IV) The particles exit the atmosphere, usually after a few days, through some combination of wet and dry deposition. **(b)** We model the overall CH_4 decomposition flux to be limited either by the reaction flux on the surface ($R_{reaction}$) or by the flux of CH_4 mass transfer to the surface ($R_{\dot{m}}$). The maximum reaction rate is calculated based on an assumed or observed rate at a given CH_4 concentration ($C_{GHG,bulk}$) and photon flux in a certain spectrum (Φ_{solar}). The maximum mass transfer rate is calculated using a closed-form solution for mass transfer to a spherical particle with a known CH_4 concentration ($C_{GHG,bulk}$) in the bulk air.

estimate particle dispersal costs of $760/ton, calculated using industry figures from aerial pesticide application.[207] This value is about half the projected cost per ton of launching aerosols at higher altitudes of ∼20km with jet aircraft.[208, 209]

A variety of other dispersion methods might be possible with modest engineering improvements, including guyed masts (up to ∼500m), tethered balloons, and kites like those used for airborne wind power generation.[208, 210–212] Aerosols could also

be lofted in the heated gases from existing smokestacks.[127] We model airplanes because they are a proven technology. Even if cheaper launch systems are possible, the particles in this system are a much greater driver of overall cost.

We estimate the levelized cost of CH_4 removal using Equation 3.14. The numerator represents the total cost per unit mass of aerosol dispersed and the denominator represents the lifetime CH_4 drawdown per unit mass of aerosol dispersed. $OPEX_{Synthesis}$ (\$/ton) is the cost to manufacture the particles and $OPEX_{Launch}$ (\$/ton) is the cost to disperse them. AF (%) is the sunlight availability factor, which accounts for temporal variations in solar intensity including clouds and day-night cycles. SSA (m^2/ton) is the mass-specific surface area of the particles. $L_{particle}$ (s) is the aerosol's atmospheric residence time, which varies with the particles' diameter and altitude.[213] Particles between about 0.1 and 1µm last ∼7 days in the lower troposphere and ∼21 days in the upper troposphere, with larger particles settling faster. $R_{reaction}$ and $R_{\dot{m}}$ (moles/m^2s) are the average reaction and mass transfer fluxes over the particle surface, illustrated in Figure 3.6, one of which is the rate-limiting step for the CH_4 drawdown process. The inputs and assumptions for this model are listed in 3.10.

$$LCOR = \frac{OPEX_{Synthesis} + OPEX_{Launch}}{AF \cdot SSA \cdot L_{particle} \cdot min(R_{reaction}, R_{\dot{m}})} \tag{3.14}$$

Description	Symbol	Value	Units	Comments
GHG Conc. in Ambient Air	$C_{GHG,Bulk}$	1.8	ppm	Aerosol-based systems are only useful at ambient CH_4 levels.
CH_4 Mean Free Path	λ_{GHG}	67	nm	Value used is for 1 bar and 23C.[214]
Incident Photon Flux	Φ_{solar}	$6.33 \cdot 10^{-5}$	moles/m^2s	Incident photons at <365nm for an AM1.5g solar spectrum.
Solar Availability Factor	AF	35	%	Assumed a modestly higher availability factor than the 25% for rooftops because aerosol particles always 'face' the sun.
Maximum Photocatalyst Layer Thickness	T_{layer}	1	µm	For TiO_2, a 1µm layer provides plenty of optical depth to efficiently use incident photons.[203]
Density of Support Material	$\rho_{support}$	2650	kg/m^3	Density of silicon dioxide.[187]
Price of Support Material	$P_{Support}$	500	$/ton	Silica in the 1-10µm range iscalled "Tripoli" and costs $278/ton in the US in 2018. Adjusting for inflation gives $345/ton.[196] We use $500 to be conservative.
Airplane Hourly Payload Capacity	P_{plane}	1.89	tons	Based on an aircraft with 500 gallon capacity for aqueous pesticide. Assumed the plane can carry an equal mass of powder.
Airplane Hourly Fuel Consumption	G_{plane}	50	gallons	Source[207]
CO_2 Emitted per Gallon of Gas	E_{gas}	8.32	kg/gallon	Source[215]
Photocatalyst Powder Dispersal Cost	$OPEX_{dispersal}$	760	$/ton	Based on the cost of dispersing liquids using piston-driven aircraft (crop-dusting).[196] Single flight cost ($1,140) is divided by the payload mass (1.9 tons) to get $600/ton. Adjusting for inflation gives $760/ton.[196]
Slowest Dry Settling Time	τ_{dry}	$6.4 \cdot 10^7$	s	Source[213]
Slowest-Settling Particle Diameter	D_{max}	0.6	µm	Source[213]
Lower Tropo. Wet Settling Time	τ_{wet}	$6.91 \cdot 10^5$	s	Equivalent to 8 days. Source[213]
Upper Tropo. Wet Settling Time	τ_{wet}	$1.81 \cdot 10^6$	s	Equivalent to 21 days. Source[213]

Table 3.10: Inputs and assumptions for the cost model of aerosolized photocatalysts.

3.5.2 Results

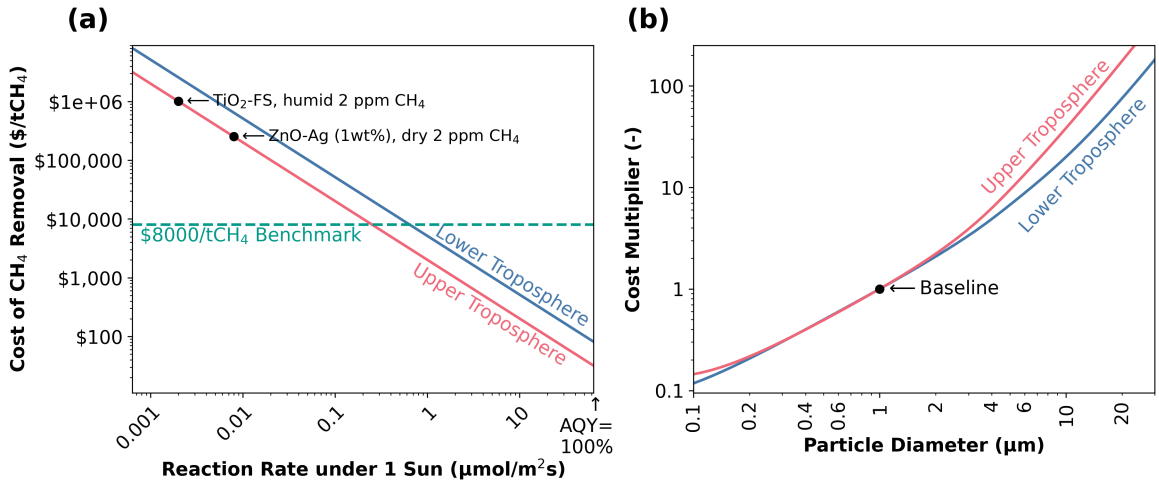

Figure 3.7: Costs of aerosol-based solar CH_4 systems. **(a)** Modeled costs with varying photocatalytic reaction rates on 1μm particles. **(b)** Effect of particle diameter on modeled costs, indexed to the cost of CH_4 removal using 1μm particles as in **(a)**.

Figure 3.7 shows the projected costs for CH_4 removal using photocatalytic aerosols. CH_4 oxidation costs of under \$1000 or even \$100 are theoretically achievable with sufficiently active photocatalysts. CH_4 mitigation cost of \$8000/tCH_4 using 1μm lower-troposphere aerosols requires a rate of around 0.8μmol/m^{2}s. This target could be decreased by a factor of 3 by moving to the upper troposphere and by a further factor of 10 by using 100nm particles (Figure 3.7**(b)**); in other words \$8000/tCH_4 might be achieved by 100nm particles in the upper troposphere with a rate of only $\sim$0.03μmol/m^{2}s. This is still a factor of 15 higher than the rate observed on TiO_2-FS, the only photocatalyst observed to work under humid conditions. However, dispersing 100nm particles in the upper troposphere is closer to cost-effectiveness than any other approach in this chapter, a result that is worth noting. Since particles need only stay active for $\leq$20 days, known photocatalysts' poor durability is less of an issue for this approach.

One concern with aerosolized photocatalysts is the effect of small aerosol particles on human and ecosystem health. Particles <10µm in size can irritate tissues in respiratory tracts, with smaller particles usually causing greater harm.[216] PM_{10}

(<10µm particles) and $PM_{2.5}$ (<2.5µm particles) are well-studied types of air pollution; a process generating them would be unlikely to be deployed if people might inhale the particles downwind. This risk makes using even smaller particles, like the 100nm particles in the previous paragraph, less attractive. Using particles large enough not to pose a health risk is costly (Figure 3.7**(b)**): going from 1µm particles to pollen-sized 20µm particles raises removal costs by ∼40x. Dispersing particles in remote areas, e.g., over oceans, could mitigate human exposure, though animals and ecosystems might still be affected.

The total amount of aerosols required is another challenge. Removing 1 gigaton of CO_2 equivalent (with CH_4's 20-year GWP) using 1µm particles at a cost of \$8000/tCH_4 would require dispersing 19 megatons of aerosols in the lower troposphere. For comparison, California's 2021 wildfires released around 1 megaton of $PM_{2.5}$.[217] While gigaton-scale drawdown is valuable, dispersing such a mass of aerosols may be impractical due to environmental impacts and social considerations. However, a better photocatalyst would both require less total aerosol mass and cost less per tCH_4 oxidized.

We also compared the airplanes' CO_2 emissions to the CH_4 drawdown effected by the particles and found that they are small compared to the overall climate benefit. If the particles contain photocatalysts with AQYs giving \$8000/tCH_4 removal costs in the lower troposphere, the planes' CO_2 emissions negate ∼0.3% of the process's climate benefit using CH_4's GWP-20.

We also note that the aerosol-based CH_4 oxidation strategy is an "open-system" intervention that would need to be explored with great care. Doing so would require serious evaluation and mitigation of unintended environmental and health effects. Considering the direct albedo of tropospheric aerosols would be especially important: on a life-cycle basis, it is possible that the direct albedo effect of such a large mass of aerosols would dwarf their CH_4-oxidizing effect. In addition, even if these concerns were addressed, obtaining a social license to test and deploy aerosolized photocatalysts would be quite challenging.

3.6 Conclusion

We wish first to emphasize the uncertainty in our cost estimates for these untried technologies. The outputs are quite sensitive to the assumed values of a few key cost drivers, as discussed in each section. Labor, component, and raw material prices can vary considerably by country and economic conditions. Though most of our estimates are from North America, many inputs may be cheaper elsewhere. Macroeconomic conditions affect the capital recovery factor, to which ground-based systems are sensitive. Additionally, although our study considers the systems' direct CH_4 drawdowns, future studies should consider all lifecycle climate effects. These include rooftop paint's effects on heating and cooling energy use, rooftops' and aerosols' direct effect on planetary albedo, and all systems' construction, energy, and material emissions. They could also consider any local air quality benefits.

Overall, taking this and the previous chapter together, the outlook for ground-based photocatalytic oxidation of dilute CH_4 is not terribly promising. In order to cost-effectively oxidize CH_4, the rooftop system requires AQYs on the order of 1% (rates on the order of $1\mu mol/m^2s$). This rate target is nearly three orders of magnitude higher than the 2-ppm-CH_4 rate of the only photocatalyst that we observed to work under realistically humid conditions (TiO_2-FS; $0.002\mu mol/m^2s$). Considering the rates observed under dry conditions, post-TPD, and/or at higher CH_4 concentrations still leaves a two-order-of-magnitude gap. Even if the rates were high enough, photocatalysts' poor real-world lifespans would need to be addressed. The situation for fan-driven photoreactors is even worse, with AQYs ten times higher ($\sim$10%) required to achieve reasonable lighting costs. The prospect of using higher inlet CH_4 concentrations in fan-driven reactors is unlikely to close that gap.

Aerosolized photocatalysts are different in that the required rates in the most optimistic scenario are only a factor of $\sim$15 higher than those observed on TiO_2-FS. Indeed, the post-TPD plain TiO_2 briefly showed a rate on 2-ppm CH_4 ($0.024\mu mol/m^2s$) that would be sufficient for \$8000/tCH_4 atmospheric CH_4 removal on 100-nm upper-tropospheric aerosols. This rate was observed under highly unrealistic conditions (an extremely dry gas stream with all surface H_2O baked off the catalyst), but it indicates what might be possible with a dedicated materials-science effort to optimize humidity-tolerant photocatalysts. However, the key question in this case is whether

photocatalytic aersols could ever be possible from a perspective of side effects and social license. In our opinion, given the vitriol directed at solar radiation management – which uses a far smaller mass of aerosols per unit of avoided warming – it is hard to imagine that photocatalytic aerosols will be a practical climate solution in the near future.

Following these campaigns, we were left with a choice between pursuing photocatalysts further and investigating other strategies for dilute CH_4 oxidation. Photocatalytic CH_4 oxidation is certainly a field with many remaining scientific puzzles. For example, the excellent rates observed on post-TPD TiO_2 suggest that far higher rates may be possible if the surface's hydrophilicity is managed even more effectively. Also, the fact that the TiO_2-FS material works *better* in humid conditions suggests that there remains much to be learned from optimizing and probing TiO_2-FS-like materials. However, in our opinion, none of these pathways offers a route to a truly useful and scalable tool to fight climate change. We therefore decided to turn our attention to other strategies for oxidizing low-concentration CH_4.

Chapter 4

Experiments on Advanced Oxidation with Chlorine

4.1 Gas-Phase Advanced Oxidation

As my colleagues and I continued our research on photocatalysts, we became aware of ongoing work on catalyst-free, purely gas-phase processes for dilute methane oxidation. In general, these processes introduce a gaseous "radical precursor" into the CH_4-laden air stream, then use ultraviolet light to photolyze that precursor into radicals that then oxidize CH_4. Since many of the challenges in our photocatalyst work seemed to stem from CH_4's unwillingness to adsorb on or interact with any photocatalyst surface, a process that avoided catalyst surfaces entirely was qualitatively appealing. These processes are termed "gas-phase advanced oxidation" (GPAO) processes, a name that references "advanced oxidation" processes in wastewater treatment where aqueous ozone or hydrogen peroxide are photolyzed to form aqueous oxidizing radicals.[119, 120]

GPAO can be done with a number of radical precursors, including ozone (O_3), hydrogen peroxide (H_2O_2), water (H_2O), and chlorine (Cl_2). The reactions for each of these processes are listed in Chapter 1, Section 1.2.4 and the reactions for Cl_2. GPAO can be in principle be employed on CH_4 or on any other reducing gases such as ammonia (NH_3) or volatile organic compounds (VOCs). An O_3-based GPAO process that degraded VOCs for odor control was the first to be reported.[119] A Cl_2-based process for removing CH_4 from a spectrometer's gaseous analyte was the next to be reported [131], followed by a similar process for mitigating CH_4's global warming potential.[120] To our knowledge, experiments on GPAO with an H_2O_2 precursor have not been reported in the literature. A GPAO process using H_2O as the precursor has also been reported much more recently, well after we conducted this experimental campaign.[122]

When we began developing our setup, we considered the precursors O_3 and H_2O_2 (to generate OH•) and Cl_2 (to generate Cl•). Using values from literature, we did some rough calculations to get a sense of which precursor was most likely to cost-effectively oxidize CH_4. These calculations are visualized in the Sankey plot in Figure 4.1, which shows the mass and cost of precursors required to oxidize one ton of CH_4.

To make this calculation for each candidate precursor, we considered the cost per ton of each precursor, the number of radicals generated per mole and per ton of the precursor, and the number of CH_4 molecules oxidized per generated radical. We used

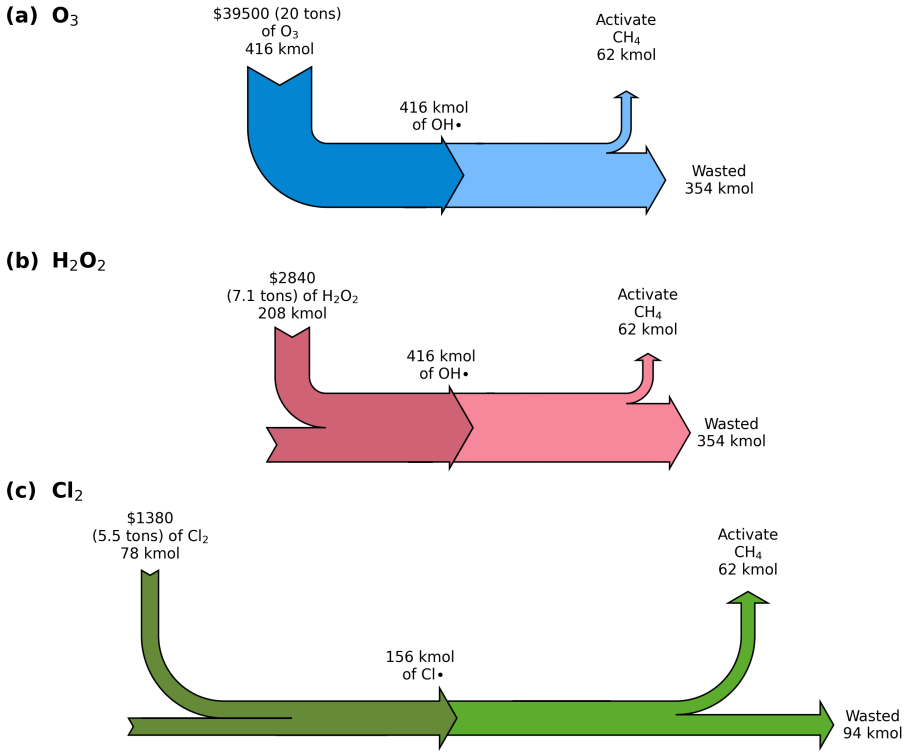

Figure 4.1: Estimated quantities and costs of radical precursors required to oxidize one ton of CH_4. Values are in kilomoles unless otherwise noted.

an H_2O_2 cost of \$400 per ton.[218, 219] and an O_3 cost of \$1980 per ton (converted from \$0.9 per pound [220]). We used a Cl_2 cost of \$250 per ton.[125] These are only synthesis costs and do not include transport to any particular point of use. Based on their photolysis reactions, each molecule of O_3 produces one OH•, while each molecule of H_2O_2 produces 2OH• and each molecule of Cl_2 produces 2Cl•. Finally, we found estimates for the number of CH_4 oxidized by each radical. The value for OH• (15%) is the fraction of OH• *in the bulk atmosphere* that oxidize CH_4.[218] The value for Cl• (33%) is estimated from the reaction network for CH_4 oxidation, in which 3 steps involving Cl• are needed to oxidize CH_4 to CO.[120] The higher value for Cl• reflects the greater selectivity of Cl• for CH_4 compared to OH•.

These calculations motivated our choice to pursue Cl_2-based gas-phase advanced

oxidation (Cl_2-GPAO) first. Cl_2-GPAO offered the lowest modeled input costs, and although many questions remained unanswered, the process had already been demonstrated on dilute CH_4. We expected that this would make it easier to design and debug our first GPAO reactor. GPAO with O_3 was clearly the least attractive of the three options, due mainly to the relative expense of ozone as a precursor. H_2O_2-GPAO looked moderately appealing on a cost basis, as well as for the relative benignity of H_2O_2 compared to Cl_2. However, its effectiveness on CH_4 had not been experimentally demonstrated, making it a less attractive choice for our first GPAO reactor. We resolved to return to H_2O_2 later, as we do in Chapter 6.

4.2 Introduction to Cl_2-GPAO

This chapter focuses on GPAO with Cl_2 as a radical precursor, which we term Cl_2-GPAO and has elsewhere been referred to as the 'methane eradication photochemical system' (MEPS).[120] These systems take advantage of the chlorine radical's extraordinary reactivity towards otherwise-stable CH_4. As mentioned above, Cl• has a higher rate constant with CH_4 than OH• and has fewer quenching mechanisms besides the desired reaction with CH_4. These traits enable high UV fluxes, high radical creation rates, and high steady-state radical concentrations in the photoreactor, which can in theory allow faster CH_4 conversions, shorter residence times of air in the reactor, and smaller reactor volumes..[120] The major downside is the toxicity of Cl_2 and the downstream product HCl, which must be scrubbed from the reactor effluent at additional cost. The basic elements and key reactions of a Cl_2-GPAO system are shown in Figure 4.2

Existing studies have confirmed Cl_2-GPAO's effectiveness on dilute and atmospheric CH_4, but many questions have remained unanswered. Polat, *et al.* first explored the process, using ∼50 ppm of Cl_2 to remove ambient (∼2 ppm) CH_4 that would otherwise interfere with spectrometric analysis of nitrous oxide in air.[131] Krogsbøll, *et al.* then proposed applying the same chemistry to control CH_4 emissions from point sources, describing the overall system layout for Cl_2-GPAO (with an electrolyzer, UV photolysis chamber, and caustic scrubber) and using ∼100 ppm Cl_2 and UV radiation to oxidize ∼50% of 50 ppm CH_4.[120] They additionally found CH_4

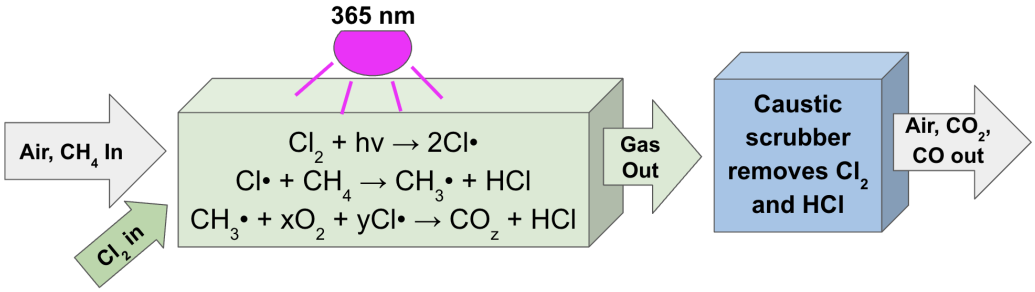

Figure 4.2: Graphical representation of gas-phase advanced oxidation with chlorine (Cl_2-GPAO). The third line in the photoreactor block summarizes multiple reactions that convert the methyl radical (CH_3•) into CO and CO_2. The numbers of O_2 (x) and Cl• (y) consumed and the relative amount of CO_2 to CO (z) depend on the reaction conditions. Krogsboll *et al.* gives a good summary of the entire reaction system following the initial C-H bond activation.[120]

conversion to vary approximately linearly with inlet Cl_2 concentration. The same study modeled that CH_4 would be converted into a combination of CO and CO_2 in a roughly 2:1 ratio, with minimal (<0.01%) conversion of CH_4 into chlorinated methanes that are of concern for their high GWPs. The authors recently conducted a small-scale field trial at a livestock facility, finding the process to effectively convert CH_4, ammonia (NH_3), and other odorous compounds.[70]

Despite these promising results, several key uncertainties have made it difficult to judge whether and how Cl_2-GPAO might be practical at large scale. To date, the number of photogenerated Cl• consumed per oxidized CH_4 molecule has not been quantified or reported in published literature. The inlet Cl_2 concentration required to oxidize a certain CH_4 concentration at a specified conversion efficiency has also not been studied in detail. The effects of process parameters such as CH_4 concentration, Cl_2 concentration, humidity, light intensity, and the presence of contaminants on all of the above metrics have remained largely unexplored. Finally, at the time that we conducted this research, the production of chlorinated methanes in these systems had also not been measured or reported.

In the research described in this chapter, we explored the effect of various parameters and operating conditions on Cl_2-GPAO's efficiencies and reaction products. We employed a benchtop reactor with a residence time representative of large-scale

applications in which inlet CH_4, Cl_2, H_2O, NH_3, nitric oxide (NO), hydrogen sulfide (H_2S), and toluene ($C_6H_5CH_3$) concentrations are finely tuned. We used infrared spectroscopy to measure CH_4 conversions and major reaction products. Having measured the reactor's total Cl• production rate, we report the process's efficiency under various conditions in terms of Cl_2-used-per-CH_4-oxidized and Cl•-consumed-per-CH_4-oxidized. For a subset of operating conditions, we also employed sensitive mass spectrometry to check for unintended chlorinated CH_4 production at part per billion (ppb) levels. These measurements help inform the cost modeling of Cl_2-GPAO that we present in the next chapter.

4.3 Experimental Setup and Reactor Qualification

Cl_2-GPAO experiments were conducted in the reactor setup shown in Figures 4.3 and 4.4. The reactor itself was a glass flow photoreactor with an internal volume of ∼600 cm^3. Each experiment used a total of 200 mL/min of flow to obtain a 3-minute residence time, comparable to that used by Krogsbøll, *et al.*[120] The gas composition was set by mass flow controllers (MFCs) to be 20% O_2, 1% H_2O (∼35% relative humidity), various concentrations of CH_4 and Cl_2, and balanced in N_2. An array of 365 nm UV LEDs and a set of UV reflectors were assembled such that, in the presence of excess CH_4, ∼75% of Cl_2 was photolyzed during the gas's residence time in the reactor. The reactor effluent then passed through a Cl_2 sensor, optionally a scrubber system (comprising a bubbler of 1M sodium hydroxide, a molecular sieve, and an activated carbon filter) to remove Cl_2 and HCl, and finally a pair of infrared spectrometers.

Synthetic air was created from gas tanks using MFSCs as outlined in Table 4.2. Tanks with different concentrations of the same gas were used to achieve accurate gas concentrations across wide concentration ranges, keeping the mass flow controllers within their intended flow ranges. Humid N_2 was generated by passing dry N_2 through a bubbler of deionized water, creating a stream with ∼80% relative humidity which was then mixed with the other gasses to achieve a desired humidity. A humidity sensor (Atlas Scientific EZO-HUM) was positioned upstream of the Cl_2 injection point to avoid steel fittings between the Cl_2 injection point and Cl_2 sensor. The raw humidity

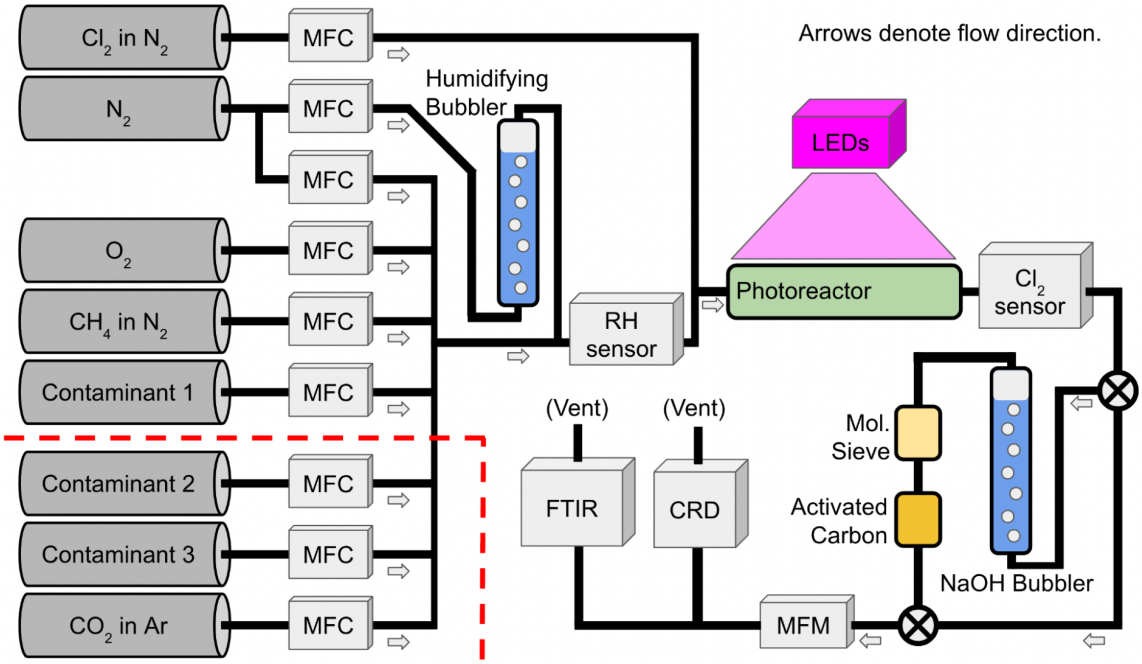

Figure 4.3: Schematic of photoreactor system. The dark-grey cylinders at left represent gas tanks. MFC stands for 'mass flow controller' and MFM for 'mass flow meter'. FTIR represents an MKS "Multi-Gas 2000" fourier transform infrared gas analyzer. CRD represents a Picarro "g2210-i" cavity ringdown gas analyzer. The components inside the red dashed line were only present during the application-based trials on simulated atmospheric, barn, and sewer air

readings were adjusted to account for dilution by the added Cl_2 gas. Another reason Cl_2 was added into the gas stream just before the photoreactor was to mitigate the effects of Cl_2 reacting in the dark with any co-fed contaminant gases.

The UV photolysis system consisted of a UV light, photoreactor, and reflectors (Fig. 4.4). The photoreactor was a borosilicate glass cylinder, 30 cm in length, 5.7 cm in diameter, and fitted with ~5mm radial hose barbs at either end (Adams Chittenden Scientific Glass). We found that even small amounts of stainless steel rapidly reacted with Cl_2 in the presence of H_2O and, in addition to corroding the steel, had large effects on the amount of Cl_2 reaching the reactor and the Cl_2 sensor. Consequently, only plastic fittings were used between where the Cl_2 was added to the gas stream and the photoreactor. The fittings in and around the reactor were verified to cause no

conversion of Cl_2 by comparing Cl_2 sensor measurements with and without the reactor bypassed. The UV light, consisting of a board of 365 nm LEDs with a total power draw of 50W, was suspended 28 cm above the photoreactor in typical experiments. Three panels of UV-reflective PTFE (Thorlabs) were positioned around the tube to increase the UV intensity inside the photoreactor. All components aside from the reactor were covered in UV-opaque plastic during experiments to prevent photolysis of Cl_2 from occurring anywhere except in the photoreactor.

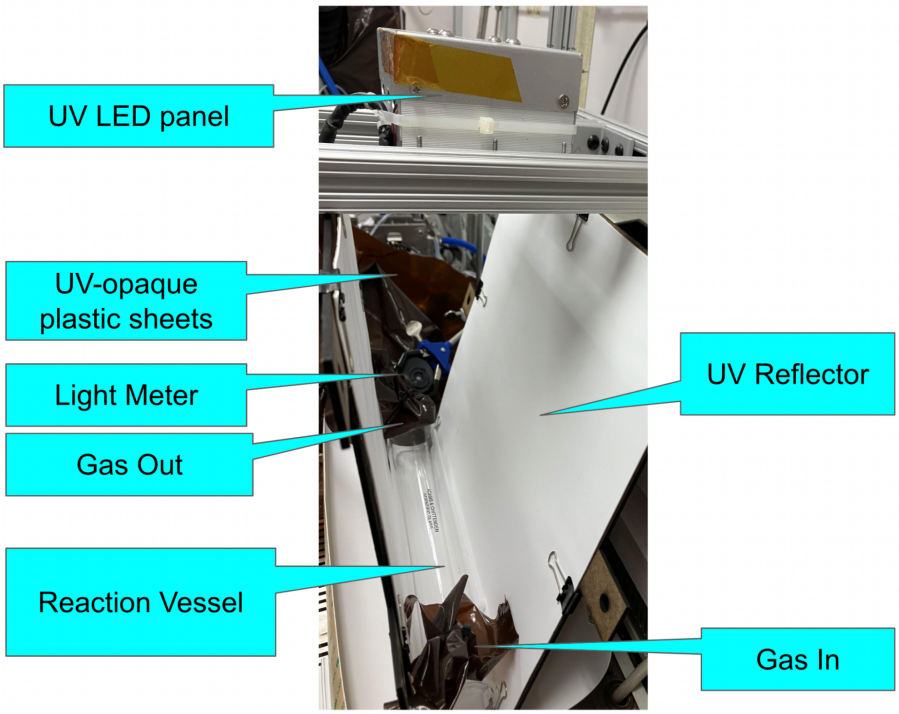

Figure 4.4: Details of photoreactor. The photoreactor is shown with the light in its 'default' position of 28cm above the reactor centerline and with some of the UV-shielding sheets removed.

Gas	**Cylinder Composition**	**Cylinder Supplier**	**MFC Model**
Nitrogen (N_2)	100% N_2	Linde	MKS Mass-Flo Controller (dry N2); Aalborg DPC (humidified N2)
Oxygen (O_2)	100% O_2	Linde	Aalborg DPC
Methane (CH_4)	1000 ppm CH4 in N_2 10 ppm CH4 in N_2	Linde Linde	Aalborg DPC
Carbon dioxide (CO2)	5% CO2 in Ar	Linde	MKS Mass-Flo Controller
Chlorine (Cl_2)	1000 ppm Cl_2 in N_2 100 ppm Cl_2 in N_2 20 ppm Cl_2 in N_2	GASCO GASCO MESA Gas	Aalborg DFC
Nitric oxide (NO)	200 ppm NO in N_2	MESA Gas	Aalborg DPC
Ammonia (NH_3)	200 ppm NH_3 in N_2	GASCO	Aalborg DPC
Toluene ($C_6H_5CH_3$)	100 ppm $C_6H_5CH_3$ in N_2	GASCO	Aalborg DPC
Hydrogen sulfide (H_2S)	50 ppm H_2S in N_2	GASCO	Aalborg DPC

Table 4.2: Gas tanks used in Cl_2 experiments.

An electrochemical Cl_2 sensor (Membrapor Cl/C-200 with a gas cap for flow sampling) was situated just downstream of the reactor. The sensor was attached to a Membrapor analog transmitter board, which generated a 4-20mV signal read by a LabJack U6 data acquisition board. At the beginning of the experimental campaign, the sensor was calibrated against a 100 ppm Cl_2 standard tank (GASCO) and verified that the MFC setup accurately and repeatably generate the desired Cl_2 concentrations, as well as that the light-off Cl_2 concentrations upstream and downstream of the reactor were the same. While Cl_2 readings were quite stable within any one experiment, we found that the readings drifted slightly over time. This could be due in part to the Cl_2 sensor's strong sensitivity to the absolute pressure within the system, which varied slightly from experiment to experiment due to factors like the level of liquid in the NaOH bubbler. To allow for this variation, we used the 30 ppm Cl_2 flowed by the MFC setup as a de facto calibration during each run, allowing us to adjust the

Cl_2 sensor's readings (in mV) to Cl_2 concentrations (in ppm). Previous trials showed the MFCs' ability to accurately set and hold a specified Cl_2 concentration.

A scrubber system downstream of the reactor and Cl_2 sensor was used to remove Cl_2 and HCl from the gas stream. It consisted of a bubbler of 20 mL 1M NaOH, a molecular sieve physisorbent (United Filtration Systems DIA-MN4A), and an activated carbon filter (United Filtration Systems DIA-MNCC). The scrubber system had a very small (<3%) effect on CH_4 and CO concentrations; hence, those gasses could be sampled continuously while the gas passed through the scrubbers. To allow for sampling of other gasses such as CO_2 whose concentrations were affected by the bubbler and filters, the gas temporarily bypassed the scrubber system and went directly to the analyzers. The bypass was used for ∼10 minutes in every trial (∼10% of time on-stream) so as to expose the analyzers to Cl_2 and HCl for only short periods of time, which was confirmed safe by the manufacturers.

A mass flow meter (Aalborg DFM) was sited just upstream of the gas analyzers to check for leaks in the system. Gas analysis used a Picarro G2210-i cavity ring-down spectrometer and an MKS MultiGas 2000 FTIR spectrometer. The Picarro instrument provided CH_4 measurements with tens-of-ppb precision for up to 35 ppm CH_4, as well as CO_2 and H_2O concentrations, at 1Hz frequency. We disconnected the Picarro whenever CH_4 concentrations >35 ppm were expected. We configured the MKS instrument to scan for CO, CO_2, CH_4, H_2O, CH_2O, CH_2O_2, NO, NH_3, HCl, and CH_3Cl. It sampled once every 12 seconds, with a detection limit of ∼500 ppb for most gasses.

Table 4.4 outlines the steps in a standard Cl_2-GPAO trial. For each experimental condition, a desired inlet gas composition was set and the UV light was cycled on and off while measuring the change in gas concentrations exiting the photoreactor. While the light was on, the scrubber system was bypassed for 10 minutes in order to sample the full range of gasses exiting the reactor. Bypassing the scrubber had a negligible effect on the measured CH_4 concentration. We report the CH_4 conversion ($-\Delta CH_4$), as well as the production of CO and CO_2. No experiment showed significant infrared signals of other C_1 products such as formaldehyde (CH_2O) or formic acid (CH_2O_2).

Step	Action	Time before next step
1	Set MFCs	10 min
2	Sample baseline CH_4 and Cl_2	5 min
3	Turn light on	15 min
4	Bypass scrubber	5 min
5	Sample other gasses	5 min
6	Un-bypass scrubber	5 min
7	Sample converted CH_4 and Cl_2	5 min
8	Turn light off	10 min
	Repeat steps 1-8	

Table 4.4: Steps in a standard Cl_2-based CH_4 conversion experiment.

4.3.1 Lessons Learned in Apparatus Design

Working with Cl_2 required various adjustments to the system that we used for our experiments with photocatalysts. The most important lesson was that, in the presence of moisture, Cl_2 adsorbs on any metal pipe fittings and fails to pass downstream. This led to an initially baffling situation in which Cl_2 gas entered the system but failed to reach the photoreactor. If we flowed 30 ppm of Cl_2 in dry N_2 through a metal fitting we would measure 30 ppm of Cl_2 downstream, but then if we humidified the gas stream to 30% RH, the measured Cl_2 concentration would sharply decline and approach zero. We attributed this effect to the condensation of Cl_2 and HCl-containing water droplets on the metal fitting surfaces.

Our solution was to remove any metal pipe components between the point where the Cl_2 and the humid gas mixed and the point where the Cl_2 concentration was measured. We replaced all Swagelok compression fittings with plastic barb fittings and all metal and PTFE tubing with vinyl hoses. We replaced our initial photoreactor design, which was a glass tube with metal fittings on the ends, with a custom-made all-glass photoreactor with hose barb connections. Following these changes we had no problem getting consistent Cl_2 measurements throughout the reactor system.

The other aspects of the system were fairly straightforward. The gas supply assembly and infrared gas analyzers were largely the same as in the photocatalyst experiments, with the addition of some extra flow controllers for additional co-fed gases. Using calibration gas tanks rather than custom full-sized gas tanks proved to

be a very easy way to test many different gases with relatively short lead times. The electrochemical Cl_2 sensors proved very stable and reliable, so long as we were careful not to flood them with excessive concentrations of chlorine, which we learned could permanently damage them.

4.3.2 A Typical Experiment with 30-ppm CH_4

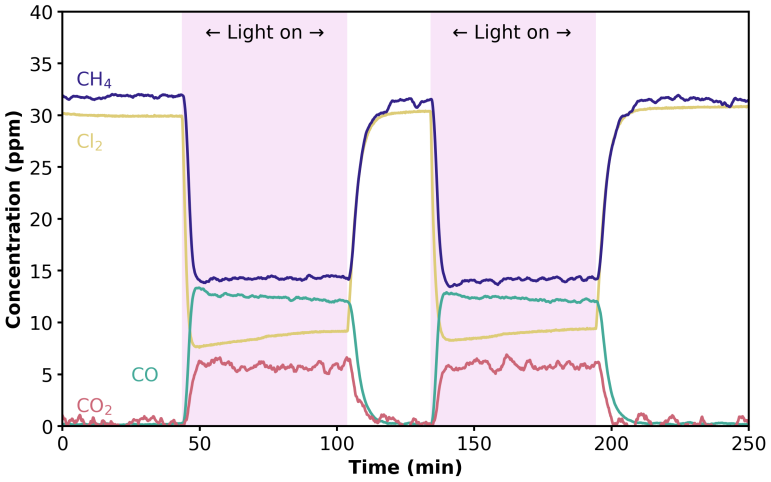

Figure 4.5: Chlorine-based gas-phase advanced oxidation of CH_4. Base-case experiment co-feeding 30 ppm CH_4, 30 ppm Cl_2, 20% O_2, 1% H_2O (∼35% RH), and balance N_2 into the reactor inlet. Time series are shown of gas concentrations measured at the reactor outlet during two cycles of turning the UV light off/on.

In our base-case experiment, we observed Cl_2-GPAO to rapidly oxidize methane, converting 62% of the 30 ppm inlet CH_4. We chose 30 ppm because it is the highest CH_4 concentration detectable by our more sensitive cavity-ringdown gas analyzer. It is also in the middle of the range of CH_4 source concentrations that are of practical interest to us. Fig. 4.5 shows the time series of gas concentrations at the reactor outlet for this trial. When the light was turned on, Cl_2 and CH_4 are removed while CO, CO_2, and HCl were produced. Due to its tendency to condense on and react with analyzer components, we could not accurately quantify HCl and it is not shown. The other gases' decomposition and production rates are repeatable across many on/off cycles of the light. We initially chose a 1:1 Cl_2-CH_4 ratio because it had been

previously used in literature [120], but that value would also later turn out to be the best Cl_2-CH_4 ratio for achieving high CH_4 conversions while wasting as few Cl• as possible.

4.3.3 Chlorine Radical Counting Methodology

In experiments like the one above, it is useful to know how the production rate of chlorine radicals (Cl•) compares to the oxidation rate of CH_4. If all the 30 ppm of Cl_2 in the reactor were photolyzed instantaneously, one would have 60 ppm of Cl•. This is unlikely to occur without a vast excess of UV light, begging the question of what fraction of Cl_2 *does* photolyze into Cl• during its transit of the reactor. One cannot answer that question by simply measuring the outlet Cl_2 concentration during a CH_4 oxidation experiment. This is because in some cases a substantial fraction of Cl• recombines into Cl_2, which would cause some photogenerated Cl• not to be counted. This subsection details how we overcome this issue to accurately know the budget of available Cl• under a given reaction conition.

In our reactor, the amounts of CH_4 converted and byproducts produced have units of micromoles per minute. However, the changes in concentrations of gases across the reactor are measured in ppm. For some gas X, these quantities are related by the equation:

$$\Phi_{\mathrm{X}} = K_{reactor} \cdot \Delta[\mathrm{X}] \tag{4.1}$$

Where $K_{reactor}$ is the molar flow rate of gas through the reactor in moles/minute, Δ[X] is the change of concentration of X in ppm, and Φ_{X} is the net production of X in micromoles/minute.

The productions of reaction intermediates like Cl• also have units of micromoles per minute, but since they are also consumed, there is no change in their concentration across the reactor. However, for convenience, we can define the 'Total Cl• production' ($Cl\bullet_{produced}$) that has units of ppm:

$$Cl\bullet_{produced} = \Phi_{Cl\bullet} \div K_{reactor} \tag{4.2}$$

This can also be interpreted as the amount of Cl• that would be measured if all

photogenerated Cl• were to accumulate to be measured at the reactor outlet, rather than being consumed rapidly as occurs in actuality. For example, in the base-case experiment above, it will turn out that $Cl\bullet_{produced}$=51.2 ppm. This amount of Cl• is able to oxidize 17.1 ppm of CH_4.

As stated above, $Cl\bullet_{\text{produced}}$ cannot be estimated from $\Delta[Cl_2]$ under reaction conditions because a substantial fraction of Cl• recombines to Cl_2. Avoiding this situation requires supplying a radical scavenger that will react with essentially all Cl• before it is able to recombine. Prior studies have used nitrosyl chloride and vinyl bromide as radical scavengers, both of whose products are detectable at very low quantities and both of which generate few if any byproducts.[221, 222] Alternatively, a high concentration of a reducing agent such as H_2 or CH_4 can be used to scavenge all of the available Cl• for a given inlet Cl_2 concentration and the change in the Cl_2 concentration can be observed.[223] Since our system uses high concentrations of Cl_2 that can easily be detected with electrochemical sensors, we used the latter approach.

Our radical-counting experiments aimed to determine $Cl\bullet_{produced}$ as a function of the inlet Cl_2 concentration for the full range of Cl_2 concentrations used in our experiments. In each, we performed a light-on/light-off cycle on a gas mixture containing some concentration of Cl_2, 1.25% CH_4, 20% O_2, ∼1% H_2O, and balance N_2. The great excess of CH_4 guaranteed that every Cl• generated would encounter many CH_4 molecules before encountering another Cl•, making the chlorine atom much more likely to participate in CH_4 oxidation and eventually become HCl than to recombine with another Cl• and become Cl_2. A total flow rate of 200 mL/min was used for all radical-counting experiments, except in the experiments to calculate $Cl\bullet_{produced}$ under alternative residence times.

With negligible recombination, the total Cl• production in the reactor is twice the Cl_2 conversion ($-\Delta Cl_2$) measured at the electrochemical chlorine sensor:

$$\Phi_{Cl\bullet}([Cl_{2,\text{inlet}}]) = -2 \cdot K_{reactor} \cdot \Delta Cl_2|_{\text{inlet Cl2, excess CH4}} \tag{4.3}$$

$$Cl\bullet_{produced}([Cl_{2,\text{inlet}}]) = -2 \cdot \Delta Cl_2|_{\text{inlet Cl2, excess CH4}} \tag{4.4}$$

As a concrete example, in the radical-counting experiment corresponding to the

base case (30 ppm Cl_2 and excess CH_4) we observed a $-\Delta Cl_2$ of 25.6 ppm, giving $Cl\bullet_{produced}$(30 ppm $Cl_{2,inlet}$)=51.2 ppm.

Fig. 4.6 shows the $Cl\bullet_{produced}$ as a function of $[Cl_2]$ for the full range of $[Cl_2]$ from 1-90 ppm. We performed linear interpolation on these data to evaluate $Cl\bullet_{produced}([Cl_2])$ for any $[Cl_2]$ used in our experiments. We note that across concentrations, ∼80% of Cl_2 was photolyzed, with the rest evidently passing through the reactor without encountering an UV photon. These values of $Cl\bullet_{produced}$ will be reffered to throughout this chapter.

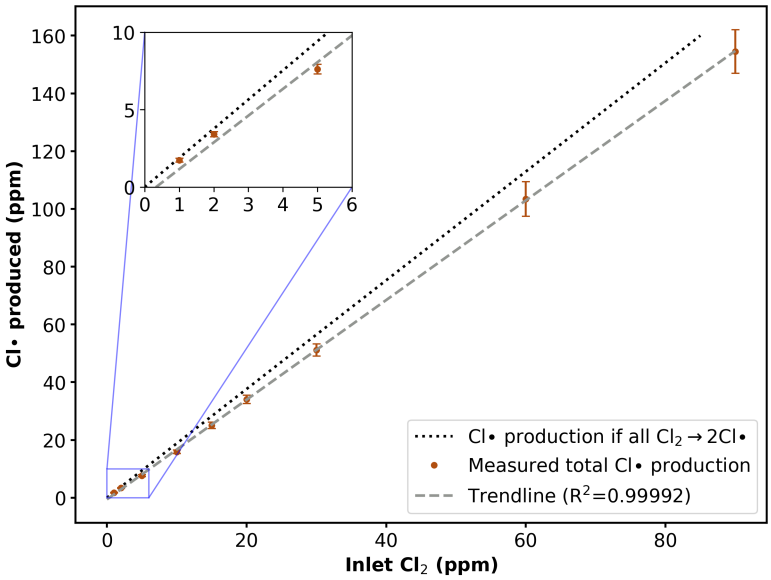

Figure 4.6: Cl radical-counting. Total Cl• produced as a function of Cl2 concentration, with error bars showing two standard deviations (95% confidence intervals). The linear trendline of these data (dashed line) was used in the experiments to evaluate total Cl• production for the corresponding Cl_2 concentration. Based on the dotted line, showing Cl• production if all Cl_2 was photolyzed to Cl•, ∼80% of Cl_2 in this reactor was photolyzed.

4.3.4 Figures of Merit: Cl_2 and Cl• Efficiencies

In each experimental condition, we report the number of CH_4 molecules oxidized per chlorine radical consumed, a figure of merit we term the "Cl• usage efficiency" ($\eta_{Cl\bullet}$). This value is the quotient of the CH_4 conversion, measured in a CH_4 conversion experiment, and the total Cl• production, measured in a radical-counting experiment:

$$\eta_{Cl\bullet} = (-\Delta CH_4) \div Cl\bullet_{produced}([Cl_{2,inlet}]) \tag{4.5}$$

Prior studies on Cl_2-GPAO have reported the process's quantum yield (defined as moles of CH_4 oxidized per mole of generated UV photons) for specific reactors, a value that depends on $\eta_{Cl\bullet}$ but also on the reactor size and geometry.[70, 120] In contrast, $\eta_{Cl\bullet}$ should be consistent across different reactors for a fixed inlet gas composition and residence time. We show later how $\eta_{Cl\bullet}$ can be used to estimate a scaled-up system's lighting costs.

Another useful value is the number of CH_4 oxidized per Cl_2 molecule added to the system, a figure of merit we term the "Cl_2 usage efficiency" (η_{Cl2}). This quantity is easily calculated from values measured during a CH_4 oxidation experiment.

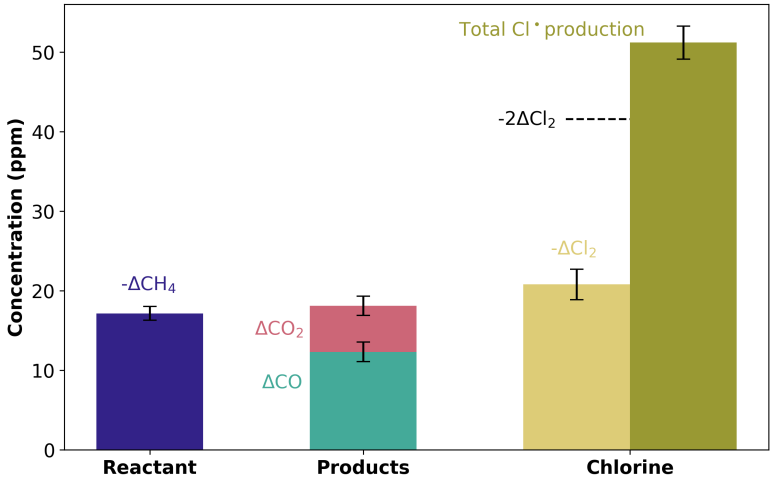

Figure 4.7: Chlorine-based gas-phase advanced oxidation of CH_4. Base-case experiment co-feeding 30 ppm CH_4, 30 ppm Cl_2, 20% O_2, 1% H_2O (~35% RH), and balance N_2 into the reactor inlet. CH_4 conversion, reaction products, and chlorine radical production.

Figure 4.7 illustrates these values for the same base-case experiment shown in Figure 4.5. In that trial, 17.1 ppm of CH_4 was oxidized to a mixture of CO and CO_2. The radical-counting experiment with 30 ppm inlet Cl_2 found that $Cl\bullet_{produced}$=51.2 ppm. Attempting to measure $Cl\bullet_{produced}$ as $-2\Delta Cl_2$ would have substantially undercounted the amount of Cl• produced. The chlorine radical efficiency ($\eta_{Cl\bullet}$) equals ($17.1/51.2 = 0.33$). Since the inlet Cl_2 concentration was 30 ppm, $\eta_{Cl2} = (17.1/30) = 0.57$. The same types of calculations are repeated wherever we report $\eta_{Cl\bullet}$) and η_{Cl2}.

4.4 Cl_2-GPAO Reaction Products

The majority reaction products of Cl_2-GPAO were CO and CO_2, as illustrated in Figure 4.7. This result is consistent with previous work [120] and with the understood reaction mechanism for this process, in which CO oxidation to CO_2 by Cl• is a slow reaction compared to Cl• attack of C-H bonds. The relative quantities of CO and CO_2 depended somewhat on reaction conditions, as we discuss later (Figure 4.9). Our infrared spectrometer detected no formaldehyde (CH_2O) or formic acid (CH_2O_2) in the reaction products under any reaction conditions.

4.4.1 Screening for Chlorinated Hydrocarbons

A concern of Cl_2-GPAO is the potential production of chlorinated methanes, some of which are toxic and have ppm-level exposure limits. Prior works' modeling of Cl_2-GPAO has suggested a 0.01% yield for each successive replacement of a hydrogen atom with chlorine in CH_4 to create CH_3Cl, CH_2Cl_2, $CHCl_3$, and finally CCl_4, meaning that CH_3Cl should be the most abundant.[120] To experimentally measure chlorinated CH_4 production, we screened for CH_3Cl in the base-case experiment using the EPA Method TO-15 for analysis of organic compounds in air with gas chromatography/mass spectrometry (GC/MS).[224]

We found that Cl_2-GPAO in the base-case produced only 1.0±0.3 parts per billion of CH_3Cl, well within safe levels. This is a <0.01% yield of CH_3Cl given the CH_4 conversion of ∼20 ppm, as expected from theory.[120] The concentration is several orders of magnitude below the 8-hour workplace exposure limit of 100 ppm CH_3Cl.[225] Given CH_3Cl's 20-year global warming potential of 45, such a low concentration would

negligibly affect Cl_2-GPAO's climate benefit.[120] The TO-15 gas analysis method does not measure other relevant chlorinated methanes, leaving them a topic for future measurements.

4.5 Effects of Varying the Residence Time

In the next campaign of experiments, we aimed to clarify the role of the residence time. This value is of commercial interest because if the residence time can be shortened and the light intensity increased without adversely affecting the reactor's efficiency, a relatively small reactor can be used to rapidly strip CH_4 from large volumes of air. In particular, we wished to vary the residence time while maintaining a fixed ratio of Cl• production to inlet CH_4.

To do so, as we modified the residence time by changing the total gas flow rate, we adjusted the UV intensity until the measured Cl• production was the same as in the base-case. For instance, when the residence time was lengthened for a given light flux, the total Cl• production from Cl_2 photolysis increased, so we reduced the light flux until the Cl• production returned to its baseline value ($\sim$50 ppm of Cl• production during the gas's residence in the reactor).

In the base-case with the 3-minute residence time, the 50W LED panel was positioned 28 cm above the center of the reactor. For an 8-minute residence time, we moved the same LED panel to an increased distance of 64 cm above the reactor. For a 2-minute residence time, we used a more powerful 365nm LED panel suspended 28 cm above the reactor. This panel was connected directly to a DC power supply and consumed $\sim$100W of electrical power. 2 minutes was the shortest residence time we could practically test because, at higher flow rates, significant back pressure tended to build in the tubing downstream of the reactor.

Fig. 4.8 shows the intermediate values and results of these experiments. By varying the light intensity for a given residence time, we attempted to hold the Cl• production constant. We then conducted a CH_4 conversion trial with 30 ppm inlet CH_4, 30 ppm inlet Cl_2, and $\sim$35% RH under the new flow rate and light intensity. We then observed whether and how the observed CH_4 conversions and Cl• usage efficiencies varied amongst the three residence time/lighting conditions.

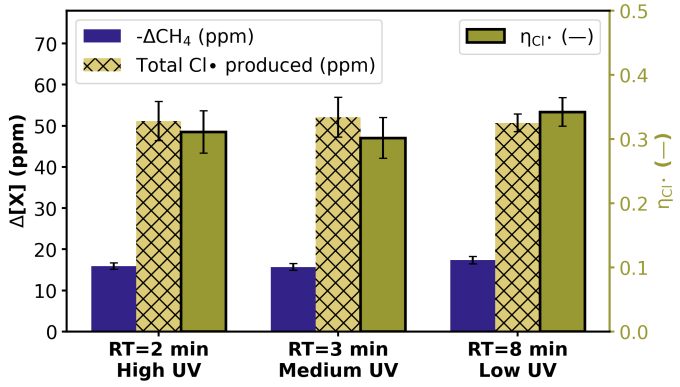

Figure 4.8: Effect of residence time (RT). CH_4 conversion shown by blue bars, and Cl• usage efficiency shown by solid olive bars. For 2 and 8 minutes residence times, the UV light intensity was adjusted until the total Cl• production (hatched gold bars) measured in the radical-counting procedure matched that of the base-case (RT = 3 min).

We found that varying the residence time of air through the reactor did not significantly affect CH_4 conversions given a constant total Cl• production. This result suggests that boosting the throughput of scaled-up systems by using higher light intensities and shorter residence times may not necessarily reduce the $\eta_{Cl\bullet}$ of the system. Given the practical limitations on our setup's light intensity and flow rate, we were unable to test residence times shorter than 2 minutes, although residence times of 1 minute or less would likely be of interest in a full-scale Cl_2-GPAO system.

4.6 Effects of Varying Inlet Cl_2, CH_4, and H_2O

As we increased the inlet Cl_2 concentration in successive experiments with all other parameters held constant, the observed CH_4 conversion rose, although beyond a 1:1 inlet Cl_2-CH_4 ratio there were diminishing returns of CH_4 oxidized per Cl_2 supplied (Fig. 4.9**(a)**). The CH_4 conversion increased linearly with inlet Cl_2 concentrations between 10 and 30 ppm, then increased more slowly as the Cl_2 concentration was raised further. The highest $\eta_{Cl\bullet}$ was observed for inlet Cl_2 concentrations of 10-30 ppm, with 30 ppm of Cl_2 giving both a high $\eta_{Cl\bullet}$ and high CH_4 conversion, leading to our default choice of 1:1 Cl_2-CH_4 ratios for most experiments. Applying our input

cost model to the results of this sweep revealed that the condition with 30 ppm of Cl_2 (i.e., 1:1 Cl_2-CH_4 ratio) would have the lowest Cl_2 and lighting cost per unit of CH_4 oxidized (Table S3), further justifying that choice.

As the inlet ratio of Cl_2 to CH_4 increased, the balance of products shifted from CO to CO_2. This is consistent with the reaction pathways laid out in Krogsbøll, *et al.*[120] In this system, Cl• reacts rapidly with compounds containing C-H bonds such as CH_4 and CH_2O, eventually producing CO that cannot be reacted in the same way. Still, with additional Cl• present, a slower reaction generates the intermediate ClCO which becomes CO_2 through one of several pathways that regenerate Cl• or Cl_2. Clarifying the exact mechanism at work is beyond the scope of this study, but the results suggests that Cl• may also have a catalytic role in oxidizing CO to CO_2.

The measured Cl_2 conversion was consistently ∼1.25 times the CH_4 conversion regardless of the inlet Cl_2 concentration or the Cl• production (Fig. S2.2). This result likely reflects that any Cl• that attacks a C-H bond ends up as HCl, but otherwise is quenched back to Cl_2, either by directly recombining with another Cl• or as part of the CO-to-CO_2 conversion process. Even where our radical-counting procedure showed very high Cl• production (e.g., 77 ppm of 90 ppm inlet Cl_2 photolyzed to Cl•), the Cl_2 conversions in the experiment with 30 ppm inlet CH_4 remained low (34 ppm), suggesting that most of the additional available Cl• eventually recombined to Cl_2.

Varying the inlet CH_4 and Cl_2 in a fixed proportion to one another did not substantially change the percent CH_4 conversion, product yields, or Cl• usage efficiency (Fig. 4.9**(b)**). In the 1:1 sweep experiments the composition of the products, ∼70% CO and ∼30% CO_2, remained unchanged, as did the ∼60% CH_4 conversion. $\eta_{Cl\bullet}$ changed fairly little across the inlet CH_4 concentrations >10 ppm, though it began to fall at low CH_4 concentrations, as we discuss further below. These results suggest that, at least for inlet CH_4 concentrations >10ppm, the percent conversions and $\eta_{Cl\bullet}$ measured at 30 ppm inlet CH_4 can likely be used at other inlet CH_4 concentrations so long as the ratio of CH_4 to other gases is the same. We also found that varying the inlet gas's moisture from 5% to 60% relative humidity (RH) had a minimal effect on the product composition and $\eta_{Cl\bullet}$ (Fig. 4.9**(c)**).

Fig. 4.10 shows the divergence between Cl_2 conversion and total Cl• production

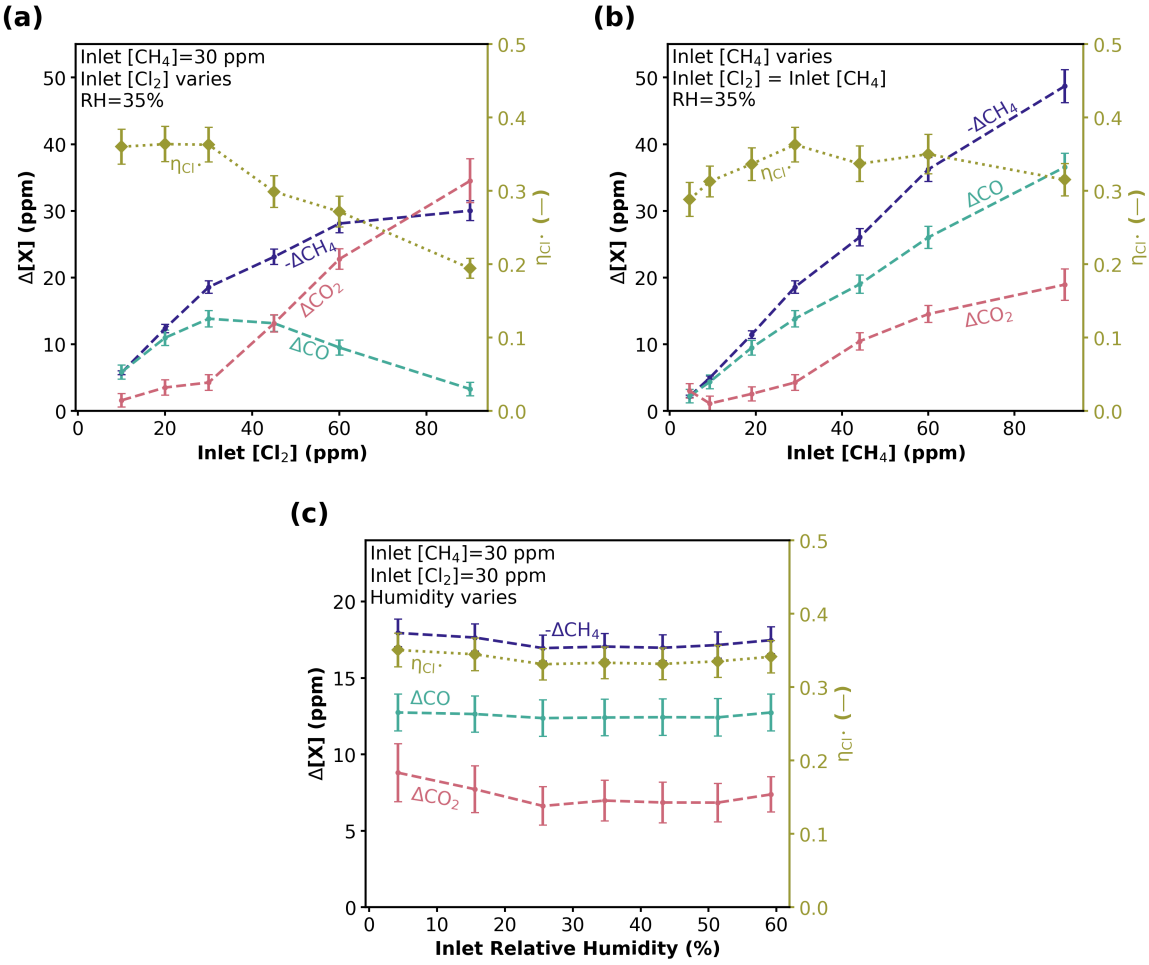

Figure 4.9: Parametric studies from base-case. **(a)** 10-90 ppm Cl_2 while holding fixed 30 ppm CH_4 and 35% RH. **(b)** 5-90 ppm CH_4 and Cl2 at a 1:1 ratio while holding fixed 35% RH. **(c)** 5-60% RH while holding fixed 30 ppm CH_4 and 30 ppm Cl_2.

from experiments varying inlet CH_4 and Cl_2 (same experiments as Figs. 2a and 2b). In each case, available Cl• increases in proportion to the inlet Cl_2 concentration. However, moving to the right of subplot **(a)**, as all the CH_4 is consumed, Cl• recombines into Cl_2 rather than reacting with C-H bonds. Thus the Cl_2 conversion tapers off, diverging from the Cl• production. $\eta_{Cl•}$ drops as this difference becomes larger. In subplot **(b)**, the inlet CH_4 concentration is increased in tandem with the inlet Cl_2 concentration, so the CH_4 is never entirely depleted and Cl• continue to mainly

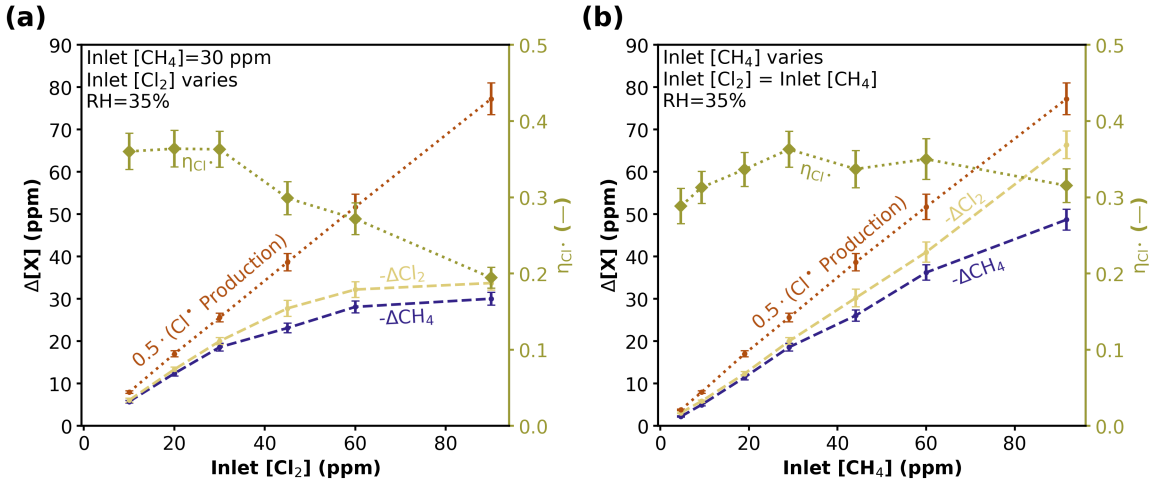

Figure 4.10: Effect of varying inlet CH_4 and Cl_2 concentration on Cl_2 conversion and Cl• production. **(a)** Effects of varying the inlet Cl_2 concentration with a fixed inlet CH_4 concentration of 30 ppm. **(b)** Effect of varying CH_4 and Cl_2 concentrations together in a fixed 1:1 proportion. Cl• production is measured using the radical-counting procedure and is scaled by 0.5 to make it fit on the left axis.

react with C-H bonds rather than recombine. Thus, the Cl• and -ΔCl_2 lines do not diverge.

4.7 Effects of Co-Fed Gases

In our next experimental campaign, we tested the effects of four gaseous contaminants: ammonia (NH_3), hydrogen sulfide (H_2S), toluene ($C_6H_5CH_3$), and nitric oxide (NO). The first three may be present at ppm-levels at emissions sources on which Cl_2-GPAO might be deployed, such as dairy barns and sewers.[226, 227] We used toluene as a proxy for volatile organic compounds. NO was of interest for its potential to aid CH_4 oxidation through reactions with intermediate hydrocarbons and from the assistance of generating OH•.[120] We conducted four CH_4 conversion experiments, each varying the concentration of one contaminant gas while keeping base-case values for the inlet Cl_2, CH_4, and humidity.

Increasing the amount of each contaminant gas caused the CH_4 conversion to

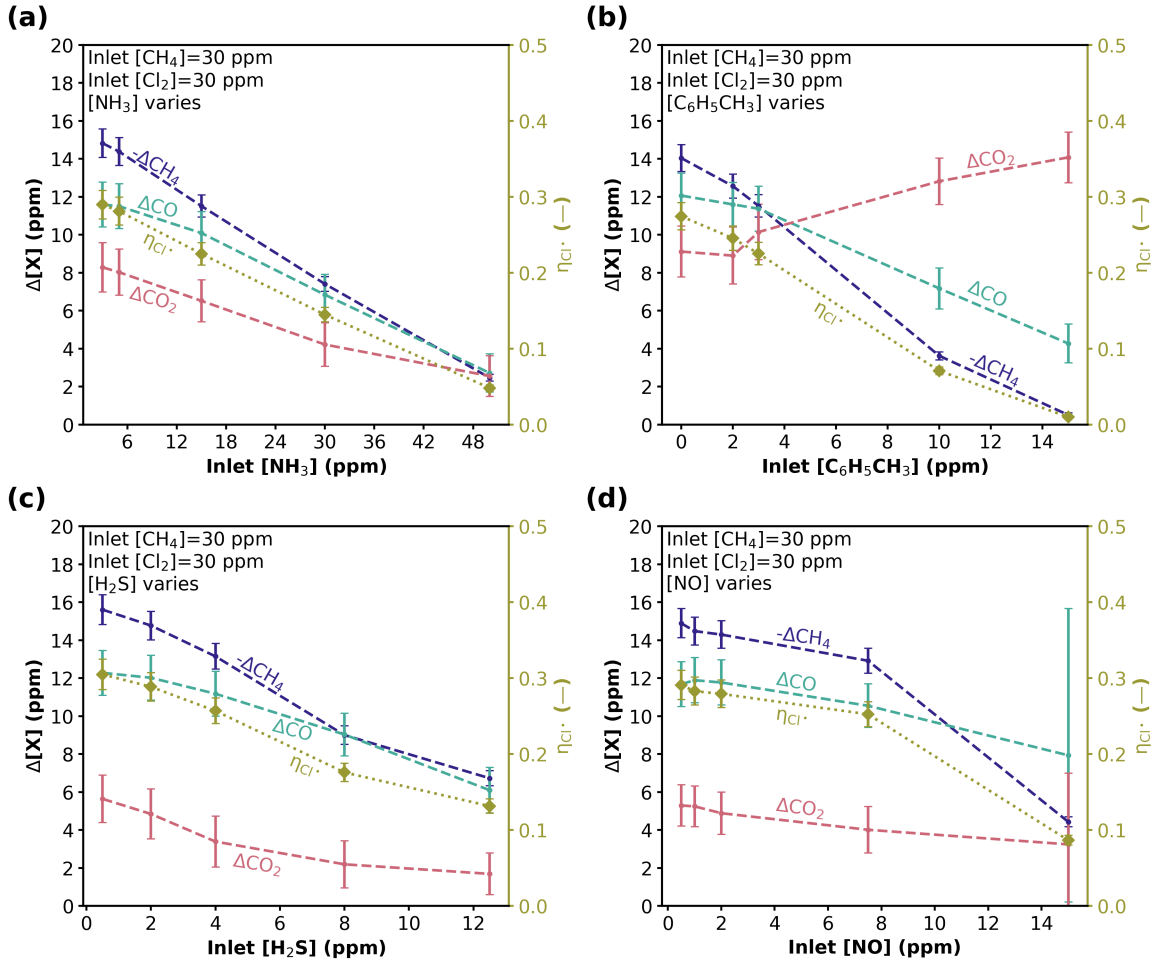

Figure 4.11: Effect of contaminants. Change in concentration is shown on the left axis, and $\eta_{Cl\bullet}$ is shown on the right axis. Error bars show two standard deviations (95% confidence intervals). **(a)** 1-50 ppm ammonia (NH_3). **(b)** 0-15 ppm toluene ($C_6H_5CH_3$). **(c)** 0.5-12.5 ppm hydrogen sulfide (H_2S). **(d)** 0.5-15 ppm nitric oxide (NO). Dashed lines show the changes for CH_4, CO, and CO_2 in purple, aqua, and pink, respectively. The dotted olive line shows the 'Cl• usage efficiency' ($\eta_{Cl\bullet}$)

decrease, with toluene causing the sharpest decrease followed by H_2S, NO, and NH_3 (Fig. 4.11). These effects are likely the result of two mechanisms: **(a)** contaminants reacting with Cl_2 in the dark before it could photolyze under UV light; and **(b)** contaminants scavenging Cl• that might otherwise have reacted with CH_4. Of these gases, NH_3, H_2S, and NO are known to react with Cl_2 in the dark to respectively

produce ammonium chloride or chloramine, sulfur, and nitrosyl chloride. We would expect these reactions to decrease the overall supply of Cl_2 in the reactor and thereby of Cl• as well.[228–230] While we saw evidence of Cl_2 consumption in the Cl_2 sensor, those products were produced in too small quantities to be visible or detectable. Each contaminant may also inhibit the reaction by scavenging Cl•. The many C-H bonds in toluene in particular make it a highly effective Cl• scavenger; the CO_2 produced from its oxidation can be seen in Fig. 4.11**(b)**. In short, Cl_2-GPAO continues to work in the presence of moderate levels of these gases, whose effects we explore further in the following section.

Scenario	**CH_4 ppm**	**Cl_2 ppm**	**Ar %**	**CO_2 ppm**	**O_2 %**	**NH_3 ppm**	**H_2S ppm**	**$C_6H_5CH_3$ ppm**	**N_2**	**RH %**	**Ref.**
Atmosphere	1.9	1.9	425	0.8	20	--	--	--	bal.	35	[231]
Dairy Barn	50	50	1000	1.9	20	25	5	1	bal.	35	[226, 232–235]
Sewer	300	300	1000	1.9	20	25	5	1	bal.	55	[227, 236–238]

Table 4.6: Gas mixtures used in the application-based experiments. The Cl_2 concentration was chosen to maintain an inlet Cl_2-CH_4 ratio of 1:1.

4.8 Application-Based Experiments

In our final Cl_2-GPAO experimental campaign, we tested Cl_2-GPAO using gas mixtures representative of three 'application-based,' real-world deployment scenarios. Variants of Cl_2-GPAO have been discussed as a possible tool for atmospheric CH_4 removal, so we conducted an experiment on simulated atmospheric air with 1.9 ppm CH_4. Additionally, agricultural facilities and wastewater treatment plants release substantial amounts of low-concentration (<1,000 ppm) CH_4 and are, as such, possible candidates for eventual Cl_2-GPAO deployment. We focused on dairy barn ventilation air and sewer headspace as representative gas streams from these industries, choosing typical gas concentrations from the literature. Toluene was again used as a representative volatile organic compound. Table 4.6 shows the gas compositions used in the three experiments, with a 1:1 Cl_2-CH_4 ratio used throughout. We note that Ar and CO_2 were supplied from the same tank, so their concentrations are coupled, causing the Ar concentrations to be slightly different from air's true value of ∼0.9%.

The reactor setup was modified slightly to allow for the simulated experiments on atmospheric, dairy barn, and sewer headspace. To the existing setup with flow controllers for dry and humid N_2, O_2, CH_4, and toluene, we added three additional flow controllers attached to cylinders of 50 ppm H_2S in N_2, 200 ppm NH_3 in N_2, and 5% CO_2 in Argon. We re-routed all N_2 and O_2 flow through the water bubbler in order to achieve higher relative humidities. In the sewer gas experiment, we used a Cl_2 sensor suitable for higher Cl_2 concentrations (Membrapor Cl/C-2000).

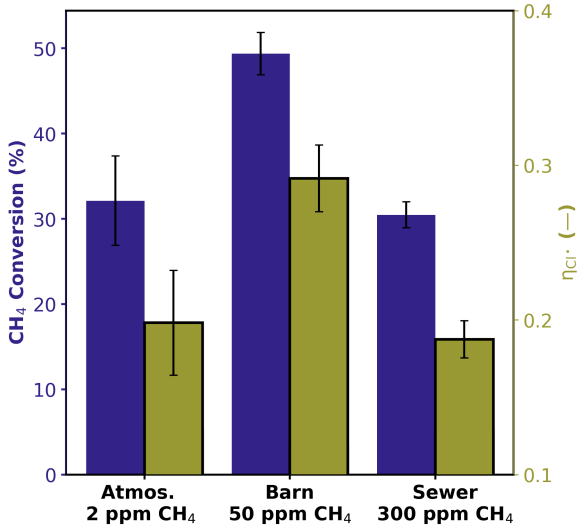

Figure 4.12: Application-based experiments for atmospheric methane, a dairy barn, and sewer gas. **(a)** CH_4 conversion (left axis) and $\eta_{Cl\bullet}$ (right axis) for each application. Error bars show two standard deviations (95% confidence intervals).

All three application-based experiments representing real-world deployment scenarios showed substantial CH_4 conversions; however, these conversions and the associated $\eta_{Cl\bullet}$ were each somewhat lower than in the base-case. This result can be explained by a combination of contaminant and concentration effects (Fig 4a). The barn air experiment's percent CH_4 conversion and $\eta_{Cl\bullet}$ were only ~10% worse than in the previous experiment with similar inlet CH_4 and Cl_2 but without contaminants (Fig. 4.9**(b)**; 45 ppm CH_4), showing that the contaminants had an overall modest effect. The sewer gas experiment's percent CH_4 conversion was about two-thirds lower than the barn air experiment's percent CH_4 conversion, despite having a lower ratio of contaminants to CH_4. The percent CH_4 conversion and the $\eta_{Cl\bullet}$ on the simulated atmospheric air were around half that in the base-case. These values were lower than those seen in the 1:1 Cl_2-CH_4 experiments at 5 ppm and 10 ppm inlet CH_4 and Cl_2, continuing the trend in Fig. 4.9**(b)** of lower $\eta_{Cl\bullet}$ at lower inlet CH_4 and Cl_2 concentrations.

4.9 Conclusion

In summary, we found that Cl_2-GPAO was able to rapidly convert dilute CH_4 across a range of operating conditions. After testing a variety of inlet Cl_2-to-CH_4 ratios, we learned that a 1:1 ratio gave a high (62%) CH_4 conversion while avoiding Cl• wastage, so we suggest using this ratio as a default for future studies. We made, to our knowledge, the first measurement of Cl• consumption in a Cl_2-GPAO reactor, finding that a minimum of 3 Cl• were consumed per CH_4 oxidized. We found the process to behave similarly at a variety of humidities, residence times, and inlet CH_4 concentrations (with equimolar inlet Cl_2). We also found the production of CH_3Cl in our base-case to be extremely small ($\sim$1 ppb), suggesting that chlorinated CH_4 production may not be a critical barrier to safe deployment, at least for this chemical species.

We also discovered the process of Cl_2-GPAO to be fairly resilient to the gas-phase contaminants H_2S, NH_3, NO, and $C_6H_5CH_3$. Low levels of the contaminants did not greatly affect CH_4 conversions and Cl• usage efficiencies compared to the base-case, although sufficient levels of each contaminant gas caused the CH_4 conversion to drop by half or more. This result was due to contaminants either scavenging Cl• or reacting with Cl_2 before it could photolyze. We additionally conducted application-based experiments with gas mixtures representing three possible Cl_2-GPAO deployment locations – the open atmosphere, a barn, and a sewer – finding that in each case, the percent CH_4 conversion was substantial although lower than in the base-case. These results suggest that Cl_2-GPAO can likely work in many real-world settings so long as the contaminants are not present in comparable concentrations to the CH_4 itself. The fact that the "open atmosphere" experiment showed a relatively Cl• efficiency despite the absence of contaminants is surprising, and is worth replicating in a smog chamber or larger reactor to rule out the possibility of wall effects or ppb-level contaminants in our gas tanks.

Much like with the photocatalyst work, our intent in collecting these data was to inform simple but accurate cost models that can shed light on whether Cl_2-GPAO is likely to be commercially viable in real-world settings. We take up that task in the following chapter.

Chapter 5

Cost Modeling of Advanced Oxidation with Chlorine

5.1 Introduction

As with the photocatalyst research, the goal of our chlorine campaign was to combine experiments and cost modeling to understand whether and where Cl_2-GPAO could be a practical CH_4 mitigation solution. My collaborators and I planned our Cl_2 experiments to measure figures of merit that would be key inputs for any cost model of a scaled-up system. The two main such metrics were η_{Cl2} and $\eta_{Cl\bullet}$. Our next task was to build a cost model to give a lower bound on the cost of a full-size Cl_2-GPAO system in various scenarios. The key cost drivers that we wished to include were the Cl_2 supply, lighting hardare and electricity, and gas-scrubbing equipment to remove Cl_2 and HCl downstream of the Cl_2-GPAO reactor.

Despite ongoing commercialization efforts on Cl_2-GPAO [70], few cost modeling results for the process have yet been published. The process's developers mainly report the CH_4 conversion and the apparent quantum yield (AQY) for each iteration of their reactor, with the latest reactor at the time of writing reaching CH_4 conversions >95% and quantum yields as high as 1.5%. A recent preprint reported a modeled cost of \$500/tCO_2e or, using CH_4's GWP-20, \$40000/tCH_4 for the current iteration of the reactor. However, the methodology behind this estimate was not explained.

In private conversations, the process's developers have noted that clients seem more interested in a high percentage of CH_4 destruction than on a low cost per ton of CH_4. This likely reflects that "99% less methane!" makes for a better slogan on a milk carton than "60% less methane at \$2000/tCH_4!". It likely also reflects that milk's unit economics may create a relatively high cost tolerance per ton of CH_4, as discussed in Chapter 1 Section 1.2.3. However, as the process scales, we suspect that unit economics will become an ever more critical criterion for adoption.

We have tailored our cost model to reflect current scale-up efforts in several ways. Commercialization efforts to date have focused on CH_4 from livestock, so we made sure to include barn air as one of our cost modeling scenarios. Efforts have also focused on packaging units in standard shipping containers for transport, so our plot of modeled reactor sizes includes 20 and 40-foot shipping container lengths for reference. Demonstrations to date have used on-site electrochemical Cl_2 generators that were manufactured for swimming pool sanitation, so we included these devices among other options in our range of modeled Cl_2 sources.

5.2 Modeling Reactor Sizes and Efficiencies

Before modeling the costs of this system, we wished to explore the general effects of reactor size on key assumed values. In particular, the fraction of Cl_2 that undergoes photolysis (Δ_{Cl2}) and the fraction of UV photons that are absorbed by Cl_2 molecules ($\eta_{reflectors}$) are two key assumptions that strongly influence modeled costs. If the former is too low, more inlet Cl_2 is required to produce a given quantity of $\bullet$Cl. If the latter is too low, more electricity and lighting hardware are required to do the same.

Although both of these efficiencies can be pushed arbitrarily high in an arbitrarily large reactor, designing a reactor of finite size requires tradeoffs in one or both of them. In a small reactor with internal reflectors, the number of reflections per meter of optical path length is higher, so the fraction of light lost to reflector inefficiencies is greater than in a larger reactor. In a reactor of a given size with a lower Cl_2 conversion, the average Cl_2 concentration over the length of the reactor is greater (since the Cl_2 concentration ranges from, say, 50 to 10 ppm rather than from 50 to 1 ppm). Thus, a reactor with lower Cl_2 conversion has a greater average rate of photon absorption by Cl_2 per meter of optical path length, causing a greater fraction of photons to be absorbed by Cl_2. In short, one can make a reactor smaller by accepting either a lower Cl_2 conversion (essentially a lower η_{Cl2}) or a lower photonic efficiency (a lower $\eta_{reflectors}$, as we term it, and a lower AQY). To inform the $\eta_{reflectors}$ and η_{Cl2} that we assume in our models, it is useful to understand how these values relate to reactor size at different inlet Cl_2 concentrations.

5.2.1 UV-Cl_2 Absorption Model with Internal Reflection

We built a simplified 1-dimensional model of Cl_2 absorption in an internally-reflective photoreactor to gain intuition around this issue. For simplicity, the model assumes that the Cl_2 concentration is radially uniform and drops exponentially from the specified inlet Cl_2 concentration to the specified outlet Cl_2 concentration. The model assumes that the UV light is generated at one end of the reactor and travels only in the axial direction, with some fraction getting absorbed by Cl_2 as it transits the reactor and the remainder hitting a reflector at the opposite end. We discuss reflection modeling further below.

The model computes UV absorption on a single pass by discretizing the reactor's length into 100 cells. In each cell, we compute the fraction of the UV light that is absorbed by Cl_2. Let that fraction for the i^{th} cell be α_i. Let A_{Cl2} be the absorption cross-section of a Cl_2 molecule, which at 365nm is $8.4 \cdot 10^{-24}$ m^{-2} per molecule.[239] Let L_{cell} be the length of each cell, one fiftieth of the length of the modeled reactor. Suppose the cell has a frontal area A_{cell} (m^2) and let its volume be V_{cell} (m^3).

$$V_{cell} = A_{cell} \cdot L_{cell} \tag{5.1}$$

A mole of gas at standard conditions takes up 22.4L, so a cubic meter of air contains $(1000/22.4) = 44.6$ moles of gas. Let $[Cl_2]$ be the concentration of Cl_2 in the cell in ppm. The number of Cl_2 molecules, n_{Cl2}, in the cell is therefore:

$$n_{Cl2} = A_{cell} \cdot L_{cell} \cdot (44.6 \text{ moles/m}^3) \cdot (6.022 \cdot 10^{23} \text{ molecules/mole}) \cdot ([Cl_2] \cdot 10^{-6}) \tag{5.2}$$

The total frontal area presented by Cl_2 molecules in the cell, $A_{absorption}$ (m^2), is therefore:

$$A_{absorption} = A_{Cl2} \cdot A_{cell} \cdot L_{cell} \cdot (44.6 \text{ moles/m}^3) \cdot (6.022 \cdot 10^{23} \text{ molecules/mole}) \cdot ([Cl_2] \cdot 10^{-6}) \tag{5.3}$$

Using the definition of the absorption cross section, the fraction of light absorbed by Cl_2 in the cell is therefore:

$$\alpha_i = A_{absorption} \div A_{cell} \tag{5.4}$$

We note that the above relation is only valid for a sufficiently thin cell, such that a fairly small fraction of the light is absorbed. We increased the number of cells until the results converged (i.e., adding more cells did not change the model outputs), finding 100 cells to be a good number.

$$\alpha_i = A_{\mathrm{Cl2}} \cdot L_{cell} \cdot (44.6 \text{ moles/m}^3) \cdot (6.022 \cdot 10^{23} \text{ molecules/mole}) \cdot ([\mathrm{Cl_2}] \cdot 10^{-6}) \quad (5.5)$$

Let α_{pass} be the fraction of light that is absorbed by Cl_2 on a single pass through the reactor. Then, accounting for the Cl_2 absorption in all the cells:

$$\alpha_{pass} = 1 - \Pi_{i=1}^{100}(1 - \alpha_i) \quad (5.6)$$

The light is modeled to reflect back and forth between the ends of the reactor. On each pass, some fraction of light absorbed by Cl_2 and some is absorbed by the reflector afterwards, with the remainder passing back through the reactor in the opposite direction. After 50 modeled reflections, the vast majority of the light has been absorbed, and we tally and report the fractions of light absorbed by Cl_2 and lost to reflector inefficiencies. The one-dimensional model assumes that light only travels axially through the reactor; accounting for 3-dimensional absorption and reflection would be considerably more complex.

A wrapper takes a desired $\eta_{\text{reflectors}}$ and repeatedly calls the above model with a given inlet Cl_2 concentration and outlet Cl_2 concentration, increasing the reactor length until the desired $\eta_{\text{reflectors}}$ is reached. Thus, the final output is the reactor length required to ensure that a given fraction of photons are absorbed by Cl_2 for a given inlet Cl_2 concentration and a given Cl_2 conversion.

5.2.2 Model Outputs for Reactor Size

Figure 5.1 shows the outputs of this modeling exercise. Each colored line can be understood to embody "target" values for Δ_{Cl2} (Cl_2 conversion) and $\eta_{\text{reflectors}}$ (percent UV absorption by Cl_2 as opposed to reflector loss). Five of the lines assume PTFE reflectors that reflect 93% of incident UV light and one assumes cheaper aluminum reflectors that only reflect 80%.[240] The x-axis shows the Cl_2 concentration at the reactor inlet; the reactor outlet Cl_2 concentration is determined by the assumed Δ_{Cl2}. The y-axis shows the reactor length that is required in order to achieve the desired target value $\eta_{\text{reflectors}}$ for the specified Δ_{Cl2}, inlet Cl_2 concentration, and reflector materials. As the targets for $\eta_{\text{reflectors}}$ and Δ_{Cl2} get higher and as the inlet

Cl_2 concentration gets lower, the required reactor size increases.

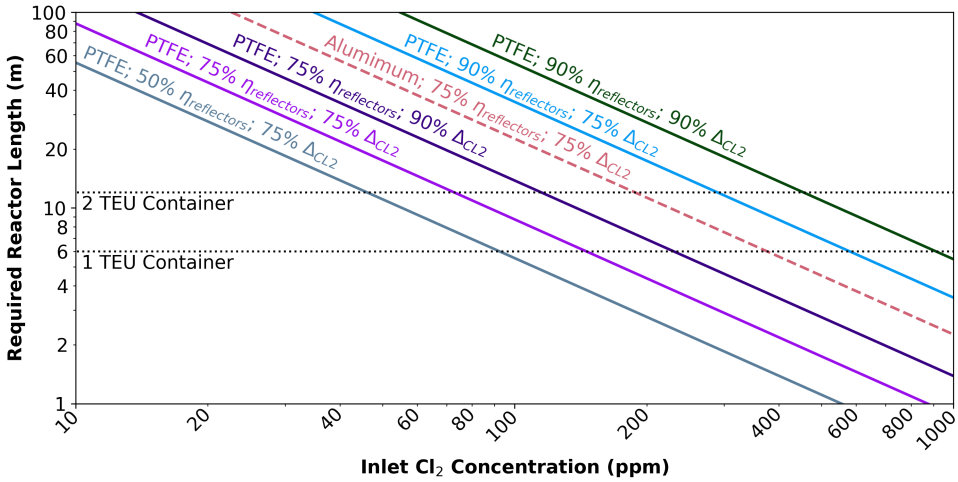

Figure 5.1: Relationships between chlorine photoreactor size and efficiencies. Each plotted line represents a desired Δ_{Cl2} (Cl_2 conversion) and $\eta_{\text{reflectors}}$ (percent UV absorption by Cl_2 as opposed to reflector loss) as well as a certain reflector material. The y-axis shows the modeled length of reactor required to achieve those metrics for the inlet Cl_2 concentration indicated on the x-axis and for the reflector material specified.

Several conclusions arise from this plot. Although it would be economically beneficial, achieving both 90% Δ_{Cl2} and 90% $\eta_{\text{reflectors}}$ requires very large reactors at inlet Cl_2 concentrations below 300 ppm. Reactors larger than 2 TEU shipping containers would be rather impractical to mass-produce and deploy. Thus, assuming 90% Δ_{Cl2} and 90% $\eta_{\text{reflectors}}$ for low CH_4/Cl_2 concentrations would be unrealistic in our later cost models. For low ($\sim$30%) CH_4/Cl_2 concentrations, values of $\sim$50% for both may be more realistic. These values should be treated as very rough estimates; it is quite possible that real-world photonic efficiencies are far lower than these due to unmodeled loss mechanisms.

For our modeling purposes, based on Figure 5.1 we select different Δ_{Cl2} and $\eta_{\text{reflectors}}$ values for different inlet Cl_2 concentrations. For the scenarios with 50 ppm inlet Cl_2, we model $\Delta_{Cl2} = 75\%$ and $\eta_{\text{reflectors}} = 50\%$. For the scenarios with 100 ppm inlet Cl_2, we model $\Delta_{Cl2} = 75\%$ and $\eta_{\text{reflectors}} = 75\%$. For the scenarios with 300 ppm inlet Cl_2, we model $\Delta_{Cl2} = 75\%$ and $\eta_{\text{reflectors}} = 90\%$.

5.3 Structure of the Cl_2-GPAO Cost Model

Our Cl_2-GPAO cost model included the costs of reagent (Cl_2 and NaOH) supply, lighting hardware and electricity, and gas-scrubbing equipment. We chose to exclude the photoreactor capital and air-circulation costs because they are highly complex to model, likely requiring multiparameter optimizations like those in Chapter 3. Additionally, since the Cl_2-GPAO reactor is a hollow optical cavity with a low pressure drop, we expected those costs to be small compared to the cost drivers listed. We felt that modeling Cl_2, lighting, and gas scrubbing would provide a good floor on Cl_2-GPAO's costs in the envisioned configuration, sufficient to rule out its use in certain scenarios, and that this would be a useful contribution to discourse on dilute CH_4 mitigation. As is always the case, more detailed and accurate cost models can and should be built in the future.

5.3.1 Assumed Reagent, Electricity, and LED Prices

There are a number of different plausible scenarios for reagent supply with widely varying prices, summarized in Figure 5.2**(a)**. The main required reagent is Cl_2 for the photoreactor, but sodium hydroxide (NaOH) is also required for the acid gas scrubber. Because NaOH must always be replaced in stoichiometric proportion to the number of Cl atoms scrubbed (whether as Cl_2 or HCl), and because some Cl_2 supply strategies co-produce NaOH for free and some do not, it makes sense to consider NaOH prices in this section as well.

The cheapest way to obtain Cl_2 is to buy it directly at its point of production, which is usually an industrial-scale chlor-alkali plant. We obtained low and high Cl_2 prices from a document published by the European trade association for chlor-alkali plant operators.[125] Chlor-alkali plants co-produce NaOH along with Cl_2 in stoichiometric proportion, so no additional NaOH price must be considered.

Although few if any CH_4 point sources are colocated with chlor-alkali plants, Cl_2 can also be transported in liquefied form to its point of use. Bulk liquefied Cl_2 is routinely sold for use in wastewater treatment[241] and we include low and high prices for Cl_2 prices taken from wastewater plants in California.[242] In this case, NaOH must also be delivered. NaOH prices of around $300 per ton are typical,

which accounting for the scrubbing reaction stoichiometry equals an additional $340 of NaOH required per ton of Cl_2 used.

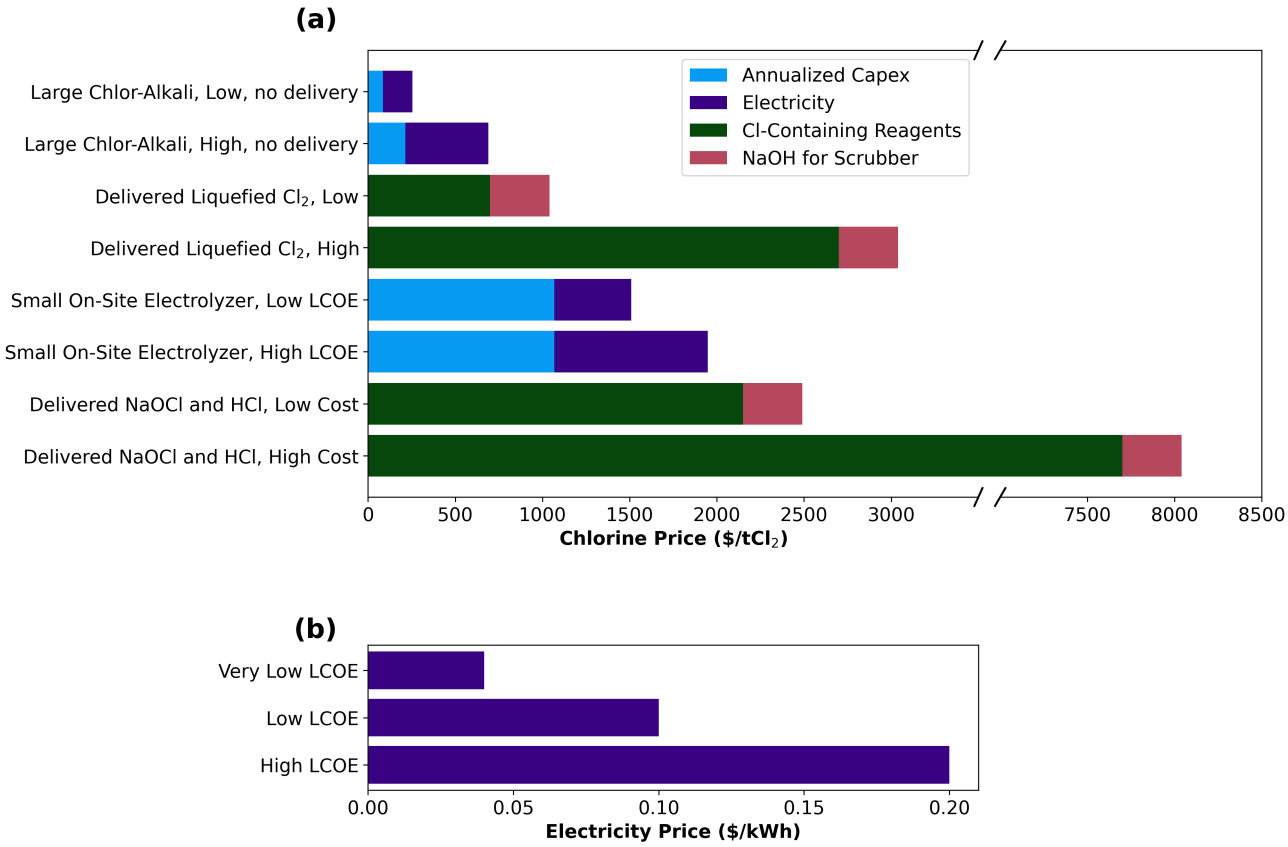

Figure 5.2: Costs of chlorine and electricity in different scenarios. NaOH is included here because it must be supplied to the scrubber in equal proportion to the system's Cl_2 consumption and because only some Cl_2 supply strategies require the separate delivery of NaOH.

An alternative that avoids the transport of toxic chemicals is to electrochemically generate Cl_2 on-site. Self-contained electrolyzers that produce Cl_2 from salt water are commercially available for use in large saltwater swimming pools, which (unlike wastewater plants) typically do not require enough chlorine to justify liquefied Cl_2 infrastructure. They also co-produce NaOH, avoiding the need for NaOH delivery. Swimming pool Cl_2 generators have been used for existing Cl_2-GPAO field trials.[70] We compared several online vendors' offerings and found a representative capital

cost to be \$26000 for a system generating 10 kg of Cl_2 per day (3.65 tons of Cl_2 per year).[243, 244] It appears that costs scale linearly with daily Cl_2 capacity; i.e., there are not substantial cost efficiencies larger pool electrolyzers. At a 1:1 Cl_2-CH_4 feed ratio, the 10 kg per day unit would supply enough Cl_2 to mitigate 2.3 kg of CH_4 per day, equal to about 10 cows' CH_4 production. Applying a capital recovery factor of 0.15 gives a levelized capital cost of \$1070/tCl_2. These devices use about 4.4kWh/kgCl_2, which we use to calculate their electricity costs.[245]

Finally, Cl_2 could be generated on-site by the reaction of industrial bleach (sodium hypochlorite; NaOCl) with hydrochloric acid (HCl) as follows:

$$NaOCl + 2HCl \rightarrow Cl_2 + H_2O + NaCl \tag{5.7}$$

These aqueous reagents are somewhat easier to transport than liquefied Cl_2, although they are still hazardous.[241] Drums of 12.5% NaOCl cost between \$1 and \$4 per gallon, with each gallon containing 0.57 kg of NaOCl, which according to the reaction above generates 0.54 kg of Cl_2.[242] This gives an NaOCl cost range of \$1850-\$7400/tCl_2. Additionally, 33% HCl costs about \$100 per ton.[246] Thus, one ton of HCl costs \$300 and helps produce 1.0 ton of Cl_2. The HCl cost is therefore an additional \$300/tCl_2. NaOH for scrubbing must also be delivered, contributing another \$340/tCl_2. This gives a total range of \$2490-\$8040/tCl_2.

According to these estimates, liquefied Cl_2 delivery is the lowest-cost option for sites that are not colocated with a chlor-alkali plant. On-site electrolysis is moderately cost-effective and might prove more practical given the challenges of Cl_2 delivery. On-site Cl_2 generation from NaOCl and HCl appears not to be cost-effective. For simplicity in later models, we distill these various Cl_2 (and, in some cases, NaOH) prices into a "Low Reagent Price" of \$1000/tCl_2 a "High Reagent Price" of \$2000/tCl_2. Each price includes all reagents (whether Cl_2, NaOH, NaOCl, or HCl) associated with adding 1 ton of Cl_2 at the reactor inlet. Reagent costs in the \$250-\$500/tCl_2 range are only possible on-site at large chlor-alkali plants and so are only considered for one scenario related to atmospheric CH_4 removal.

Electricity prices (levelized costs of electricity, or LCOE; \$/kWh) can also vary widely. A deployed Cl_2-GPAO unit would most likely pay an industrial electricity tariff. In the point-source CH_4 control scenarios, we consider two LCOEs, also shown

in Figure 5.2**(b)**. The "Low LCOE" assumes an electricity price of \$0.10/kWh, a typical industrial rate for the American midwest. The "High LCOE" assumes an electricity price of \$0.20/kWh, a typical industrial rate for California or Europe.[247, 248] For only the low-range chlor-alkali Cl_2 price (the uppermost bar in 5.2**(a)**), we modeled a "Very Low LCOE" of \$0.04c/kWh, since such plants sometimes have direct access to large-scale hydropower or other renewables.[125]

We model ultraviolet LED costs in the same manner as Chapter 3. Dividing a state-of-the-art UV LED's purchase price (\$5 [204]) by the product of it power consumption (1.6 kW [204]) and their lifetime (50000 hours [205]) gives a levelized LED hardware cost of \$0.074/kWh. Thus, lighting hardware contributes 27-43% of the cost of the "lighting subsystem," with the remainder consisting of purchased electricity.

5.3.2 Relating Efficiencies to Cl_2 and Lighting Costs

The next task is to calculate the costs of reagent supply and lighting on a per-ton-CH_4 basis. To do so, we must use $\eta_{\text{reflectors}}$, $\eta_{\bullet\text{Cl}}$ and η_{Cl2} to calculate the amount of CH_4 oxidized per unit of added Cl_2 or input electricity.

Calculating the lighting cost begins with the following expression for the mass of CH_4 oxidized (T_{CH4}; metric tons CH_4) as a function of the amount of energy added in the form of UV photons (E_{light}; kJ). "γ" refers to UV photons and "#" refers to the number of a given species in moles.

$$T_{\text{CH4}} = E_{light} \cdot \eta_{reflectors} \cdot (\#\gamma/kJ) \cdot (\#\text{Cl}\bullet/\#\gamma) \cdot (\text{CH}_4/\#\text{CH}_4) \cdot \eta_{\text{Cl}\bullet} \tag{5.8}$$

We assume a reflector efficiency ($\eta_{reflectors}$) of 90%.[193] Since 1 mole of 365 nm photons contains ~340 kJ of energy, ($\#\gamma$ / kJ) = (1 mole photons / 340 kJ).[193] We assume that the quantum yield of Cl_2 photolysis is 1, meaning that (#Cl• / #γ) = (2 moles Cl• / mole photons). Additionally, (tCH_4 / #CH_4) = (1 tCH_4 / 62340 moles CH_4). $\eta_{\text{Cl}\bullet}$ is the number of CH_4 molecules oxidized per chlorine radical consumed, as defined previously. The above expression simplifies to:

$$T_{\mathrm{CH4}} = E_{light} \cdot (8.49 \cdot 10^{-8} \mathrm{CH_4}/kJ) \cdot \eta_{\mathrm{Cl}\bullet} \tag{5.9}$$

To express the amount of CH_4 oxidized in terms of the electrical energy used ($E_{electrical}$; kWh), we account for the efficiency of the LED (η_{LED}), which we assume to be 60%.[193] We also convert from kJ to kWh.

$$T_{\mathrm{CH4}} = E_{electrical} \cdot \eta_{LED} \cdot (3600 kJ/kWh) \cdot (8.49 \cdot 10^{-8} \mathrm{tCH_4}/kWh) \cdot \eta_{\mathrm{Cl}\bullet} \tag{5.10}$$

$$T_{\mathrm{CH4}} = E_{electrical} \cdot (1.83 \cdot 10^{-4} \mathrm{tCH_4}/kWh) \cdot \eta_{\mathrm{Cl}\bullet} \tag{5.11}$$

$$E_{electrical} = T_{\mathrm{CH4}} \cdot (\eta_{\mathrm{Cl}\bullet})^{-1} \cdot (5450 kWh/\mathrm{tCH_4}) \tag{5.12}$$

Lighting costs ($C_{lighting}$; \$) are the sum of the assumed electricity price ($LCOE$; \$/kWh) and the LED hardware cost (\$0.074/kWh). Therefore:

$$C_{lighting} = T_{\mathrm{CH4}} \cdot (\eta_{\mathrm{Cl}\bullet})^{-1} \cdot (5450 kWh/\mathrm{tCH_4}) \cdot (\$0.074/kWh + LCOE) \tag{5.13}$$

We then turn to computing the reagent cost ($C_{\mathrm{reactents}}$; \$/$\mathrm{tCH_4}$).

η_{Cl2} is defined as the mole ratio of CH_4 converted to Cl_2 added at the reactor inlet. The following equation expresses what mass of Cl_2 must be added to the reactor in order to oxidize a certain massof methane:

$$T_{\mathrm{Cl2}} = T_{\mathrm{CH4}} \cdot (\eta_{\mathrm{Cl2}})^{-1} \cdot (1\ \mathrm{tCl_2}\ /14100\ \mathrm{moles\ Cl_2}) \cdot (62340\ \mathrm{moles\ CH_4/tCH_4}) \tag{5.14}$$

Where T_{Cl2} is the mass of chlorine added to the reactor in metric tons, P_{reagents} (\$/$\mathrm{tCl_2}$) is the assumed cost of all reagents (e.g, Cl_2 and NaOH) per ton of Cl_2 introduced into the reactor, and η_{Cl2} is the mole ratio of CH_4 converted to Cl_2 added at the reactor inlet.

$$C_{\text{reagents}} = T_{\text{Cl2}} \cdot P_{\text{reagents}} \tag{5.15}$$

$$C_{\text{reagents}} = T_{\text{CH4}} \cdot (\eta_{\text{Cl2}})^{-1} \cdot P_{\text{reagents}} \cdot (4.42\ \text{tCl}_2/\text{tCH}_4) \tag{5.16}$$

Wherever reagent or lighting costs are reported, Equations 5.13 and 5.16 are evaluated for a unit mass of CH_4 (T_{CH4}=1 tCH_4).

5.3.3 Modeling Cl_2 and HCl Scrubbing Costs

We modeled the cost of the HCl and Cl_2 scrubber using an existing cost model produced by the U.S. Environmental Protection Agency (EPA). The model is called the "Air Pollution Control Spreadsheet for Wet and Dry Scrubbers for Acid Gas Control".[249] It exists to facilitate a fair and uniform process for determining whether polluters must install acid gas scrubbers on their industrial facilities. The model allows the user to tune numerous parameters to produce cost estimates that are accurate for their use case. Its output is a scrubbing cost per unit volume of air processed. The "wet scrubber" sub-model within the spreadsheet is intended for use with HCl and Cl_2. The model does not discriminate between HCl and Cl_2; it only considers the total inlet and outlet concentratrions of both gases.

All inputs in the wet scrubber model were left at their default values except for the inlet Cl_2+HCl concentration, outlet Cl_2+HCl concentration, electricity price, and sodium hydroxide (NaOH) price. The inlet Cl_2+HCl concentration varied with the different scenarios that we modeled. Based on our experiments, we assumed that 75% of the Cl_2 entering the photoreactor eventually became 2HCl and 25% remained as Cl_2. For instance, in the case with 100 ppm inlet Cl_2, we modeled a scrubber-inlet Cl_2+HCl concentration of 175 ppm. The outlet concentration of Cl_2+HCl is fixed at 12 ppm based the relevant EPA emissions limit.[250] We note that the scrubber cost is not very sensitive to the outlet concentration; for example, specifying an outlet concentration of 1 ppm does not substantially raise the cost per tCl_2 scrubbed. The electricity price varied by scenario as described above. Finally, since the NaOH consumed by the scrubber is included in the reagent costs as described above, the NaOH price in the EPA model is set to zero.

We used the Pycel package to allow us to access the spreadsheet's functionality using Python code.[251] Finally, we added logic downstream of the model to compute the cost per m^3 of air processes into a cost per ton of Cl_2/HCl scrubbed and a cost per tCH_4 mitigated (for a given η_{Cl2}).

5.4 Total Cl_2-GPAO Costs in Different Scenarios

The outputs of the Cl_2-GPAO cost model for a number of different scenarios are shown in Figure 5.3. We consider five different CH_4 point sources: three ideal (contaminant-free) CH_4 streams of different CH_4 concentrations and realistic (contaminanted) streams from a dairy barn and a wastewater treatment plant. The ideal streams contain 50, 100, and 300 ppm CH_4; the dairy barn stream has 50 ppm CH_4; and the wastewater treatment plant stream has 300 ppm CH_4. For each CH_4 source, we consider scenarios with low and high reagent and electricity prices. Finally, we consider open-air Cl_2 release for atmospheric CH_4 removal, as discussed in Chapter 1, Section 1.2.4. This system involves no lighting or scrubber, so we only consider scenarios with very low, low, and high Cl_2 prices.

The different components of the modeled costs are calculated as described in the previous sections. In all cases, we modeled a 1:1 Cl_2-CH_4 feed ratio, since that was what we used throughout our experiments. We use our own measured values of η_{Cl2} and $\eta_{\bullet Cl}$ from Chapter 4. The values for the barn and wastewater treatment plant are from the application-based trials. The values for the ideal cases are from the contaminant-free experiments that varied Cl_2 and CH_4 in a 1:1 ratio. To make the scenarios more consistent, for the 50 ppm ideal scenario we used η_{Cl2} and $\eta_{\bullet Cl}$ values from the experiment with 45 ppm CH_4, and for the 100 ppm and 300 ppm ideal scenarios we used the values from the 90 ppm experiment (our highest-concentration contaminant-free experiment). We judged using efficiencies measured at different CH_4 concentrations to be a valid approximation because, for a fixed 1:1 inlet Cl_2-CH_4 ratio, we observed those efficiencies to be largely independent of inlet CH_4 concentrations.

Our assumed values of $\eta_{reflectors}$ and Δ_{Cl2} are informed by the reactor size model described above. For the scenarios with 50 ppm inlet Cl_2, we model $\Delta_{Cl2} = 75\%$ and $\eta_{\text{reflectors}} = 50\%$. For the scenarios with 100 ppm inlet Cl_2, we model $\Delta_{Cl2} = 75\%$ and

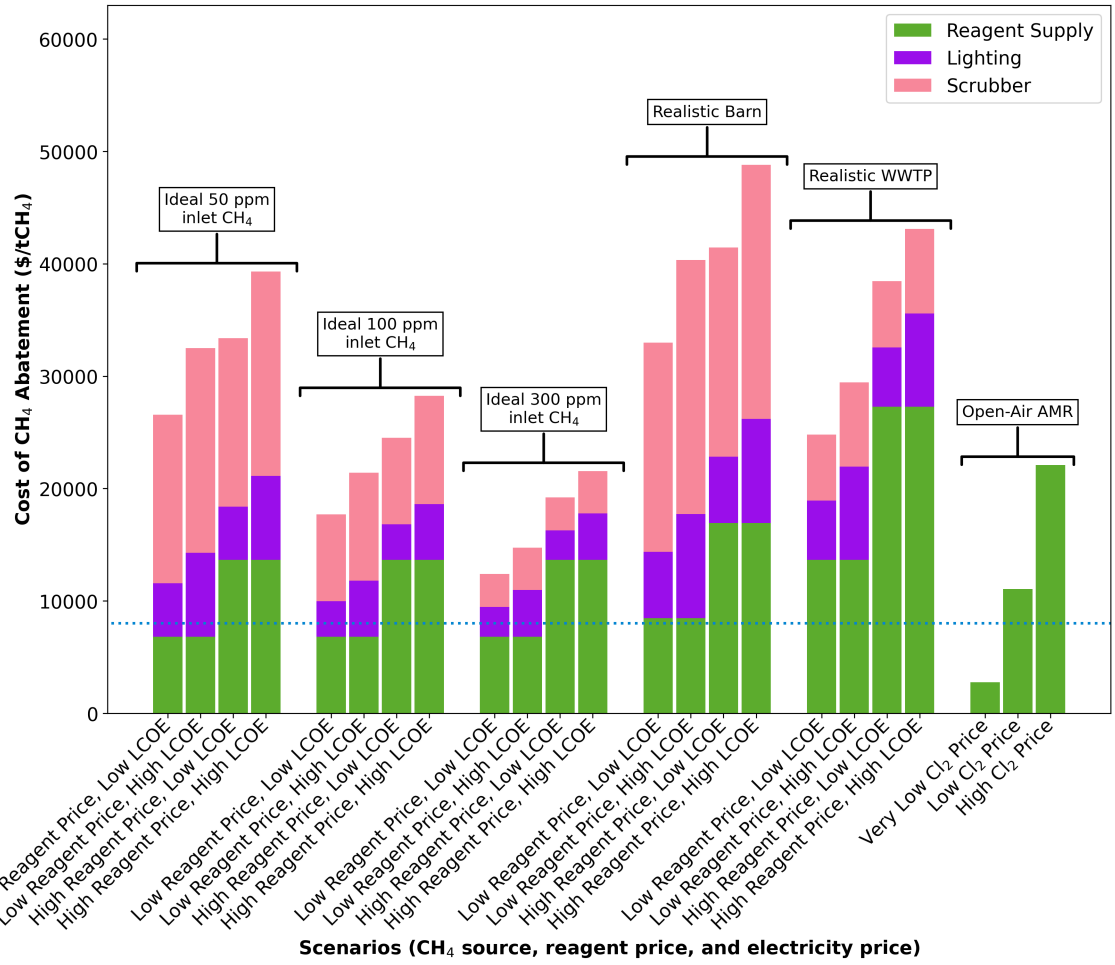

Figure 5.3: Chlorine-based CH_4 oxidation costs in different scenarios. Results are shown for ideal (contaminant-free) CH_4 streams at 50, 100, and 300 ppm and for realistic (contaminated) CH_4 streams from a barn at 50 ppm and a wastewater treatment plant (WWTP) at 300 ppm. For each source, we consider scenarios with low and high reagent and electricity prices, as discussed above. We also consider atmospheric CH_4 removal (AMR) via open-air Cl_2 release, considering the same low and high reagent (Cl_2) costs as the other CH_4 sources as well as one scenario with an even lower Cl_2 price. A cost target of \$8000/tCH_4 is shown as a benchmark (dotted horizontal line).

$\eta_{\text{reflectors}} = 75\%$. For the scenarios with 300 ppm inlet Cl_2, we model $\Delta_{Cl2} = 75\%$ and $\eta_{\text{reflectors}} = 90\%$.

In all cases for point-source Cl_2 mitigation, the modeled Cl_2-GPAO costs exceed our \$8000/tCH_4 benchmark. Only the most optimistic scenario for an ideal 300-ppm CH_4 source comes relatively close (\$13000/tCH_4). All modeled costs greatly exceed the \$1000-\$3000/tCH_4 range that we feel would indicate a truly scalable process. The modeled values for the ideal 50-ppm source (\$27000/tCH_4-%39000/tCH_4) and the realistic barn (\$35000/tCH_4-\$50000/tCH_4) are generally consistent with the single published cost estimate of \$40000/tCH_4 (\$500/tCO_2e) for a scaled-up Cl_2-GPAO process.[70]

In all cases, the reagent (mostly Cl_2) supply and the acid gas scrubber are the largest contributors to the cost. The reagent and lighting costs depend weakly on the source CH_4 concentration but are higher in the realistic scenarios. This behavior occurs because the experimentally-measured Cl_2 efficiencies do not depend strongly on the source CH_4 concentration but decrease when contaminants are present. In contrast, the scrubber cost rises at lower inlet CH_4 concentrations. This is because scrubbers have an approximately constant cost per volume of air throughput but the required air throughput per tCH_4 oxidized increases in inverse proportion to the source CH_4 concentration. Because contaminants also decrease the amount of CH_4 oxidized per unit air throughput, they increase the effective cost of the scrubber on a per-tCH_4 basis.

The "open-system" atmospheric Cl_2 release values at the far right of Figure 5.3 looks somewhat more promising, though we strongly emphasize the safety and social-license challenges of this approach. The best-case atmospheric Cl_2 release scenario had a modeled cost of only \$2700/tCl_2, by far the lowest of any scenario. This strategy's low costs arise for two reasons. First, the system uses sunlight for photolysis, avoiding the need for LEDs or electricity, and does not involve a Cl_2 scrubber, eliminating two major cost components. Second, since atmospheric CH_4 removal can be done anywhere, such a system could have access to cheap Cl_2 at its point of industrial-scale production. Thus, Cl_2 costs in the \$250/tCl_2-\$500/tCl_2 range are possible, since Cl_2 liquefaction or less-efficient on-site Cl_2 generators are not necessary. As discussed in Chapter 1, the net flux of acidic Cl_2 and HCl into the atmosphere would still need to be mitigated even if their concentrations are too low to be acutely hazardous; strategies to do so have not yet been developed.

The modeled Cl_2 release costs per tCH_4 are subject to substantial uncertainties. Measuring η_{Cl2} and $\eta_{\bullet Cl}$ at only 2 ppm CH_4 and Cl_2 is quite challenging and pushed the limits of our small flow reactor setup. For reasons that are unclear to us, the measured radical efficiencies at 2 ppm CH_4 were about half those measured at all higher CH_4 concentrations (5-90 ppm), an effect that could be explained by trace reducing contaminants in our gas supply. It is quite possible that the true efficiencies at 2 ppm CH_4 are higher than those we measured and modeled, which would cause our modeled costs to be too high. On the other hand, since a released plume of Cl_2 would simultaneously diffuse, react with CH_4, and participate in complex atmospheric chemistry processes, the measurements from a flow reactor containing a uniform 2 ppm CH_4 and Cl_2 may be inaccurate. While our results are tentatively promising, further modeling and experiments are therefore necessary.

5.5 Conclusion

This chapter's results cast some doubt on the large-scale commercial prospects of Cl_2-GPAO. Once the costs of gas scrubbing, lighting, and the supply of Cl_2 to remote field sites are accounted for, the modeled costs in all scenarios substantially exceed the range of CH_4 mitigation costs that we feel would be most transformative for global emissions. In particular, existing discourse on Cl_2-GPAO has somewhat neglected the costs of acid gas scrubbing on dilute gas streams, which rather negates the benefit of a Cl_2-GPAO photoreactor with a negligible pressure drop. Cl_2 supply at actual field sites is likely to be several times more expensive than posted Cl_2 "commodity prices" that exclude delivery, making it easy to underestimate the costs of Cl_2 supply or generation.

Even so, only the real-world scale-up efforts already under way can answer whether Cl_2-GPAO is viable at scale. Engineering improvements in the process may reveal our modeled costs to be overestimates. Sectors like dairy, at least in some markets, may have an appetite for Cl_2-GPAO's costs. It would be an excellent outcome for global CH_4 mitigation if our cost models were proven wrong. In any case, Cl_2-GPAO is far closer to cost-effective dilute CH_4 mitigation than is photocatalysis.

Finally, our model still allows for the possibility of cost-effective open-air Cl_2 release for atmospheric CH_4 removal, as discussed in Chapter 1, Section 1.2.4. Such an approach is appealing because it can be sited wherever energy and/or Cl_2 are cheapest, in involves no scrubbers or LEDs, and it does not require any site-specific engineering for particular CH_4 sources. However, many uncertainties remain regarding the effectiveness of the open-air $\bullet$Cl-CH_4 oxidation chemistry and regarding unintended environmental impacts.

Chapter 6

Experiments on Advanced Oxidation with Hydrogen Peroxide

6.1 Introduction

Hydrogen peroxide (H_2O_2) may also be able serve as a radical precursor in a gas-phase advanced oxidation process. We refer to such a process as H_2O_2-GPAO. Gaseous hydrogen peroxide photolyzes into two hydroxyl radicals (OH•) and can oxidize methane according to the following reactions:

$$H_2O_2 + hv_{254\ nm} \rightarrow 2OH\bullet \tag{6.1}$$

$$OH\bullet + CH_4 \rightarrow H_2O + CH_3\bullet \tag{6.2}$$

Further reactions that convert $\bullet CH_3$ to CO and CO_2 are not shown. Although the photolysis reaction can proceed with light wavelengths as large as 555 nm, the quantum yield for OH• is higher at lower wavelengths, and we chose to use 254 nm light.[123] Gaseous OH• is responsible for the vast majority of CH_4 oxidation that naturally occurs in the bulk atmosphere. Hydrogen peroxide vapor is also commonly used as a disinfectant in medical settings.[252]

The great appeal of H_2O_2-GPAO is that, unlike in Cl_2-GPAO, no scrubbing process would be needed downstream of the photoreactor. As we found in the previous chapter, downstream scrubbers are quite costly, so avoiding the need for one is qualitatively appealing. In Cl_2-GPAO, each C-H attack by Cl• produces HCl which must be removed downstream; the unused Cl_2 precursor must also be scrubbed. In H_2O_2-GPAO, each C-H bond attach by OH• would produce only H_2O. Unused H_2O_2 vapor is far milder than Cl_2 and would rapidly break down in sunlight or upon contact with surfaces to eventually produce H_2O.

As shown in the Sankey plot in Figure 4.1 in Chapter 4, preliminary estimates showed that H_2O_2-GPAO could plausibly be cost-effective. If H_2O_2 costs \$400/ton, each H_2O_2 produces 2 OH•, and each OH• oxidizes 0.15 CH_4 molecules, it would take \$2840 of H_2O_2 to oxidize one ton of CH_4. \$400/ton is representative of current global H_2O_2 prices using the incumbent carbon-intensive H_2O_2 process, which uses fossil-derived hydrogen (H_2) as a feedstock.[253, 254] However, cost modeling studies have found that H_2O_2 could be electrochemically synthesized at a similar cost.[219] The number 0.15 CH_4 per OH• is an average value over the entire atmosphere.[255]

A key question that we wished to explore was whether H_2O_2-mediated CH_4 oxidation in a flow reactor would exhibit a CH_4-oxidized-per-OH• value greater than or less than that observed in the bulk atmosphere.

At the outset of this chapter's research, we identified plausible reasons that this value might surpass or fall short of the open-air value of 0.15 CH_4 per OH•. On one hand, we reasoned that perhaps in the atmosphere background levels of CO and volatile organic compounds scavenge the few available OH•, competing with CH_4 for limited oxidizing capacity. In a flow reactor, any trace CO or organics might be rapidly depleted by the far higher density of OH•, leaving a regime in which CH_4 is the main available OH• scavenger. On the other hand, it was also plausible that the high density of OH• in a reactor would cause OH• to quench with itself or other radicals rather than react with CH_4. Given the complex reaction networks at play involving numerous reactive oxygen species, as well as our limited experience with atmospheric chemistry modeling, we felt that experiments would be the best way to resolve this uncertainty. We found the latter of these scenarios to prevail in reality.

6.2 Experimental Setup and Reactor Qualification

Our setup for H_2O_2-GPAO is shown in Figures 6.1 and 6.2. The setup was considerably simpler than that for Cl_2-GPAO, as it was intended to test a smaller range of conditions. The non-precursor gas supply system included mass flow controllers (MFCs) for only CH_4, dry N_2, and O_2. The precursor gas supply system was a single MFC controlling a flow of dry N_2 that was directed through a bubbler containing 50% aqueous H_2O_2 solution. The gas flowed through a quartz photoreactor lit by a low-pressure mercury lamp, an electrochemical H_2O_2 sensor, a Fourier-transform infrared (FTIR) spectrometer, and a cavity ringdown spectrometer. These components are described in detail below.

The H_2O_2 bubbler was necessary because, unlike Cl_2, H_2O_2 vapor is too unstable to be sold in gas tanks. The vapor pressure of 50% H_2O_2 solution at room temperature is about 50 Pa, corresponding to a gas-phase equilibrium concentration of (50 Pa ÷ 101325 Pa ≈ 500 ppm).[256] The bubbles never appeared to reach their equilibrium concentration, exiting the bubbler with an H_2O_2 concentration of about 60 ppm,

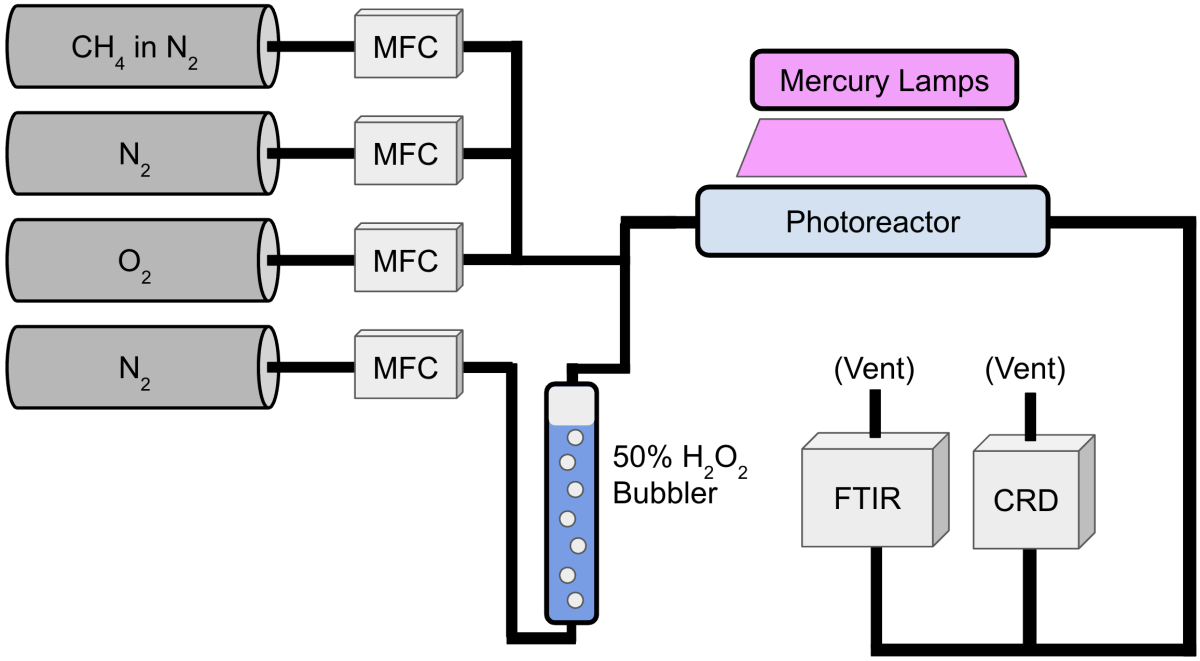

Figure 6.1: Schematic of the experimental setup for CH_4 oxidation with hydrogen peroxide.

evidenced by a measured H_2O_2 concentration of about 30 ppm after the stream from the bubbler was diluted by an equal proportion of dry air. Diluting the stream from the bubbler directly after the bubbler exit proved important to avoid issues with condensation.

Our experiments used a total flow rate of 600 mL/min. This value, substantially higher than the ∼200 mL/min used in the chlorine experiments, was necessary to minimize variations in H_2O_2 concentration throughout the system due to H_2O_2 sticking to internal walls. This flow rate resulted in a residence time of about 1.5 minutes, half that used in the Cl_2-GPAO experiments but, as we later verified, still long enough for plenty of light absorption and H_2O_2 photolysis to take place. We used a 10% O_2 concentration (using the maximum flow rate of our O_2 MFC) and a 30 ppm CH_4 concentration (the maximum measurable by our more sensitive spectrometer). 300 mL/min of the N_2 flow was directed through the bubbler to generate an H_2O_2 concentration of around 30 ppm. The balance gas was dry N_2. H_2O from the bubbler

resulted in a final relative humidity of about 40%.

The photoreactor itself was a quartz vessel lit from both sides by a pair of low-pressure mercury lamps. The vessel was a tube, 5 cm in diameter and 45 cm in length, with rounded ends capped with hose barbs to mate with silicone tubing. Its internal volume of approximately 900 mL gave us the residence time of 1.5 minutes with the flow rate of 600 mL/min. Each of the UVC lights was a "30W UV Sanitizer Light" manufactured by COOSPIDER UV with a nominal emissions peak of 254nm. As shown in Figure 6.2, two such lights were placed parallel to the reactor at a distance of around 5 cm, ensuring a strong dose of UVC light throughout the reaction volume. The lights were connected to the same power strip and were controlled in tandem via a serial-connected AC relay.

The gas analysis setup consisted of the same infrared spectrometers used in the previous chapters. The MKS MultiGas 2000 FTIR spectrometer could be run in one of two modes corresponding to different cavity temperature setpoints, one measuring only H_2O_2 and H_2O and one measuring CH_4, CO_2, CO, and H_2O. In most of our experiments, used it in H_2O_2-measuring mode and relied on the Picarro g2210-i cavity-ringdown spectrometer to measure CH_4, CO_2, and H_2O.

We also experimented with an electrochemical H_2O_2 sensor, which was a Membrapor H_2O_2/MB-100 with a flow-sampling cap attached to a Membrapor analog transmitter board, which generated a 4-20mV signal read by a LabJack U6 data acquisition device. However, as is discussed in the next section, we found the FTIR spectrometer to be a better tool for measuring H_2O_2 concentrations and therefore omitted the electrochemical H_2O_2 sensor from the final setup.

6.2.1 Lessons Learned in Apparatus Design

As in our early experience with Cl_2, getting a steady stream of H_2O_2 into our reactor proved to be less trivial than we expected. The initial symptom was a lack of a signal at the electrochemical H_2O_2 sensor even when placed directly downstream of the bubbler. We initially tried heating the bubbler (to boost the vapor pressure of H_2O_2), using fresher hydrogen peroxide (in case it had degraded in storage), and replacing the electrochemical sensor, none of which fixed the issue. We then replaced all the vinyl tubing in our system with silicone tubing based on a previous paper's

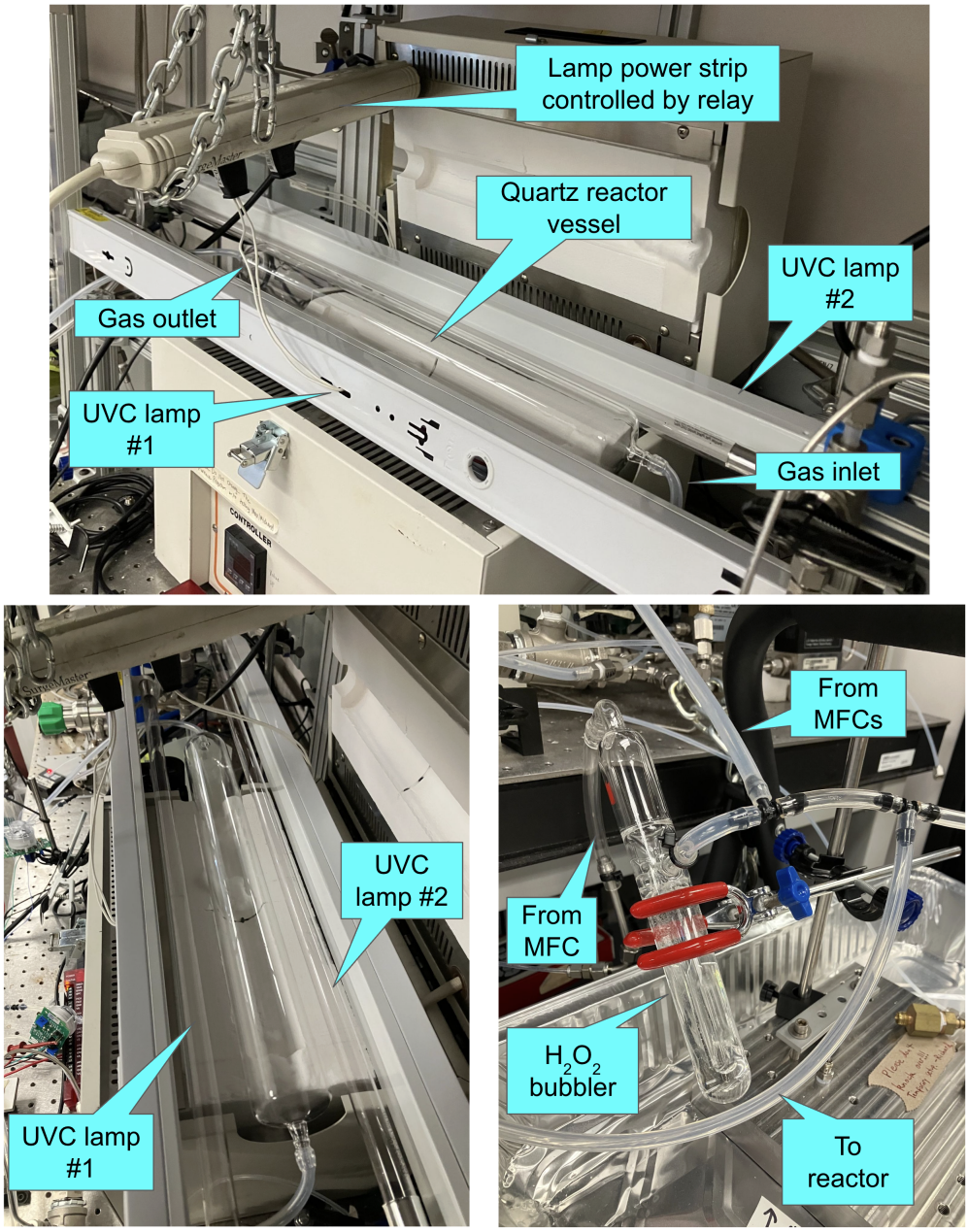

Figure 6.2: Images of the final reactor and bubbler setup for CH_4 oxidation with hydrogen peroxide. The top and bottom-left images show different angles of the same components. The UV shielding has been removed for visibility. The two UVC mercury lamps are controlled by the same relay and always operate in tandem. The infrared spectrometers are not shown.

suggestion, which helped somewhat.[257] After isolating different sections of tubing, we also found that metal fittings were condensing or reacting H_2O_2, as they did with Cl_2. We herefore removed all metal from the system upstream of the infrared spectrometer (whose inlet contained unremovable metal fittings). Finally, since higher flow rates mitigate wall effects' contribution to downstream gas concentrations, we used the 600 mL/min flow rate mentioned above.

Though we initially planned to use the electrochemical H_2O_2 sensor as our main H_2O_2 measurement, we ultimately found infrared measurement of H_2O_2 to be easier and more reliable. The electrochemical sensor required regular calibration with SO_2, since H_2O_2 calibration tanks are unavailable and the bubbler effluent's H_2O_2 concentration is not predictable enough to use as a calibration standard. Its measurements were also sensitive to pressure, with pressure drops throughout the system elevated by the high flow rate. The electrochemical sensors' transmitter boards also sometimes experienced a "saturated" state in which the measured voltage got stuck at a high reading and failed to note drops in the H_2O_2 concentration for 10 minutes or more.

As a result, the electrochemical sensor was sometimes useful for measuring percent changes in H_2O_2 concentrations, but we generally found the FTIR spectrometer to be better at reliably measuring both absolute H_2O_2 concentrations and percent H_2O_2 conversions. Additionally, the electrochemical sensor's manufacturer advised us not to run the FTIR H_2O_2 method downstream of the electrochemical sensor because the sensor consumes some amount of H_2O_2, which would have caused the FTIR's reading to be inaccurate. As a result, for our final exeriments we exclusively relied on the FTIR spectrometer for H_2O_2 measurement.

With all of these improvements and, we were able to observe stable tens-of-ppm H_2O_2 concentrations throughout the system downstream of the bubbler, with agreement between the infrared and electrochemical H_2O_2 measurements.

6.3 Initial Attempts at H_2O_2-GPAO

Our experiments on H_2O_2-GPAO spanned several months and went through many iterations. Throughout this period, the high-level apparatus design remained the same: a bank of flow controllers, including one connected to an H_2O_2 bubbler; a

reaction vessel lit by an ultraviolet light; and sensors measuring CH_4, H_2O_2, and other effluent gases. Also, the general type of experiment remained the same: cycling the UV light and hoping to observe H_2O_2 and CH_4 conversion. However, at no point in the campaign did we observe any CH_4 oxidation.

With each successive negative result, we continued to modify the setup in order to eliminate possible engineering failure modes and isolate the failure to the underlying H_2O_2-GPAO chemistry. The results of our final experiments in our best reactor iteration, in which H_2O_2 underwent photolysis but no CH_4 was oxidized, are presented in the next subsection. This subsection briefly narrates the work that led to that reactor setup and those results.

Our investigation of H_2O_2-GPAO began with an illusory observation of CH_4 oxidation that proved upon examination to be an artifact of our flow controller setup. In these experiments, the CH_4 concentration appeared to drop when H_2O_2 was added under continuous illimination. However, upon closer examination we discovered that one of our flow controllers was slightly miscalibrated. The miscalibration caused the CH_4 stream to be diluted by about 10% when we switched from dry nitrogen to nirogen passing through the H_2O_2 bubbler. This dilution created the appearance of CH_4 oxidation (*i.e.,* a dip in the CH_4 concentration time series). Recognizing this issue, in all subsequent tests, we kept the setpoints of all flow controllers constant and only used light on/off cycles to check for CH_4 oxidation.

After resolving the above issue, we then observed no CH_4 oxidation upon light cycling in the nominal presence of H_2O_2 (*i.e.,* with half of the total gas flow passing through the H_2O_2 bubbler). We then focused on ensuring that H_2O_2 was actually reaching the reactor and transiting the system without sticking or condensing anyplace. This effort resulted in the lessons above about using silicone tubing, avoiding metal fittings, ensuring high flow rates, and allowing long stabilization times for the H_2O_2 signal. We also began using the infrared spectrometer to complement and eventually replace the electrochemical H_2O_2 sensor. These adjustments made us confident that we could reliably achieve the desired tens of ppm of H_2O_2 in the reactor.

However, after those adjustments, CH_4 oxidation remained elusive. We also observed no H_2O_2 conversion under illumination (*i.e.,* no drop in the H_2O_2 signal on either the electrochemical sensor or infrared spectrometer). This led us to suspect

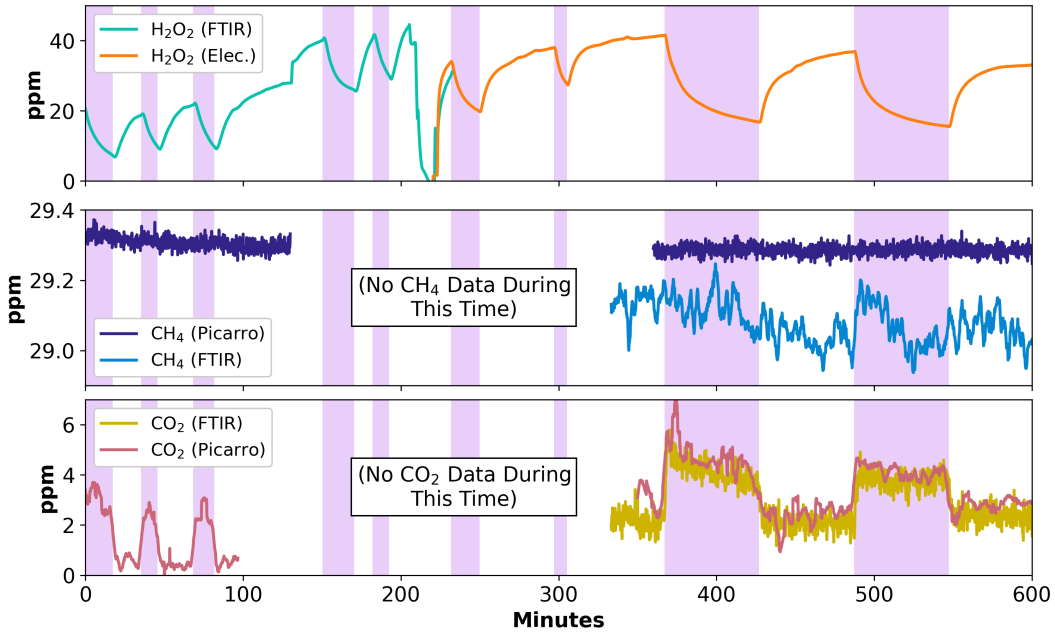

Figure 6.3: Early experimental results for CH_4 oxidation with hydrogen peroxide. This experiment was conducted with a different reaction vessel than our final setup and is included mainly for narrative purposes. Refer to the later Figure 6.4 for this chapter's main results. In this plot, the violet-shaded regions denote times when the UVC light was on. The left-hand side of the plot used the FTIR with a cavity temperature of 50°C to measure H_2O_2. The right-hand side of the plot used the FTIR with a cavity temperature of 191°C to measure CH_4 and CO_2 and the electrochemical sensor ("Elec." in the legend) to measure H_2O_2. Between minutes 100 and 340, we were varying the gas flows and/or ramping the FTIR cavity temperature such that the CH_4 and CO_2 concentration measurements were either unavailable or not useful.

that our reaction tube vessel was not as UVC transparent as we had believed. We then tried a number of vessels that we had in our lab. Although commercially-available quartz tubes were a clear option, mating them to the rest of the system without metal components proved challenging. Also, their small diameters necessitated very short residence times, while we wished to maximize the residence time in order to boost any H_2O_2 or CH_4 conversion to measurable levels.

We eventually obtained a quartz vessel with hose-barb fittings that resolved these issues. Because the lab from which we borrowed it had used it in UVC-driven wastewater treatment experiments, we knew it was UVC transpoarent. In this vessel, we

finally observed H_2O_2 conversion under UVC illumination, though still no CH_4 was oxidized. A time series from this experiment is shown in Figure 6.3. In this experiment, we verified H_2O_2 conversion under illumination with both the FTIR spectrometer and the electrochemical sensor before later switching to exclusive use of the FTIR spectrometer for that purpose. Neither the FTIR or cavity-ringdown spectrometer showed any CH_4 conversion.

Finally, we considered the possibility that this vessel (although it appeared completely clean and clear) had residual organics on its interior that were scavenging photogenerated OH• and preventing its reaction with CH_4. The vessel also had an irregular shape consisting of a cylindrical shell surrounding an empty cavity. We worried that its large internal surface area might exacerbate wall-related radical quenching. To eliminate these possible failure modes, we ordered a custom-made quartz reaction vessel consisting of a single hollow tube with hose barbs on the ends, a geometry similar to that of the vessel used in our Cl_2-GPAO experiments. This completed our "final" reactor setup that was pictured in Figure 6.2.

6.4 No CH_4 Oxidation in Our Final Reactor Setup

With the setup built and validated to the best of our abilities as shown in Figure 6.2, we conducted a final series of H_2O_2-GPAO experiments. While we observed a fairly stable baseline reactor-outlet H_2O_2 concentration and reliable H_2O_2 conversion under UVC light, in no case did we observe statistically signficant CH_4 conversion.

Time series from one such experiment are shown in Figure 6.4. The experiment included four UVC light on-off cycles with a gas mixture containing 30 ppm CH_4, 25-30 ppm H_2O_2, and about 40% relative humidity. During each light-on period, we observed a $\sim$30% drop in the H_2O_2 signal, indicating successful UVC-light-induced H_2O_2 photolysis.

During the light-on periods, neither spectrometer observed any CH_4 oxidation. In particular, the cavity ringdown spectrometer is extremely sensitive and in the photocatalysis experiments was able to observe $<$0.05 ppm CH_4 conversion, which for 30 ppm inlet CH_4 would be an 0.15% conversion. However, no CH_4 conversion whatsoever was seen, despite careful analysis of the spectrometer's signal. From

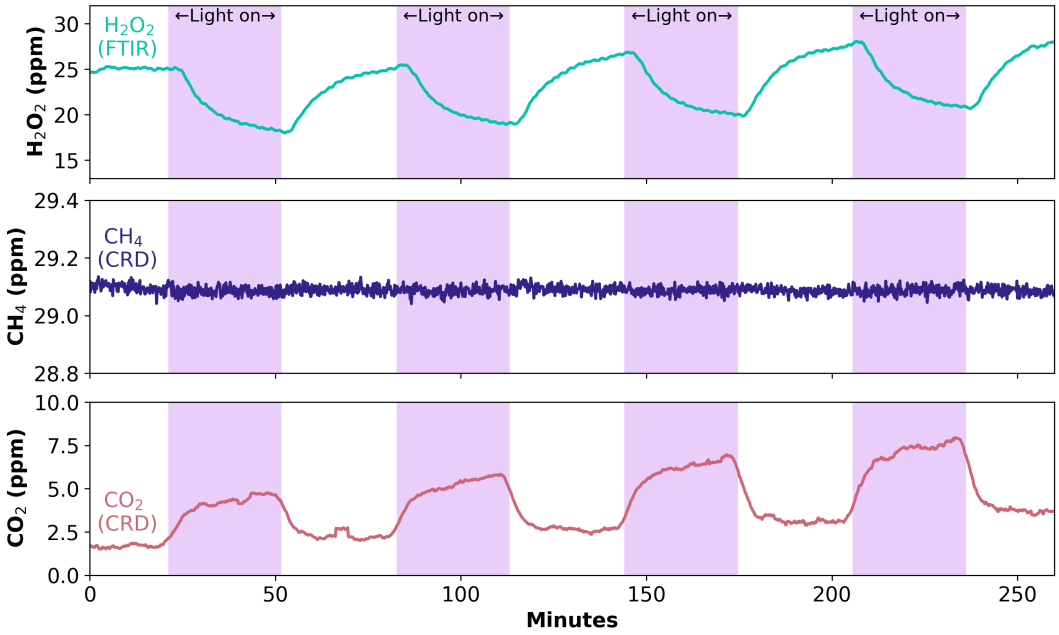

Figure 6.4: Final experimental results for CH_4 oxidation with hydrogen peroxide. In this experiment, the outlet H_2O_2 concentration was measured with the MKS Instruments FTIR spectrometer while CH_4 and CO_2 concentrations were measured with the Picarro cavity ringdown (CRD) spectrometer. Shaded regions indicate times when the UV light was turned on, during which the H_2O_2 signals decreased but the CH_4 signals did not, even upon very close examination of the CH_4 signal. The CO_2 signal reflects physisorbed CO_2 offgassing from the reactor under UVC light, as occurred in each of our reactors, rather than the oxidation of CH_4 or any other organic compounds.

these results, we conclude that the underlying H_2O_2-GPAO chemistry is not effective at oxidizing dilute CH_4, at least not in the configuration that we originally envisioned (tens of ppm CH_4; roughly equimolar H_2O_2 and CH_4). Some possible reasons for this ineffectiveness are outlined in the next section.

A few ppm of CO_2 were released from the reactor when the UVC light turned on, which we attribute to UV light driving adsorbed CO_2 off internal surfaces. Similar small CO_2 signals were observed in the photocatalysis and Cl_2 experiments.

6.5 A Kinetic Basis for H_2O_2's Poor Performance

Prior literature on OH•'s various reactions helps to explain why H_2O_2-GPAO fails to oxidize CH_4 where Cl_2-GPAO succeeds. In particular, it is useful to compare the rates of the desired radical reactions (OH• + CH_4; Cl• + CH_4) with those of the undesired radical-quenching reactions. These rates are well-known and are tabulated in databases for purposes of atmospheric chemistry modeling.[258, 259] Given the complexity of processes involving OH•, whose presence gives rise to a number of reactive oxygen species (ROS), these kinetic considerations were not grounds to *a priori* discount H2O_2-GPAO; in other words, the process was still well worth tresting experimentally. However, in their light, our results are not entirely surprising.

One factor, as mentioned in Chapter 4, is that OH• has a much lower rate constant than Cl• with respect to CH_4. The rate constant of the Cl•-CH_4 reaction at standard conditions is about $1 \cdot 10^{-13}$cm^3/molecule $\cdot$ s, while that of the OH•-CH_4 reaction is about $6 \cdot 10^{-15}$cm^3/molecule$\cdot$s, slower by a factor of $\sim$17.[258] If there were few other sinks for photogenerated OH•, this might not be a problem, since OH• would simply persist longer and eventually react with CH_4. However, in reality, other OH• sinks do exist.

Another factor is the far faster self-recombination of OH• compared to Cl•. The rate constant of the Cl•-Cl• recombination reaction at standard conditions is about $5 \cdot 10^{-13}$cm^3/molecule $\cdot$ s, while that of the OH•-OH• reaction is about $6 \cdot 10^{-11}$cm^3/molecule $\cdot$ s.[259] Thus, the rate constant of OH• recombination is $\sim$40 times higher than that of Cl•.

Additionally, unlike in the Cl_2 system where essentially all Cl• either attacks a C-H bond or recombines to Cl_2, H can be quenched in ways other than recombination to H_2O_2. In particular, OH• and H_2O_2 can react to form HO_2• according to the following reaction:

$$OH\bullet + H_2O_2 \rightarrow H_2O + HO_2\bullet \tag{6.3}$$

This reaction has a rate constant of $2 \cdot 10^{-12}$cm^3/molecule$\cdot$s, 2 orders of magnitude greater than that of the OH•-CH_4 reaction.[258] With comparable levels of CH_4 and H_2O_2 present (tens of ppm of each), HO_2 production would proceed more rapidly than

CH_4 oxidation. $HO_2\bullet$ can then react with $OH\bullet$ according to the following reaction, ending the radical chain:

$$OH\bullet + HO_2\bullet \rightarrow H_2O + O_2 \tag{6.4}$$

The presence of the two reactions above explains why radical precursor conversion (*i.e.,* H_2O_2 conversion) is observed even when no C-H bond activation (*i.e.,* CH_4 oxidation) takes place (Fig. 6.4). This stands in contrast to Cl_2-GPAO, in which $Cl\bullet$ recombination is the main radical-quenching pathway, so Cl_2 conversion is observed if and only if $Cl\bullet$ scavenges H from reducing molecules like CH_4.

These phenomena can explain why $OH\bullet$ oxidizes CH_4 in the open atmosphere but, unlike $Cl\bullet$, fails to do so in a flow reactor. In open air with 2 ppm CH_4, about 15% of $OH\bullet$ end up reacting with CH_4.[218] However, in our flow reactor experiment, the CH_4 concentration is only 15 times higher than in the atmosphere, while the rate of $OH\bullet$ generation and the concentration of hydrogen peroxide are each many orders of magnitude higher. For the latter case, the reactor uses $\sim$30 ppm of hydrogen peroxide, while the steady-state concentration in the upper troposphere is on the order of 1 ppb.[260] Thus from atmosphere to reactor, the rate of the $OH\bullet$-$OH\bullet$ and $OH\bullet$-H_2O_2 reactions increases much more than the rate of the $OH\bullet$-CH_4 reaction. Consequently, in the reactor a very small fraction of $OH\bullet$ ends up reacting with CH_4. In the case of Cl_2-GPAO, radical recombination still competes with C-H bond attack for the available budget of $Cl\bullet$. However, evidently $Cl\bullet$ recombination is slow enough that $Cl\bullet$ mostly attachs C-H bonds rather than recombining, even at the relatively high steady-state $Cl\bullet$ concentrations needed for flow reactors with few-minute residence times.

6.6 Conclusion and Future Possibilities

In this campaign of work, we attempted to iterate our system to give H_2O_2-GPAO the best possible chance of working. However, we consistently failed to observe CH_4 oxidation despite observing H_2O_2 photolysis under UVC light. Our final negative result appears to reflect key challenges with the underlying gas-phase chemistry rather

than issues with our particular implementation of the reactor system. In short, undesired radical-quenching reactions appear to scavenge all OH• before it has a chance to attack CH_4.

At the time of writing, we do not see a clear next step to take towards a practical H_2O_2-GPAO flow reactor of the type we originally envisioned (*i.e.,* using ppm-level H_2O_2 to mitigate ppm-level CH_4). Since no CH_4 conversion whatsoever was observed—not even a fraction of a percent—it is unlikely that simply extending the residence time or slightly adjusting other system parameters would achieve a substantial fraction of CH_4 conversion. Even if boosting the light flux, extending the residence time, increasing the inlet H_2O_2 concentration, or applying even more sensitive instruments did result in some detected CH_4 oxidation, the photon-to-oxidized-CH_4 efficiency would likely be quite low. While it is possible that a vast excess of OH• would oxidize a useful fraction of CH_4, H_2O_2-GPAO would only be of interest for scale-up if the system could achieve precursor and photonic efficiencies comparable to those of Cl_2-GPAO.

Even so, gaseous-OH•-based CH_4 oxidation may prove possible in other processes and contexts. The H_2O-GPAO process (known as "VUMOX"), which generates and splits ozone in a single photoreactor, has been shown to rapidly oxidize CH_4 at a variety of CH_4 concentrations.[122] That result complicates the claim that OH•-based reactors are ineffective on CH_4, leaving room for further study. It is possible that the presence of oxygen atoms (•O) in addition to OH• makes that process more effective or that the absence of ppm-level H_2O_2 eliminates a key radical sink. It is also possible that since every O_2 and H_2O molecule in air effectively acts as a radical precursor, this system simply uses an overwhelming radical production rate to overcome kinetics-related inefficiencies. In an entirely different direction, atmospheric H_2O_2 release for CH_4 removal may circumvent the kinetic issues present in H_2O_2 flow reactors, though such systems' effectiveness and practicality have been called into doubt.[124] Given the qualitative appeal of OH• systems' lower toxicity than Cl• systems, continued research on these pathways would be worthwhile.

Chapter 7

Concluding Remarks

The fields of dilute methane mitigation and atmospheric methane removal (AMR) have evolved considerably in the last few years. When I began my doctoral research, numerous possible strategies for both had been suggested. However, there was little sense of how close any given approach was to practical viability. For a minority of approaches, oxidation of dilute or 2 ppm CH_4 had been observed, but in no case had the cost of scaled-up CH_4 oxidation been modeled with experimentally-observed rates. In short, there were many approaches that appeared plausible, but no way to judge which might actually be possible in a climate-relevant time frame.

Research in the last few years has helped to close this knowledge gap considerably. Our lab's work, including the research in this thesis, has attempted to do so for photocatalysis, Cl_2-GPAO, and H_2O_2-GPAO. Other researchers have been hard at work exploring different technologies. For dilute point-source mitigation, in addition to various lab-scale and modeling works, there have been valuable efforts to perform field trials of new thermal oxidizers, thermal catalytic oxidizers, and Cl_2-GPAO systems. In the AMR space, I find the collective effort by dozens of researchers over several years to understand the iron-salt aerosol process to be singularly impressive.

To voice my personal opinion based on this body of work, there are fairly few technologies that I earnestly think might oxidize dilute CH_4 in volumes and time-frames useful for meeting global climate targets. The list of dilute point-source mitigation strategies that might be cost-effective is quite short; the list of plausibly cost-effective and socially-acceptable AMR approaches is even shorter. For the most part, the promising point-source oxidation technologies require field trials and scale-up more than basic science research, though I highlight some opportunities below. In contrast, with no approaches ready for scale-up, atmospheric CH_4 removal remains squarely in the basic research stage.

7.1 Research Directions for CH_4 Point Sources

The following are several areas that I believe could be fruitful for further academic research on dilute point-source CH_4 oxidation. I note that I have no firsthand experience with or particular expertise in CH_4 biofilters, so their absence in this section does not reflect any judgment for or against them.

7.1.1 Thermal Oxidizers

As discussed in Chapter 1, regenerative/recuperative thermal oxidizers (RTOs) are the most mature technology for oxidizing sub-flammability-limit CH_4 at as low as 1000 ppm. Extending these devices' working range to oxidize 100's of ppm of CH_4 is a clear and promising path to better point-source CH_4 oxidation. Given the prodigious energy and input costs associated with room-temperature strategies like Cl_2-GPAO, simply using CH_4's reaction enthalpy at in an RTO becomes quite attractive. Since the rate is determined by heat transfer to bulk air rather than CH_4 mass transfer to catalyst active sites, one would expect RTOs to be more compact and more resilient to contaminants than thermal catalytic oxidizers.

Because RTOs are a mature industrial technology, most information on their design seems to exist within companies rather than in published literature. It is difficult to tell whether any fundamental barrier prevents them from operating at lower CH_4 concentrations. Conventional wisdom suggests that the required heat exchangers would be too large and costly and could not achieve efficient enough heat recovery.[42] However, this assumption is worth questioning, since it is possible that despite the technical ability to do so there was simply no commercial need in the past to build RTOs that could operate at 100s of ppm of CH_4.

The answers to this question are likely known in industry, especially inside incumbent RTO manufacturers. In addition, the startup Resolute Methane is attempting to design mass-producible, low-pressure-drop heat exchangers optimized for dilute CH_4 RTOs.[93] However, it would be useful to the field to see a clear explanation in peer-reviewed literature of the trade-offs between CH_4 concentration and RTO/heat exchanger size, cost, and fan energy use. It might be possible to estimate these trade-offs simply by using a chemical engineering handbook's data on heat exchanger size, cost, and efficiency, though perspectives from industry would be preferable. With such knowledge as a baseline, academic research on improved heat recovery architectures might also be possible.

7.1.2 Thermal Catalytic Oxidizers

Thermal catalytic oxidizers, referred to in industry as regenerative/recuperative catalytic oxidizers (RCOs), offer the prospect of thermal CH_4 oxidation at temperatures of ∼300°C instead of 900°C. This should make it easier to achieve the required reaction temperature with only the reaction enthalpy of CH_4 oxidation, allowing for the use of cheaper and/or smaller heat recovery devices than an RTO. Copper-based zeolite catalysts have been shown to oxidize a wide range of CH_4 concentrations at modest temperatures and are currently the front-runner for commercialization.[94]

Even so, RCOs are not simple "better RTOs". In exchange for lower temperatures, other challenges arise. In RTOs, the "active" surfaces are inert and stable ceramics whose only job is to transfer heat. With thermal catalysts, the difficulty of absorbing CH_4 onto activie sites is a challenge, as it is with photocatalysts. Catalysts can also be poisoned by contaminants or deactivated by humidity in ways that heat transfer surfaces cannot.

At the time of writing, the Plata group at the Massachusetts Institute of Technology and the associated startup Moxair seem to be pursuing the clear next steps for RCOs.[96] These include studying catalyst durability and poisoning, better quantifying catalyst rates, and planning field trials with actual emitters. Although the known category of copper zeolite catalysts can always be improved upon, most of the critical-path work to determine RCOs' commercial viability is already under way.

One possible direction for thermocatalyst research would be to explore metal-organic frameworks (MOFs). In CO_2 capture, enthusiasm for zeolites eventually turned into enthusiasm for MOFs, which in theory can offer similar benefits with even better selectivity for certain chemicals. The prospect is especially interesting given the great difficulty of binding CH_4 on traditional catalyst materials in order to chemically activate it. Additionally, the design space for MOFs is very large, perhaps giving more opportunities for tuning than simply loading Cu, Pd, or other metals on zeolites. MOFs have already been used for oxidation of high-concentration CH_4 to high-value products like CH_3OH and it might be interesting to see MOF specialists try their hand at dilute CH_4 oxidation.[261] On the other hand, cost-effectively producing MOFs at scale for CO_2 capture has proven difficult, so enthuasism for their use in CH_4 oxidation should be tempered.

7.1.3 Gas-Phase Advanced Oxidation

GPAO is a very exciting field deserving of further study, our Cl_2-GPAO cost modeling results notwithstanding. The prospect of a purely gas-phase, room-temperature CH_4 oxidation process is very appealing given the challenge of getting CH_4 to interact with catalyst surfaces. The purely gas-phase reaction offers very low pressure drops, improving the economics of processing huge volumes of air. However, the inputs of GPAO – UV light and, in most cases, chemical reagents – can become quite costly. Whether any GPAO process for CH_4 will be viable at scale is an open question.

Cl_2-GPAO is the process farthest along the road to deployment. While $\bullet$Cl is highly effective at oxidizing CH_4, the need for a downstream acid gas scrubber negates some of the benefit of a catalyst-free, low-pressure-drop system. Well-instrumented field trials of this system are under way and it is not clear that more academic experimental work on the subject is needed at present. Though our cost model gives some cause for concern, our results should be replicated by independent cost models and validated to the extent possible by scale-up efforts before any final judgment is passed on Cl_2-GPAO's commercial prospects.

Although H_2O_2-GPAO would be appealing because it would need no downstream scrubbing process, our experiments found it to be ineffective at oxidizing CH_4. Before discounting the approach entirely, it might be worth replicating the result in a larger reactor with fewer wall effects. It would also be interesting to build a detailed chemical model of an H_2O_2-GPAO reactor containing a variety of reactive oxygen species and reaction pathways. Such a process would help to clarify the process's inherent chemical limitations.

The recently-reported "VUMOX" O_2-GPAO system is exciting because it requires neither an added radical precursor molecule nor a downstream scrubbing step.[122] Instead, O_2 and H_2O already in the gas stream serve as the radical precursors. This chemistry has been shown to oxidize CH_4 of various concentrations. It would be useful to perform a combined experimental and cost modeling on O_2-GPAO like we did on Cl_2-GPAO. One would need to find a way to count the number of radicals generated and derive a radical-to-CH_4 efficiency similar to our $\eta_{Cl\bullet}$. The main cost to model would be that of lighting, both hardware and electricity.

7.1.4 Product-Market Fit and Whole-System Design

Finally, I believe there is a need for researchers to go into the field and learn more about the practical use cases for their CH_4 scrubbers. In my opinion, being "ready" to mitigate a certain CH_4 source class cannot simply be equated with hitting a certain cost target for a certain CH_4 concentration (say, \$8000/tCH_4 at 100 ppm). Failing to account for factors like the variability of the inlet CH_4 concentration or the practicality of generating a single CH_4-laden airstream (i.e., sealing a barn or wastewater plant) could give a falsely optimistic outlook. On the other hand, it would also be easy to ignore opportunities for full-system design to make the CH_4 scrubber's task easier. For instance, can the air flow in a dairy barn be slowed by half in order to double its CH_4 concentration? This is more a question of bovine health than of chemical engineering but it would make the design of the CH_4 scrubber dramatically easier.

Although researchers working on startups and/or field trials have likely learned some of these things on an ad-hoc basis, it would be useful to collect and publish them for the field's benefit. A lesson of recent CH_4 oxidation research is that achieving "brute force" point source control with a scrubber that can easily and cheaply treat any CH_4 concentration above 30 ppm may not be realistic. One path forward could be to expand the design space to include the entire scrubber-source system. For example, we could hope to improve thermal oxidizers to mitigate 200 ppm CH_4 and also develop process controls that raise the CH_4 concentration in barn's ventilation air from $\sim$ 50 ppm to 200 ppm. This might be more achievable than treating the 50 ppm CH_4 stream as a given and attempting to develop a standalone machine to deal with it (as we have tried to do).

A useful place to start this effort might be a review or perspective paper describing the detailed needs and constraints of several specific classes of CH_4 point sources. This work should include CH_4 concentrations and variability, contaminant concentrations, and typical existing flow rates. It should discuss the relative ease or difficulty of collecting all the CH_4-containing air into a single flow, as well as any obvious opportunities to boost the CH_4 concentration by manipulating flow rates. The waste/wastewater, livestock, and coal sectors seem especially important to consider.

7.2 Research Directions for AMR

The outlook for many proposed AMR strategies seems rather bleak. None of the ground-based photocatalytic approaches that we modeled appeared promising. Although the photocatalyst aerosol strategy might theoretically be cost-effective with relatively modest catalyst improvements, I feel that the associated air quality issues, the similarity to aerosol-based solar radiation management, and the fact that our "humidity-tolerant photocatalyst" is coated in a fluorinated "forever chemical" all constitute near-insuperable barriers to real-world deployment. Research by my labmates has shown that thermal catalysis is not useful for AMR.[42] To our knowledge, no electrochemical approach has demonstrated conversion of 2-ppm CH_4. The H_2O_2-GPAO system about which we were hopeful appears to be ineffective at CH_4 oxidation.

On a brighter note, I remain hopeful about several AMR approaches. In my opinion, open-system Cl_2 release ought to be studied further, as I discuss below. Microbial CH_4 oxidation seems promising, especially if deployed cheaply over areas of land to enhance the natural soil CH_4 sink. Iron-salt aerosols have long been a frontrunner for AMR and remain an area of intense research. Because methanotrophy and iron-salt aerosols are each highly active fields of research in which I am neither experienced nor knowledgeable, I do not offer research directions for either of them.

7.2.1 Open-System Chlorine Release

Open-system Cl_2 release is essentially Cl_2-GPAO in open air and sunlight. A tower or tethered ballon would release Cl_2 that forms a plume and eventually photolyzes to $\bullet$Cl that can oxidize CH_4. Based on our reactor, near-complete photolysis would likely take place in 10-30 minutes. This process would likely be done in remote areas of the ocean, ensuring a ready supply of NaCl for the chlor-alkali process and also ensuring that the Cl_2-containing plume would not transit inhabited areas. The best study to date, which modeled a uniform 1250 Tg/year Cl_2 release over all ocean surfaces, found the approach to be quite effective at oxidizing atmospheric methane.[262] That study did not consider any side effects of doing so aside from impacts on local air pollution.

One concern with this strategy is the effectiveness of the core CH_4-oxidizing chemistry in an open-air environment. A plume of Cl_2 would have varying Cl_2 concentrations and •Cl production rates throughout. Thus, although they are useful for intuition, the efficiencies observed in a Cl_2-GPAO reactor with 2-ppm CH_4 and Cl_2 likely cannot be straightforwardly applied. Side-reactions with nitrogen oxides and ozone also need to be considered, especially in regions with low •Cl production rates, as these can diminish the net CH_4 drawdown and in extreme cases negate it.[130]

A key figure of merit would be the amount of CH_4 oxidized per unit of Cl_2 released. A rough analysis in Chapter 1 suggested that in the model, about 1 ton of CH_4 got oxidized per 3 tons of Cl_2 released. For comparison, in our experiments with 2 ppm CH_4 and Cl_2, about 11 tons of Cl_2 were needed per ton of CH_4 oxidized. For a \$250/ton Cl_2 price, either figure could create an economically plausible process. However, it would be very useful to develop more accurate multiphysics model of a Cl_2 plume in atmospheric air in order to better bound this value. This would mainly be an atmospheric chemistry and atmospheric dispersion modeling effort.

Another key concern is the net flux of acid into the atmosphere and, eventually, nearby oceans and land. Releasing unmitigated plumes of HCl at a large scale could cause acid rain or local ocean acidification. The question is whether this issue can be mitigated without compromising methane-oxidizing performance. The most obvious way to do so would be to release NaOH in equal proportion to HCl. Since NaOH is stoichiometrically co-generated with Cl_2, an open-air Cl_2 release system would already have the required amount of NaOH on hand. Releasing NaOH in the ocean and Cl_2 in the air for AMR has already been proposed in literature. NaOH could also be released as an aerosol, which might lead it to neutralize HCl back to NaCl more quickly. Determining whether either of these strategies could be effective would be another complex multiphysics modeling effort that I believe would be well worth doing.

7.3 Final Words

When I began working in this field, I was hopeful that a practical and cheap pathway to AMR would be found. A viable AMR strategy could offset CH_4 emissions

from agriculture, waste management, and other hard-to-abate sectors, solving many emissions sources in one fell swoop. Moreover, it could manage CH_4 emissions due to natural feedbacks and tipping points, a problem for which few other solutions exist. Many chemical approaches for AMR had been suggested; it was now time to test and improve them. This felt like a motivating and exciting problem for my doctoral research.

Thus far, our hopes for a viable AMR process have not been realized. Many proposed strategies appear quite unlikely to succeed. A handful remain within the realm of possibility and are well worth pursuing. Many of the unviable AMR processes might instead be practical as "methane scrubbers" on dilute point sources. Recognizing the technical challenge of AMR, many researchers have turned their attention to dilute point-source CH_4 oxidation, as I did to some extent during the course of my doctoral work.

However, point-source CH_4 oxidation brings different challenges and solves a somewhat more limited range of problems than AMR. In theory, AMR can go anywhere and offset any CH_4 source. If we instead focus on CH_4 point sources, we must ask ourselves, "on what subset of CH_4 emissions do we really think these could be deployed?". For example, only a small fraction of the world's cows spend much of their time in dairy barns, and even for those that do, the site-specific engineering required to install a CH_4 scrubber there is daunting. Low-concentration CH_4 emitters like rice paddies are entirely unsuitable for flow reactor-based oxidation, as are natural CH_4 emisions resulting from climate feedbacks or tipping points. Researchers switching from AMR to dilute point-source CH_4 oxidation should be aware of these trade-offs.

Even so, the total amount of emissions addressable by dilute point-source oxidiation is large in absolute terms. Coal mine emissions alone, about 30 megatons of CH_4 per year, equal 0.6 gigatons of CO_2 per year on a GWP-100 basis, about the same as all global aviation.[33] Thus, even a "niche" solution compared to AMR could have a large impact. Waste CH_4 emissions are comparable to coal and livestock emissions are several times larger, so even dealing with a fraction of livestock CH_4 would be significant.[42]

In conclusion, after several years of research, atmospheric methane removal remains a grand challenge for climate change mitigation. Although it is surpassingly

difficult to achieve, it would be world-changing if proven and scaled successfully. Efforts towards AMR have also considerably advanced the state of the art of methane scrubbers for dilute point sources. Whether or not AMR becomes a reality, methane scrubbers could prove a valuable climate change mitigation tool in their own right. Much exciting work remains to be done in each of these two complementary fields.

Appendix A

An Open-Source Lab Automation Software Package

A.1 Introduction

The software package described in this chapter was developed as a labor-saving tool for the benchtop chemistry experiments in this thesis. My first research experience at Stanford was a benchtop chemical-engineering project on methane pyrolysis. The standard operating procedure for each experiment involved launching individual pieces of software to control the mass flow controllers, thermocouples, mass spectrometer, flow meter, and tube furnace. Data logging for each device had to be configured separately before each experiment and the log files had to be painstakingly combined afterwards. Additionally, one had to remain nearby in order to flip valves and change conditions during the experiment. Feeling that there had to be a better way, I developed a Python program to control this apparatus. It consisted of an on-screen dashboard to control the various instruments, a routine to log data from all of them to a common .csv file, and a way to control them with a Python script.

Following a successful demonstration on the pyrolysis experiment, my collaborators and I continued using the software as we built our methane oxidation setup. It went through two major updates and many minor ones. The first update brought the software in alignment with object-oriented standards, using class inheritance to let the user customize various aspects of their control system without worrying about the system's complex innards. The second update implemented multithreading, allowing more complex control systems to run without latency. During the second update, we also published comprehensive online documentation on the project. We also changed its name from the tongue-in-cheek working name *RichardView* to its current name, *PyOpticon*. This chapter begins by describing the general landscape of laboratory control software. It then describes PyOpticon's functionality, explains its internal structure, and demonstrates its use on a photocatalytic CH_4 oxidation experiment.

A.2 The Need for Laboratory Control Software

Well-designed systems for laboratory data acquisition, controls, and automation can greatly improve the pace and quality of research in physical sciences and engineering.[263] Such systems' main goal is to economize researchers' time and to free them

from repetitive tasks. They share many traits with 'supervisory control, automation, and data acquisition' (SCADA) software that is ubiquitous in industrial settings, whose purpose is to visualize, log, and command the state of a physical system.[264] Integrated control and data acquisition systems are also prerequisites for 'high-throughput' experimentation, with many samples synthesized and/or tested in parallel, and with the iteration and improvement of samples also partially automated as 'self-driving labs'.[265–267]

Though such tools can apply to many workflows in physical science and engineering, and thereby quite general, we mainly provide examples related to our research on heterogeneous photocatalysis. Experimental workflows in this context often involve launching and configuring many desktop programs, manually flipping valves or cycling lights at frequent intervals for several hours during its course, and then painstakingly combining several differently-formatted log files in order to fully understand the outcome. A unified data acquisition, automation, and control system can offer many benefits in that context, including:

- Saving researchers time on experimental setup, shutdown, and data analysis by reducing the number or programs to launch and log files to postprocess.
- Allowing researchers to do other tasks while an automated experiment runs.
- Increasing repeatability by avoiding human errors and variations in experimental setup and execution.
- Making it easier and faster to retroactively diagnose equipment failures that led to unexpected results.
- Enabling longer experiments and higher utilization rates of experimental setups, unlimited by how long a researcher can stay awake or present in the lab.
- Responding to errors in real time, e.g. pausing an experiment and notifying an operator if an instrument goes offline, minimizing failed experiments and wasted system time.
- Enhancing safety by automatically detecting dangerous conditions based on one or multiple sensor readings, warning operators of them, and returning the

system to a predefined "safe mode" to avert risk until the operator can respond.

Various commercial and open-source tools for these purposes already exist; indeed, industrial SCADA is mostly a solved problem.[263, 264, 268] Such systems provide graphical control panels, referred to as 'human-machine interfaces' (HMIs), to visualize and control many instruments at once, allow the execution of experimental 'recipes,' and log the entire setup state to a central log file. National Instruments' *LabVIEW*, with a large ecosystem of programmers and instrument drivers, is very widely used in commercial settings and in large research projects.[269] Other laboratory control software includes Siemens' *WinCC* and Inductive Automation's *Ignition*.[270–272] However, the prevalence of manual workflows in academic settings suggests that these solutions are either ill-suited to academic research or that their benefits are not widely understood. Barriers to adoption may include some of the following:

- Few researchers have exposure to or formal training in industrial SCADA.
- Licenses for commercial SCADA solutions may be costly.
- Resources may be too constrained to hire a professional SCADA developer.
- Experimental setups may be reconfigured too frequently to justify the upfront cost of a professionally-installed system that will be difficult to modify.
- Researchers used to text-based programming languages (Python, MATLAB, C, etc.) may be unfamiliar with the graphical programming environments that many commercial SCADA platforms use.

As an alternative to commercial SCADA software, several open-source Python projects have been developed to control laboratory instruments. Examples include *Lantz*, *PyVISA*, and *PLACE*.[273–275] These projects take advantage of the Python languages's readability, conciseness, powerful libraries, and presence in many science curricula.[275–277] Researchers curious about automation's benefits can experiment with these tools at no cost besides their time, a key trait for many academic research labs.[263] These packages allow one to create Python objects that can query data

from and send commands to a physical device. through themWhile it is then easy to program a sequence of actions (e.g. actuating a valve according to a schedule), a great deal of coding and debugging is still required to turn these objects into a streamlined application with a graphical interface, recipe execution, logging, and other capabilities comparable to commercial SCADA software. That coding is unlikely to be worthwhile on an ad-hoc basis for an individual project, but is suitable for inclusion in a general Python package that can apply to many projects, like that presented here.

To meet these needs in our own lab, we have developed *PyOpticon*, an open-source laboratory control, data acquisition, and automation package written in Python. PyOpticon allows one to create on-screen control panels for physical setups (Figure A.1). These control panels, termed "dashboards", can also log data, execute Python automation scripts, and be manipulated via remote desktop applications. Dashboards are constructed in a modular fashion from interfaces for individual devices, termed "widgets," which are configured using simple object-oriented Python code. PyOpticon is available on the Python Package Index, its source code is available on Github at https://github.com/richardsrandall/pyopticon, and its documentation and tutorials are available on ReadTheDocs at https://pyopticon.readthedocs.io.

A.3 Software Capabilities and Functionality

Each PyOpticon dashboard is a Python script that can be launched from a desktop shortcut like any other application (Figure A.1). A dashboard contains one or more 'widgets,' each usually providing a graphical interface for one physical device (Figure A.2). After launching the dashboard, the user clicks the 'Start Polling Devices' button, causing the dashboard to begin regularly updating its component widgets according to methods in the widgets' class definitions. Updating a widget usually involves querying a physical device via some type of serial connection, parsing the response, and displaying the resulting values in a graphical field. Each widget updates with a period of some integer number of seconds, with updating every second the default. Most widgets also have text or dropdown input fields. Updating an input field and pressing the 'Confirm' usually prompts the widget to send a serial command to update the relevant parameters in the physical device.

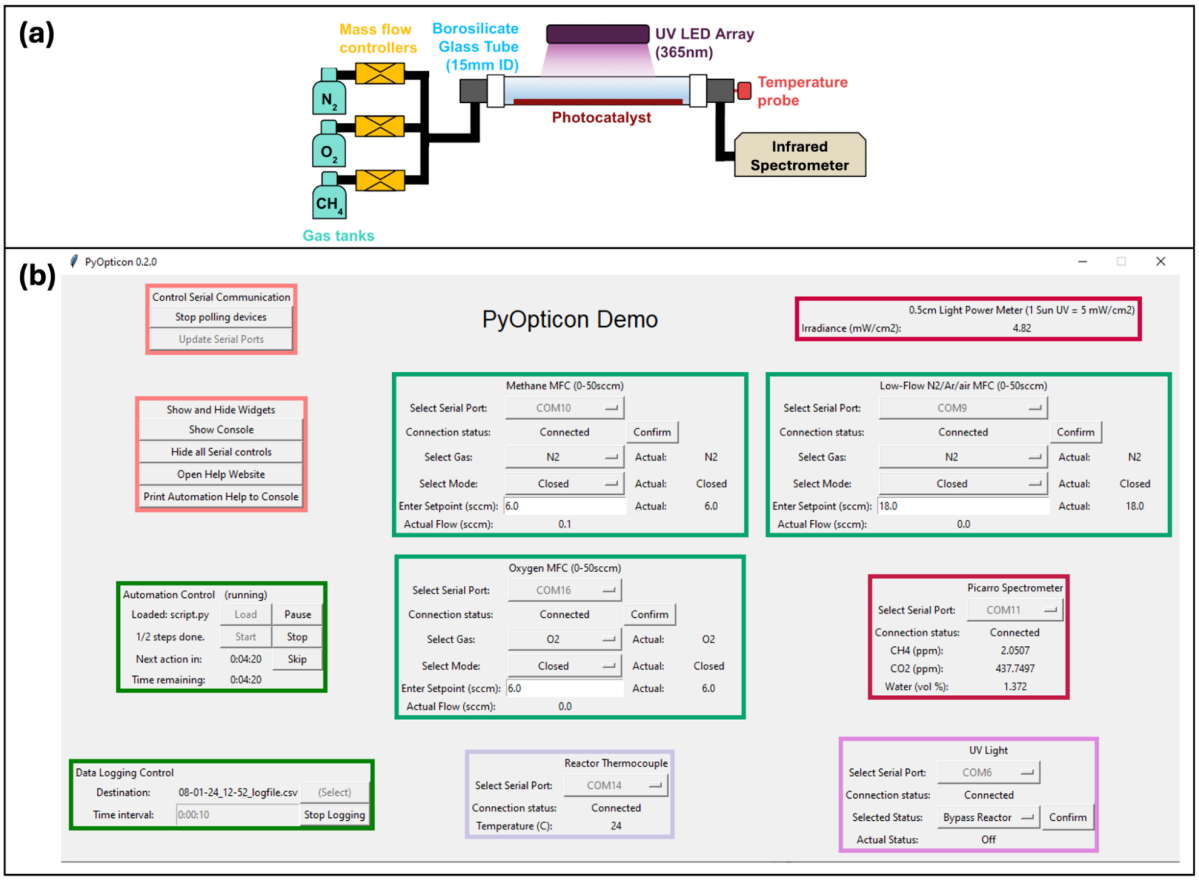

Figure A.1: A simple PyOpticon dashboard in operation. The dashboard represents a flow photoreactor **(a)** designed to measure photocatalytic conversion of CH_4 to carbon dioxide. It is a simplified subset of the setup used in Chapter 2. The setup contains three mass flow controllers, one gas analyzer, a thermocouple, an ultraviolet light, and a light power meter. The light power meter is not pictured in the schematic. The corresponding dashboard **(b)** is organized into three columns and four rows of rectangular 'widgets'. The four widgets in the leftmost column control system-level functions and are present in all dashboards. The other widgets, aside from the 'PyOpticon Demo' title, each represent a physical device. In this example, the system state is being logged every ten seconds (leftmost column, bottom row), and an automation script is running (leftmost column, second row from bottom).

Widgets are defined in Python classes, as will be described below. The script that launches a dashboard contains the code to instantiate all of the dashboard's widgets

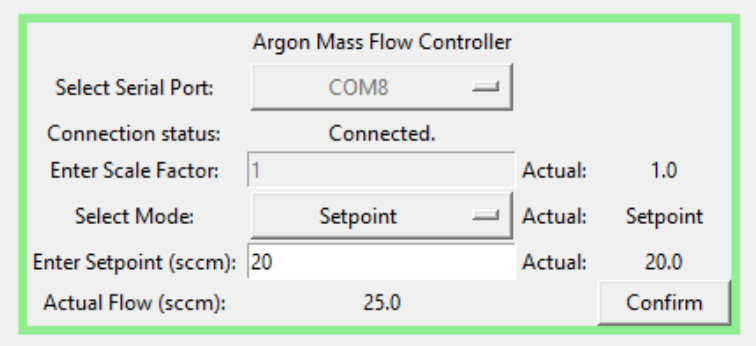

Figure A.2: Detail image of a PyOpticon widget for a mass flow controller.

and add them to the dashboard in specified positions. Each widget is instantiated by passing a constructor method certain values unique to that physical device, such as a device nickname, a default serial address, or labels for different valve positions. A minimal example is as follows:

```
import pyopticon.majumdar_lab_widgets as mlw
import pyopticon.built_in_widgets as biw
from pyopticon.dashboard import PyOpticonDashboard
# Create a dashboard object
dashboard = PyOpticonDashboard(dashboard_name = "PyOpticon Demo",
use_serial_emulators=True,
polling_interval_ms=1000,
window_resizeable=False)
# Add a title block
dashboard.add_widget(biw.TitleWidget(dashboard,"PyOpticon
↪  Demo",20),row=0,column=1)
# Add a thermocouple widget
tc1 = mlw.OmegaUSBUTCWidget(parent_dashboard=dashboard,
name='My Thermocouple',
nickname='My TC',
default_serial_port='COM14')
dashboard.add_widget(tc1,row=3,column=3)
# Start the dashboard
dashboard.start()
```

The PyOpticon package contains widgets for several instruments in our own lab

(Table A.2) and contains tools to allow users to create widgets for their own instruments. Numerous commercial instruments have serial communication protocols that can be used to create widgets to interface with them, and widgets are also well-suited to controlling homemade electromechanical devices run by microcontrollers like Arduinos. Early PyOpticon users will likely need to write a widget for every type of instrument they wish to control, using a process outlined below, unless they happen to be using a device for which we provide a built-in widget. However, we hope that users will share the widgets they develop, creating a crowdsourced ecosystem of ready-made widgets for a variety of devices that other users can easily download and use. We intend to post links to any packages of widgets that are shared with us at https://pyopticon.readthedocs.io/en/latest/available_widgets.html.

A dashboard can log data and perform safety checks based on values read from physical devices. When data logging is active, the value of every input and output field of every widget is saved to a comma-separated value file at a regular interval, with ten seconds the default. This single log file can speed up data processing compared to workflows that require combining several different programs' log files with varying formats and sampling times. Safety checks (termed 'interlocks') are Python functions, defined in the same file in which the dashboard is configured, that are called every second by the dashboard to examine the values of certain widget fields and respond if undesirable conditions are detected. For example, if the reading of a reactor thermocouple ever exceeds a certain value, an interlock can switch from flowing reaction gasses to flowing inert glasses. The package also includes a tool to facilitate sending emails and text messages, so it is possible to configure an interlock to notify the researcher if a certain instrument goes offline or deviates from its desired parameters for a certain number of update cycles.

PyOpticon provides two ways to run automated experiments. For the first, termed 'automation scripts,' the user writes a Python script containing certain functions [e.g., *schedule_action(...)*, *schedule_delay(...)*] and control structures, then 'loads' that script via an onscreen button. Once the script is loaded, the sequence of actions can be started, paused, unpaused, and aborted via on-screen buttons, while its progress and remaining time can be monitored with on-screen readouts. The script can contain certain structures like for-loops and function definitions to make automation scripts

Manufacturer	**Device**	**Update Protocol**	**Comments**
Omega Engineering	USB-UTC Thermocouple Adapter	Text-based serial via USB	Reads a single K-type thermocouple's temperature in °C.
VICI Valco	2-Position Valve with EUHA Actuator	Text-based serial via RS232	Reads and writes the valve's position; allows the user to name the valve's positions.
VICI Valco	8-Position Selector Valve with EUHA Actuator	Text-based serial via RS232	Reads and writes the valve's position; allows the user to name the valve's positions.
MKS Instruments	Mass-Flo Controllers controlled by Series 946 Vacuum System Controller	Text-based serial via RS232	Reads and writes the valve mode, flow setpoint, and scale factor; also reads the actual gas flow rate. Allows the use of a user-specified calibration curve.
Aalborg Instruments	DPC Mass Flow Controller	Text-based serial via RS232	Reads and writes the valve mode, flow setpoint, and gas selection; also reads the actual gas flow rate. Allows the use of a user-specified calibration curve.
Thorlabs	PM100D Light Power Meter	Python driver supplied by device manufacturer	Reports the power or irradiance reading from a single light power meter.
SRI Instruments	8610c Gas Chromatograph	Watches log file of PeakSimple desktop program	Reads peak areas and reports gas concentrations for a user-specified set of gases and calibration curves. Does not directly control the instrument.
MKS Instruments	Multi-Gas 2000 FTIR Spectrometer	Watches log file of MG2000 desktop program	Reports gas concentrations for a user-specified set of gases. Does not directly control the instrument.
Picarro	G2210-i Cavity Ringdown Spectrometer	Text-based serial via RS232	Reports ppm-level concentrations of CH_4 and carbon dioxide and percent-level concentration of water.

Table A.2: List of PyOpticon widgets in the initial public release.

more concise. An example script is included in the *Demonstration* section below.

The following brief snippet, which adjusts an MFC setpoint and then flickers a light on and off, gives a sense of the syntax and basic functions:

```
schedule_action('Methane MFC','Setpoint Entry','30',False)
schedule_action('Methane MFC','Mode Selection','Setpoint',True) # Command
↪  the MFC to flow
for i in range(4): # Flicker the light
schedule_delay('0:01:00')
schedule_action('UV Light','Status Selection','On')
schedule_delay('0:01:00')
schedule_action('UV Light','Status Selection','Off')
schedule_action('Methane MFC','Mode Selection','Closed',True) # Command
↪  the MFC to close
```

Since these automation scripts are poorly suited for implementing conditional logic (e.g., if-then and while structures), we also provide an interface to query and set dashboard fields from an entirely separate Python program via a socket connection. This interface would be useful if using a dashboard as part of a more complex lab automation setup where automated adjustments or feedback control based on measured values are part of the workflow.

A minimal example of the socket interface is as follows:

```
from pyopticon.socket_client import PyOpticonSocketClient
import time
s = PyOpticonSocketClient(handle_errors='exception') # Initialize the
↪  socket client
s.set_field("UV Light","Status Selection","On") # Prepare to turn the
↪  light on
s.do_confirm("UV Light") # Turn the light on
time.sleep(10)
s.set_field("UV Light","Status Selection","Off") # Prepare to turn the
↪  light off
s.do_confirm("UV Light") # Turn the light off
s.close() # Close the connection
```

A.4 Software Architecture

Here, we briefly describe the workings of PyOpticon dashboards, especially as they affect the workflow of building new dashboards and widget classes. These workings are described in detail in the project's documentation. The same site also contains thorough tutorials for using dashboards, writing automation scripts, writing interlocks, assembling dashboards from existing widgets, and defining new widgets to interface with specific devices.

A dashboard's tasks are split between several threads to minimize latency. A main thread manages the graphical interface, data logging, and automation. By default, each widget also runs in its own thread, allowing widgets to make blocking queries to their serial devices without causing the dashboard to lag or become unresponsive. This setup is useful when using OEM drivers or serial packages that do not offer non-blocking ways to query information from devices. It also allows the use of *time.sleep(...)* to create delays between successive queries or between queries and responses in widget serial protocols, making them more legible and simpler to write. One can also override this behavior to force multiple widgets to share a thread and operate synchronously, e.g., to prevent them from attempting to access a shared serial resource simultaneously. Threading is implemented in internal classes and, in normal usage, the user need not be familiar with Python multithreading in order to implement new widgets.

While writing a class for a new type of widget is somewhat more involved than creating an automation script or configuring a dashboard, we have attempted to streamline the process as much as possible. New widget classes are created as subclasses of a superclass called *GenericWidget*. This superclass contains code to auto-generate graphical elements, log data, execute automated actions, and manage serial connections. One need only define the different input and output fields' names and types, specify how to update the fields, and specify what actions to take when the 'confirm' button is pressed. Python's built-in text processing functions, as well as powerful free packages like NumPy, make it easy to implement these functions given knowledge of a device's serial protocol.[276] Little to no knowledge of graphical and serial libraries is required, and the tutorials discuss the process in greater detail.

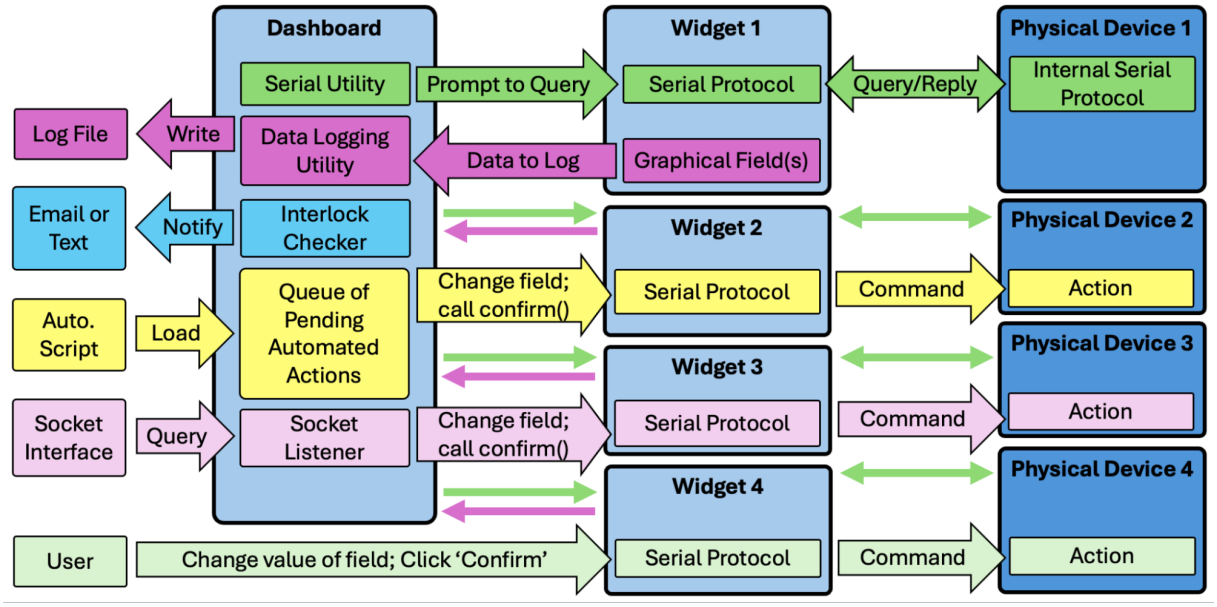

Figure A.3: A graphical representation of the concurrent processes and information flows in an active PyOpticon dashboard. Each widget runs in its own thread, as does the main dashboard. The dashboard regularly prompts each widget to poll its physical device for new measurements, parse the response, and update its graphics with the new data (dark green arrows/boxes). The dashboard also regularly asks each widget for new data to log, aggregates the results, and logs them to a central file (magenta arrows/boxes). The user can change a widget's input field, e.g. a setpoint entry text box, and then press 'Confirm,' which prompts the widget to send the device a command with the desired state (light green arrows/boxes). Automation scripts, whose steps are stored in a queue once loaded, emulate user inputs by automatically changing an input field's value and then emulating a 'Confirm' button press (yellow arrows/boxes). The socket interface can update widget fields and emulate 'Confirm' presses in a similar way (light purple arrows/boxes). The interlock checker continuously runs any interlock functions and responds as needed (turquoise arrows).

Widgets can update themselves in a variety of ways to support a wide variety of instruments, with the choice usually dictated by what protocol a given device supports. In our experience, the most common setup is communication with a physical device using a text-based serial protocol over a RS-232, RS-485, or USB connection. PyOpticon can automatically initialize a PySerial object for this purpose. Alternatively, the user can manually initialize a different type of serial connection, for instance by

using a Python driver written by an instrument's manufacturer, or by using a free package that implements a different serial protocol like MODBUS or VISA.[273, 278] In principle, any communications protocol for which a Python package exists can be used so long as the device supports it, though to date we have exclusively used wired serial protocols.

Other widget setups are useful in certain scenarios. A widget can 'watch' the logfile of another program, bringing the external logfile's latest values into the dashboard's graphical interface and the unified PyOpticon logfile. This is useful for devices like gas analyzers that are best controlled by their manufacturers' standalone applications, but whose measured values (i.e., gas concentrations) one wishes to include in the dashboard's log files. Finally, one can also create widgets with purely software-related functions that do not interface with a device at all; for instance, we use a 'flow rate calculator' widget that quickly computes the MFC setpoints needed to achieve a desired gas mixture and total flow. The package's built-in widget classes contain examples of all of the above options, some of which are also discussed in the online tutorials.

A.5 Safety and Pitfalls

We stress that, while we have debugged PyOpticon to the best of our ability, it cannot and should not be wholly relied upon to ensure human safety or the safety of expensive equipment. Researchers using the package must ensure that no combination of software commands could create a dangerous condition, for instance, creating a combustible mixture in the presence of an ignition source or causing a piece of equipment to severely overheat. The interlock feature is intended to respond to or warn the user of mishaps that may affect data quality or waste researchers' time, not to identify or correct conditions that are unsafe to people or equipment. Where human safety is at stake or where expensive equipment damage is possible, hardware should be designed such that no combination of PyOpticon commands would create a dangerous condition, or else thoroughly-tested commercial software should be used instead.

PyOpticon is best-suited to open-loop control, i.e., communicating setpoint or

mode commands to external devices that implement the logic necessary to achieve those setpoints and modes. It is possible to implement closed-loop control laws (e.g., PID) within PyOpticon in a widget's update cycles or within an interlock, which may be useful if one physical device needs to be controlled based on a reading from another device. However, this should be done with great care, since undefined behavior may result if the dashboard is unexpectedly closed or loses serial communications or if the computer running the dashboard shuts down unexpectedly. Additionally, PyOpticon does not contain tools for tuning control laws. Where possible, we therefore recommend using well-tested (and ideally commercially available) external control devices that can receive serial commands. For instance, using a commercial temperature controller that can receive RS-232 commands is much preferred to implementing a Python PID control loop between a PyOpticon widget for a thermocouple and a widget for a relay connected to a heating element.

A.6 Demonstrations

The example below uses PyOpticon to interface with the photoreactor described in Chapter 2. The devices that require controls are three Aalborg DFC mass flow controllers (dilute methane, dry nitrogen, and humidified nitrogen), one MKS Mass-Flo controller for oxygen gas controlled by an MKS 946 Vacuum Controller, and a DigitalLoggers IoT Relay that controls an ultraviolet LED array. The devices requiring data acquisition are an Omega USB-UTC thermocouple adapter, a Thorlabs PM100D light flux meter, and an MKS Multi-Gas 2000 infrared gas analyzer. The dashboard for this setup is shown in Figure A.4.

This experiment aimed to measure CH_4 conversion on zinc oxide (ZnO) nanoparticles at inlet CH_4 concentrations of 100, 200, and 500 ppm under dry (<500 ppm H_2O) conditions. The ZnO sample was loaded in the reactor as described in Chapter 2. For each reaction condition, the CH_4 concentration was allowed to stabilize, then the ultraviolet light was cycled on and off several times to generate several transitions between 'light' and 'dark' conditions, shown in Figure A.5.

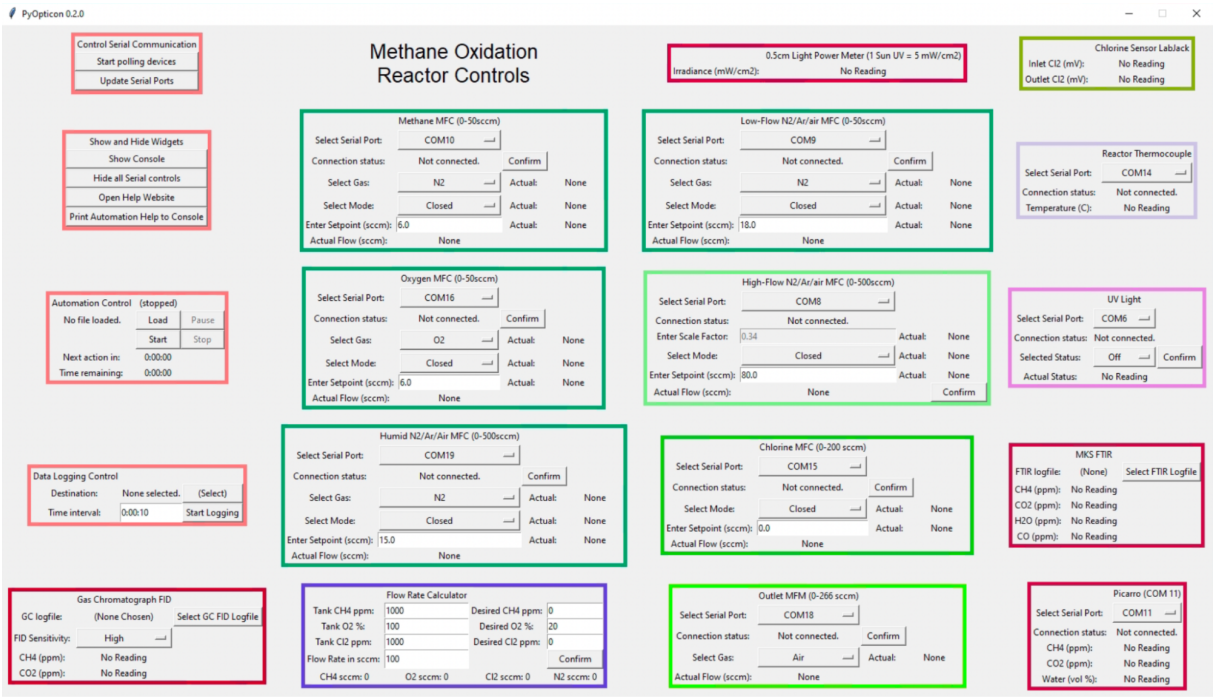

Figure A.4: The dashboard used in the demonstration. Note that several of these widgets (e.g., the 'Chlorine Sensor Labjack') are specific to our own lab and are not included in the public release of PyOpticon due to a lower standard of testing and documentation. However, those widgets were not an active part of the demonstration experiment. The widgets used to control and measure the demonstration experiment (Methane/Low-Flow N2/Oxygen MFC's, UV Light, MKS FTIR, Thermocouple, and Light Power Meter) are all part of the public release.

To achieve this, the automation script below was used. For brevity, the function *flow_at_CH4_ppm*, which commands the three mass flow controllers to flow a gas mixture with a given concentration of CH_4, has been omitted.

```
# The cadence of the light on/off cycle can be adjusted here
UV_off_duration='0:10:00'
UV_on_duration='0:20:00'

# First purge with N2 for an hour
schedule_action('LF N2 MFC','Mode Selection','Setpoint',False)
schedule_action('LF N2 MFC','Setpoint Entry',80,True)
schedule_action('O2 MFC','Mode Selection','Setpoint',False)
```

```
schedule_action('O2 MFC','Setpoint Entry',20,True)
schedule_delay('1:00:00')

# Step through the desired concentrations
for CH4_ppm in (100,200,500):
flow_at_CH4_ppm(CH4_ppm,ch4_tank_ppm=10,total_flowrate=30)
schedule_delay(UV_off_duration) # Start with extra time to get CH4
↪  stabilized
for i in range(4):
schedule_delay(UV_off_duration)
schedule_action('UV Light','Status Selection','On')
schedule_delay(UV_on_duration)
schedule_action('UV Light','Status Selection','Off')
schedule_delay(UV_off_duration) # Extra time at end to get CH4 stabilized
↪  again

# Shut down the flows
schedule_action('Methane MFC','Mode Selection','Closed',True)
schedule_action('O2 MFC','Mode Selection','Closed',True)
schedule_action('LF N2 MFC','Mode Selection','Closed',True)
# Experiment ends
```

Figure A.5 shows several outputs from the same experiment including gas concentrations, light fluxes, and device setpoints. All inputs were controlled automatically with the automation script above, requiring no human intervention after the experiment's start. All of the plots were made directly from the PyOpticon log file using a simple Python script and the Matplotlib package. The data indicate slow but clearly visible photocatalytic oxidation of CH_4 on ZnO at each of the three tested CH_4 concentrations, as explained in the caption. The PyOpticon log file contains many additional measured values at each time step, such as other gasses' concentrations and the mass flow controllers' measured flows, that are not plotted here.

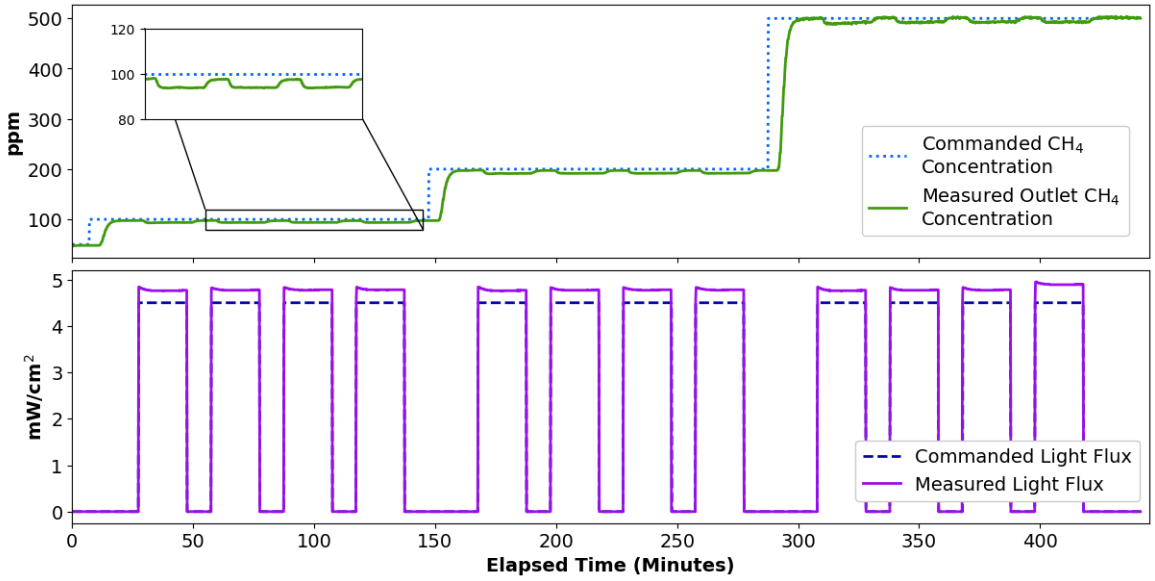

Figure A.5: Outputs from a photocatalytic CH_4 conversion experiment with controls and data acquisition handled by a PyOpticon dashboard. A script causes the mass flow controllers to step through nominal CH_4 concentrations of 100, 200, and 500 ppm. At each concentration, the ultraviolet light is automatically cycled on and off. While the light is on, a small fraction of the CH_4 is converted, causing the CH_4 concentration measured at the reactor outlet to decrease. The conversions were intentionally kept low for the purposes of making rate measurements. Further data processing could extract the reaction rates and quantum yields of photocatalytic CH_4 oxidation under each condition.

A.7 Conclusion

We have developed the open-source Python package PyOpticon to supply academic labs in chemistry and materials science with high-quality, "do it yourself"-friendly control software. The software can equip many benchtop systems with on-screen control panels, unified data acquisition and logging, safety interlocks, and powerful automation tools. These capabilities can streamline experiment setup and shutdown, simplify data processing, increase repeatability, allow longer experiments, enable remote operation, and boost apparatuses' utilization rates. The software can quickly be adapted to interface with a wide variety of instruments using a variety of modes of communication. These features made PyOpticon very useful in executing and streamlining

this thesis's experimental work on photocatalysis and gas-phase advanced oxidation.

While a number of software tools exist for this purpose, PyOpticon's novelty lies in its free and open-source nature, as well as its accessibility to relatively inexperienced coders. We have tried to write transparent and well-documented code that allows most users to ignore the details of how graphics, multithreading, data logging, and automation are implemented, letting them focus only on defining widgets' fields and the protocols to update them. We have also written what we believe are detailed and comprehensive online tutorials for those starting to use PyOpticon. We hope that these traits will make it a very low-risk and "do it yourself"-friendly proposition for researchers to test PyOpticon's applicability to their own work, and that they will end up with powerful laboratory control systems that they can build, maintain, and reconfigure as their needs change.

References

1. Henny, L. & Kim, K.-M. The Changing Nature of Atmospheric Rivers. *AMS Journal of Climate* **38,** 1435–1456. https://journals.ametsoc.org/view/journals/clim/38/6/JCLI-D-24-0234.1.xml (Mar. 6, 2025).
2. Cai, W. *et al.* Increasing Frequency of Extreme El Niño Events Due to Greenhouse Warming. *Nature Climate Change* **4,** 111–116. ISSN: 1758-6798. https://www.nature.com/articles/nclimate2100 (Feb. 2014).
3. Amrouni, O., Heggy, E. & Hzami, A. Shoreline Retreat and Beach Nourishment Are Projected to Increase in Southern California. *Communications Earth & Environment* **5,** 1–17. ISSN: 2662-4435. https://www.nature.com/articles/s43247-024-01388-6 (May 22, 2024).
4. *Copernicus: June 2024 Marks 12th Month of Global Temperature Reaching 1.5°C above Pre-Industrial — Copernicus* https://climate.copernicus.eu/copernicus-june-2024-marks-12th-month-global-temperature-reaching-15degc-above-pre-industrial (accessed Apr. 8, 2025).
5. *State of the Global Climate 2024* World Meteorological Organization. https://wmo.int/publication-series/state-of-global-climate-2024 (accessed Apr. 8, 2025).
6. *2024 Extreme Events Dashboard* https://experience.arcgis.com/experience/5cb119c71c6c4f8a89b837bf5cf353b8 (accessed Apr. 8, 2025).
7. Leach, N. J. *et al.* Heatwave Attribution Based on Reliable Operational Weather Forecasts. *Nature Communications* **15,** 4530. ISSN: 2041-1723. https://www.nature.com/articles/s41467-024-48280-7 (May 30, 2024).

8. Philip, S. Y. *et al.* Rapid Attribution Analysis of the Extraordinary Heat Wave on the Pacific Coast of the US and Canada in June 2021. *Earth System Dynamics* **13,** 1689–1713. ISSN: 2190-4979. https://esd.copernicus.org/articles/13/1689/2022/ (Dec. 8, 2022).

9. Cheng, L. *et al.* Record High Temperatures in the Ocean in 2024. *Advances in Atmospheric Sciences,* 1–18. ISSN: 1861-9533. https://doi.org/10.1007/s00376-025-4541-3 (Jan. 10, 2025).

10. *NOAA Coral Reef Watch Current Global Bleaching: Status Update & Data Submission* https://coralreefwatch.noaa.gov/satellite/research/coral_bleaching_report.php (accessed Apr. 8, 2025).

11. *Coral Bleaching During & Since the 2014-2017 Global Coral Bleaching Event Status and an Appeal for Observations* (NOAA Coral Reef Watch). https://coralreefwatch.noaa.gov/satellite/analyses_guidance/global_coral_bleaching_2014-17_status.php#:~:text=More%20than%2070%25%20of%20coral,three%2Dyear%20long%20global%20event..

12. Hughes, T. P. *et al.* Global Warming Transforms Coral Reef Assemblages. *Nature* **556,** 492–496. ISSN: 1476-4687. https://www.nature.com/articles/s41586-018-0041-2 (Apr. 2018).

13. Hoffmann, R., Abel, G., Malpede, M., Muttarak, R. & Percoco, M. Drought and Aridity Influence Internal Migration Worldwide. *Nature Climate Change* **14,** 1245–1253. ISSN: 1758-6798. https://www.nature.com/articles/s41558-024-02165-1 (Dec. 2024).

14. Vousdoukas, M. I. *et al.* Small Island Developing States under Threat by Rising Seas Even in a 1.5 °C Warming World. *Nature Sustainability* **6,** 1552–1564. ISSN: 2398-9629. https://www.nature.com/articles/s41893-023-01230-5 (Dec. 2023).

15. *Vanishing Shores: This Is the Impact of Rising Sea Levels in Guinea-Bissau* World Economic Forum. https://www.weforum.org/stories/2024/10/vanishing-shores-the-human-toll-of-rising-seas-in-guinea-bissau/ (accessed Apr. 8, 2025).

16. Almulhim, A. I. *et al.* Climate-Induced Migration in the Global South: An in Depth Analysis. *npj Climate Action* **3,** 1–12. ISSN: 2731-9814. https://www.nature.com/articles/s44168-024-00133-1 (June 14, 2024).

17. *Event Papers – World Weather Attribution* https://www.worldweatherattribution.org/event-papers/ (accessed Apr. 8, 2025).

18. Kimutai, J. *et al.* Human-Induced Climate Change Increased 2021–2022 Drought Severity in Horn of Africa. *Weather and Climate Extremes* **47,** 100745. ISSN: 2212-0947. https://doi.org/10.1016/j.wace.2025.100745 (Mar. 1, 2025).

19. White, R. H. *et al.* The Unprecedented Pacific Northwest Heatwave of June 2021. *Nature Communications* **14,** 727. ISSN: 2041-1723. https://www.nature.com/articles/s41467-023-36289-3 (Feb. 9, 2023).

20. *FAQ 1.3 - AR4 WGI Chapter 1: Historical Overview of Climate Change Science* https://archive.ipcc.ch/publications_and_data/ar4/wg1/en/faq-1-3.html (accessed Apr. 8, 2025).

21. *WGI Summary for Policymakers Headline Statements* https://www.ipcc.ch/report/ar6/wg1/resources/spm-headline-statements/ (accessed Apr. 8, 2025).

22. Nzotungicimpaye, C.-M., MacIsaac, A. J. & Zickfeld, K. Delaying Methane Mitigation Increases the Risk of Breaching the 2 °C Warming Limit. *Communications Earth & Environment* **4,** 1–8. ISSN: 2662-4435. https://www.nature.com/articles/s43247-023-00898-z (July 12, 2023).

23. *Figure AR6 WG1* IPCC Sixth Assessment Report, Working Group 1: The Physical Science Basis. https://www.ipcc.ch/report/ar6/wg1/figures/chapter-7/figure-7-6 (accessed July 28, 2023).

24. Jackson, R. B. *et al.* Human Activities Now Fuel Two-Thirds of Global Methane Emissions. *Environmental Research Letters* **19,** 101002. ISSN: 1748-9326. https://dx.doi.org/10.1088/1748-9326/ad6463 (Sept. 2024).

25. *Methane — Vital Signs* Climate Change: Vital Signs of the Planet. https://climate.nasa.gov/vital-signs/methane?intent=121 (accessed Apr. 8, 2025).

26. *Trends in CH4 - NOAA Global Monitoring Laboratory* https://gml.noaa.gov/ccgg/trends_ch4/index.html (accessed Apr. 8, 2025).

27. Etheridge, D. M., Steele, L. P., Francey, R. J. & Langenfelds, R. L. Atmospheric Methane between 1000 A.D. and Present: Evidence of Anthropogenic Emissions and Climatic Variability. *Journal of Geophysical Research: Atmospheres* **103,** 15979–15993. ISSN: 2156-2202. https://doi.org/10.1029/98JD00923 (1998).

28. *Climate Change 2021: The Physical Science Basis. Contribution of Working Group I to the Sixth Assessment Report of the Intergovernmental Panel on Climate Change. Chapter 7 Supplementary Material.* 923-1054 (Cambridge University Press, Cambridge, United Kingdom, 2021).

29. Skea, J. *et al.* in *Climate Change 2022: Mitigation of Climate Change. Contribution of Working Group III to the Sixth Assessment Report of the Intergovernmental Panel on Climate Change* (eds Shukla, P. R. *et al.*) 1–48 (Cambridge University Press, Cambridge, UK and New York, NY, USA, 2022).

30. *Trends in Electric Cars – Global EV Outlook 2024 – Analysis* IEA. https://www.iea.org/reports/global-ev-outlook-2024/trends-in-electric-cars (accessed Apr. 9, 2025).

31. *Chapter 9: Buildings* https://www.ipcc.ch/report/ar6/wg3/chapter/chapter-9/ (accessed Apr. 11, 2025).

32. *Chapter 11: Industry* https://www.ipcc.ch/report/ar6/wg3/chapter/chapter-11/ (accessed Apr. 11, 2025).

33. Davis, S. J. *et al.* Net-Zero Emissions Energy Systems. *Science* **360,** eaas9793. https://www.science.org/doi/10.1126/science.aas9793 (June 29, 2018).

34. Edelenbosch, O. Y. *et al.* Reducing Sectoral Hard-to-Abate Emissions to Limit Reliance on Carbon Dioxide Removal. *Nature Climate Change* **14,** 715–722. ISSN: 1758-6798. https://www.nature.com/articles/s41558-024-02025-y (July 2024).

35. Harmsen, M. *et al.* The Role of Methane in Future Climate Strategies: Mitigation Potentials and Climate Impacts. *Climatic Change* **163,** 1409–1425. ISSN: 1573-1480. https://doi.org/10.1007/s10584-019-02437-2 (Dec. 1, 2020).

36. *Methane Emissions Must Fall for World to Hit Temperature Targets* World Economic Forum. https://www.weforum.org/stories/2022/11/methane-emissions-must-fall-to-hit-temperature-targets/ (accessed Apr. 11, 2025).

37. Rumsa, M., John, M. & Biswas, W. Global Steel Decarbonisation Roadmaps: Near-zero by 2050. *Environmental Impact Assessment Review* **112,** 107807. ISSN: 0195-9255. https://doi.org/10.1016/j.eiar.2025.107807 (Mar. 1, 2025).

38. Nisbet, E. G. *et al.* Practical Paths towards Quantifying and Mitigating Agricultural Methane Emissions. *Proceedings of the Royal Society A: Mathematical, Physical and Engineering Sciences* **481,** 20240390. https://royalsocietypublishing.org/doi/full/10.1098/rspa.2024.0390 (Mar. 5, 2025).

39. in. *Climate Change 2022 - Mitigation of Climate Change* (ed Intergovernmental Panel On Climate Change (Ipcc)) 1st ed., 295–408 (Cambridge University Press, Aug. 17, 2023). ISBN: 978-1-00-915792-6. https://www.cambridge.org/core/product/identifier/9781009157926%23c3/type/book_part (accessed Apr. 11, 2025).

40. *Archive.Ipcc.Ch/Ipccreports/Tar/Wg1/249.Htm* https://archive.ipcc.ch/ipccreports/tar/wg1/249.htm (accessed Apr. 12, 2025).

41. *Carbon Monoxide* Occupational Safety and Health Administration. https://www.osha.gov/chemicaldata/462 (accessed Apr. 12, 2025).

42. Abernethy, S., Kessler, M. I. & Jackson, R. B. Assessing the Potential Benefits of Methane Oxidation Technologies Using a Concentration-Based Framework. *Environmental Research Letters* **18,** 094064. ISSN: 1748-9326. https://dx.doi.org/10.1088/1748-9326/acf603 (Sept. 2023).

43. Plant, G. *et al.* Inefficient and Unlit Natural Gas Flares Both Emit Large Quantities of Methane. *Science* **377,** 1566–1571. https://www.science.org/doi/10.1126/science.abq0385 (Sept. 30, 2022).

44. *Chapter 6: Energy Systems* https://www.ipcc.ch/report/ar6/wg3/chapter/chapter-6/ (accessed Apr. 12, 2025).

45. Parisi, P. *et al. Toward 2050: Critical Analysis of Energy and Economic Requirements of Carbon Capture and Storage in Post Combustion Capture* in (). https://dx.doi.org/10.2118/220020-MS (accessed Apr. 12, 2025).

46. Jackson, R. B. *et al.* Atmospheric Methane Removal: A Research Agenda. *Philosophical Transactions of the Royal Society A: Mathematical, Physical and Engineering Sciences* **379,** 20200454. ISSN: 1364-503X, 1471-2962. https://royalsocietypublishing.org/doi/10.1098/rsta.2020.0454 (Nov. 15, 2021).

47. Caballero, A. & Pérez, P. J. Methane as Raw Material in Synthetic Chemistry: The Final Frontier. *Chemical Society Reviews* **42,** 8809–8820. ISSN: 1460-4744. https://pubs.rsc.org/en/content/articlelanding/2013/cs/c3cs60120j (Nov. 4, 2013).

48. Vaughan, N. *et al.* The State of Carbon Dioxide Removal - 2nd Edition. https://osf.io/f85qj/ (2024).

49. Jackson, R. B., Solomon, E. I., Canadell, J. G., Cargnello, M. & Field, C. B. Methane Removal and Atmospheric Restoration. *Nature Sustainability* **2,** 436–438. ISSN: 2398-9629. http://www.nature.com/articles/s41893-019-0299-x (June 2019).

50. Vohra, K. *et al.* Global Mortality from Outdoor Fine Particle Pollution Generated by Fossil Fuel Combustion: Results from GEOS-Chem. *Environmental Research* **195,** 110754. ISSN: 0013-9351. https://doi.org/10.1016/j.envres.2021.110754 (Apr. 1, 2021).

51. Lelieveld, J. *et al.* Air Pollution Deaths Attributable to Fossil Fuels: Observational and Modelling Study. https://www.bmj.com/content/383/bmj-2023-077784 (Nov. 29, 2023).

52. Newbold, T. Future Effects of Climate and Land-Use Change on Terrestrial Vertebrate Community Diversity under Different Scenarios. *Proceedings of the Royal Society B: Biological Sciences* **285,** 20180792. https://royalsocietypublishing.org/doi/10.1098/rspb.2018.0792 (June 20, 2018).

53. (PDF) Biodiversity Impacts of Recent Land-Use Change Driven by Increases in Agri-Food Imports. *ResearchGate.* https://www.researchgate.net/publication/384199795_Biodiversity_impacts_of_recent_land-use_change_driven_by_increases_in_agri-food_imports (Apr. 2, 2025).

54. Naidu, R. *et al.* Chemical Pollution: A Growing Peril and Potential Catastrophic Risk to Humanity. *Environment International* **156,** 106616. ISSN: 0160-4120. https://doi.org/10.1016/j.envint.2021.106616 (Nov. 1, 2021).

55. Johnston, J. & Cushing, L. Chemical Exposures, Health and Environmental Justice in Communities Living on the Fenceline of Industry. *Current environmental health reports* **7,** 48–57. ISSN: 2196-5412. pmid: 31970715. https://www.ncbi.nlm.nih.gov/pmc/articles/PMC7035204/ (Mar. 2020).

56. Macklin, M. G. *et al.* Impacts of Metal Mining on River Systems: A Global Assessment. *Science* **381,** 1345–1350. https://www.science.org/doi/10.1126/science.adg6704 (Sept. 22, 2023).

57. Warren-Vega, W. M., Campos-Rodríguez, A., Zárate-Guzmán, A. I. & Romero-Cano, L. A. A Current Review of Water Pollutants in American Continent: Trends and Perspectives in Detection, Health Risks, and Treatment Technologies. *International Journal of Environmental Research and Public Health* **20,** 4499. ISSN: 1660-4601. https://www.mdpi.com/1660-4601/20/5/4499 (Jan. 2023).

58. Jackson, T. *Prosperity without Growth: Economics for a Finite Planet* 264 pp. (Earthscan, London ; Sterling, VA, 2009).

59. *AR6 Synthesis Report: Climate Change 2023 — IPCC* https://www.ipcc.ch/report/sixth-assessment-report-cycle/ (accessed Apr. 11, 2025).

60. Chowkwanyun, M. Environmental Justice: Where It Has Been, and Where It Might Be Going. *Annual Review of Public Health* **44,** 93–111. ISSN: 0163-7525, 1545-2093. https://www.annualreviews.org/content/journals/10.1146/annurev-publhealth-071621-064925 (Apr. 3, 2023).

61. Al-Aly, Z. We Must All Join the Effort to Dismantle Environmental Racism. *Journal of the American Society of Nephrology* **33,** 12. ISSN: 1046-6673. https://journals.lww.com/jasn/fulltext/2022/01000/we_must_all_join_the_effort_to_dismantle.6.aspx (Jan. 2022).

62. Lippert, J., Fagan, M., Huang, Christine, Clancy, Laura & Lippert, Jordan. *Economic Inequality Seen as Major Challenge Around the World* Pew Research Center. https://www.pewresearch.org/global/2025/01/09/economic-inequality-seen-as-major-challenge-around-the-world/ (accessed Apr. 11, 2025).

63. *Good Economics for Hard Times* ISBN: 978-1-5491-5262-7. https://www.hachettebookgroup.com/titles/abhijit-v-banerjee/good-economics-for-hard-times/9781549152627/?lens=publicaffairs (Mar. 5, 2019).

64. Jackson, R. B. *et al.* Human Activities Now Fuel Two-Thirds of Global Methane Emissions. *Environmental Research Letters* **19,** 101002. ISSN: 1748-9326. https://dx.doi.org/10.1088/1748-9326/ad6463 (Sept. 2024).

65. *Figure AR6 WG1* https://www.ipcc.ch/report/ar6/wg1/figures/technical-summary/figure-ts-15 (accessed Apr. 8, 2025).

66. *Medium-Term Gas Report 2023 – Analysis* IEA. https://www.iea.org/reports/medium-term-gas-report-2023 (accessed Apr. 29, 2025).

67. *Density of Gases Data* https://www.engineeringtoolbox.com/gas-density-d_158.html (accessed Apr. 29, 2025).

68. Singleton, C. M. *et al.* Methanotrophy across a Natural Permafrost Thaw Environment. *The ISME Journal* **12,** 2544–2558. ISSN: 1751-7362. https://doi.org/10.1038/s41396-018-0065-5 (Oct. 1, 2018).

69. Kizilova, A., Yurkov, A. & Kravchenko, I. Aerobic Methanotrophs in Natural and Agricultural Soils of European Russia. *Diversity* **5,** 541–556. ISSN: 1424-2818. https://www.mdpi.com/1424-2818/5/3/541 (Sept. 2013).

70. Krogsbøll, M. *et al. Removing Ammonia, Odor and Dilute Methane from Ventilation Air from Cow, Pig and Biogas Facilities* https://chemrxiv.org/engage/chemrxiv/article-details/678a699581d2151a0286e3cd (accessed Feb. 18, 2025). Pre-published.

71. *UNECE Best Practice Guidance on Ventilation Air Methane Mitigation — UNECE* https://unece.org/sustainable-energy/publications/unece-best-practice-guidance-ventilation-air-methane-mitigation (accessed Apr. 23, 2025).

72. Lackner, K. S. Practical Constraints on Atmospheric Methane Removal. *Nature Sustainability* **3,** 357–357. ISSN: 2398-9629. http://www.nature.com/articles/s41893-020-0496-7 (May 2020).

73. Nisbet-Jones, P. B. R. *et al.* Is the Destruction or Removal of Atmospheric Methane a Worthwhile Option? *Philosophical Transactions of the Royal Society A: Mathematical, Physical and Engineering Sciences* **380,** 20210108. ISSN: 1364-503X, 1471-2962. https://royalsocietypublishing.org/doi/10.1098/rsta.2021.0108 (Jan. 24, 2022).

74. Aaron, D. & and Tsouris, C. Separation of CO2 from Flue Gas: A Review. *Separation Science and Technology* **40,** 321–348. ISSN: 0149-6395. https://doi.org/10.1081/SS-200042244 (Feb. 1, 2005).

75. *Scrubber - Energy Education* https://energyeducation.ca/encyclopedia/Scrubber (accessed Apr. 12, 2025).

76. *Regulations.Gov* https://www.regulations.gov/document/EPA-HQ-OAR-2015-0341-0082 (accessed Apr. 30, 2025).

77. Spray-Chamber/Spray-Tower Wet Scrubber.

78. POWER. *Bringing down the Cost of SO2 and NOx Removal* POWER Magazine. https://www.powermag.com/bringing-down-the-cost-of-so2-and-nox-removal/ (accessed Apr. 30, 2025).

79. La, H., Hettiaratchi, J. P. A., Achari, G. & Dunfield, P. F. Biofiltration of Methane. *Bioresource Technology* **268,** 759–772. ISSN: 0960-8524. https://doi.org/10.1016/j.biortech.2018.07.043 (Nov. 1, 2018).

80. Keith, D. W., Holmes, G., St. Angelo, D. & Heidel, K. A Process for Capturing CO2 from the Atmosphere. *Joule* **2,** 1573–1594. ISSN: 2542-4351. https://doi.org/10.1016/j.joule.2018.05.006 (Aug. 15, 2018).

81. *9.4 Carbon Removal* Speed & Scale. https://speedandscale.com/okrs/9-0-innovate/9-4-carbon-removal/ (accessed Apr. 25, 2025).

82. Azar, C., Martín, J. G., Johansson, D. J. & Sterner, T. The Social Cost of Methane. *Climatic Change* **176,** 1–22. ISSN: 1573-1480. https://doi.org/10.1007/s10584-023-03540-1 (June 1, 2023).

83. Errickson, F. C., Keller, K., Collins, W. D., Srikrishnan, V. & Anthoff, D. Equity Is More Important for the Social Cost of Methane than Climate Uncertainty. *Nature* **592,** 564–570. ISSN: 1476-4687. https://www.nature.com/articles/s41586-021-03386-6 (Apr. 2021).

84. US EPA, O. P. *EPA's "Report on the Social Cost of Greenhouse Gases: Estimates Incorporating Recent Scientific Advances"* https://www.epa.gov/environmental-economics/scghg (accessed Feb. 21, 2025).

85. *Congress Votes to Kill Biden-era Methane Fee on Oil and Gas Producers — AP News* https://apnews.com/article/methane-fee-repeal-epa-oil-gas-drilling-4844558bece1e683da9246ee226c57b5 (accessed Apr. 25, 2025).

86. Smith, A. *How Much Should Dairy Farms Get Paid for Trapping Methane?* Energy Institute Blog. https://energyathaas.wordpress.com/2024/10/14/how-much-should-dairy-farms-get-paid-for-trapping-methane/ (accessed Apr. 25, 2025).

87. Pandey, S., Budhathoki, M. & Thomsen, M. Consumer Intentions and Willingness to Pay for Seaweed-Fed Cow's Milk: The Impact of Attitude, Knowledge, Taste, and Price. *Future Foods* **11,** 100539. ISSN: 2666-8335. https://doi.org/10.1016/j.fufo.2025.100539 (June 1, 2025).

88. Massaro, S. *et al.* Review of Equations to Predict Methane Emissions in Dairy Cows from Milk Fatty Acid Profiles and Their Application to Commercial Dairy Farms. *Journal of Dairy Science* **107,** 5833–5852. ISSN: 0022-0302. https://www.sciencedirect.com/science/article/pii/S0022030224009032 (Aug. 1, 2024).

89. Davidson, K. A., McFadden, B. R., Meyer, S. & Bernard, J. C. Consumer Preferences for Low-Methane Beef: The Impact of Pre-Purchase Information, Point-of-Purchase Labels, and Increasing Prices. *Food Policy* **130,** 102768. ISSN: 0306-9192. https://doi.org/10.1016/j.foodpol.2024.102768 (Jan. 1, 2025).

90. Rolfe, D. J. Economics of Reducing Methane Emissions from Cattle Production in Central Queensland. *Meat and Livestock Australia* (June 2001).

91. Wang, T. *et al.* Flammability Limit Behavior of Methane with the Addition of Gaseous Fuel at Various Relative Humidities. *Process Safety and Environmental Protection* **140,** 178–189. ISSN: 0957-5820. https://doi.org/10.1016/j.psep.2020.05.005 (Aug. 1, 2020).

92. Yang, J. *et al.* Experimental Study on Ultra-Low Concentration Methane Regenerative Thermal Oxidation. *Energies* **17,** 2109. ISSN: 1996-1073. https://www.mdpi.com/1996-1073/17/9/2109 (Jan. 2024).

93. *Resolute Methane* Activate. https://www.activate.org/resolute-methane (accessed Apr. 23, 2025).

94. Brenneis, R. J., Johnson, E. P., Shi, W. & Plata, D. L. Atmospheric- and Low-Level Methane Abatement via an Earth-Abundant Catalyst. *ACS Environmental Au* **2,** 223–231. https://doi.org/10.1021/acsenvironau.1c00034 (May 18, 2022).

95. Parker, A. *Stability and Lifetime of a Copper-Doped Zeolite Catalyst for Low-Level Methane Removal* in. American Geophysical Union 2024 (Dec. 13, 2024). https://agu.confex.com/agu/agu24/meetingapp.cgi/Person/1553743 (accessed Apr. 23, 2025).

96. *Moxair* Moxair. http://moxair.us (accessed Apr. 23, 2025).

97. Wang, Y. *et al.* Removing Low-Concentration Methane via Thermo-Catalytic Oxidation on CuOx/Zeolite. *Applied Surface Science* **682,** 161691. ISSN: 0169-4332. https://doi.org/10.1016/j.apsusc.2024.161691 (Feb. 15, 2025).

98. Oh, J., Boucly, A., van Bokhoven, J. A., Artiglia, L. & Cargnello, M. Palladium Catalysts for Methane Oxidation: Old Materials, New Challenges. *Accounts of Chemical Research* **57,** 23–36. ISSN: 0001-4842. https://doi.org/10.1021/acs.accounts.3c00454 (Jan. 2, 2024).

99. Tsopelakou, A. M., Stallard, J., Archibald, A. T., Fitzgerald, S. & Boies, A. M. Exploring the Bounds of Methane Catalysis in the Context of Atmospheric Methane Removal. *Environmental Research Letters* **19,** 054020. ISSN: 1748-9326. https://iopscience.iop.org/article/10.1088/1748-9326/ad383f (May 1, 2024).

100. Scanlon, D. O. *et al.* Band Alignment of Rutile and Anatase TiO2. *Nature Materials* **12,** 798–801. ISSN: 1476-4660. https://www.nature.com/articles/nmat3697 (Sept. 2013).

101. He, F., Jeon, W. & Choi, W. Photocatalytic Air Purification Mimicking the Self-Cleaning Process of the Atmosphere. *Nature Communications* **12,** 2528. ISSN: 2041-1723. https://www.nature.com/articles/s41467-021-22839-0 (May 5, 2021).

102. Chen, X. *et al.* Photocatalytic Oxidation of Methane over Silver Decorated Zinc Oxide Nanocatalysts. *Nature Communications* **7,** 12273. ISSN: 2041-1723. http://www.nature.com/articles/ncomms12273 (Nov. 2016).

103. Li, Z., Pan, X. & Yi, Z. Photocatalytic Oxidation of Methane over CuO-decorated ZnO Nanocatalysts. *Journal of Materials Chemistry A* **7,** 469–475. ISSN: 2050-7488, 2050-7496. http://xlink.rsc.org/?DOI=C8TA09592B (2019).

104. Sher Shah, M. S. A. *et al.* Catalytic Oxidation of Methane to Oxygenated Products: Recent Advancements and Prospects for Electrocatalytic and Photocatalytic Conversion at Low Temperatures. *Advanced Science* **7,** 2001946. ISSN: 2198-3844. https://doi.org/10.1002/advs.202001946 (2020).

105. Fjelsted, L., Scheutz, C., Christensen, A. G., Larsen, J. E. & Kjeldsen, P. Biofiltration of Diluted Landfill Gas in an Active Loaded Open-Bed Compost Filter. *Waste Management* **103,** 1–11. ISSN: 0956-053X. https://doi.org/10.1016/j.wasman.2019.12.005 (Feb. 15, 2020).

106. Gebert, J., Huber-Humer, M. & Cabral, A. R. Design of Microbial Methane Oxidation Systems for Landfills. *Frontiers in Environmental Science* **10.** ISSN: 2296-665X. https://doi.org/10.3389/fenvs.2022.907562 (Sept. 1, 2022).

107. Melse, R. W. & van der Werf, A. W. Biofiltration for Mitigation of Methane Emission from Animal Husbandry. *Environmental Science & Technology* **39,** 5460–5468. ISSN: 0013-936X. https://doi.org/10.1021/es048048q (July 1, 2005).

108. Sly, L. I., Bryant, L. J., Cox, J. M. & Anderson, J. M. Development of a Biofilter for the Removal of Methane from Coal Mine Ventilation Atmospheres. *Applied Microbiology and Biotechnology* **39,** 400–404. ISSN: 1432-0614. https://doi.org/10.1007/BF00192101 (June 1, 1993).

109. Josiane, N. & Michèle, H. The Influence of the Gas Flow Rate during Methane Biofiltration on an Inorganic Packing Material. *The Canadian Journal of Chemical Engineering* **87,** 136–142. ISSN: 1939-019X. https://doi.org/10.1002/cjce.20131 (2009).

110. He, L. *et al.* A Methanotrophic Bacterium to Enable Methane Removal for Climate Mitigation. *Proceedings of the National Academy of Sciences* **120,** e2310046120. https://doi.org/10.1073/pnas.2310046120 (Aug. 29, 2023).

111. Capture of Methane by Fungi: Evidence from Laboratory-Scale Biofilter and Chromatographic Isotherm Studies. https://doi.org/10.13031/trans.59.11595.

112. Yoon, S., Carey, J. N. & Semrau, J. D. Feasibility of Atmospheric Methane Removal Using Methanotrophic Biotrickling Filters. *Applied Microbiology and Biotechnology* **83,** 949–956. ISSN: 1432-0614. https://doi.org/10.1007/s00253-009-1977-9 (July 1, 2009).

113. Estrada, J. M. *et al.* Methane Abatement in a Gas-Recycling Biotrickling Filter: Evaluating Innovative Operational Strategies to Overcome Mass Transfer Limitations. *Chemical Engineering Journal* **253,** 385–393. ISSN: 1385-8947. https://doi.org/10.1016/j.cej.2014.05.053 (Oct. 1, 2014).

114. Tikhomirova, T. S. & But, S. Y. Laboratory Scale Bioreactor Designs in the Processes of Methane Bioconversion: Mini-review. *Biotechnology Advances* **47,** 107709. ISSN: 0734-9750. https://doi.org/10.1016/j.biotechadv.2021.107709 (Mar. 1, 2021).

115. Lidstrom, M. E. Direct Methane Removal from Air by Aerobic Methanotrophs. *Cold Spring Harbor Perspectives in Biology* **16,** a041671. ISSN: , 1943-0264. pmid: 37923397. http://cshperspectives.cshlp.org/content/16/7/a041671 (July 1, 2024).

116. Sakai, Y., Yurimoto, H. & Shima, S. Methane Monooxygenases; Physiology, Biochemistry and Structure. *Catalysis Science & Technology* **13,** 6342–6354. https://pubs.rsc.org/en/content/articlelanding/2023/cy/d3cy00737e (2023).

117. *Discover or Engineer Efficient Soluble Methane Monooxygenase* Spark Climate Solutions. https://www.sparkclimate.org/problem-statement/discover-or-engineer-efficient-soluble-methane-monooxygenase (accessed Apr. 24, 2025).

118. *A Research Agenda Toward Atmospheric Methane Removal* ISBN: 978-0-309-70665-0. https://nap.nationalacademies.org/catalog/27157 (National Academies Press, Washington, D.C., Dec. 27, 2024).

119. Adnew, G. A. *et al.* Gas-Phase Advanced Oxidation as an Integrated Air Pollution Control Technique. *AIMS Environmental Science* **3,** 141–158. ISSN: 2372-0352. http://www.aimspress.com/rticle/doi/10.3934/environsci.2016.1.141 (2016).

120. Krogsbøll, M., Russell, H. S. & Johnson, M. S. A High Efficiency Gas Phase Photoreactor for Eradication of Methane from Low-Concentration Sources. *Environmental Research Letters* **19,** 014017. ISSN: 1748-9326. https://dx.doi.org/10.1088/1748-9326/ad0e33 (Dec. 2023).

121. Johnson, M. S., Nilsson, E. J. K., Svensson, E. A. & Langer, S. Gas-Phase Advanced Oxidation for Effective, Efficient in Situ Control of Pollution. *Environmental Science & Technology* **48,** 8768–8776. ISSN: 0013-936X. https://doi.org/10.1021/es5012687 (Aug. 5, 2014).

122. Iversen, N. & Roslev, P. Mitigation of Atmospheric and Elevated Methane by Photochemical Oxidation at Ambient Conditions. *Science of The Total Environment* **976,** 179338. ISSN: 0048-9697. https://doi.org/10.1016/j.scitotenv.2025.179338 (May 10, 2025).

123. Lockhart, J. P., Gross, E. C., Sears, T. J. & Hall, G. E. Investigating the Photodissociation of H2O2 Using Frequency Modulation Laser Absorption Spectroscopy to Monitor Radical Products. *Chemical Physics Letters* **711,** 148–151. ISSN: 00092614. https://doi.org/10.1016/j.cplett.2018.09.004 (Nov. 2018).

124. Horowitz, H. M. Intended and Unintended Consequences of Atmospheric Methane Oxidation Enhancement. *EGUsphere,* 1–31. https://egusphere.copernicus.org/preprints/2024/egusphere-2024-3139/ (Dec. 5, 2024).

125. Eurochlor. *Electrolyisis Production Costs* July 2018. https://www.eurochlor.org/wp-content/uploads/2021/04/12-Electrolysis-production-costs.pdf (accessed Oct. 30, 2024).

126. Yuan, Q. *et al.* Tropospheric Methane Remediation by Enhancing Chlorine Sinks. *RSC Sustainability* **3,** 1524–1538. ISSN: 2753-8125. https://pubs.rsc.org/en/content/articlelanding/2025/su/d4su00716f (Mar. 5, 2025).

127. Oeste, F. D., de Richter, R., Ming, T. & Caillol, S. Climate Engineering by Mimicking Natural Dust Climate Control: The Iron Salt Aerosol Method. *Earth System Dynamics* **8,** 1–54. ISSN: 2190-4987. https://esd.copernicus.org/articles/8/1/2017/ (Jan. 13, 2017).

128. Gorham, K. A. *et al.* Opinion: A Research Roadmap for Exploring Atmospheric Methane Removal via Iron Salt Aerosol. *Atmospheric Chemistry and Physics* **24,** 5659–5670. ISSN: 1680-7316. https://acp.copernicus.org/articles/24/5659/2024/ (May 15, 2024).

129. Meidan, D. *et al.* Evaluating the Potential of Iron-Based Interventions in Methane Reduction and Climate Mitigation. *Environmental Research Letters* **19,** 054023. ISSN: 1748-9326. https://dx.doi.org/10.1088/1748-9326/ad3d72 (Apr. 2024).

130. Pennacchio, L., Van Herpen, M., Meidan, D., Saiz-Lopez, A. & S. Johnson, M. *Catalytic Efficiencies for Atmospheric Methane Removal in the High-Chlorine Regime* https://doi.org/10.1021/acsearthspacechem.4c00283 (accessed Apr. 26, 2024). Pre-published.

131. Polat, M., Liisberg, J. B., Krogsbøll, M., Blunier, T. & Johnson, M. S. Photochemical Method for Removing Methane Interference for Improved Gas Analysis. *Atmospheric Measurement Techniques* **14,** 8041–8067. ISSN: 1867-1381. https://amt.copernicus.org/articles/14/8041/2021/ (Dec. 23, 2021).

132. Ming, T. *et al.* A Novel Green Technology: Reducing Carbon Dioxide and Eliminating Methane from the Atmosphere. *International Journal of Energy Research* **46,** 20107–20120. ISSN: 1099-114X. https://doi.org/10.1002/er.8675 (2022).

133. *Direct Air Capture of CO2 with Chemicals* https://www.aps.org/publications/reports/direct-air-capture-co2 (accessed Apr. 20, 2025).

134. House, K. Z. *et al.* Economic and Energetic Analysis of Capturing CO2 from Ambient Air. *Proceedings of the National Academy of Sciences* **108,** 20428–20433. https://www.pnas.org/doi/full/10.1073/pnas.1012253108 (Dec. 20, 2011).

135. Holmes, G. & Keith, D. W. An Air–Liquid Contactor for Large-Scale Capture of CO2 from Air. *Philosophical Transactions of the Royal Society A: Mathematical, Physical and Engineering Sciences* **370,** 4380–4403. https://royalsocietypublishing.org/doi/abs/10.1098/rsta.2012.0137 (Sept. 13, 2012).

136. Zeman, F. Experimental Results for Capturing CO2 from the Atmosphere. *AIChE Journal* **54,** 1396–1399. ISSN: 1547-5905. https://doi.org/10.1002/aic.11452 (2008).

137. *1PointFive's South Texas Direct Air Capture Hub Awarded U.S. Department of Energy Funding* https://www.oxy.com/news/news-releases/1pointfives-south-texas-direct-air-capture-hub-awarded-u.s.-department-of-energy-funding (accessed Apr. 20, 2025).

138. Lai, Y. *et al.* Low-Temperature Oxidation of Methane on Rutile TiO2(110): Identifying the Role of Surface Oxygen Species. *JACS Au.* https://pubs.acs.org/doi/full/10.1021/jacsau.3c00771 (Mar. 26, 2024).

139. Byrne, C., Subramanian, G. & Pillai, S. C. Recent Advances in Photocatalysis for Environmental Applications. *Journal of Environmental Chemical Engineering* **6,** 3531–3555. ISSN: 22133437. https://linkinghub.elsevier.com/retrieve/pii/S2213343717303846 (June 2018).

140. Li, Q., Ouyang, Y., Li, H., Wang, L. & Zeng, J. Photocatalytic Conversion of Methane: Recent Advancements and Prospects. *Angewandte Chemie International Edition* **61.** ISSN: 1433-7851, 1521-3773. https://doi.org/10.1002/anie.202108069 (Jan. 10, 2022).

141. Donat, F. *et al.* ZnO Nanoparticles Sensitized by CuInZn x S2+x Quantum Dots as Highly Efficient Solar Light Driven Photocatalysts. *Beilstein Journal of Nanotechnology* **8,** 1080–1093. ISSN: 2190-4286. https://pubmed.ncbi.nlm.nih.gov/28685109/ (2017).

142. Sordello, F., Calza, P., Minero, C., Malato, S. & Minella, M. More than One Century of History for Photocatalysis, from Past, Present and Future Perspectives. *Catalysts* **12,** 1572. ISSN: 2073-4344. https://www.mdpi.com/2073-4344/12/12/1572 (Dec. 2022).

143. Almaie, S., Vatanpour, V., Rasoulifard, M. H. & Koyuncu, I. Volatile Organic Compounds (VOCs) Removal by Photocatalysts: A Review. *Chemosphere* **306,** 135655. ISSN: 0045-6535. https://doi.org/10.1016/j.chemosphere.2022.135655 (Nov. 1, 2022).

144. Song, H. *et al.* Direct and Selective Photocatalytic Oxidation of CH4 to Oxygenates with O2 on Cocatalysts/ZnO at Room Temperature in Water. *Journal of the American Chemical Society* **141,** 20507–20515. ISSN: 0002-7863. https://doi.org/10.1021/jacs.9b11440 (Dec. 26, 2019).

145. Pan, X., Chen, X. & Yi, Z. Photocatalytic Oxidation of Methane over SrCO $_3$ Decorated SrTiO $_3$ Nanocatalysts via a Synergistic Effect. *Physical Chemistry Chemical Physics* **18,** 31400–31409. ISSN: 1463-9076, 1463-9084. http://xlink.rsc.org/?DOI=C6CP04604E (2016).

146. Sun, C., Zhao, K., Boies, A., Xiao, S. & Yi, Z. Boosting Total Oxidation of Methane over NiO Nanocrystalline Decorated ZnO-CoNi Solid Solution via Photothermal Synergism. *Applied Catalysis B: Environmental* **339,** 123124. ISSN: 0926-3373. https://doi.org/10.1016/j.apcatb.2023.123124 (Dec. 15, 2023).

147. Xie, C. *et al.* Transport Mediating Core–Shell Photocatalyst Architecture for Selective Alkane Oxidation. *Nano Letters* **23,** 2039–2045. ISSN: 1530-6984. https://doi.org/10.1021/acs.nanolett.2c04567 (Mar. 8, 2023).

148. Ma, Z., Chen, Y., Gao, C. & Xiong, Y. A Minireview on the Role of Cocatalysts in Semiconductor-Based Photocatalytic CH $_4$ Conversion. *Energy & Fuels,* acs.energyfuels.2c01351. ISSN: 0887-0624, 1520-5029. https://pubs.acs.org/doi/10.1021/acs.energyfuels.2c01351 (June 23, 2022).

149. Xiong, H. *et al.* Experimental and Kinetic Studies on the Photocatalysis of UV–Vis Light Irradiation for Low Concentrations of the Methane. *Applied Energy* **377,** 124388. ISSN: 0306-2619. https://doi.org/10.1016/j.apenergy.2024.124388 (Jan. 1, 2025).

150. Sato, H. *et al.* Critical Impacts of Interfacial Water on C–H Activation in Photocatalytic Methane Conversion. *Communications Chemistry* **6,** 8. ISSN: 2399-3669. https://www.nature.com/articles/s42004-022-00803-3 (Jan. 20, 2023).

151. Shayegan, Z., Lee, C.-S. & Haghighat, F. TiO2 Photocatalyst for Removal of Volatile Organic Compounds in Gas Phase – A Review. *Chemical Engineering Journal* **334,** 2408–2439. ISSN: 1385-8947. https://doi.org/10.1016/j.cej.2017.09.153 (Feb. 15, 2018).

152. Mills, A., Burns, L., O'Rourke, C. & Elouali, S. Kinetics of the Photocatalysed Oxidation of NO in the ISO 22197 Reactor. *Journal of Photochemistry and Photobiology A: Chemistry* **321,** 137–142. ISSN: 1010-6030. https://doi.org/10.1016/j.jphotochem.2016.01.010 (May 1, 2016).

153. Muñoz, V., Casado, C., Suárez, S., Sánchez, B. & Marugán, J. Photocatalytic NOx Removal: Rigorous Kinetic Modelling and ISO Standard Reactor Simulation. *Catalysis Today. SI: Proc PSS2017* **326,** 82–93. ISSN: 0920-5861. https://doi.org/10.1016/j.cattod.2018.09.001 (Apr. 1, 2019).

154. Incropera, F. P. & Incropera, F. P. F. of heat and mass transfer. *Fundamentals of Heat and Mass Transfer* 1070 pp. http://archive.org/details/fundamentalsheat00incr_617 (Hoboken, NJ : John Wiley, 2007).

155. Ollis, D. F. Kinetics of Photocatalyzed Reactions: Five Lessons Learned. *Frontiers in Chemistry* **6.** ISSN: 2296-2646. https://www.frontiersin.org/articles/10.3389/fchem.2018.00378 (2018).

156. Rubin, M. B. & Braslavsky, S. E. Quantum Yield: The Term and the Symbol. A Historical Search. *Photochemical & Photobiological Sciences* **9,** 670–674. ISSN: 1474-9092. https://pubs.rsc.org/en/content/articlelanding/2010/pp/b9pp00182d (May 4, 2010).

157. Pazokifard, S., Mirabedini, S. M., Esfandeh, M. & Farrokhpay, S. Fluoroalkylsilane Treatment of TiO2 Nanoparticles in Difference pH Values: Characterization and Mechanism. *Advanced Powder Technology. Special Issue Featuring Articles from Chemeca 2011* **23,** 428–436. ISSN: 0921-8831. https://doi.org/10.1016/j.apt.2012.02.006 (July 1, 2012).

158. Loddo, V., Roda, G. C. & Parrino, F. in *Heterogeneous Photocatalysis* (eds Marcì, G. & Palmisano, L.) 215–233 (Elsevier, Jan. 1, 2019). ISBN: 978-0-444-64015-4. https://doi.org/10.1016/B978-0-444-64015-4.00007-9 (accessed July 18, 2024).

159. Ohtani, B. Photocatalysis A to Z—What We Know and What We Do Not Know in a Scientific Sense. *Journal of Photochemistry and Photobiology C: Photochemistry Reviews* **11,** 157–178. ISSN: 1389-5567. https://doi.org/10.1016/j.jphotochemrev.2011.02.001 (Dec. 1, 2010).

160. Wachs, I. E., Phivilay, S. P. & Roberts, C. A. Reporting of Reactivity for Heterogeneous Photocatalysis. *ACS Catalysis* **3,** 2606–2611. https://doi.org/10.1021/cs4005979 (Nov. 1, 2013).

161. Best Practices for Reporting on Heterogeneous Photocatalysis. *ACS Applied Materials & Interfaces* **6,** 11815–11816. ISSN: 1944-8244. https://doi.org/10.1021/am504389z (Aug. 13, 2014).

162. Benkoula, S. *et al.* Water Adsorption on TiO2 Surfaces Probed by Soft X-ray Spectroscopies: Bulk Materials vs. Isolated Nanoparticles. *Scientific Reports* **5,** 15088. ISSN: 2045-2322. https://www.nature.com/articles/srep15088 (Oct. 14, 2015).

163. Kanari, N., Mishra, D., Gaballah, I. & Dupré, B. Thermal Decomposition of Zinc Carbonate Hydroxide. *Thermochimica Acta* **410,** 93–100. ISSN: 0040-6031. https://www.sciencedirect.com/science/article/pii/S0040603103003964 (Feb. 9, 2004).

164. Wiberg, N., Holleman, A. & Wiberg, E. *Holleman-Wiberg's Inorganic Chemistry* ISBN: 978-0-08-057461-5 (Academic Press, Oct. 11, 2001).

165. Hossain, M. K., Drmosh, Q. A., Yamani, Z. H. & Tabet, N. Silver Nanoparticles on Zinc Oxide Thin Film: An Insight in Fabrication and Characterization. *IOP Conference Series: Materials Science and Engineering* **64,** 012018. ISSN: 1757-899X. https://dx.doi.org/10.1088/1757-899X/64/1/012018 (Aug. 2014).

166. Ying, Z. *et al.* In Situ TEM Study: Deactivation Mechanism and Encapsulation Behavior of Metal Nanocatalysts Deposited on Zinc Oxide Nanowires. *Microscopy and Microanalysis* **29,** 1589–1590. ISSN: 1431-9276. https://doi.org/10.1093/micmic/ozad067.817 (Aug. 1, 2023).

167. Lavrenko, V. A., Malyshevskaya, A. I., Kuznetsova, L. I., Litvinenko, V. F. & Pavlikov, V. N. Features of High-Temperature Oxidation in Air of Silver and Alloy Ag-Cu, and Adsorption of Oxygen on Silver. *Powder Metallurgy and Metal Ceramics* **45,** 476–480. ISSN: 1573-9066. https://doi.org/10.1007/s11106-006-0108-8 (Sept. 1, 2006).

168. Chaparro, D. & Goudeli, E. Oxidation Rate and Crystallinity Dynamics of Silver Nanoparticles at High Temperatures. *The Journal of Physical Chemistry C* **127,** 13389–13397. ISSN: 1932-7447. https://doi.org/10.1021/acs.jpcc.3c03163 (July 13, 2023).

169. Watanabe, T. *et al.* Superior Thermal Stability and High Photocatalytic Activity of Titanium Dioxide Nanocatalysts in Carbon Nanotubes. *The Journal of Physical Chemistry C* **127,** 16861–16869. ISSN: 1932-7447. https://doi.org/10.1021/acs.jpcc.3c03619 (Aug. 31, 2023).

170. Velin, P. *et al.* Water Inhibition in Methane Oxidation over Alumina Supported Palladium Catalysts. *The Journal of Physical Chemistry C* **123,** 25724–25737. ISSN: 1932-7447. https://doi.org/10.1021/acs.jpcc.9b07606 (Oct. 24, 2019).

171. Jiang, D. *et al.* Dynamic and Reversible Transformations of Subnanometre-Sized Palladium on Ceria for Efficient Methane Removal. *Nature Catalysis* **6,** 618–627. ISSN: 2520-1158. https://www.nature.com/articles/s41929-023-00983-8 (July 2023).

172. Kim, J.-H. *et al.* Hydrophilic/Hydrophobic Silane Grafting on TiO2 Nanoparticles: Photocatalytic Paint for Atmospheric Cleaning. *Catalysts* **11,** 193. ISSN: 2073-4344. https://www.mdpi.com/2073-4344/11/2/193 (Feb. 2021).

173. Zong, L., Wu, Y., Li, X. & Jiang, B. The Preparation of Superhydrophobic Photocatalytic Fluorosilicone/SiO2–TiO2 Coating and Its Self-Cleaning Performance. *Journal of Coatings Technology and Research* **18,** 1245–1259. ISSN: 1935-3804. https://doi.org/10.1007/s11998-021-00485-x (Sept. 1, 2021).

174. Purcar, V. *et al.* Reparation of Hydrophobic and Antireflective Hybrid Films by Sol-Gel Process Using Perfluoroalkylsilane and Tetraethoxysilane. *Revue Romaine de Chimie* **58,** 283–289. https://revroum.lew.ro/wp-content/uploads/2013/2/Art%2024.pdf (Oct. 2013).

175. Ming, T. *et al.* Perspectives on Removal of Atmospheric Methane. *Advances in Applied Energy* **5,** 100085. ISSN: 26667924. https://doi.org/10.1016/j.adapen.2022.100085 (Feb. 2022).

176. Huang, Y. *et al.* Feasibility of Solar Updraft Towers as Photocatalytic Reactors for Removal of Atmospheric Methane–The Role of Catalysts and Rate Limiting Steps. *Frontiers in Chemistry* **9.** ISSN: 2296-2646. https://www.frontiersin.org/articles/10.3389/fchem.2021.745347 (2021).

177. Xiong, H. *et al.* Numerical Analysis of Solar Chimney Power Plant Integrated with CH4 Photocatalytic Reactors for Fighting Global Warming under Ambient Crosswind. *Renewable Energy* **201,** 678–690. ISSN: 0960-1481. https://doi.org/10.1016/j.renene.2022.11.024 (Dec. 1, 2022).

178. Johannisson, J. & Hiete, M. Exploring the Photocatalytic Total Oxidation of Methane through the Lens of a Prospective LCA. *Atmospheric Environment: X* **16,** 100190. ISSN: 2590-1621. https://doi.org/10.1016/j.aeaoa.2022.100190 (Dec. 1, 2022).

179. Bloh, J. Z. A Holistic Approach to Model the Kinetics of Photocatalytic Reactions. *Frontiers in Chemistry* **7.** ISSN: 2296-2646. https://www.frontiersin.org/articles/10.3389/fchem.2019.00128 (2019).

180. Murakami, Y., Endo, K., Ohta, I., Nosaka, A. Y. & Nosaka, Y. Can OH Radicals Diffuse from the UV-Irradiated Photocatalytic TiO2 Surfaces? Laser-Induced-Fluorescence Study. *The Journal of Physical Chemistry C* **111,** 11339–11346. ISSN: 1932-7447. https://doi.org/10.1021/jp0722049 (Aug. 1, 2007).

181. Weon, S., He, F. & Choi, W. Status and Challenges in Photocatalytic Nanotechnology for Cleaning Air Polluted with Volatile Organic Compounds: Visible Light Utilization and Catalyst Deactivation. *Environmental Science: Nano* **6,** 3185–3214. ISSN: 2051-8161. https://pubs.rsc.org/en/content/articlelanding/2019/en/c9en00891h (Nov. 7, 2019).

182. *How Much Does It Cost to Get Your Roof Cleaned?* Shine Window Cleaning. https://shine-windowcleaning.com/highland-park/how-much-does-it-cost-to-get-your-roof-cleaned/ (accessed July 18, 2023).

183. Kok, J. F. *et al.* Mineral Dust Aerosol Impacts on Global Climate and Climate Change. *Nature Reviews Earth & Environment* **4,** 71–86. ISSN: 2662-138X. https://www.nature.com/articles/s43017-022-00379-5 (Feb. 2023).

184. Sizirici, B., Fseha, Y., Cho, C.-S., Yildiz, I. & Byon, Y.-J. A Review of Carbon Footprint Reduction in Construction Industry, from Design to Operation. *Materials* **14,** 6094. ISSN: 1996-1944. pmid: 34683687. https://www.ncbi.nlm.nih.gov/pmc/articles/PMC8540435/ (Oct. 15, 2021).

185. *Sustainability of Rooftop Technologies in Cold Climates: Comparative Life Cycle Assessment of White Roofs, Green Roofs, and Photovoltaic Panels - Cubi - 2016 - Journal of Industrial Ecology - Wiley Online Library* https://doi.org/10.1111/jiec.12269 (accessed Dec. 15, 2023).

186. Kakaç, S., Yener, Y. & Pramuanjaroenkij, A. *Convective Heat Transfer* Third edition. 1 p. ISBN: 978-1-4665-8347-4 (CRC Press, Boca Raton, 2014).

187. *CRC Handbook of Chemistry and Physics* 85th Edition (ed Lide, D.) (CRC Press, Cleveland, Ohio, 2005).

188. Massman, W. J. A Review of the Molecular Diffusivities of H2O, CO2, CH4, CO, O3, SO2, NH3, N2O, NO, and NO2 in Air, O2 and N2 near STP. *Atmospheric Environment* **32,** 1111–1127. ISSN: 1352-2310. https://doi.org/10.1016/S1352-2310(97)00391-9 (Mar. 1, 1998).

189. *Titanium Dioxide (TiO2) Prices, Price, Pricing, Monitor— ChemAnalyst* https://www.chemanalyst.com/Pricing-data/titanium-dioxide-52 (accessed Dec. 15, 2023).

190. *Zinc Oxide Prices, News, Market Analysis, Monitor — ChemAnalyst* https://www.chemanalyst.com/Pricing-data/zinc-oxide-1199 (accessed Dec. 15, 2023).

191. *Commodity Markets* World Bank. https://www.worldbank.org/en/research/commodity-markets (accessed Feb. 17, 2023).

192. Crundwell, F. K. *Finance for Engineers: Evaluation and Funding of Capital Projects* 1 p. (Springer, London, 2008).

193. Randall, R., Jackson, R. B. & Majumdar, A. Cost Modeling of Photocatalytic Decomposition of Atmospheric Methane and Nitrous Oxide. *Environmental Research Letters* **19,** 064015. ISSN: 1748-9326. https://dx.doi.org/10.1088/1748-9326/ad4376 (May 2024).

194. Ramasamy, V., Feldman, D., Desai, J. & Margolis, R. *U.S. Solar Photovoltaic System and Energy Storage Cost Benchmarks: Q1 2021* NREL/TP-7A40-80694, 1829460, MainId:77478 (Nov. 2, 2021), NREL/TP-7A40–80694, 1829460, MainId:77478. https://www.osti.gov/servlets/purl/1829460/ (accessed Dec. 11, 2022).

195. Clear, R. D., Gartland, L. & Winkelmann, F. C. An Empirical Correlation for the Outside Convective Air-Film Coefficient for Horizontal Roofs. *Energy and Buildings* **35,** 797–811. ISSN: 0378-7788. https://doi.org/10.1016/S0378-7788(02)00240-2 (Sept. 1, 2003).

196. *CPI Inflation Calculator* https://www.bls.gov/data/inflation_calculator.htm (accessed Dec. 16, 2023).

197. Levinson, R., Akbari, H., Konopacki, S. & Bretz, S. Inclusion of Cool Roofs in Nonresidential Title 24 Prescriptive Requirements.

198. West, R. *Roof Coating Costs and Benefits* Cleveland, Ohio — Commercial Roofing Contractor. https://westroofingsystems.com/roof-coating-costs-and-benefits/ (accessed Dec. 13, 2022).

199. *White Roof Coating Cost* https://www.choiceroofcontractors.com/white-roof-coating-cost/ (accessed Dec. 13, 2022).

200. *Roof Cleaning Cost — How Much Does It Cost to Have a Roof Cleaned?* A & J Reliable, Inc. https://ajreliable.com/how-much-does-it-cost-to-hire-professionals-to-clean-a-roof/ (accessed July 18, 2023).

201. *U.S. Wind Climatology — National Centers for Environmental Information (NCEI)* https://www.ncei.noaa.gov/access/monitoring/wind/ (accessed July 19, 2023).

202. Govender, S. & Friedrich, H. B. Monoliths: A Review of the Basics, Preparation Methods and Their Relevance to Oxidation. *Catalysts* **7,** 62. ISSN: 2073-4344. https://www.mdpi.com/2073-4344/7/2/62 (Feb. 2017).

203. Dundar, I., Mere, A., Mikli, V., Krunks, M. & Oja Acik, I. Thickness Effect on Photocatalytic Activity of TiO2 Thin Films Fabricated by Ultrasonic Spray Pyrolysis. *Catalysts* **10,** 1058. ISSN: 2073-4344. https://www.mdpi.com/2073-4344/10/9/1058 (Sept. 2020).

204. *Inflation Reduction Act 2022: Sec. 60113 and Sec. 50263 on Methane Emissions Reductions – Policies* IEA. https://www.iea.org/policies/16317-inflation-reduction-act-2022-sec-60113-and-sec-50263-on-methane-emissions-reductions (accessed Dec. 7, 2022).

205. *Phoseon UV LED - Preventing Mercury Waste* Futureprint. https://www.futureprint.tech/the-futureprint-blog/uv-led-prevents-mercury-bulb-waste-and-saves-energy (accessed Dec. 17, 2022).

206. Davis, J. & Rountree, K. *Initial Benchmarks of UV LEDs and Comparisons with White LEDs* DOE/EE-2543, 1859677, 8841 (Jan. 26, 2022), DOE/EE–2543, 1859677, 8841. https://www.osti.gov/servlets/purl/1859677/ (accessed Dec. 1, 2022).

207. Lavender, B. *How Much Does It Cost? — AgAir Update* https://agairupdate.com/2017/04/03/how-much-does-it-cost/ (accessed Dec. 20, 2022).

208. Lockley, A., MacMartin, D. & Hunt, H. An Update on Engineering Issues Concerning Stratospheric Aerosol Injection for Geoengineering. *Environmental Research Communications* **2,** 082001. ISSN: 2515-7620. https://dx.doi.org/10.1088/2515-7620/aba944 (Aug. 2020).

209. Moriyama, R. *et al.* The Cost of Stratospheric Climate Engineering Revisited. *Mitigation and Adaptation Strategies for Global Change* **22,** 1207–1228. ISSN: 1573-1596. https://doi.org/10.1007/s11027-016-9723-y (Dec. 1, 2017).

210. Davidson, P., Burgoyne, C., Hunt, H. & Causier, M. Lifting Options for Stratospheric Aerosol Geoengineering: Advantages of Tethered Balloon Systems. *Philosophical Transactions of the Royal Society A: Mathematical, Physical and Engineering Sciences*. https://royalsocietypublishing.org/doi/10.1098/rsta.2011.0639 (Sept. 13, 2012).

211. Federal Communications Commission. *Catalog of Potential Expenses and Estimated Costs* https://docs.fcc.gov/public/attachments/DA-17-154A2.pdf (accessed June 25, 2023).

212. Meghana, A., Smitha, B. & Jagwani, S. *Technological Advances in Airborne Wind Power: A Review* in *Emerging Research in Computing, Information, Communication and Applications* (eds Shetty, N. R., Patnaik, L. M., Nagaraj, H. C., Hamsavath, P. N. & Nalini, N.) (Springer, Singapore, 2022), 349–359. ISBN: 9789811613425.

213. Jaenicke, R. in *International Geophysics* (ed Hobbs, P. V.) 1–31 (Academic Press, Jan. 1, 1993). https://doi.org/10.1016/S0074-6142(08)60210-7 (accessed Feb. 17, 2023).

214. Jennings, S. G. The Mean Free Path in Air. *Journal of Aerosol Science* **19,** 159–166. ISSN: 0021-8502. https://doi.org/10.1016/0021-8502(88)90219-4 (Apr. 1, 1988).

215. *U.S. Energy Information Administration - EIA - Independent Statistics and Analysis* https://www.eia.gov/environment/emissions/co2_vol_mass.php (accessed Feb. 24, 2023).

216. Anderson, J. O., Thundiyil, J. G. & Stolbach, A. Clearing the Air: A Review of the Effects of Particulate Matter Air Pollution on Human Health. *Journal of Medical Toxicology* **8,** 166–175. ISSN: 1556-9039. pmid: 22194192. https://www.ncbi.nlm.nih.gov/pmc/articles/PMC3550231/ (June 2012).

217. California Air Resources Board. *Wildfire Emissions Estimates for 2021* California Air Resources Board, 2022. https://ww2.arb.ca.gov/sites/default/files/classic/cc/inventory/Wildfire%20Emission%20Estimates%202000-2021.pdf (accessed Mar. 10, 2023).

218. *Hydrogen Peroxide Dispersal — Atmospheric Methane Removal* Spark Climate Solutions. https://www.sparkclimate.org/methane-removal/primer/approaches/hydrogen-peroxide (accessed Oct. 30, 2024).

219. Gu, Y. *et al.* Industrial Electrosynthesis of Hydrogen Peroxide over P-Block Metal Single Sites. *Nature Synthesis* **4,** 614–621. ISSN: 2731-0582. https://www.nature.com/articles/s44160-024-00722-2 (May 2025).

220. *A Review of Ozone Systems Costs for Municipal Applications.* IOA Pan American Group, Feb. 8, 2025. http://dx.doi.org/10.1080/01919512.2018.1467187 (accessed July 22, 2025).

221. Manke, G. C. & Setser, D. W. Measuring Gas-Phase Chlorine Atom Concentrations: Rate Constants for Cl + HN3, CF3I, and C2F5I. *The Journal of Physical Chemistry A* **102,** 153–159. ISSN: 1089-5639. https://doi.org/10.1021/jp972118g (Jan. 1, 1998).

222. Park, J. Y., Slagle, I. R. & Gutman, D. Kinetics of the Reaction of Chlorine Atoms with Vinyl Bromide and Its Use for Measuring Chlorine-Atom Concentrations. *The Journal of Physical Chemistry* **87,** 1812–1818. ISSN: 0022-3654. https://doi.org/10.1021/j100233a032 (May 1, 1983).

223. Basu, S. *A Quantitative Study of the Chlorine Atom Concentration in Plasma* (Ohio University, 2008). https://etd.ohiolink.edu/acprod/odb_etd/r/etd/search/10?p10_accession_num=ohiou1204918172&clear=10&session=103197123616741 (accessed July 30, 2025).

224. US EPA, O. R. D. *EPA Air Method, Toxic Organics - 15 (TO-15): Determination of Volatile Organic Compounds (VOCs) in Air Collected in Specially-Prepared Canisters and Analyzed by Gas Chromatography/Mass Spectrometry (GC/MS)* https://19january2017snapshot.epa.gov/homeland-security-research/epa-air-method-toxic-organics-15-15-determination-volatile-organic (accessed June 30, 2025).

225. *Methyl Chloride* Occupational Safety and Health Administration. https://www.osha.gov/chemicaldata/556 (accessed Apr. 11, 2025).

226. Shi, Z., Sun, X., Lu, Y., Xi, L. & Zhao, X. Emissions of Ammonia and Hydrogen Sulfide from Typical Dairy Barns in Central China and Major Factors Influencing the Emissions. *Scientific Reports* **9,** 13821. ISSN: 2045-2322. https://www.nature.com/articles/s41598-019-50269-y (Sept. 25, 2019).

227. Koh, S.-H. & Shaw, A. R. Gaseous Emissions from Wastewater Facilities. *Water Environment Research* **90,** 1563–1575. ISSN: 1554-7531. https://doi.org/10.2175/106143018X15289915807308 (2018).

228. Ashmore, P. G. & Spencer, M. S. Concurrent Molecular and Chlorine Atom Mechanisms in the Reversible Dissociation of Nitrosyl Chloride. *Transactions of the Faraday Society* **55,** 1868–1883. ISSN: 0014-7672. https://pubs.rsc.org/en/content/articlelanding/1959/tf/tf9595501868 (Jan. 1, 1959).

229. Sisler, H. H., Neth, F. T., Drago, R. S. & Yaney, D. The Synthesis of Chloramine by the Ammonia-Chlorine Reaction in the Gas Phase. *Journal of the American Chemical Society* **76,** 3906–3909. ISSN: 0002-7863. https://doi.org/10.1021/ja01644a010 (Aug. 1, 1954).

230. Wiesehahn, M., Zimmermann, E. M. & Agar, D. W. Experimental Splitting of Hydrogen Sulfide by Halogens for Application in Reaction Cycles. *Chemie Ingenieur Technik* **94,** 1088–1095. ISSN: 1522-2640. https://doi.org/10.1002/cite.202100174 (2022).

231. *The Atmosphere — National Oceanic and Atmospheric Administration* https://www.noaa.gov/jetstream/atmosphere (accessed June 30, 2025).

232. Hempel, S. *et al.* Methane Emission Characteristics of Naturally Ventilated Cattle Buildings. *Sustainability* **12,** 4314. ISSN: 2071-1050. https://www.mdpi.com/2071-1050/12/10/4314 (Jan. 2020).

233. Herbut, P. Ammonia Concentrations in a Free-Stall Dairy Barn. *Annals of Animal Science.* https://www.cabidigitallibrary.org/doi/pdf/10.5555/20143130229 (Feb. 2014).

234. Kiliç, İ., Onuk, A., Şimşek, E. & Yaslıoğlu, E. Bir Koyun Ağılında Amonyak ve Karbondioksit Konsantrasyonları. *Kahramanmaraş Sütçü İmam Üniversitesi Doğa Bilimleri Dergisi.* ISSN: 1309-1743. https://dergipark.org.tr/tr/doi/10.18016/ksudobil.266019 (Mar. 10, 2017).

235. Yuan, B. *et al.* Emissions of Volatile Organic Compounds (VOCs) from Concentrated Animal Feeding Operations (CAFOs): Chemical Compositions and Separation of Sources. *Atmospheric Chemistry and Physics* **17,** 4945–4956. ISSN: 1680-7316. https://acp.copernicus.org/articles/17/4945/2017/ (Apr. 18, 2017).

236. Yang, Y. *et al.* Assessment of Methane and Nitrous Oxide Emissions from Urban Community Sewer Networks: Field Quantification and Insights into Environmental Factors. *Water Research X* **28,** 100307. ISSN: 2589-9147. https://doi.org/10.1016/j.wroa.2025.100307 (Sept. 1, 2025).

237. Romanova, A. & Alani, A. Monitoring CO2 and H2S Emission in Live Austrian and UK Concrete Sewer Pipes. *International Journal of Civil, Environmental, Structural, Construction and Architectural Engineering* **9,** 445–449. http://scholar.waset.org/1999.3/10001098 (2015).

238. Austigard, Å. D., Svendsen, K. & Heldal, K. K. Hydrogen Sulphide Exposure in Waste Water Treatment. *Journal of Occupational Medicine and Toxicology* **13,** 10. ISSN: 1745-6673. https://doi.org/10.1186/s12995-018-0191-z (Mar. 1, 2018).

239. Keller-Rudek, H., Moortgat, G. K., Sander, R. & Sörensen, R. The MPI-Mainz UV/VIS Spectral Atlas of Gaseous Molecules of Atmospheric Interest. *Earth System Science Data* **5,** 365–373. ISSN: 1866-3516. https://essd.copernicus.org/articles/5/365/2013/ (Dec. 3, 2013).

240. *High-Reflectance PTFE Sheets* https://www.thorlabs.com/newgrouppage9.cfm?objectgroup_id=13871 (accessed July 27, 2025).

241. *Sodium Hypochlorite vs Chlorine for Water Treatment Facilities* https://blog.safetysolutions.co.nz/sodium-hypochlorite-vs-chlorine-for-water-treatment-facilities (accessed July 26, 2025).

242. *Bay Area Chemical Consortium Price Comparison* Bay Area Clean Water Agencies, Apr. 2024. https://bacwa.org/wp-content/uploads/2024/04/2024-BACC-Price-Comparison.pdf (accessed July 26, 2025).

243. *Nexgen On-Site Chlorine Generators* Chlorking. https://chlorking.com/products/nex-gen-on-site-chlorine-generators/ (accessed July 26, 2025).

244. *Compare and Review Saltwater Chlorine Generator Prices and Features* https://www.discountsaltpool.com/compare-saltwater-chlorine-generator-systems-for-pools?srsltid=AfmBOoqLBS1y-ApO1n0yrEi0UgOr2WJBum5nHQVZtontclUyZpP (accessed July 26, 2025).

245. *On-Site Low-Strength Sodium Hypochlorite Generators, ClorTec® — De Nora* denora. https://www.denora.com/our-brands/ClorTec.html (accessed July 26, 2025).

246. *Hydrochloric Acid Price - Historical & Current — Intratec.Us* https://www.intratec.us/solutions/primary-commodity-prices/commodity/hydrochloric-acid-prices (accessed July 26, 2025).

247. *SAS Output* https://www.eia.gov/electricity/annual/html/epa_02_10.html (accessed July 25, 2025).

248. *Electricity Price Statistics* https://ec.europa.eu/eurostat/statistics-explained/index.php?title=Electricity_price_statistics (accessed July 25, 2025).

249. US EPA, O. A. R. *Cost Reports and Guidance for Air Pollution Regulations* https://www.epa.gov/economic-and-cost-analysis-air-pollution-regulations/cost-reports-and-guidance-air-pollution (accessed July 27, 2025).

250. *Regulations.Gov* https://www.regulations.gov/document/EPA-HQ-OAR-2002-0057-0042 (accessed July 27, 2025).

251. *Pycel 1.0b30: A Library for Compiling Excel Spreadsheets to Python Code & Visualizing Them as a Graph* https://github.com/stephenrauch/pycel (accessed July 27, 2025).

252. Ayub, A., Cheong, Y. K., Castro, J. C., Cumberlege, O. & Chrysanthou, A. Use of Hydrogen Peroxide Vapour for Microbiological Disinfection in Hospital Environments: A Review. *Bioengineering* **11,** 205. ISSN: 2306-5354. pmid: 38534479. https://www.ncbi.nlm.nih.gov/pmc/articles/PMC10967804/ (Feb. 22, 2024).

253. *Hydrogen Peroxide Price - Historical & Current — Intratec.Us* https://www.intratec.us/solutions/primary-commodity-prices/commodity/hydrogen-peroxide-prices (accessed July 24, 2025).

254. Kamachi, T. *et al.* Computational Exploration of the Mechanism of the Hydrogenation Step of the Anthraquinone Process for Hydrogen Peroxide Production. *The Journal of Physical Chemistry C* **119,** 8748–8754. ISSN: 1932-7447. https://doi.org/10.1021/acs.jpcc.5b01325 (Apr. 23, 2015).

255. Zhao, Y. *et al.* On the Role of Trend and Variability in the Hydroxyl Radical (OH) in the Global Methane Budget. *Atmospheric Chemistry and Physics* **20,** 13011–13022. ISSN: 1680-7324. https://acp.copernicus.org/articles/20/13011/2020/ (Nov. 6, 2020).

256. *Vapor Pressures* USP Technologies. https://usptechnologies.com/vapor-pressures/ (accessed July 23, 2025).

257. Zaib, A. & Begum, S. S. Calibration of Hydrogen Peroxide Vapour Sensor. *Advances in Chemical Engineering and Science* **12,** 163–171. ISSN: 2160-0392, 2160-0406. https://www.scirp.org/journal/doi.aspx?doi=10.4236/aces.2022.123012 (2022).

258. *JPL Data Evaluation* Jet Propulsion Laboratory. https://jpldataeval.jpl.nasa.gov/index.html (accessed Oct. 28, 2025).

259. *NIST Chemical Kinetics Database* National Institute of Standards and Technology. https://kinetics.nist.gov/kinetics/index.jsp (accessed Oct. 28, 2025).

260. Hamryszczak, Z. *et al.* Measurement Report: Hydrogen Peroxide in the Upper Tropical Troposphere over the Atlantic Ocean and Western Africa during the CAFE-Africa Aircraft Campaign. *Atmospheric Chemistry and Physics* **23,** 5929–5943. ISSN: 1680-7316. https://acp.copernicus.org/articles/23/5929/2023/ (May 30, 2023).

261. Andrade, L. S. *et al.* Metal–Organic Frameworks as Catalysts and Biocatalysts for Methane Oxidation: The Current State of the Art. *Coordination Chemistry Reviews* **481,** 215042. ISSN: 0010-8545. https://doi.org/10.1016/j.ccr.2023.215042 (Apr. 15, 2023).

262. Horowitz, H. M. Impacts of Iron Salt Aerosol and Hydroxyl Radical Release on the Methane Lifetime. *National Academies Press* (2024).

263. Christopher, P. Automating Academic Laboratories: Promoting Reliability, Productivity, and Safety. *ACS Energy Letters* **5,** 2737–2738. https://doi.org/10.1021/acsenergylett.0c01644 (Aug. 14, 2020).

264. Bailey, D. & Wright, E. in *Practical SCADA for Industry* (eds Bailey, D. & Wright, E.) 11–63 (Newnes, Oxford, Jan. 1, 2003). ISBN: 978-0-7506-5805-8. https://doi.org/10.1016/B978-075065805-8/50002-7 (accessed Nov. 29, 2023).

265. Abolhasani, M. & Kumacheva, E. The Rise of Self-Driving Labs in Chemical and Materials Sciences. *Nature Synthesis* **2,** 483–492. ISSN: 2731-0582. https://www.nature.com/articles/s44160-022-00231-0 (June 2023).

266. Selekman, J. A. *et al.* High-Throughput Automation in Chemical Process Development. *Annual Review of Chemical and Biomolecular Engineering* **8,** 525–547. pmid: 28460183. https://doi.org/10.1146/annurev-chembioeng-060816-101411 (2017).

267. Shevlin, M. Practical High-Throughput Experimentation for Chemists. *ACS Medicinal Chemistry Letters* **8,** 601–607. https://doi.org/10.1021/acsmedchemlett.7b00165 (June 8, 2017).

268. Mehta, B. R. & Reddy, Y. J. in *Industrial Process Automation Systems* (eds Mehta, B. R. & Reddy, Y. J.) 1–36 (Butterworth-Heinemann, Oxford, Jan. 1, 2015). ISBN: 978-0-12-800939-0. https://doi.org/10.1016/B978-0-12-800939-0.00001-2 (accessed May 12, 2025).

269. Elliott, C., Vijayakumar, V., Zink, W. & Hansen, R. National Instruments LabVIEW: A Programming Environment for Laboratory Automation and Measurement. *SLAS Technology. Special Issue: Programming Languages and Automation* **12,** 17–24. ISSN: 2472-6303. https://doi.org/10.1016/j.jala.2006.07.012 (Feb. 1, 2007).

270. *CSS - Content / Spec* https://www.certif.com/content/spec/ (accessed May 12, 2025).

271. Inductive Automation. *Innovative SCADA Software for Process Control and Data Management* https://inductiveautomation.com/scada-software/ (accessed Nov. 29, 2023).

272. Siemens AG. *SIMATIC WinCC V7 / V8* https://www.siemens.com/global/en/products/automation/industry-software/automation-software/scada/simatic-wincc-v7.html (accessed Nov. 29, 2023).

273. Bronger, T., Thalhammer, G. *PyVISA: Control Your Instruments with Python* https://pyvisa.readthedocs.io/en/latest/ (accessed Nov. 29, 2023).

274. Grecco, H. E., Masip, M., Jais, P., et al. *Lantz: An Automation and Instrumentation Toolkit in Python.* https://lantz.readthedocs.io/en/0.3/ (accessed Nov. 29, 2023).

275. Johnson, J. L., tom Wörden, H. & van Wijk, K. PLACE: An Open-Source Python Package for Laboratory Automation, Control, and Experimentation. *SLAS Technology* **20,** 10–16. ISSN: 2472-6303. https://doi.org/10.1177/2211068214553022 (Feb. 1, 2015).

276. Oliphant, T. E. Python for Scientific Computing. *Computing in Science & Engineering* **9,** 10–20. ISSN: 1558-366X. https://ieeexplore.ieee.org/abstract/document/4160250 (May 2007).

277. Prechelt, L. in *Advances in Computers* 205–270 (Elsevier, Jan. 1, 2003). https://doi.org/10.1016/S0065-2458(03)57005-X (accessed Nov. 29, 2023).

278. Galen Collins et al. *PyModbus - A Python Modbus Stack* https://pymodbus.readthedocs.io/en/latest/ (accessed Nov. 30, 2023).